UNIVERSITÀ DEGLI STUDI DI CAMERINO

School of Advanced Studies

DOCTORAL COURSE IN

Chemical Sciences

XXXIV cycle

SYNTHESIS, CHARACTERISATION AND APPLICATION OF RU(II) AND OS(II) COMPLEXES AND POROUS FRAMEWORK MATERIALS

PhD Student

Dr. Fenghe Duan

Supervisors

Prof. Riccardo Pettinari

Co- supervisors

Prof. Liming Zhou

Table of Contents

Abbreviations

AA	Ascorbic acid
AE	Au electrode
AFs	aflatoxins
bdcurcH	Bisdemethoxycurcumin
BE	Binding energy
BET	Brunauer-Emmett-Teller
biph	Biphenyl
BSA	Bovine serum albumin
CB	Conduction band
COFs	Covalent organic frameworks
CDT	Chemodynamic therapy
CRC	Colorectal cancer
CLSM	Confocal laser scanning microscopy
CT26	Colorectal cancer
CTC	Chlortetracycline
CuPc-TA	Amino-decorated Cu phthalocyanine
CV	Cyclic Voltammetry
curcH	Curcumin
DA	Dopamine
DCF	2,7-dichlorofluorescein
DCFH-DA	2',7'-dichlorodiacetate
DON	Deoxynivalenol
DLS	Dynamic light scattering
DMF	Dimethylformammide
DMEM	Dulbecco's modified Eagle's medium
DMSO	Dimethyl sulfoxide
DMSO-d_6	Deuterated dimethyl sulfoxide

DNA	Deoxyribonucleic acid
DPBF	1,3-diphenylisobenzopyran
DPV	Differential Pulse Voltammetry
EDS	Energy-dispersive X-ray spectroscopy
EB	Ethidium bromide
EIS	Electrochemical Impedance Spectroscopy
EPR	electron paramagnetic resonance
ESI-MS	Electrospray ionization mass spectrometry
ESR	Electron spin resonance
FB 1	fumonisin B 1
FE-SEM	Field emission scanning electron microcopy
FT-IR	Fourier Transform-Infra-Red
GCE	Glassy carbon electrode
H&E	Hematoxylin-eosin
HER2	Human epidermal growth factor receptor-2
HOMO	Molecular orbital
H_2BDC	1,4-benzenedicarboxylic acid
IC_{50}	Half maximal inhibitory concentration
ICG	Indocyanine green
ICP-MS	Inductively Coupled Plasma - Mass Spectrometry
LOD	limit of detection
LUMO	Lowest unoccupied molecular orbital
MB	Methylene blue
MCF7	Human breast cancer cell line
MCOF	Magnetic COF
MOFs	Metal–organic frameworks
MTT	3-(4,5-dimethylthiazol-2-yl)-2,5-diphenyltetrazolium bromide
MTV Ti-MOFs	Multivariate polymertitanium-MOFs
MTT	3-(4,5-dimethyl-2-thiazolyl)-2,5-diphenyl-2H-tetrazolium bromide
NPs	Nanoparticles

NLDFT	Non-local density functional theory
NMR	Nuclear Magnetic Resonance spectroscopy
NIR	Near-infrared
OTC	Oxytetracycline
PBS	phosphate buffered saline
***p*-cym**	*para*-cymene
PCE	Photothermal conversion efficiencies
PET	Polyethylene terephthalate
ph	Phenyl
phen	Phenantroline
PAI	Photoacoustic imaging
PDT	Photodynamic therapy
PEG	Polyethylene glycol
PL	Photo-luminescence
PTA	1,3,5-triaza-7-phosphaadamantane
PTA-Me	*N*-Methyl-1,3,5-triaza-7-phosphaadamantane
PTT	Photothermal therapy
PXRD	Powder X-ray diffraction
RAED	Ruthenium Arene Ethylene Diamine
RAPTA	Ruthenium(II)-Arene-PTA complexes
RAPTA-B	[Ru(η^6-benzene)Cl_2(PTA)]
RAPTA-C	[Ru(η^6-*p*-cym)Cl_2(PTA)]
RAPTA-T	[Ru(η^6-toluene)Cl_2(PTA)]
Renca	Mouse Renal Carcinoma
TEM	Transmission Electron Microscope
Pc	Phthalocyanine
PS	Photosensitizer
ROS	Reactive oxygen species
RPMI	Roswell Park Memorial Institute
SAED	Selective-area electron diffractometry

SD	Standard deviation
TEMP	2,2,6,6-tetramethylpiperidine
TME	Tumor microenvironment
TET	Tetracycline
XPS	X-ray photo-electron spectroscopy
ZEN	Zearalenone
UA	uric acid
UV-Vis	Ultraviolet–Visible spectroscopy
4T1	Mouse breast cancer cells
5-HT	Serotonin
bTDC	2,2′-Bithiophenyl-5,5′-dicarbaldehyde

Chapter 1. Ruthenium and Osmium compounds

Nowadays, cancer diseases have a massive global impact on our health services, economies, and resources. Cancer research has undoubtedly become one of the most important pursuits of modern science due to high mortality rates. Cancer is caused by malfunctioning cells, which cause them to divide rapidly, grow to abnormal sizes, and infiltrate neighbouring organs, eventually leading to death. Due to abnormal resistance of cancerous cells to naturally released apoptotic signals, three main treatment strategies for cancer are initiated: surgical removal of the tumour, chemical intrusion into the cancer cells, and chemotherapy [1].

1.1 Organometallic complexes for cancer therapy

To date, metals and metal-containing complexes have developed rapidly in biology, particularly its branch, biological organometallic chemistry, which investigates the role of metal complexes with direct metal-carbon bonds. Among them, vitamin B12 is the most well-known natural bioorganometallic compound as it contains cobalt bound directly to a carbon atom.

Currently, organometallic chemistry has great potential for the development of novel therapeutic agents because of its novel mechanism of action. Based on its advantages including the ability to design a variety of different molecular structures due to different coordination numbers and geometries, metal and ligand choices, oxidation states, and overall reactivity and charge, which make it can serve as a scaffold for further functionalized and design. Nowadays, metal complexes and organic molecules are both commonly used in cancer treatment. Organometallic compounds have sparked a surge of interest in their use to treat cancer and other diseases in recent years. Many transition metal complexes have been synthesized and tested for anticancer activity since the discovery of cisplatin.

Metal complexes such as platinum, ruthenium, osmium, rhodium, iridium, palladium, copper, and iron are currently being investigated as possible anticancer

drugs. Non-radioactive indium(III) complexes are also of interest to scientists.

Since the anti-tumor properties of the complex cis-diaminedichloroplatinum (II) (cisplatin) were studied, it remains the gold standard in cancer treatment to this day [2]. Cisplatin ($PtCl_2(NH_3)_2$) was the first metal-based anticancer drug to be approved for use in humans. Cisplatin and its derivatives are widely used to treat cancers of the lungs, colon, ovary, testicles, bladder, cervix, and other organs. However, cisplatin-based therapy has a number of drawbacks: it is extremely toxic, and cancer cells can quickly develop resistance. Despite its widespread use, cisplatin and its derivatives are linked to a variety of toxicities, including nephrotoxicity, ototoxicity, gastrotoxicity, and neurotoxicity[3]. New cisplatin derivatives are being considered to overcome these pharmacological limitations. For example, Pt(II) complexes can effectively kill differentiated tumor cells but not cancer stem cells [4]. New Pt(IV) complexes can be used as prodrugs to activate differentiated tumor cells. Furthermore, the arsenal of platinum-based anticancer agents has been expanded to include multi-action anticancer prodrugs, whose structures are exhibit in **Figure 1**.

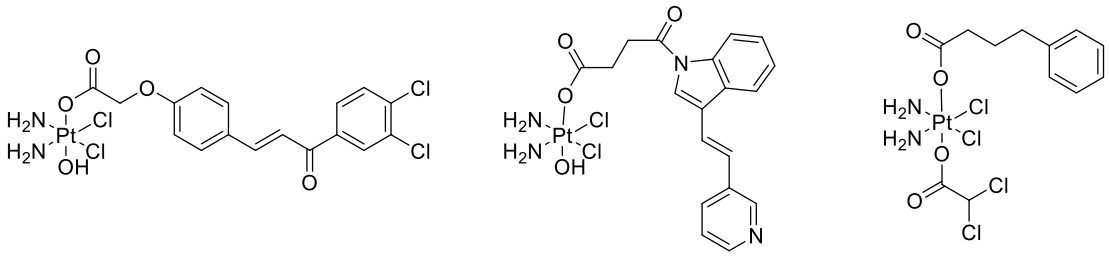

Figure 1. Structures of cisplatin multi-action derivatives 1–3[4].

To overcome the shortcomings of cisplatin, seeking proper alternatives continues among other metals including but not limited to Ru, Os, Rh, Ir, Cu, and Fe. Up to now, Ru and Rh complexes are used to as a substitute for less toxic platinum anticancer complexes [5,6]; In pre-clinical research, ferrocifen is the most characteristic of the anticancer agents in clinical; Cu(II) complexes with 2-pyridylbenzimidazole derivatives or Gly-Leu dipeptide as ligands can kill cancer cells by damaging their DNA. In addition, the Os(II) complex was found to be cytotoxic to breast cancer cells[7].

Osmium, which is in the same period as platinum, is a ruthenium analog, so it is

reasonable to assume that complexes of osmium might exhibit similar anticancer properties. In comparison to platinum and ruthenium, however, there have been far fewer studies on osmium and ruthenium complexes. Therefore, a series of osmium and ruthenium complexes were synthesized and explored their properties.

1.2 Arene- ruthenium and osmium complexes

Since the successful separation of bis(phenyl)chromium by Winkhaus and Singer in 1967, organometallic chemistry materials with different roles have been synthesized and then applied in various fields. Organometallic chemistry mainly studies the synthesis and property of transition metal complexes with coordinating aromatic ligands [8], it has been applied in many fields in modern chemistry. Based on the above work, Winkhaus and Singer first synthesized half-sandwich (η^6-arene)-ruthenium(II) complexes with excellent properties in 1967[9]. which were easily to synthesize the dimer precursor [{RuCl(μ-Cl) (η6-arene)}$_2$] by reaction with after dehydrogenation of cyclohexadiene derivatives with $RuCl_3 \cdot nH_2O$. Since the rich reactivity of the dimer facilitates the exchange and functionalization of coordinating arenes, it is possible to introduce a variety of mono-, bi- and tridentate P-, N-, O-, S-, or C-donor ligands via cleavage and substitution of chlorine ligands in the coordination layer of the metal through chlorine bridges [10]. Given that the high structural diversity and the fine adjustment of the stereo-electronic properties of the metal centre of this kind of complexes, (η^6-arene)-ruthenium(II) complexes currently represent one of the most versatile families of organometallic ruthenium compounds affords their application in different fields, such as medicinal and supramolecular chemistry and homogeneous catalysis [11].

Werner described that electrophilic the metal centre of half-sandwich-type complexes were classified into two categories: [(η^5-C_5H_5)M(PMe_3)$_2$] (M=Co, Rh and Ir) and [(η^6-C_6H_6)M(PMe_3)$_2$] (M= Ru and Os) [12].Thus, Os(II) arene complexes is a kind of half-sandwich organometallic complexes, which have a similar structural Ru(II) arene complexes. As shown in **Figure 2**, this kind of complexes both adopting the presence of a metal centre in a pseudo-octahedral coordination environment with three

coordination sites occupied by an aromatic arene ring bound in a 6-manner and three other coordination sites occupied by different ligands. The geometry of these half-sandwich compounds can be depicted as octahedral if the six-electron donor arene ligand occupies three facial coordination positions, or as pseudo-tetrahedral, also known as piano-stool geometry, if it occupies only one coordination position (**Figure 2**)[1].

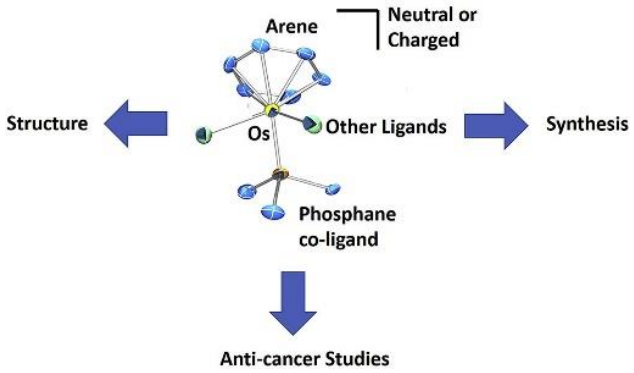

Figure 2. Structure of piano-stool Osmium(II)-arene complexes.

The exploration of arene osmium complexes bearing a phosphane co-ligand with concomitant anti-tumourigenic studies began surprisingly late, in 2005[13]. Such a late appearance is surprising, as it had been known for a long time that the ruthenium analogues were biologically active [14]. Using the synthetic protocol for the well-known ruthenium RAPTA-C [15] complex Dorcier et al. prepared and characterised three related novel osmium compounds: [Os(η^6-p-cymene)(PTA)Cl_2] **(4)**, [Os(η^6-p-cymene)Cl_2(PTA-Me)]Cl, **(5)** [Os(η6-benzene)(PTA)Cl_2] **(6)** (**Scheme 1**, **Figure 3**). They tested the compounds reactivity towards a single-stranded 14-mer oligonucleotide (5′-ATACATGGTACATA-3′) by using electrospray ionisation mass spectrometry. It was noted that PTA and PTA-Me^+ ligands remain at the complex during association to oligomers. In addition, the PTA-Me^+ species was shown to be more reactive and less selective than the PTA analogue. Such reactivity was attributed to the positive charge of the agent being more attracted to the polyanion. The researchers proved that at lower pH values the compounds bind more actively to the oligomer chains. This phenomenon was attributed to pH dependency of PTA ligands.

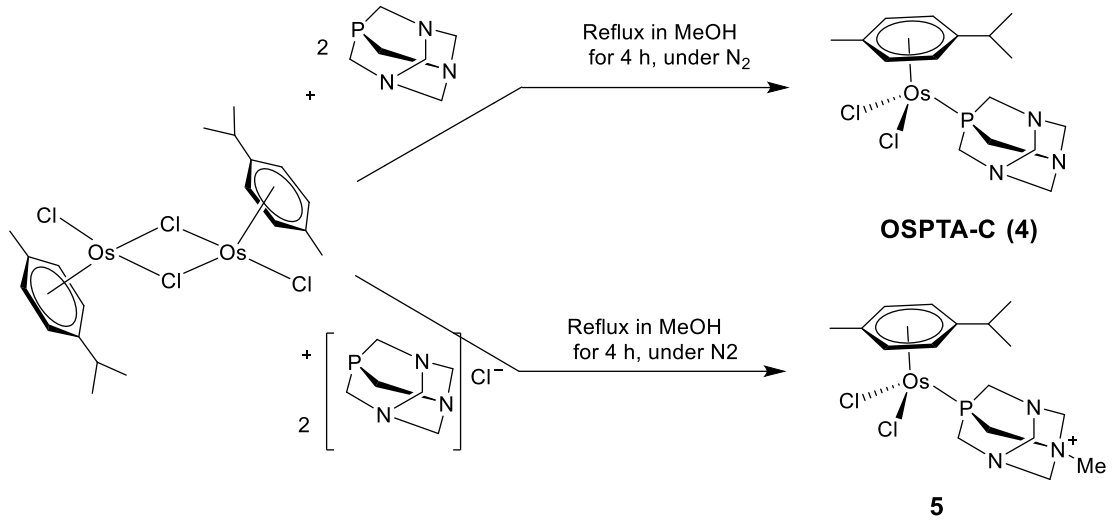

Scheme 1. Synthetic routes for RAPTA-C osmium analogues: OSPTA-C (4) and 5.

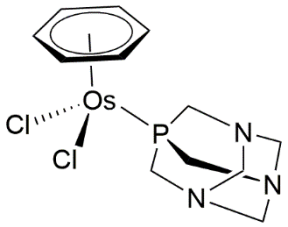

Figure 3. Structure of (Os(η^6-benzene)(PTA)Cl_2).

1.2.1 Ruthenium anticancer compounds

Today, to overcome the challenges of Pt-based drugs, complexes of almost all transition metals have been synthesized and investigated as potential anticancer agents. Each compound follows a discrete mechanism in the cell that is influenced by its coordination geometry and ligand set. Among various metal complexes, some of the most promising results have been achieved with ruthenium [15]. Ruthenium(III) and (II) complexes have been intensively studied and different properties and mechanisms of action have been observed. Despite their differences, the compounds were discovered to be active, and some of them were put into clinical trials. The most promising Ru (III) candidates were thought to be KP1019 and NAMI-A. However, due to dose-dependent toxicity and the occurrence of side effects, NAMI-A was discontinued at stage II of clinical trials [16]. Nonetheless, NAMI-A was found to be effective against solid tumors in clinical trials[17]. Both KP1019 and its water-soluble derivative (N)KP1339 were found to be effective against several cancers with only minor side effects in phase I

clinical trials. Since 2001, studies have shown that new classes of Ru (II) arene compounds with phosphane co-ligands are much less cytotoxic but have other antitumor properties, treating cancer cells in a variety of ways [18]. For example, one of them includes attachment of the RAPTA-C complex (**Figure 4**) to the histone protein core in chromatin where two chlorides dissociate leading to tumour growth suppression [19].

However, it has also been shown that some (lower than cisplatin) nuclei penetrate and interact with DNA[18]. While the mechanism is not fully understood, it is obviously that low-dose RAPTA-C combine with other drugs offers a potential alternative approach to treat metastatic cells. RAPTA-C showed low cytotoxicity in vitro, while it can inhibit tumour growth extensively in vivo. As mentioned above, studies of the behaviour of complexes with various metal centers, coordination geometry and organic ligands is very important, not only in vitro but also in vivo. RAPTA-C outperforms many platinum derivatives by overcoming drug resistance and significantly reducing toxicity, thanks to a mechanism that differs from cisplatin [16]. Cisplatin enters the cell in a variety of ways, including passive diffusion. RAPTA-C, on the other hand, tracks receptor-mediated cellular uptake and specifically increases uptake in metastatic cells. Cisplatin can enter the cell through passive diffusion. However, RAPTA-C tracks receptor-mediated cellular uptake, which is increased in metastatic cells specifically. Furthermore, the protonation susceptibility of the PTA (PTA = 1,3,5-Triaza-7-phosphaadamantane) ligand increases RAPTA compound selectivity toward more hypoxic cells [15]. Cancer cells have a low pH because their metabolism has been altered by increased cell division [15]. Dyson et al., forerunners in the development of RAPTA compounds, observed that protonation of PTA in the cytoplasm produces a species that causes more DNA damage than the unprotonated compound.

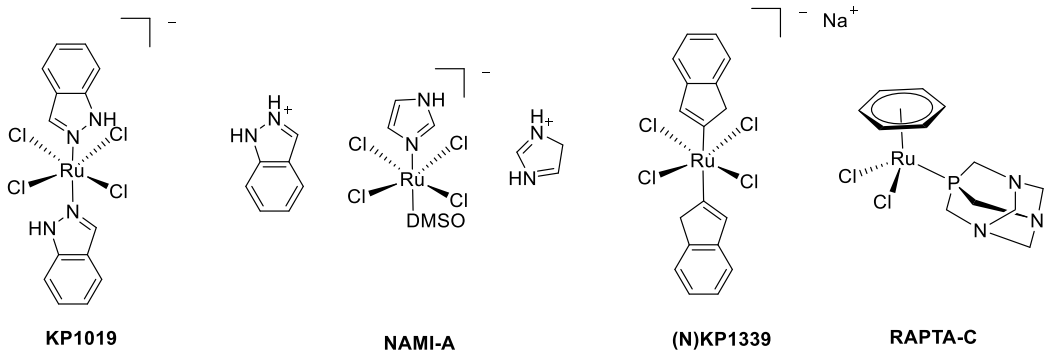

Figure 4. Structures of Ru (III) (KP1019, NAMI-A and (N)KP1339) and Ru (II) (RAPTA-C) compounds[20].

1.2.2 Osmium anticancer compounds

Following the seminal discovery of the anticancer activity of DNA-targeting cisplatin and later its analogous carboplatin and oxaliplatin, the field of inorganic medicinal chemistry has exploded in recent years. Nowadays, these platinum-based drugs are used in about half of all cancer treatment regimens[21]. However, their therapeutic efficacy is limited as it is for many other chemotherapeutics, by the emergence of drug resistance and severe adverse effects[22]. Given the clinical success of platinum-based compounds, extensive research has been focused on the anticancer activity of complexes containing alternative metal ions. To avoid the limitations of the platinum drugs, some studies were focused on the novel therapeutic potential of other inorganic complexes. Despite their high toxicity, some osmium coordination complexes show non-toxic ways to potentially treat tumours [23]. In recent years, as an analogue of ruthenium, Os complex has become the most promising class of non-platinum compound in cancer research. Osmium exhibits many beneficial and unique properties such as slow ligand exchange kinetics[24], predilection for higher oxidation states, as well as stronger π-backdonation when in low oxidation states. Given that their relative inertness and sufficient stability under physiological conditions, osmium complexes are regarded as promising alternatives to ruthenium-based anticancer agents.

Osmium and ruthenium are heavy metal elements in the same main group. According to the periodic law of elements, osmium and ruthenium demonstrate similar properties. Thereby, they can be served as a potential anticancer drug. Compared with

the complexes of the same element ruthenium, the synthesis conditions of osmium complexes are milder. Since 2006, there have been more and more studies on osmium complexes in inhibiting tumors. The application of osmium complexes in anticancer has the potential to replace ruthenium complexes. Previous reports on the toxicity of the complexes indicate that the osmium compound OsO_4 is highly toxic, the Os(II) and Os(III) complexes have little toxicity, and the aryl Os(II) complexes exhibit potential anticancer activity compared to Cisplatin [25].

Some osmium compounds were synthesized and measured as anticancer agents [26]. The majority of the structures tested were analogous to ruthenium complexes, and some of them demonstrated the benefits of using osmium as the metal [13]. The analogues had the same or greater anti-proliferative activity as the parent ruthenium structures. Other osmium arene compounds have demonstrated cytotoxic levels comparable to cisplatin and carboplatin, though their mechanism involved DNA unwinding rather than bending[27]. Because the chemical structure and oxidation state of osmium are different, the observed mechanism of action is also different. For example, both synthesised octahedral complexes **6** and **7** (**Figure 5**) are capable of apoptosis: 1a is disrupted the replication cycle at the G2/M phase causes apoptosis while 1b induces apoptosis by inducing endoplasmic reticulum stress and enlargement and upregulation of the protein p53 [28]. Most importantly, 1a has been shown to be effective against cancer stem cells, which are responsible for recurrence and reappearance of cancer. Another osmium complex, FY26, inhibits tumor growth by increasing the production of reactive oxygen species (ROS) inside the target cells, similar to RAPTA-C [29].

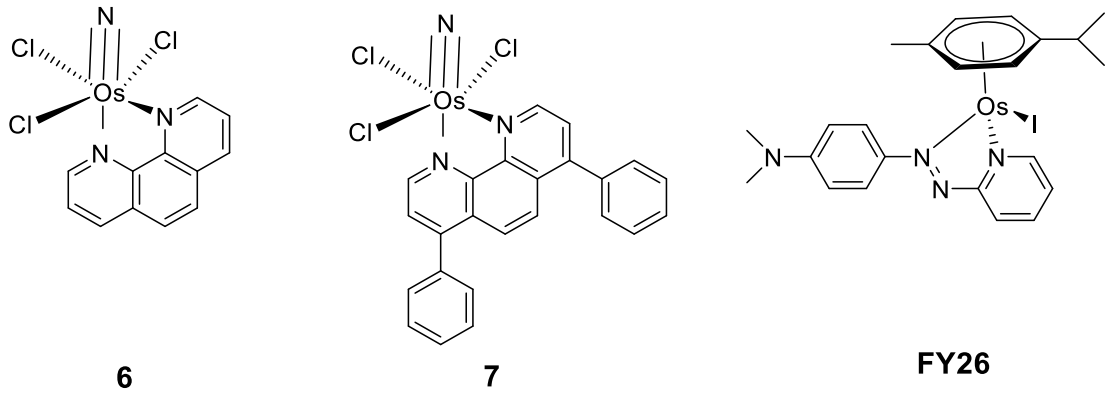

Figure 5. Previously synthesised osmium anti-cancer agents [29].

Chapter 2. Porous framework materials

2. The porous framework materials: MOF and COF Materials

The advancement of porous nanomaterials has been remarkable over the last few decades. Metal–organic frameworks (MOFs) and covalent organic frameworks (COFs) have been widely used as novel porous framework materials in a variety of fields. MOFs, also known as porous coordination polymers, are a type of porous crystal organic–inorganic hybrid material made up of metal nodes and organic ligands. COFs are a type of non-metal porous material made up of selected organic blocks joined together by covalent bonds. Both they also gotten a lot of attention in biosensing and phototherapy. High biocompatibility, tunable structure, and higher crystallinity make MOFs have higher utilization space compared with other materials [30]. Due to the tunable structure and high specific surface area, MOFs/COFs have advantages in loading aptamers. In addition, the simple structure of MOFs/COFs can be widely used in phototherapy by incorporating specific structures into the ligands. Based on the above characteristics, different porous frameworks materials can be designed through their own expected material structure, so that the final product can have the unique characteristics of another material, expand the application field of porous frame materials, and can also make up for other fields of materials. Exploring this field has produced (and will continue to produce) materials with entirely novel, unexpected properties, pushing the boundaries of materials in current applications, while also paving the way for more novel applications.

Porous framework nanoparticles containing active building blocks are a bold endeavor. Different from the traditional methods that only use nanoparticles as passive scaffolds or carriers, nanoparticles are directly composed of functional components that can perform specific functions to form a framework structure. Since nanoparticles are often used in biosensing and biomedical applications, usually as sensitive membranes for biosensors and as carriers to directly load drugs, nanoparticles do not contribute to

therapeutic effects in biomedicine. These ineffective nanoparticles and their metabolites have the potential to cause various side effects in the body before being excreted after drug release. To maximize the functional efficiency of nanoparticles in any other application. A nanoparticulate material that can itself be used in biotherapeutics must be synthesized for maximum multifunctional efficiency, and the number of inactive components must be minimized. All components of an ideal nanoparticle actively participate in as many functions as possible, resulting in efficient multifunctional tools[31].

To this end, porous framework nanoparticles with active building blocks are particularly interesting in this regard. Thus, a series of porous framework materials and then explored their biological applications.

2.1 Synthesis of porous framework nanoparticles

The synthesis of porous framework nanoparticles is difficult because it requires uniform shapes with smaller scale sizes. These are difficult to monitor by simple methods. Nanoporous frameworks must possess the characteristics of both frameworks and nanoparticles, such as high crystallinity, uniform morphology, good colloidal stability, and uniform size distribution. All of this can be achieved with controlled nucleation/crystal growth and efficient agglomeration inhibition[32]. Since the surface of the porous framework material has uncoordinated unsaturated metals and connection points, resulting in a high surface energy that promotes agglomeration, most of the porous framework material will agglomerate. Especially in the synthesis of colloidally stabilized COF nanoparticles, materials often agglomerate to form insoluble microcrystalline powders [33]. Fortunately, COF nanoparticle chemistry is still in its infancy, so we believe that the creativity of researchers in porous framework materials will address this challenge soon. Typically, wet chemical techniques are used to prepare porous framework nanoparticles. A three-step LaMer mechanism can be used to describe the formation of nanoparticles under these condition [34]:

1) Precursor dissolution results in supersaturation of the reaction solution and the formation of reactive monomers;

2) The concentration of reactive monomer increases until it reaches the critical

nucleation concentration;

3) Consistent crystal growth until the precursors and crystals achieve equilibrium[35].

Many factors that affect this process include temperature, solvents, precursors, concentrations and/or the presence of modifiers. The balance of substeps and side reactions, such as linker deprotonation, solvent degradation, and Ostwald ripening or digestion ripening, also contribute to the final size and shape of the porous framework nanoparticles[36]. Based on the above factors, we can change the amount of one or several factors to synthesize many nano-particle materials to find the optimal material.

2.2 Application of porous framework nanoparticles

The unique performance of MOFs and COFs in gas separation and storage, steam adsorption, catalysis, chemical sensing, biomedical applications and ionic conductors[36]. But this paper focuses on the enormous potential of materials for biological applications.

Compared with traditional nanomaterials applied in biosensors and biomedicine, porous framework materials with nanometer dimensions have superior bioactivity, chemical and colloidal stability, efficient surface modification, and improved biodistribution. However, most MOFs and COFs have limited multifunctionality and poor stability in a variety of environments, including acidic and alkaline media or the physiological environment. Chemical stability and biocompatibility are essential for effective sensing and therapy. MOF stability is influenced by several factors, including the ligand, metal oxidation state and ionic radius of metal ions, metal–ligand coordination geometry, and pore surface hydrophobicity.

Among them, to obtain stable coordination bonds, the metal-ligand bond strength should be high because it controls the stability of MOFs in various applications. The hard/soft acid/base (HSAB) principle is commonly used to predict the stability of metal-ligand bonds. Biocompatibility is another important concern in the fields of biosensing and biomedicine, so metal ions, ligands, or monomers with low or no toxicity are used to prepare porous framework materials and their derivatives. To increase the application efficiency of such materials, the materials should contain monomers that require specific structures, such as phthalocyanines and porphyrins, to achieve desired

functions, such as light harvesting. Various MOFs or COFs have been investigated as biosensor platforms.

2.2.1 Biosensing strategies

Due to abundant building blocks and combinations, MOFs and COFs have diverse structures and different functional properties such as large specific surface area, high porosity, fluorescence quenching, high loading efficiency, easy functionalization, and tunable pore size [38]. Among them, biosensing is a promising direction with the following advantages: (1) large specific surface areas and high porosity for probe adsorption and fluorescence quenching; (2) adjustable pores with specific shape and sizes via building blocks of varying lengths; (3) selectivity enabled by specific pore size allowing small molecules to enter while excluding large molecules; (4) abundant functional groups and positively charged metal ions provide various interactions such as electrostatic interactions, hydrogen bonding; (5) MOFs' reduced background fluorescence signals and increased sensitivities[39]. COFs were proposed as biosensing components in 2014 [40], with amino functionalisation allowing the adsorption of DNA and proteins in the framework.

MOFs or COFs can be used as a sensitive layer for the development of biosensors because of the immobilization interactions between aptamer strands and MOF or COF networks, such as π–π stacking, van der Waals force, hydrogen bonds, and possible coordination networks [41]. In the development of biosensors, MOFs or COFs can be used as a sensitive layer. The corresponding targets of the aptamers or antibodies can also be detected using these biosensors (biomarkers, antibiotics, or heavy metal ions) [42].

2.2.1.1 Construction of biosensors based on MOFs and MOFs-relevant materials

2.2.1.1.1 Construction of biosensors based on MOFs

MOFs have the advantages of adjustable structures, large surface area and porosity, abundant exposed active sites, and excellent biocompatibility. MOFs have also been used as great potential platforms with enhanced immobilization ability toward antibiotics and biomolecules such as glucose, antibodies, and aptamers due to the presence of functional groups of $–NH_2$ or –COOH on MOFs[43]. At present, many

biosensors based on various MOFs have been developed for detecting various targets, such as small biomolecules, using various determination techniques, such as electrochemical methods, fluorescence approaches, electrochemiluminescence. For example, Katherine and co-worker constructed a biosensor based 2D layered conductive MOFs as a platform to detect small organic molecule such as AA, DA, UA, and 5-HT in 0.1 M PBS (pH = 7.4) (**Scheme 2** (a))[44]. A ratiometric fluorescent bisoensor is proposed by Gao group based on aptamer as fluorescence emitter and PCN-222 as a fluorescence quencher for the detection of chloramphenicol with high performance (**Scheme 2** (b))[45]. A novel Py-M-COF-based aptasensors anchored many DNA aptamer strands has a low the limit of detection (LOD) in detecting enrofloxacin and ampicillin, respectively (**Scheme 2** (c))[46]. Among them, the electrochemical method is an efficient technique for the detection of biomolecules in the biological field.

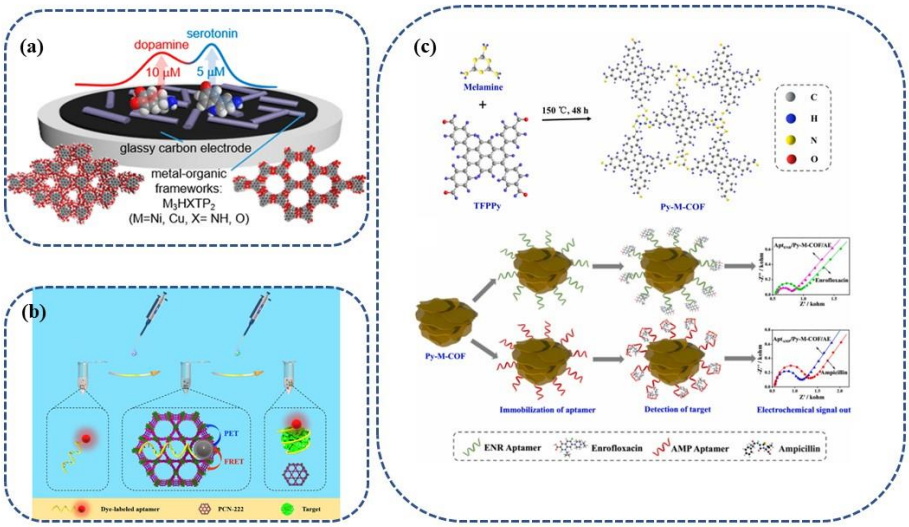

Scheme 2. (a) A film of MOF dispersed in H_2O is drop-casted directly on the top of a glassy carbon electrode (GCE) to enable voltammetric sensing of neurochemicals[44]. (b) Schematic illustration of the fluorescent assay with PCN-222 and dye-labeled aptamer as sensing platforms[45]. (c) Scheme of electrochemical detection of ENR and AMP using the Py-M-COF-based aptasensors[46].

2.2.1.1.2 Construction of biosensors based on MOFs-relevant materials

The application of most individual MOF components as electrochemical biosensors is severely limited due to flaws such as poor electrochemical activity, low stability, and a narrow linear concentration range of targets. To overcome the

disadvantages of MOFs, other components such as inorganic NPs, conducting polymers, quantum dots, carbon nanomaterials, biomolecules, and other types of MOFs have been combined with MOFs. For example, Ma et al.[47] developed a conductive sensor based on UiO-66-NH_2@PANI for the detection of Cd^{2+}(**Scheme 3**(a)). A unique Ni(TPA)-SWCNT possessed chemical stability and the electrochemical activity was synthesized by Wang group [48] and then explored as an platform for the detection of glucose, which exhibits excellent performance low LOD (4.6 μM) with a wide linear range, good practicality, and fast response. (<5 s) for glucose detection. Zhang et al. synthesized a CDs@ZrHf-MOF as a platform to construct aptasensor for the detection of HER2 and living HER2-overexpressed MCF-7 cells (**Scheme 3** (b))[42]. Based on the electrocatalytic ability of Ni-MOF, Lu et al. developed a UiO-67@Ni-MOF based bisoensor to detect glucose. Accordingly, the of UiO-67 gives UiO-67@Ni-MOF excellent performance due to the advantage, such as large specific area and highly electrocatalytic ability, while Ni-MOF showed high electrochemical catalytic ability for glucose (**Scheme 3** (c))[49].

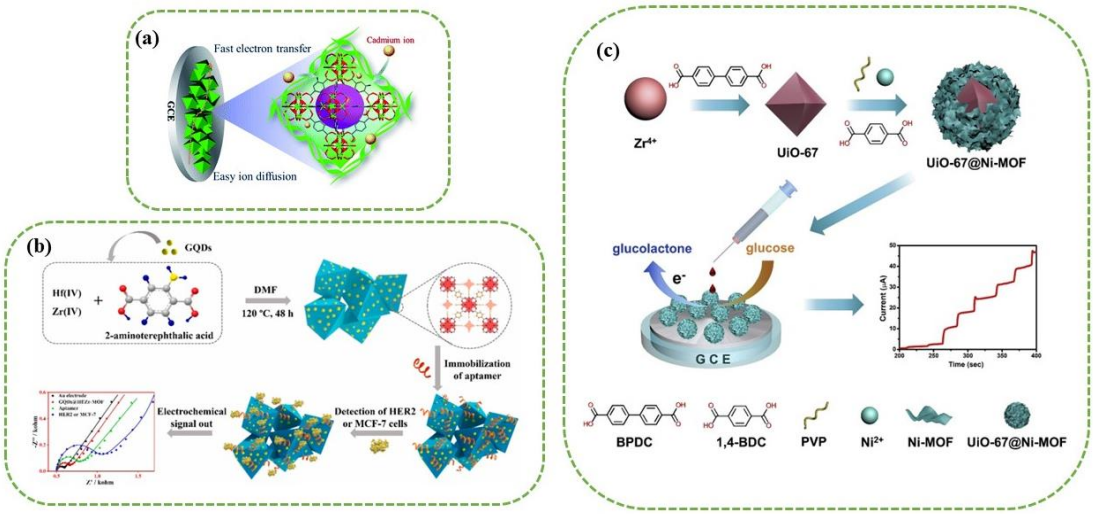

Scheme 3. (a) A conductive electrochemical sensor based on UiO-66-NH_2@PANI[47]. (b) Schematic diagram of the fabrication procedure of CDs@ZrHf-MOF-based aptasensor for detecting HER2[42]. (c) Schematic illustration of the synthesis process of core-shell UiO-67@Ni-MOF composites and sensing performance of glucose by UiO-67@Ni-MOF-modified electrode[49].

2.2.1.2 Construction of biosensors based on COFs and COFs-relevant materials

COFs, on the other hand, have unique structural properties, a large specific area,

and chemical and physical stability. They are made up of strong covalent bonds and have superior biosensing performance toward various targets, as well as a wide range of biomedical applications[50,51].

In recent years, COFs have gradually become electrode materials in the field of electrochemistry in recent years. A novel COFs TpBD synthesized by Pang [52] and co-worker (**Scheme 4** (a))was used for electrochemical biosensing of aflatoxin M1 in milk samples. The developed electrochemical biosensor exhibited high selectivity, sensitivity, and good stability, which retained 76% of the initial signal after 15 days storage at room temperature.

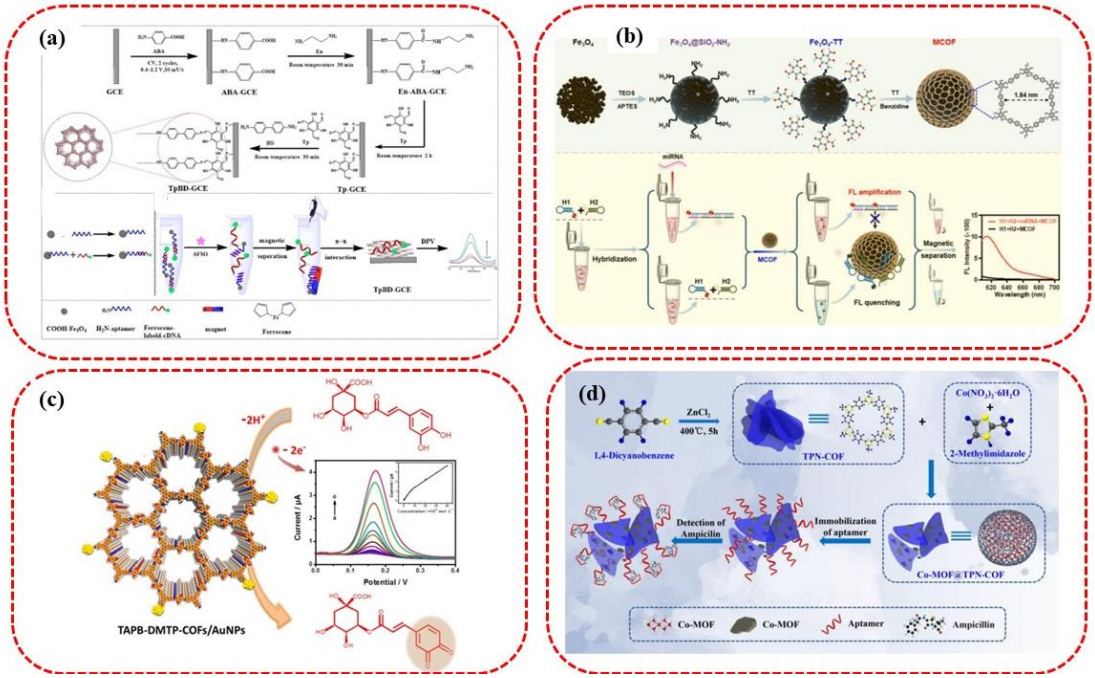

Scheme 4. (a) The proposed electrochemical biosensor based on TpBD for determination of AFM1.[52] (b) Schematic diagram of the constructed a biosensor based on COF-coated Fe_3O_4 magnetic nanospheres (MCOF) for the detection of miRNA-182 [54]. (c) The schematic diagram of an electrochemical sensor based on TAPB-DMTP-COFs@AuNPs for the immobilization of chitosan [55]. (d) The schematic diagram of the construction of the Co-MOF@TPN-COF-based aptasensor for detecting ampicillin. [56]

However, Most COFs, on the other hand, suffer from severe aggregation, low crystallization, and easy degradation (instability) [53], all of which significantly reduce their biosensing capabilities. COFs-relevant materials were synthesized to overcome

this shortcoming. Such as, a biosensor based on magnetic COF nanospheres (MCOF) with uniformed size and high crystallinity were prepared by Huang group [54] to realize the sensitive detection of miRNA-182 in different matrixes possessed a low LOD, 0.991 pM (**Scheme 4** (b)). Zhang et al. constructed a chlorognic electrochemical sensor based on TAPB-DMTP-COFs@AuNPs, and then immobilizing it with chitosan [55] (**Scheme 4** (c)). Liu et al.[56] developed a Co-MOF@TPN-COF based biosensor to detecte ampicillin sensitively and selectively by electrochemical impedance (**Scheme 4** (d)).

To sum up, the performance of biosensors based on MOF or COF is limited, MOF or COF-relevant materials can improve the sensing performance of materials. The preparation of sensitive, feasible, and wearable electrochemical biosensors using these porous organic frameworks as electrode materials is not yet mature, so further research in the field of biosensing is needed.

2.2.2 Cancer therapy

The complex environment of living organisms is an ongoing challenge to the selectivity of traditional small-molecule fluorescent probes in bioimaging [57]. The porous framework materials have advantages for bioimaging because of their predesigned topological structure, engineered internal pore surface, excellent biocompatibility, and hypotoxicity. Formalized paraphrase Furthermore, some porous framework materials exfoliated from bulk materials have improved luminescence, limited photobleaching, high solution stability, and benign dispersibility within the cell. As a result, they have a wide range of applications in cancer therapy [58].

Due to the unique advantages of MOFs and COFs, such as regular pore structure, high specific surface area/porosity, low density, tunable pore size, easy surface modification, and chemical structure design, these materials have begun to be used in cancer therapy [59]. The excellent biocompatibility and biodegradability of NanoMOFs and small-sized COFs (approximately 200–300 nm) have been experimentally demonstrated, suggesting that they can be used in cancer therapy [60]. Different types of MOFs containing metal ions or organic ligands with catalytic performances have been explored not only as anticancer drug carriers but also as catalysts for chemodynamic

therapy (CDT) photothermal therapy (PTT) and photodynamic therapy (PDT). Organic dyes like porphyrin, chlorin, phthalocyanine, boron-dipyrromethene, and cyanine are used as photosensitizers or photothermal agents in clinical and preclinical studies [61]. The MOF loading these organic molecules materials were used for photothermal therapy. For example, Liu et al. [62] synthesized a nanoscale Cu-MOF to load a photosensitizer (PS) with inhibited sensitization at high loading weight percentage. In vitro and in vivo experiments demonstrate that the rod-like Cu-MOF can afford excellent antitumor properties. Tian and co-worker [63] demonstrated an MOF as a PS unsing in tumor cancer theranostic. This MOF combine drug therapy and phototherapy after labeling targeting peptide iRGD under an 808 nm laser. To simplify the materials, some MOFs with small organic molecules as ligands have been synthesized for photothermal therapy (**Scheme 5**).

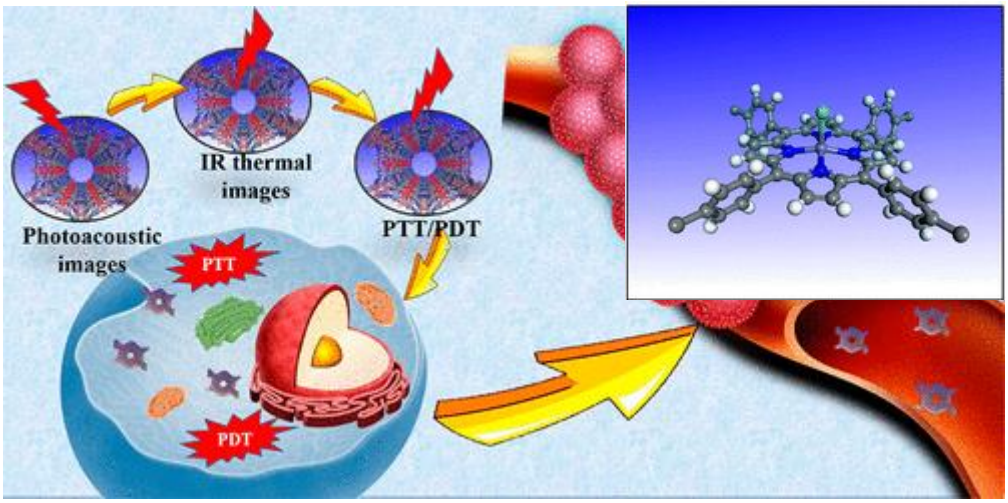

Scheme 5. Schematic Illustration of P-MOF contains NIR-Stimulation of single atom iron can be used toefficient cancer phototherapy via PDT and PTT, as well as PAI cancer imaging (B) crystal structure of a Fe porphyrin center in P-MOF [63].

Zhou and co-worlers synthesized a porphyrin-MOF (denoted as P-MOF) with photoacoustic imaging (PAI) guided PDT/PTT effect and then evaluated the performance under NIR (808 nm) irradiation[64]. Others MOFs such as Cu-TCPP MOF nanosheets[65] and TCPC-UiO [66] also been synthesized possesses both PDT and PTT simultaneously for phototherapy. This work demonstrates the great future potential of MOFs as PS for cancer treatment.

However, cancer treatment that is both effective and gentle on normal tissues is critical[67]. As a result, non-drug treatments are receiving a lot of attention. Thus, MOF-derived nanocomposite is synthesized on a nano-scale. Yin et al.[68] (**Scheme 6**) synthesized a Cu/Zn-MOF and then heated in the presence of manganese(II) acetylacetonate ($Mn(acac)_2$) to obtain hollow Mn/Cu/Zn-MOF@MnO_2. After that ICG@Mn/Cu/Zn-MOF@MnO_2 was obtained by the hollow structure loading photosensitizer indocyanine green (ICG), which exhibits a simple and effective strategy that PTI/FLI/MRI trimodality imaging-guided synergistic PTT/PDT/CDT treatment.

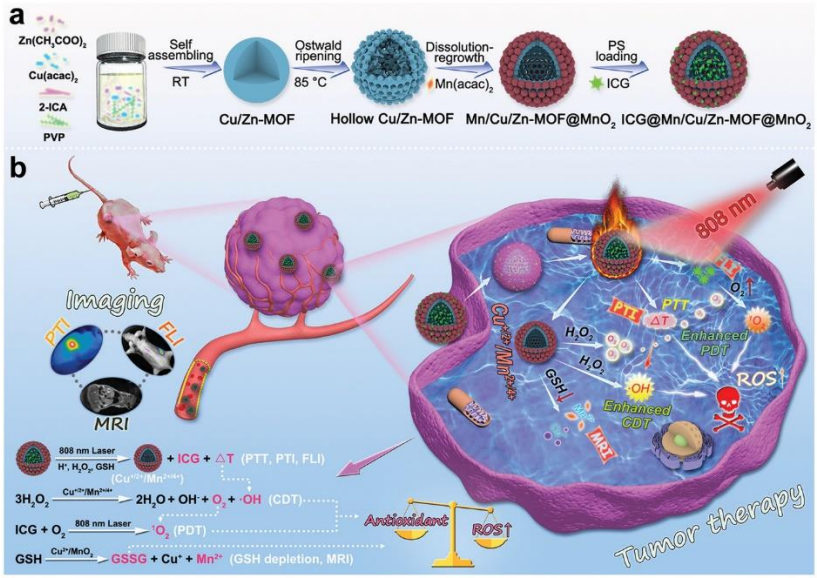

Scheme 6 a) ICG@Mn/Cu/Zn-MOF@MnO_2 was synthesized as an platform for PTI/ FLI/MRI guided ROS-augmented synergistic PTT/PDT/CDT[68].

COFs have unique advantages, such as high crystallinity, inherent pores, and large specific surface areas, which remarkably improve their loading ability toward different cancer drugs. For example, a magnetic COFs as a novel and effective drug carrier with good surface modification, excellent photothermal performance and high drug loading capacity was reported in the application of cancer chemo-photothermal therapy **(Scheme 7)** [69].

Most importantly, structure and function modularity can be realized by logically selecting functional monomers, which endow COFs with different functionality, such as photosensitizers for PDT and photothermal therapy (PTT). Given that their good aqueous dispersion, excellent biodegradability, strong light conversion, and efficient

reactive oxygen species (ROS) generation ability, COFs have been investigated as multifunctional cancer therapeutic reagents for tumor hypoxia relief and PDT, chemo-PTT, and PT/PDT. A novel dual functional photosensitizer COF–CuSe were prepared and possesses an excellent synergistic PTT and PDT effect. The in vitro and in vivo experiments revealed an improved therapeutic effect on cancer cell death and tumor growth inhibition (**Scheme 8**)[70].

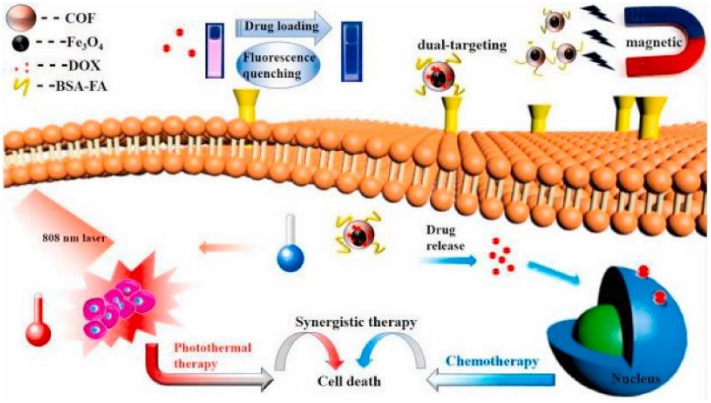

Scheme 7. Schematic diagram for constructing Fe_3O_4@COF-BSA-FA drug delivery system and synergistic treatment[69].

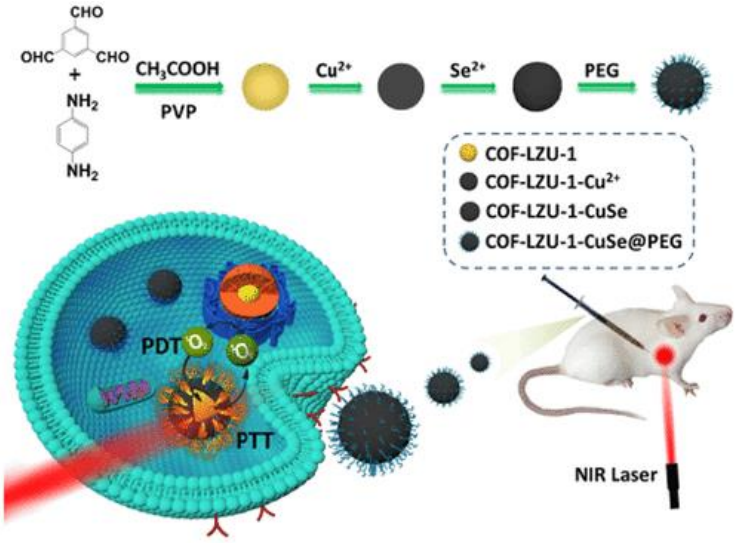

Scheme 8. Schematic illustration of the synthesis of COF−CuSe, and application for combined PTT and PDT [70].

Nowadays, as an important category of photosensitizers, phthalocyanine (Pc) and porphyrins, were used in cancer therapy owing to these molecules with electronic delocalization of 18-electrons exhibit excellent NIR region absorption, low

phototoxicity, and high extinction owing to highly conjugated planar structure and coordination ability toward diverse metal ions. Thereby, varieties of metal Pc (MPcs) have been exploited as PSs for efficient tumor therapy, especially for cancer therapy, such as ClAlPc/SLNs, ZnPc-PDT@DOX, and ZnTcPc-G. In addition, a porphyrin-based COF-366 NPs (**Scheme 9**) [71] were synthesized to provide the simultaneous therapy of PDT and PTT under a single wavelength light source with the monitoring of photoacoustic (PA) imaging. COF-366 NPs had achieved good PTT/PDT synergistic effect even in cancer therapy.

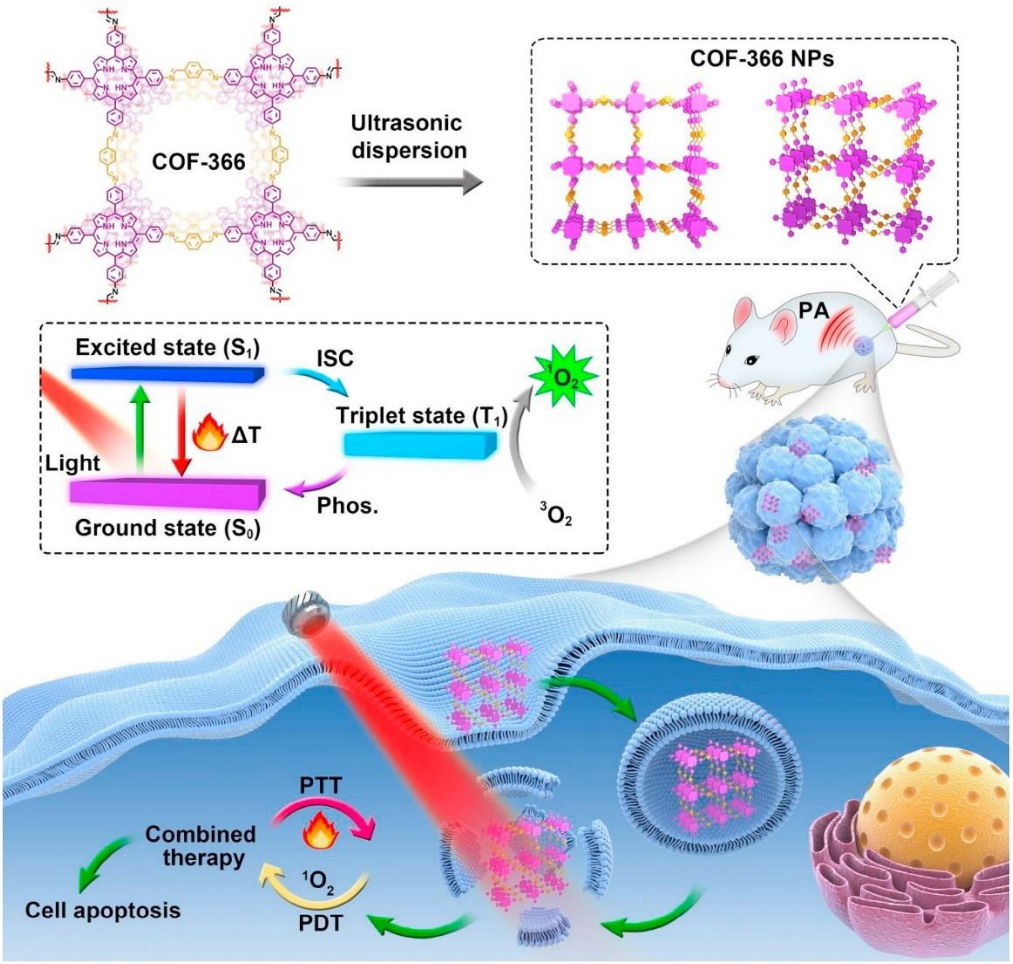

Scheme 9. COF-366 NPs is used for photoacoustic imaging-guided phototherapy under light irradiation[71].

COFs are an ideal nanocarrier to load hydrophobic organic molecular photosensitizers and photothermal agents into multifunctional nanomedicines for PDT/PTT combination therapy using both bonding defect functionalization and guest

encapsulation approaches. For example, Dong and co-wokers synthesized a dual-modal PDT/PTT VONc@COF-Por, which has a high photothermal conversion ability (55.9%), consequently providing an excellent PDT/PTT synergistic therapy on MCF-7 tumor cell cancer therapy (**Scheme 10**)[72].

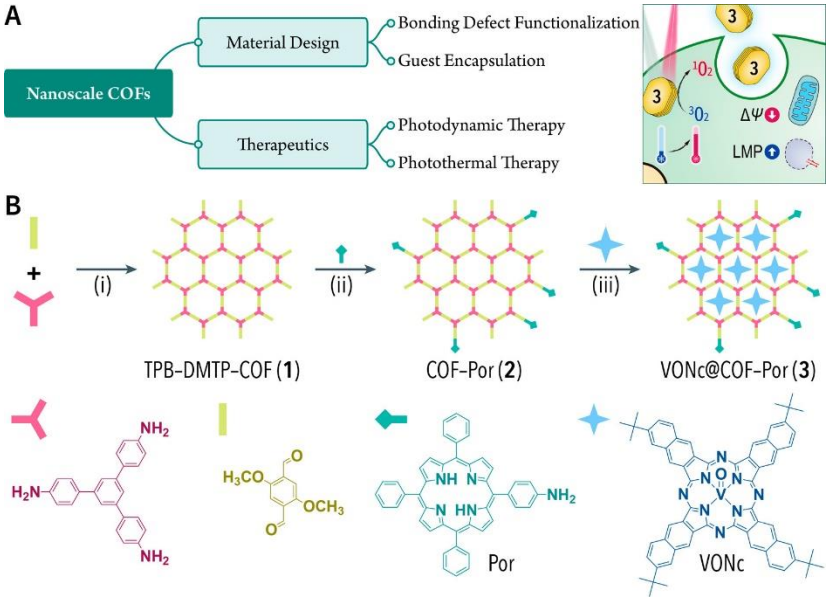

Scheme 10. Material design and synthesis[72].

However, phthalocyanine based COF is rarely used in cancer treatment. Based on the simple structure of COF and the advantages of phthalocyanine as a photosensitizer, phthalocyanine or porphyrin-based COF will become a new hot spot in cancer treatment.

Chapter 3. Aim of work

Organometallic complexes have attracted a considerable interest in medicinal chemistry, especially as putative anticancer compounds. The combination of an organometallic scaffold with bioactive ligands has proved to be a key strategy in the search of new anticancer agents [73].

The advancement of porous nanomaterials has been remarkable over the last few decades. MOFs and COFs, as novel porous framework materials, have found widespread application in a variety of fields. They've also gotten a lot of attention as novel carriers for aptamer immobilization. MOFs/COFs are considered potential candidate materials of biosensor and phototherapy due to the stability of these porous framework materials themselves, as well as fascinating merits such as unique pore structure, large specific surface area, diverse structure, and easy functionalization or post-modification, among others.

My PhD thesis focuses on two parts: (i) the design, the synthesis and the study of biological properties of novel ruthenium(II) and osmium(II) complexes with potential anticancer activity coupled with bioactive chelating ligands; (ii) synthesis series of porous framework materials and study these materials in biosensing or cancer therapy.

The first part of the work deals with the synthesis of p-cymene osmium acylpyrazolone complexes, p-cymene osmium bis(pyrazolyl)alkane complexes, which differ from each other only in the presence of different substituents on the ligand, and ruthenium(II) 1,4,7-Trithiacyclononane complexes, which different from complexes mentioned above. The aim of the work is at first the synthesis and the characterization of the complexes. Subsequently, the work is focused on the evaluation of their cytotoxic activity towards both cancer and non-tumorous cell lines. The goal of the work is to evaluate how the different ligand can influence the biological properties, and in particular the antitumor activity, of this class of complexes.

In the second part, I synthesized four kind of porous framework materials

(multivariate polymertitanium-MOFs (MTV Ti-MOFs), Chromium-based MOFs embedded with cobalt phthalocyanine nanoparticles (Cr-MOFs@CoPc), CuPc-bTDC-COF and manganese-doped cobalt phthalocyanine and $Ti_3C_2T_x$ MXene nanosheets (CoPc-TA/Mn@$Ti_3C_2T_x$)) and then and explored MTV Ti-MOFs and Cr-MOFs@CoPc as the platforms for immobilizing the targeted aptamer strands for detecting zearalenone and colorectal cancer (CT26) cells, respectively. After that, these complexes have been fully characterized by in field emission scanning electron microcopy (FE-SEM) and Transmission Electron Microscope (TEM), in field emission scanning electron microcopy (FE-SEM) and Transmission Electron Microscope (TEM), Brunauer-Emmett-Teller (BET) and so on. Furthermore, some electrochemical methods, such as Electrochemical Impedance Spectroscopy (EIS), Differential Pulse Voltammetry (DPV), and Cyclic Voltammetry (CV), were used to assess the performances of biosensors based on materials. As for CuPc-bTDC-COF, we report the successful application of a Cu phthalocyanine-containing COFs and then evaluated the performance of the CuPc-bTDC-COF for cancer treatment by photodynamic therapy (PDT and PTT) under NIR (808 nm) irradiation. After synthesizing the material, the above characterization of the CuPc-bTDC-COF was carried out. It can be found from the Ultraviolet–visible spectroscopy (Uv-vis) that the CuPc-bTDC-COF has absorption peak in the near infrared region, so it can be used for phototherapy. After that, we explored the phototherapeutic properties and cytotoxicity of the CuPc-bTDC-COF. Finally, mouse experiments were carried out to evaluated the performance in vivo. I also synthesized a Schottky junction nanozyme of CoPc-TA/Mn@$Ti_3C_2T_x$. Due to its unique structure forming a Schottky junction, the material has a type I PDT effect in addition to the normal CDT/PDT/PTT effect, so it can promote the synergistic effect and make the material better in anti-tumor effect.

Chapter 4. P-cymene osmium acylpyrazolone complexes

Despite the problems associated with drug toxicity and drug resistance, platinum-based chemotherapeutics are currently most used in anticancer therapy, but it has problems associated with drug toxicity and drug resistance. Therefore, it is necessary to prepare a new metal-based anticancer complex with less side effects, and at the same time, it should be cytotoxic to tumor cell lines including chemoresistant. Over the past decade, the half-sandwich arene Ru(II) complex has emerged as a potential alternative to platinum-based drugs due to its redox-accessible oxidation state, biocompatible ligand exchange rate, and compatibility with DNA and / or protein covalent binding, low toxicity and other properties. Therefore, RAPTA-like compounds $[Ru(\eta^6\text{-arene})(PTA)Cl_2]$ (PTA = 1,3,5-triaza-7-phosphaadamantane) were investigated on a large scale. Osmium composites are analogues of ruthenium composites, so we synthesized a series of osmium composites and explored their antitumor effects.

4.1 Experimental

4.1.1 General procedures

All other materials were obtained commercially and used exactly as received. PTA was purchased from Aldrich. On a PerkinElmer Frontier FT-IR instrument, IR spectra were recorded from 4000 to 30 cm^{-1}. The ^{1}H, ^{13}C, and ^{31}P NMR spectra were obtained using a 400 Mercury Plus Varian instrument at room temperature (400 MHz for 1H and 100 MHz for ^{13}C relative to TMS, and 162 MHz relative to 85 percent H_3PO_4). Positive and negative ion electrospray ionization mass spectra (ESI-MS) were obtained using methanol as the mobile phase on a Series 1100 MSI detector HP spectrometer. Reagent-grade methanol was used to prepare solutions (3 mg mL^{-1}) for analysis. The calculated masses and intensities were compared to those obtained using the IsoPro Isotopic Abundance Simulator, version 2.1.28. Melting points were measured using an uncorrected STMP3 Stuart scientific instrument and a capillary apparatus. Microanalysis samples were dried in vacuo to constant weight (20 °C, approximately 0.1 Torr) before being analyzed on a Fisons Instruments 1108 CHNS-O elemental analyzer. At room temperature, electrical conductivity measurements (M, reported as S cm^{-2} mol^{-1}) of the

complexes' acetonitrile solutions were taken using a Eutech Instruments CON2700.

4.1.2 Synthesis and characterization of the complexes

The **HQ'** ($HQ^{Ph,Ph}$, $HQ^{Ph,Bipy}$, and $HQ^{Me,Me}$) igands were synthesized according to the previous report[74].

The dimers **$[Os(cym)Cl_2]Cl_2$** were prepared as previously described[75].

$[Os(cym)(HQ^{Ph,Ph})Cl]$ (1). $HQ^{Ph,Ph}$ (55.7 mg, 0.1 mmol) was dissolved in methanol (20 mL). Then CH_3ONa (10.8 mg, 0.2 mmol) was added into the solution under stirring for 1 h at room temperature. Afterwards, $[Os(cym)Cl_2]_2$ (79.1 mg, 0.1 mmol) was added into the mixture and the reaction allowed to process for 24 h at room temperature. The solvent was removed by rotary evaporation. The residue was dissolved in dichloromethane (4 mL) and the mixture was filtered to remove potassium chloride. Finally, excess of n-hexane was added to the filtrate and stored at 4 ºC affording yellow precipitate. The precipitate was dissoved in methanol and stored at 4 ºC affording red crystals. Obtained 58 mg, 0.091 mmol, yield 45.5%. It is soluble in methanol, DMSO, DMF, chlorinated solvents, acetonitrile and acetone and slightly soluble in diethyl ether. Mp: 196-198 C. M_W: 639.15. Anal. Calcd for $C_{27}H_{27}ClN_2O_2Os$: C, 50.81; H, 4.42; N, 4.39%. Found: C, 50.04; H, 4.29; N, 4.25%. Λ_M (DMSO, 10^{-3} mol L^{-1}): 3.14 S cm^2 mol^{-1} (T = 298 K).. IR (cm^{-1}): 3052w, 2961w (C_{arom-H}), 1593m, 1567vs ν(C=O), 1472vs, 1380vs ν(C=C, C=N, C−N), 1057s, 759vs, 691s and 661m *ν*(Os−OH), 623s, 515m, 461m(Os–O), 281s *νs*(Os–Cl). ^{1}H NMR ($CDCl_3$, 298 K): δ =1.36 (d, 6H, CH_3-C_6H_4-CH(CH_3)$_2$, ^3J=6.9 Hz), 1.74(s, 3 H, CH_3-C_3), 2.23 (s, 3 H, CH_3-C_6H_4-CH(CH_3)$_2$), 2.81 (m, 1 H, CH_3-C_6H_4-CH(CH_3)$_2$, ^3J = 6.85 Hz,], 5.83 (d, 2 H, c,c' of CH_3-C_6H_4-CH(CH_3)$_2$, ^3J = 4.7 Hz), 6.08 (d, 2 H, b,b' of CH_3-C_6H_4-CH(CH_3)$_2$, ^3J = 6.8 Hz), 7.23(t,1 H , ^3J = 7.4 Hz), 7.39-7.55(d, 7H_{arom} of $HQ^{Ph,Ph}$), 7.90 (d, 2H, H of $HQ^{Ph,Ph}$). ^{13}C NMR ($CDCl_3$, 298 K): δ = 18.39 (s, C_3-CH_3, C of $HQ^{Ph,Ph}$), 22.67 (s, CH_3-C_6H_4-CH(CH_3)$_2$), 22.73 (s, CH_3-C_6H_4-CH(CH_3)$_2$), 31.48 (s, CH_3-C_6H_4-CH(CH_3)$_2$), 69.38 (d, c,c' of CH_3-C_6H_4-CH(CH_3)$_2$), 73.89 (d, b,b' of CH_3-C_6H_4-CH(CH_3)$_2$), 87.89 (s, a of CH_3-C_6H_4-CH(CH_3)$_2$), 89.48 (s, d of CH_3-C_6H_4-CH(CH_3)$_2$), 106.84 (s, C_3 of $HQ^{Ph,Ph}$), 121.06-138.38 (14C, C of $HQ^{Ph,Ph}$), 149.35 (s, C_4 of $HQ^{Ph,Ph}$), 163.13 (s, C_5 of $HQ^{Ph,Ph}$), and 187.95(s, C_{10} of $HQ^{Ph,Ph}$).ESI-MS (+) (CH_3CN) (m/z, relative intensity %): 603 [100] $[Os(cym)(HQ^{Ph,Ph})]^+$.

$[Os(cym)(HQ^{Ph,Bipy})Cl]$ (2). The synthesized method of [Os(cym)($HQ^{Ph,Bipy}$)Cl] is similar to 1 by using the proligand $HQ^{Ph,Bipy}$. Yield 42%. It is soluble in DMSO, DMF, acetonitrile,

acetone and chlorinated solvents and slightly soluble in methanol. Mp: 138-141 °C. M_W: 714.3. Anal. Calcd for $C_{33}H_{31}ClN_2O_2Os$: C, 55.49; H, 4.52; N, 3.92%. Found: C, 52.68; H, 4.06; N, 3.46%. Λ_M (DMSO, 10^{-3} mol L^{-1}): 4.32 S cm^2 mol^{-1} (T = 298 K).IR (cm^{-1}): 3057w, 2961w (C_{arom-H}), 1591w, 1574vs ν(C=O), 1472vs, 1379vs ν(C=C, C=N, C−N), 1057m, 759vs, 693s and 656m *ν*(Os−OH), 622s , 511m, 453m(Os–O), 286s *νs*(Os–Cl). ^{1}H NMR ($CDCl_3$, 298 K): δ = 1.37 (d, 6H, CH_3-C_6H_4-CH(CH_3)$_2$, ^3J=6.9 Hz), 1.83(s, 3 H, CH_3-C_3), 2.30 (s, 3 H, CH_3-C_6H_4-CH(CH_3)$_2$), 2.84 (m, 1 H, CH_3-C_6H_4-CH(CH_3)$_2$, ^3J = 7 Hz), 5.85 (d, 2 H, c,c' of CH_3-C_6H_4-CH(CH_3)$_2$, ^3J = 4.6 Hz), 6.10 (d, 2 H, b,b' of CH_3-C_6H_4-CH(CH_3)$_2$, ^3J = 5.4 Hz), 7.40 (t,1 H , ^3J = 7.3 Hz), 7.40-7.70 (d, 11H_{arom} of $HQ^{Ph,Bipy}$), 7.92 (2H, H of $HQ^{Ph,Bipy}$). ^{13}C NMR ($CDCl_3$, 298 K): δ = 16.45 (s, C_3-CH_3, C of $HQ^{Ph,Bipy}$), 18.42 (s, CH_3-C_6H_4-CH(CH_3)$_2$), 22.72 (s, CH_3-C_6H_4-CH(CH_3)$_2$), 31.49 (s, CH_3-C_6H_4-CH(CH_3)$_2$), 69.43 (s, c,c' of CH_3-C_6H_4-CH(CH_3)$_2$), 73.91 (s, b,b' of CH_3-C_6H_4-CH(CH_3)$_2$), 87.89 (s, a of CH_3-C_6H_4-CH(CH_3)$_2$), 89.48 (s, d of CH_3-C_6H_4-CH(CH_3)$_2$), 106.89 (s, C_3 of $HQ^{Ph,Bipy}$), 121.06-143.54 (18 C, C of $HQ^{Ph,Bipy}$), 149.26 (s, C_4 of $HQ^{Ph,Bipy}$), 163.13 (s, C_5 of $HQ^{Ph,Bipy}$), and 187.50 (s, C_{10} of $HQ^{Ph,Bipy}$). ESI-MS (+) (CH_3CN) (m/z, relative intensity %): 678 [100] [Os(cym)($HQ^{Ph,Bipy}$)]$^+$

[Os(cym)($HQ^{Me,Me}$)Cl] (3). Complex **3** has been synthesized similarly to **1** by using the proligand **$HQ^{Me,Me}$**. Yield 42.8%. It is soluble in MeOH, DMSO, DMF, $CHCl_3$, acetonitrile and acetone and slightly soluble in diethyl ether. Mp: 140-143 C. M_W: 514. Anal. Calcd for $C_{17}H_{23}ClN_2O_2Os$: C, 39.72; H, 4.71; N, 5.45%. Found: C, 39.56; H, 5.29; N, 4.28%. Λ_M (DMSO, 10^{-3} mol L^{-1}): 2.03 S cm^2 mol^{-1} (T = 298 K). IR (cm^{-1}): 3061w, 2960w (C_{arom-H}), 1591vs ν(C=O), 1495s, 1383s ν(C=C, C=N, C−N), 1083s, 991m, 691w and 661m *ν*(Os−OH), 605s, 445m(Os–O), 270*νs*(Os–Cl). ^{1}H NMR ($CDCl_3$, 293 K): δ = 1.35 (d, 6 H, CH_3-C_6H_4-CH(CH_3)$_{22}$, ^3J=6.9 Hz), 2.29 (d, 6H CH_3-C_3, CH_3-C_7), 2.39 (s, 3 H, CH_3-C_6H_4-CH(CH_3)$_2$), 2.80 (d, 1 H, CH_3-C_6H_4-CH(CH_3)$_2$, ^3J = 6.8 Hz), 3.46 (m, 3 H, N^+CH_3), 5.78 (d, 2 H, b,b' of CH_3-C_6H_4-CH(CH_3)$_2$, ^3J = 6 Hz), and 6.04 (d, 2 H, c,c' of CH_3-C_6H_4-CH(CH_3)$_2$, ^3J = 5.4 Hz), ^{13}C NMR ($CDCl_3$, 298 K): δ = 16.73 (s, C_3-CH_3, C of $HQ^{Me,Me}$), 18.17 (s, C_7-CH_3, C of $HQ^{Me,Me}$) 22.65 (s, CH_3-C_6H_4-CH(CH_3)$_2$), 25.99 (s, CH_3-C_6H_4-CH(CH_3)$_2$), 31.55 (s, N^+CH_3, C of $HQ^{Me,Me}$), 31.92 (s, CH_3-C_6H_4-CH(CH_3)$_2$), 69.00 (s, c,c' of CH_3-C_6H_4-CH(CH_3)$_2$), 73.62 (s, b,b' of CH_3-C_6H_4-CH(CH_3)$_2$), 87.81 (s, a of CH_3-C_6H_4-CH(CH_3)$_2$), 89.23 (s, d of CH_3-C_6H_4-CH(CH_3)$_2$), 105.63 (s, C_3 of $HQ^{Me,Me}$), 147.49 (C, C_4 of $HQ^{Me,Me}$), 163.37 (s, C_5 of $HQ^{Me,Me}$), and

189.05 (s, C_7 of $HQ^{Me,Me}$). ESI-MS (+) (CH_3CN) (m/z, relative intensity %): 478 [100] $[Os(cym)(HQ^{Me,Me})]^+$

[Os(cym)($HQ^{Ph,Ph}$)PTA][SO_3CF_3] (4). $AgSO_3CF_3$ (41.1 mg, 0.16 mmol) was added to the solution of Os(cym)($HQ^{Ph,Ph}$)Cl (100 mg, 0.16 mmol, 102.3 mg) in methanol (15 mL) under stirring for 1 h and filtered to remove AgCl. Afterwards, PTA (PTA = 1,3,5-triaza-7-phosphaadamantane; 25.1 mg, 0.16 mmol) was added to the filtrate under stirring for 24h at room temperature. Lastly, the clear yellow solution was dried by rotary evaporation and dichloromethane (2 mL) and an excess of n-hexane were added, which was stored at 4 C. The yellow powder obtained after several days. Yield 73%. It is soluble in DMSO, DMF, acetonitrile, acetone, chlorinated solvents and methanol. Mp: 217-220 °C. M_W: 910.2. Anal. Calcd for $C_{34}H_{38}F_3N_5O_5OsPS$: C, 44.9; H, 4.; N, 8.60. Found: C, 48.84; H, 4.76; N, 8.43%. Λ_M (DMSO, T= 298 K, 10^{-3} mol L^{-1}): 25.01 S cm^2 mol^{-1}. IR (cm^{-1}): 3050w, 2922w (C_{arom}−H), 1583w, 1566s ν(C=O), 1463m, 1441m, 1386m ν(C=C, C=N, C−N), 1252vs, 1156m, 1029vs, 971s, 947s, 802m, 738s, 637vs, 577s, 514m, 454m ν(Os–O). ^{1}H NMR ($CDCl_3$, 298 K): δ = 1.28 (d, 6H, CH_3-C_6H_4-CH(CH_3)$_2$, ^3J=6.9 Hz), 1.87 (s, 3 H, CH_3-C_3), 2.12 (s, 3 H, CH_3-C_6H_4-CH(CH_3)$_2$), 2.54 (m, 1 H, CH_3-C_6H_4-CH(CH_3)$_2$, ^3J = 6.9 Hz), 4.25 (s, 6H, P-CH^AH^BN, PTA), 4.56 (s, 6H, N-CH^AH^BN, PTA), 6.18-6.23 (d, 4 H, c,c' and b,b' of CH_3-C_6H_4-$CH(CH_3)_2$), 7.34-7.84 (d, 10H_{arom} of $HQ^{Ph,Ph}$). ^{13}C NMR ($CDCl_3$, 298 K): δ = 16.68 (s, C_3-CH_3, C of $HQ^{Ph,Ph}$), 17.65 (s, CH_3-C_6H_4-$CH(CH_3)_2$), 22.52-29.94 (s, CH_3-C_6H_4-CH(CH_3)$_2$), 31.29 (s, CH_3-C_6H_4-$CH(CH_3)_2$), 69.40 (s, P-CH^AH^BN, PTA), 72.73 (s, 6H, N-CH^AH^BN, PTA), 82.25 (s, c,c' of CH_3-C_6H_4-$CH(CH_3)_2$), 81.05 (s, b,b' of CH_3-C_6H_4-$CH(CH_3)_2$), 90.11 (s, d of CH_3-C_6H_4-$CH(CH_3)_2$), 94.49 (s, a of CH_3-C_6H_4-$CH(CH_3)_2$), 108.38 (s, C_3 of $HQ^{Ph,Ph}$), 120.58-138.38 (14C, C of $HQ^{Ph,Ph}$), 149.47 (s, C_4 of $HQ^{Ph,Ph}$), 161.81 (s, C_5 of $HQ^{Ph,Ph}$), and 190.30 (s, C_{10} of $HQ^{Ph,Ph}$). ^{31}P NMR ($CDCl_3$, 298 K): , -65,3s. ESI-MS (+) (CH_3CN) (m/z, relative intensity %): 759.9 [100] $[Os(cym)(HQ^{Ph,Ph})(PTA)]^+$.

[Os(cym)($HQ^{Ph,Bipy}$)PTA][SO_3CF_3] (5). The synthesized methods of Complex **5** was similar to **4** using complex **2** as precursor. Yield 79.6%. It is soluble in DMSO, DMF, acetonitrile, chlorinated solvents and acetone. M.p.: 237-239 C. M_W: 986.24. Anal. Calcd for $C_{40}H_{42}F_3N_5O_5OsPS$: C, 48.87; H, 4.31; N, 7.12; F, 5.79. Found: C, 51.48; H, 4.82; N, 7.96%. Λ_M (DMSO, T = 298 K, 10^{-3} mol L^{-1}): 20.35 S cm^2 mol^{-1}. IR (cm^{-1}): 3061w, 2924w (C_{arom-H}), 1593m, 1572s ν(C=O), 1474m, 1382m ν(C=C, C=N,

C−N),1256vs, 1146m, 1030m, 947m, 802m, 739s, 636vs, 573vs, 513m, 455m *ν*(Os–O). ^{1}H NMR (C*D*$_3$CN, 298 K): δ = 1.31m (m ,6H, CH_3-C_6H_4-CH(C*H*$_3$)$_2$, ^{3}J=6.9 Hz), 1.99 (s, 3 H, C*H*$_3$-C$_3$), 2.15 (s, 3 H, *C*H$_3$-C_6H_4-CH(C*H*$_3$)$_2$), 2.57 (m, 1 H, CH_3-C_6H_4-C*H*(C*H*$_3$)$_2$, ^{3}J = 6.9 Hz) , 4.27 (s, 6H, P-C*H*^{A}*H*^{B}N, PTA), 4.58 (s, 6H, N-C*H*^{A}*H*^{B}N, PTA), 6.19-6.24 (d, 4 H, c,c' and b,b' of CH_3-C_6H_4-CH(CH_3)$_2$), 7.33-7.85 (d, 14H$_{arom}$ of HQ^{Ph,Bipy}). ^{13}C NMR ($CDCl_3$, 298 K): δ = 16.90 (s, C_3-*C*H$_3$, C of HQ^{Ph,Bipy}), 17.76 (s, *C*H$_3$-C_6H_4-CH(CH_3)$_2$), 22.54 and 22.95 (s, CH_3-C_6H_4-CH(*C*H$_3$)$_2$), 31.33 (s, CH_3-C_6H_4-*C*H(CH_3)$_2$), 50.55 (d, P-*C*H$_2$-N, PTA), 73.02 (d, N-*C*H$_2$-N, PTA), 79.73 and 80.11 (s, c,c' of CH_3-*C*$_6$H$_4$-CH(CH_3)$_2$), 81.82 and 82,09 (s, b,b' of CH_3-*C*$_6$H$_4$-CH(CH_3)$_2$), 90.23 (s, d of CH_3-*C*$_6$H$_4$-CH(CH_3)$_2$), 94.25 (s, a of CH_3-*C*$_6$H$_4$-CH(CH_3)$_2$), 108.37 (s, C_3 of HQ^{Ph,Bipy}), 120.56-145.54 (18C, C of HQ^{Ph,Bipy}), 149.35 (s, C_4 of HQ^{Ph,Bipy}), 161.98 (s, C_5 of HQ^{Ph,Bipy}), and 189.83 (s, C_{10} of HQ^{Ph,Bipy}). ^{31}P NMR (CD_3Cl_3, 298 K): -66.36s. ESI-MS (+) (CH_3CN) (m/z, relative intensity %): 836 [100] [Os(cym) (HQ^{Ph,Bipy}) (PTA)]$^{+}$.

[Os(cym)(HQ^{Me,Me})PTA][SO$_3$CF$_3$] (6). The synthesized methods of Complex **6** was similar to **4** using complex **3** as precursor. Yield 76.3%. It is soluble in DMSO, DMF, acetonitrile, chlorinated solvents and acetone. M.p.: 199-203 C. M$_W$: 786.17. Anal. Calcd for $C_{24}H_{34}F_3N_5O_5OsPS$: C, 36.73; H, 4.62; N, 8.92; F, 7.26. Found: C, 36.64; H, 4.49; N, 8.31%. Λ$_M$ (DMSO, T = 298 K, 10^{-3} mol L^{-1}): 24.06 S cm^2 mol^{-1}. IR (cm^{-1}): 3066w, 2930w (C_{arom-H}), 1587m ν(C=O), 1489m, 1383w ν(C=C, C=N, C−N), 1258vs, 1148m, 1030m, 972m, 947m, 802m, 741m, 637vs, 579vs, 516m, 454m *ν*(Os–O). ^{1}H NMR ($CDCl_3$, 293 K): δ = 1.31 (d, 6 H, CH_3-C_6H_4-CH(*CH*$_3$)$_{22}$, ^{3}J=6.9 Hz), 2.12 (s, 3H C*H*$_3$-C_6H_4-CH(*C*H$_3$)$_2$), 2.35 (s, 3H, C*H*$_3$-C$_3$,), 2.40 (s, 3 H, C*H*$_3$-C$_7$), 2.57 (d, 1 H, CH_3-C_6H_4-CH(*CH*$_3$)$_2$, ^{3}J = 6.8 Hz), 3.47 (s, 3 H, N^{+}CH$_3$), 4.15 (s, 6H, P-C*H*^{A}*H*^{B}N, PTA), 4.54 (s, 6H, N-C*H*^{A}*H*^{B}N, PTA), 6.1 (m, 4 H, c,c' and d,d'of CH_3-C_6H_4-CH(CH_3)$_2$), ^{13}C NMR ($CDCl_3$, 298 K): δ = 16.93 (s, C_3-*C*H$_3$, C of HQ^{Me,Me}), 17.30 (s, C_7-*C*H$_3$, C of HQ^{Me,Me}) 22.65 (s, CH_3-C_6H_4-CH(*C*H$_3$)$_2$), 25.73 (s, *C*H$_3$-C_6H_4-CH(CH_3)$_2$), 31.38 (s, N^{+}*C*H$_3$, C of HQ^{Me,Me}), 32.19 (s, CH_3-C_6H_4-*C*H(CH_3)$_2$), 49.98 (d, P-*C*H$_2$-N, PTA), 73.03 (d, N-*C*H$_2$-N, PTA), 79.78 and 80.18 (s, c,c' of CH_3-*C*$_6$H$_4$-CH(CH_3)$_2$), 80.64 and 81.21 (s, b,b' of CH_3-*C*$_6$H$_4$-CH(CH_3)$_2$), 90.01 (s, a of CH_3-*C*$_6$H$_4$-CH(CH_3)$_2$), 94.02 (s, d of CH_3-*C*$_6$H$_4$-CH(CH_3)$_2$), 107.07 (s, C_3 of Q^{Bi,Ph}), 147.49 (C, C_4 of HQ^{Me,Me}), 163.37 (s, C_5 of HQ^{Me,Me}), and 189.05 (s, C_7 of HQ^{Me,Me}) .^{31}P NMR (CD_3Cl_3, 298 K): δ = -66.36s. ESI-MS (+) (CH_3CN) (m/z, relative intensity %): 836 [100] [Os(cym) (HQ^{Me,Me})PTA]$^{+}$.

4.1.3 X-ray diffraction structural analysis

The X-ray studies were performed by Prof. Miao Du at the College of Material and Chemical Engineering, Zhengzhou University of Light Industry, Zhengzhou, China.

X-ray intensity data were measured on a Bruker SMART 2000 CCD area detector diffractometer. Cell size and orientation matrices were initially determined from least-squares refinement of reflections measured in three sets of 20 exposures, collected in three different ω regions, and finally refined for all data. A full sphere of reciprocal space was scanned in 0.3° steps for all crystals. The SMART (37) software was used to collect data frames, index reflections, and calculate lattice parameters. The SAINT program was used to integrate the collected frames, and SADABS was used to apply an empirical absorption correction. The structures were solved using direct methods (SIR 97) and subsequent Fourier syntheses on F2 (SHELXTL), with anisotropic thermal parameters for all non-hydrogen atoms.

4.1.4 Cell culture and inhibition of cell growth

Cell culture and inhibition of cell growth studies were performed in the College of Material and Chemical Engineering, Zhengzhou University of Light Industry, Zhengzhou, China.

4.1.4.1 Cells

MCF-7 (human breast cancer), 4T1 (Mouse breast cancer cells), CT26 (Mouse colon cancer cells), and Renca (Mouse Renal Carcinoma) were purchased from Procell Life Science&Technology Co.,Ltd.

Cell lines were cultured in Dulbecco's modified Eagle's medium (DMEM) and Roswell Park Memorial Institute (RPMI) medium (Beijing Soleibao Technology Co., Ltd) supplemented with 10% bovine serum albumin (BSA). Cell lines were maintained at 37 °C with 5% CO_2 and 95% humidity.

4.1.4.2 MTT assay

Typically, cells (1×10^5) were seeded into 96-well plates and cultured for 24 h (37 °C, 5% CO_2), and then separately incubated with different concentrations of p-cymene osmium acylpyrazolone complexes suspensions for 48 h. The cells were rinsed gently with PBS to remove incompletely internalized materials, and 200 μL medium was added to each well. After further incubation for 12 h at 37 °C , 20 μL of MTT (5 mg mL^{-1} in PBS) was added into per well and cultured in the incubator for 4 h. At last, the medium was removed, following by added 150 μL of DMSO to per well. The cell viability was monitored by measuring the absorbance at

570 nm using a microplate reader (WD-2102A).

4.1.4.3 Statistical analysis

The data presented represent the mean and standard deviation (SD) of at least 3 independent experiments. The statistical significance was determined by Student's t-test; *, $^{\#}$, $^{\S}p < 0.01$. The statistical analysis of IC_{50} levels was performed using Prism 5.0a (Graph Pad).

4.2 Result and discussion

4.2.1 Synthesis and spectroscopic characterization of osmium complexes

Complexes **1-3** were prepared in high yield in a single step by interaction of acylpyrazolone (**Figure 6**) and the appropriate $[(arene)OsCl_2]_2$ as shown in **Scheme 11**.

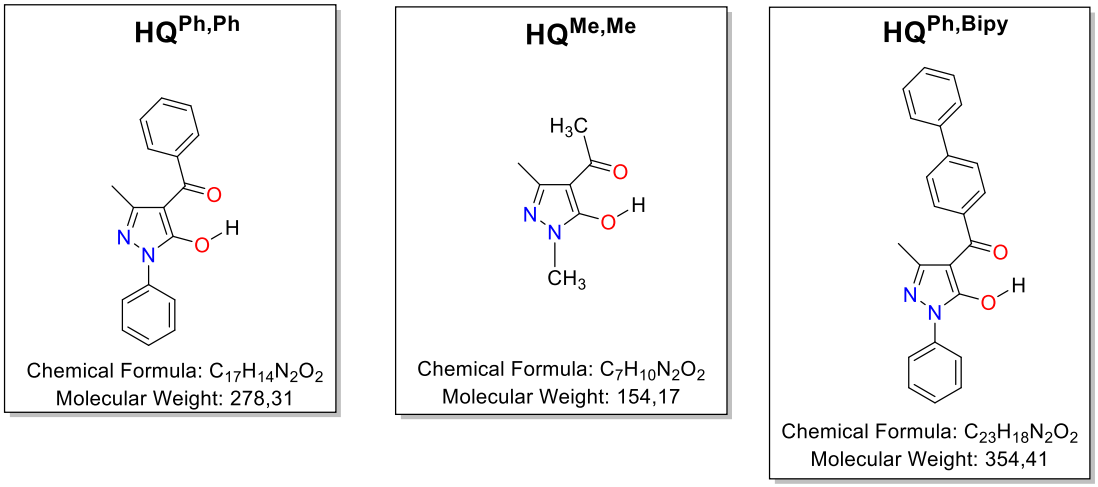

Figure 6 the structure of acylpyrazolone ligand.

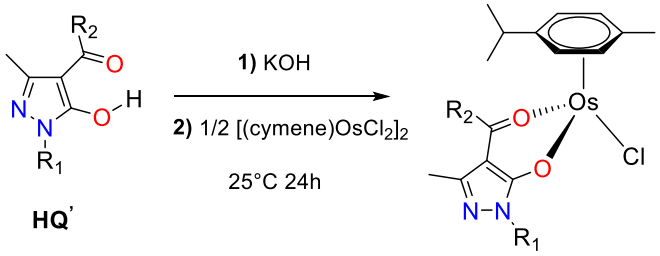

1) $[(cymene)Os(Q^{Ph,Ph})Cl]$

2) $[(cymene)Os(Q^{Ph,Bipy})Cl]$

3) $[(cymene)Os(Q^{Me,Me})Cl]$

Scheme 11. Synthesis of complexes **1-3**.

The ionic derivatives **4-6** were obtained by substituting the chloride ligand of the precursors **1-2** with PTA in the ruthenium coordination environment. The substitution was accomplished by first adding silver salts, namely $AgSO_3CF_3$, and then PTA (**Scheme 12**).

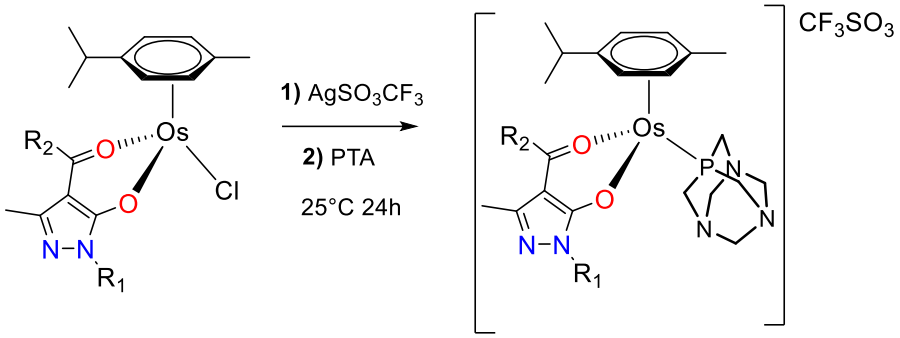

4) [(cymene)Os($Q^{Ph,Ph}$)PTA]SO_3CF_3

5) [(cymene)Os($Q^{Ph,Bipy}$)PTA]SO_3CF_3

6) [(cymene)Os($Q^{Me,Me}$)PTA]SO_3CF_3

Scheme 12. Synthesis of ionic complexes **4-6**.

Complexes **1-6** are air and moisture-stable; they are soluble in methanol, DMSO, DMF, chlorinated solvents, acetonitrile, and acetone and slightly soluble in diethyl ether. and the ionic complexes **4-6** are also slightly soluble in water.

The IR spectra of **1-3** show the typical shift of the ν(C=O) vibrations to lower wavenumbers when the acylpyrazolone ligand is coordinated to the metal ion in the O,O′-bidentate chelating mode[74]. In terms of ionic complexes, the IR spectra of **4-6** show the characteristic absorption pattern of the CF_3SO_3 counterion in the region 1000–1200 cm^{-1} [76], Furthermore, upon coordination, new medium-to-strong absorption bands appear, which can be assigned to ν(Os-O) and (Os-Cl) vibrations.

The ^1H and ^{13}C NMR spectra of **1−3** recorded in $CDCl_3$ display the expected distinct changes in frequency for the resonances of the acylpyrazolone protons and carbon atoms in comparison to the free proligands. As shown in ^1H NMR spectra of **1** (**Figure 7**), the proton resonances attributable to the p-cymene ring are in the range of 5.70−6.20 ppm, which is typical of osmium−arene systems[77]. Six different p-cymene ring carbon peaks in the range of 69.1−89.6 ppm are observed in the ^{13}C NMR spectrum of **1** (**Figure 8**), along with peaks corresponding to two different methyl groups of the isopropyl moiety in the range of 22.4−22.8 ppm. A similar pattern was observed in the ^1H NMR and ^{13}C NMR spectra of 2 and 3, but with two sets of signals.

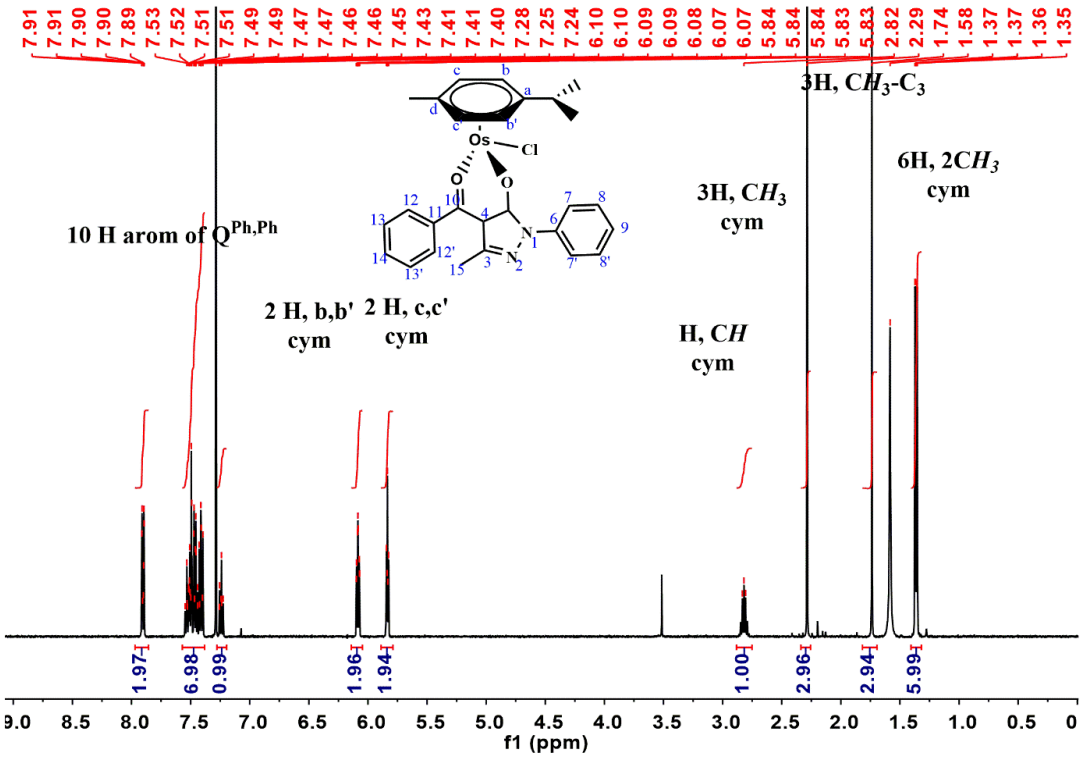

Figure 7. ^{1}H NMR spectrum of [Os(cym)(HQ^{Ph,Ph})]Cl, **1** in CD_3Cl_3.

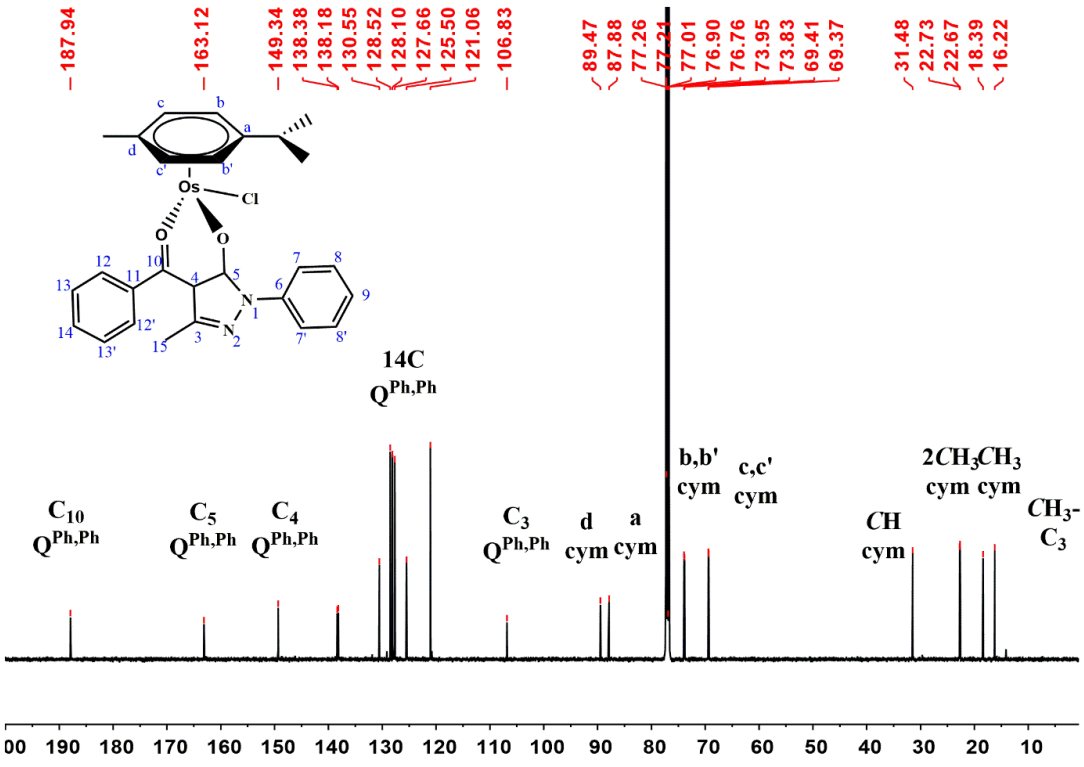

Figure 8. ^{13}C NMR spectrum of [Os(cym)(HQ^{Ph,Ph})]Cl, **1** in CD_3Cl_3.

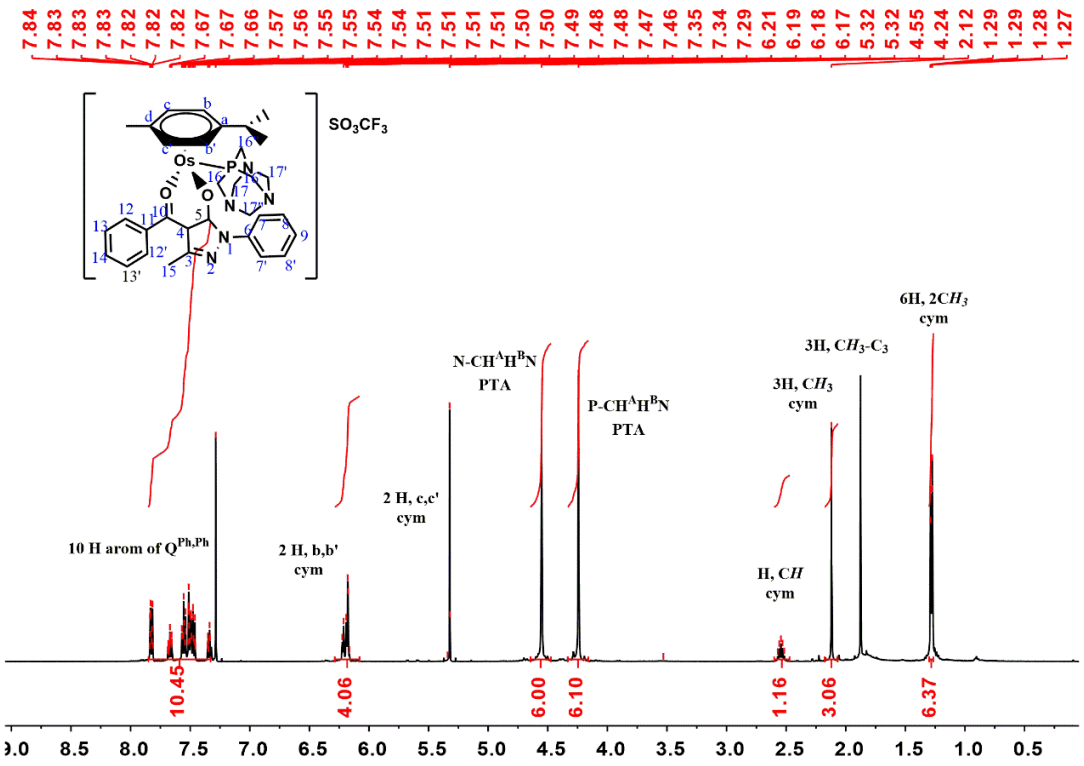

Figure 9. ^{1}H NMR spectrum of [Os(cym)(HQ^{Ph,Ph})PTA][SO_3CF_3], **4** in CD_3Cl_3.

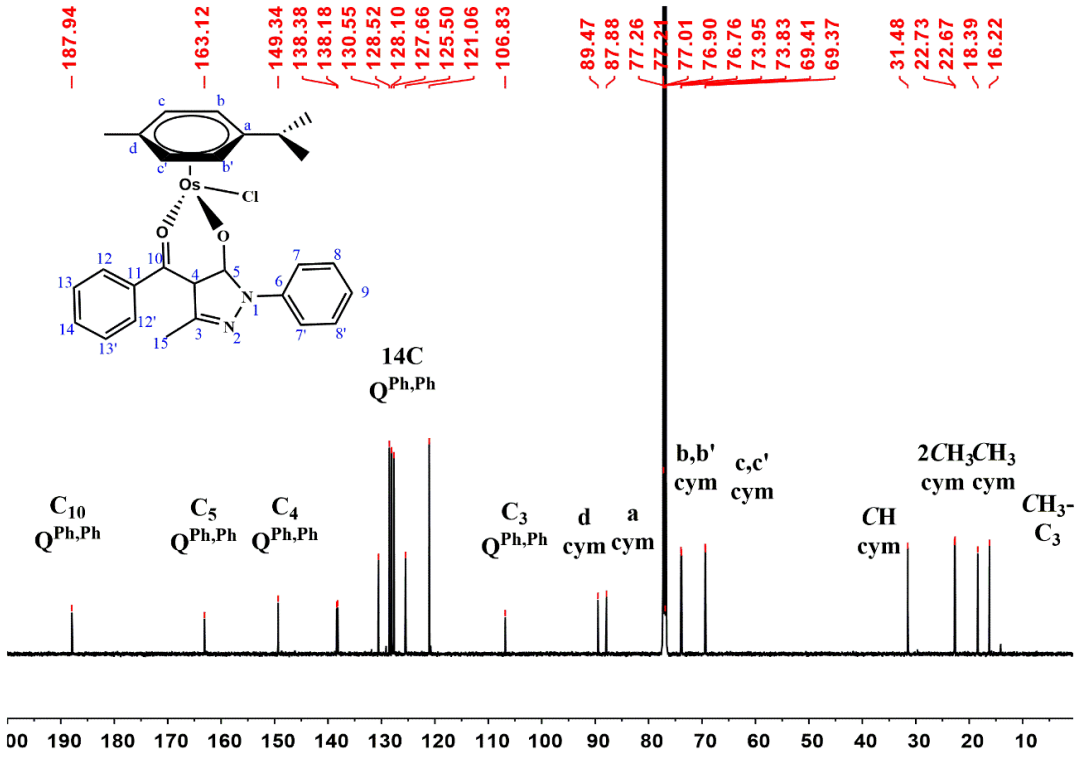

Figure 10. ^{13}C NMR spectrum of [Os(cym)(HQ^{Ph,Ph})PTA][SO_3CF_3], **4** in CD_3Cl_3.

The ^{1}H and ^{13}C NMR spectra of all the complexes display all the expected signals

ascribable to the acylpyrazolone ligand and to arene rings after coordination, and for ionic complexes **4-6** (**Figure 9** and **10**) it is possible to detect also the signals originated from the coordination of PTA to the metal center. In fact the resonances due to the PTA ligand are shifted to lower field with respect to those of uncoordinated PTA confirming its coordination to the osmium center.[1]

The ^{31}P NMR spectra of **4** − **6**, containing the cym moiety, show a singlet centered at *ca.*−65.33 ppm due to PTA, in a range typical of related compounds and in accordance with the existence of only one species in solution (**Figure 11**).

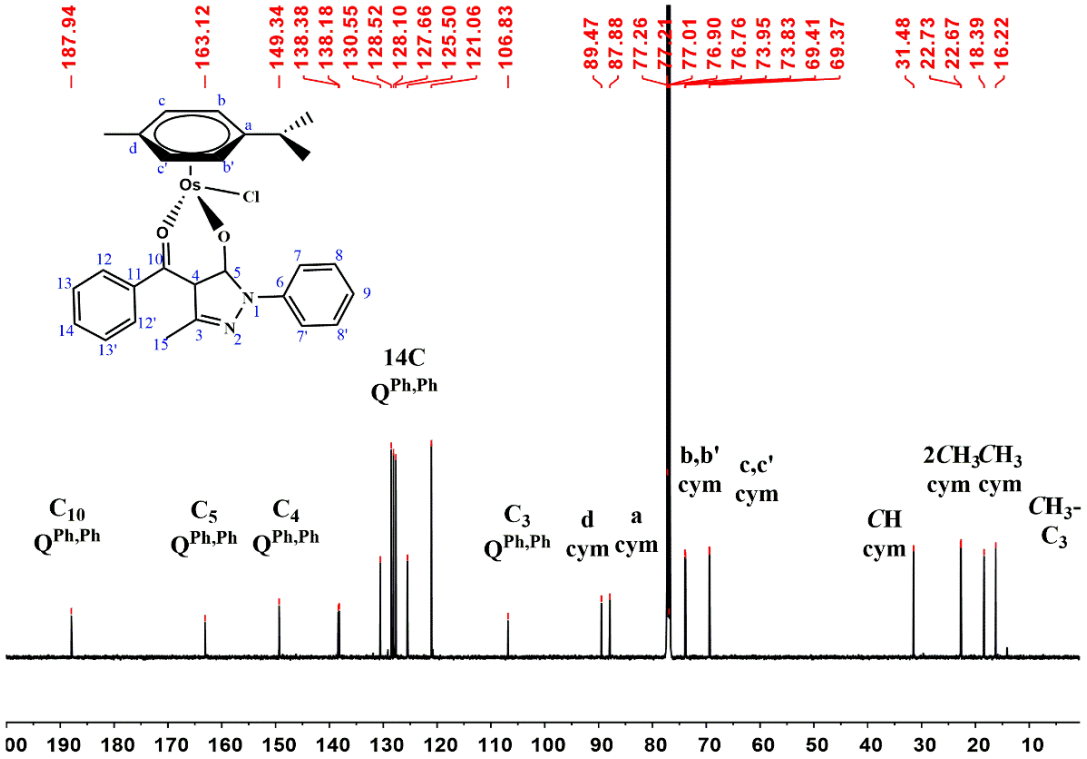

Figure 11. ^{31}P NMR spectrum of [Os(cym)(HQ^{Ph,Ph})PTA][SO_3CF_3], **4** in CD_3Cl_3.

The ESI mass spectra of neutral complexes **1-3** show a main peak that corresponds to the fragment $[Os(cym)(Q)]^+$. The ESI mass spectra of the ionic complexes **4-6** show one main peaks: the one of highest relative intensity corresponds to the cationic fragment of the complex.

The solid state structures of **1, 3** and **5** were established by X-ray crystallography. Their structures are shown in **Figures 12-14**, selected bond lengths and angles are given in captures and principal bond parameters are given in Table 1. In general, the structure of these complexes consists in a half sandwich structure due to the osmium-arene moiety bound to ligand and to the chloride (compound **1** and **3**) or PTA (compounds **6**).

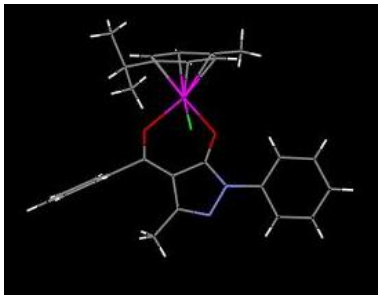

Figure 12. Molecular structure of compound 1. Hydrogen atoms have been omitted for clarity. Bond distances: Os-Cl 2.4042(8) Å, Os-O 2.097(2) and 2.101(2)Å. Cl-Os-O angles in the range 82.95(7)- 83.64°(7).

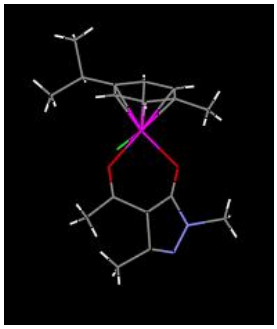

Figure 13. Molecular structure of compound 3. Hydrogen atoms have been omitted for clarity. Bond distances: Os-Cl 2.32(13) Å, Os-O 2.12(2) and 2.085(19) Å. Cl-Os-O angles in the range 80(3)-92°(3).

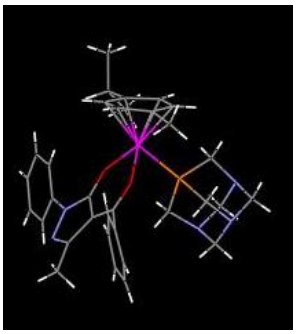

Figure 14. Molecular structure of compound **5**. Anion and hydrogen atoms have been omitted for clarity. Bond distances: Os-P 2.3265(8) Å, Os-O 2.110(2) and 2.098(2) Å. P-Os-O angles in the range 87.35(7)-88.05°(7).

Table 1. Crystallographic data and structural refinement details for **1, 3** and **5**. [a] R(F) = å||F_o| - |F_c||/å|F_o|; $wR(F^2)$ = [å$w(F_o^2 - F_c^2)^2$/åwF^4]$^{1/2}$.

Compound	**1**	**3**	**5**
Chemical formula	$C_{27}H_{27}ClN_2O_2Os$	$C_{17}H_{23}ClN_2O_2Os$	$C_{40}H_{45}F_3N_5O_5OsPS$
M/gmol^{-1}	637.15	513.02	986.04
T (K)	293.44(17)	293.91(10)	294.42(10)
Crystal system	monoclinic	monoclinic	monoclinic
Space group	$P2_1/c$	$P2_1/c$	$P2_1/c$
a (Å)	16.4870(3)	10.5890(7)	10.02760(10)
b (Å)	8.22240(10)	14.1269(9)	23.1592(2)
c (Å)	17.7399(3)	12.5337(8)	17.4266(2)
β (°)	91.957(2)	90	103.0190(10)
V (Å3)	2403.47(7)	1842.0(2)	3942.97(7)
Z	4	4	4
ρ (g cm^{-3})	1.761	1.850	1.661
μ (mm^{-1})	11.257	14.493	7.543
Unique reflections	15439	11385	26108
R_{int}	0. 0365	0. 0658	0. 0395
Goodness-of-fit (GOF) on F^2	1.039	1.137	1.065
*R*1 [$I > 2\sigma(I)$][a]	0.0241	0.1165	0.0294
*wR*2 [$I > 2\sigma(I)$][a]	0.0626	0.2904	0.0755

4.2.2 Biological studies

4.2.2.1 Cytotoxicity tests

The ability of complexes **1-6** used at different doses (1-200 μM) to affect the viability of cancer cells (such as human breast cancer (MCF-7), Mouse breast cancer cells (4T1), Mouse colon cancer cells (CT26), and Mouse Renal Carcinoma (Renca)) to evaluate by MTT assay. Both the neutral complexes **1-3** and the ionic ones **4-6** have displayed the ability of reducing the viability of both MCF-7 cells, in a time- and dose-dependent manner starting from 48 h post-treatments. IC_{50} values (calculated at 72 h post-treatments, Table 2) indicate that the complexes studied are able to reduce cell viability in different extent.

Table 2. IC_{50} of the complexes **1-6** on cancer cell lines. Data shown are expressed as mean ± SE of three separate experiments.

Complex	MCF-7 **IC_{50} [μM]**	4T1 **IC_{50} [μM]**	CT26 **IC_{50} [μM]**	Renca **IC_{50} [μM]**
cis-Pt	8.4 ± 0.13	0.178±0.15	0.045±0.3	11.94±0.14
1	314±1.2	>500	>500	264.66±3.0
2	89±2.4	>500	>500	469.96±2.8
3	95±3.5	>500	>500	>500
4	14±1.7	>500	>500	>500
5	15±2.1	>500	>500	29.96±1.9
6	18±1.8	>500	>500	>500

All complexes tested reduced cell viability in a dose- and cell-dependent manner, with the parent ligands having only minor effects. Among the neutral complexes **1-3**, both are exhibit less activity in the medium micromolar range against 4T1, CT26, and Renca cancer cell lines compared with MCF-7 cell lines. The hydrophobicity of the $HQ^{ph,ph}$, $HQ^{Ph,Bipy}$, and $HQ^{Me,Me}$ ligands are correlated with the cytotoxicity of the complexes **1-3**; that is, the complexes with the $HQ^{Ph,Bipy}$ -derived ligand are the most cytotoxic. Notably, for all cell lines tested, the combination of ligand and PTA ligand produced the most cytotoxic complexes (**4-6**) with potency comparable to that of cisplatin against MCF-7. The strong cytotoxicity of **4-6** is particularly notable, as they can be considered to produce the same class of prodrugs intracellularly as OSPTA-C, which is not intrinsically cytotoxic [78]. Moreover, the high cytotoxicity could not be attributed to the released, free acylpyrazolinic acid ligand, which showed only modest activity. In contrast, complexes **1-3** does not produce the same type of active species as OSPTA-C and complexes **4-6**, and therefore may operate through a different mechanism.

4.3 Conclusions

To investigate the effect of aliphatic substituents on anticancer activity in vitro,

osmium(II)–arene complexes containing acylpyrazolones bearing aliphatic groups in the acyl moiety were prepared. The neutral [Os(arene)(Q^R)Cl] and cationic [Os(arene)(Q^R)(PTA)]$^+$ complexes display a typical piano-stool geometry crystal structures with acylpyrazolone ligands always O,-O′ coordinated to the osmium ion. Furthermore, some of the complexes are cytotoxic, and, interestingly, the combination of the HQC and PTA ligands produced the most cytotoxic compounds (**4, 5** and **6**) for MCF-7.

Chapter 5. P-cymene osmium bis(pyrazolyl)alkane complexes

Our group has previously synthesized a series of complexes of arene Ru(II) complexes containing bis(pyrazolyl)methane ligands. These ruthenium composites possess better water solubility, which is important for chemotherapy, so we synthesized $[Os(cym)Cl(\mu\text{-}Cl)]_2$ and [Os(cym) (L′)Cl][Os(cym) Cl_3] composites and evaluated the the cytotoxicity of the proligands and metal complexes in vitro against cancer cells. In general, the [Os(cym) (L′)Cl]Cl complexes are more cytotoxic.

5.1 Experimental

5.1.1 General procedures

ESI-MS were recorded by a Thermo-Finnigan LCQ Deca XP Plus quadropole ion-trap instrument operated in positive-ion mode. Perkin-Elmer Frontier Spectrometer FT-IR/FIR Instrument was used to collected IR spectra from 4000 to 200 cm^{-1}. ^{1}H and ^{13}C NMR spectra were measured by a Bruker Avance III 400 spectrometer operating at room temperature (400 MHz for ^{1}H, 100 MHz for ^{13}C) relative to TMS. Bruker Avance III 400 spectrometer at room temperature, 162 MHz relative to 85% H_3PO_4 was used to record ^{31}P NMR spectra. The melting points were measured using an uncorrected STMP3 Stuart scientific instrument and a capillary apparatus. The microanalytical laboratory at EPFL's Institute of Chemical Sciences and Engineering in Lausanne examined samples for microanalysis.

5.1.2 Synthesis and characterization of the complexes

The L’ (L_1, L_2, L_3, and L_4) ligands were synthesized according to the previous report [74].

[Os(cym) (L_1)Cl]Cl (7).

[{Os(cym)Cl_2}$_2$] (79.1 mg, 0.1 mmol) was dissolved in methanol (10 mL) under stirring

for 30 min. Afterwards, L_1 (29.6 mg, 0.2 mmol) was added to the solution which immediately changed to yellow under stirring for 24 h at room temperature. Finally, the resulting yellow solution was evaporated to dryness and redissolved in dichloromethane (4 mL) and n-hexane (0.1 mL). Slow evaporation afforded a yellow powder, which was washed with *n*-hexane and dried under reduced pressure and denoted as derivative **7**. It is very soluble in water, alcohols, chlorinated solvents, DMSO, and DMF and slight soluble in acetonitrile. Yield 73%. Mp 176-178 °C. ΛM (DMSO, 10^{-3} M): 37.89 Ω^{-1} cm^2 mol^{-1}. Anal. Calcd. for $C_{17}H_{22}Cl_2N_4Os$: C. 37.57; H, 4.08; N, 10.31. Found: C. 36.82; H, 4.34; N, 10.18%. IR (cm^{-1}): 3098m *ν*(Carom-H), 1627w *ν*(C=N), 1513m *ν*(*C*=N + C=C), 1469m, 1416s, 1279s, 1073m, 759vs, 598m, 452w, 440w, 415w, 400.89m ν(Os-C), 295s *ν*(Os-Cl), 237m (Os-N). ^{1}H (DMSO): *δ*=1.21 (d, 6H, J = 6.9 Hz, CH_3-C_6H_4-CH(C*H*$_3$)$_2$), 2.05 (s, 3H, C*H*$_3$-C_6H_4-CH(CH_3)$_2$), 2.73 (m, 1H, ^3J = 6.8 Hz, CH_3-C_6H_4-C*H*(CH_3)$_2$), 6.25, 6.34 (d, 4H, AA'BB' spin system, $^4J_{AA'}$: 5.8 Hz, $^3J_{AB}$: 14.2 Hz, CH_3-C_6H_4-CH(CH_3)$_2$), 6.62 (t, 2H, $H_{6,6'}$ of L_1),7.23 (d, 2H, $H_{3,3'}$ of L_1), 6.07 7.29 (d, 2H, AX spin system, $^2J_{AX}$: 15 Hz, H_2C of L_1), 7.87 (d, 2H, $H_{5,5'}$ of L_1), 8.17 (d, 2H, $H_{4,4'}$ of L_1).^{13}C (DMSO): *δ*= 18.0 (s, *C*H_3-C_6H_4-CH(CH_3)$_2$), 22.5 (s, CH_3-C_6H_4-CH(*C*H_3)$_2$), 30.8 (s, CH_3-C_6H_4-*C*H(CH_3)$_2$), 63.6 (s, $C_{3,3'}$- of L_1), 74.8, 77.1, 91.8, 95.7 (s, CH_3-*C*$_6$H$_4$-CH(CH_3)$_2$), 108.4 (s, H_2C of L_1), 135.2 (s, $C_{4,4'}$ of L_1), 147.2 (s, $C_{5,5'}$ of L_1). ESI-MS (MeCN) (+): *m*/*z* (%)) 508 (100) [Os(cym)(L_1)Cl]$^+$.

[Os(cym)(L_2)Cl]Cl (8). Derivative **8** was synthesized according to **7**. It is very soluble in DMSO, DMF, chlorinated solvents, and acetonitrile, and slight soluble in alcohols and acetone. Yield 78%. Mp 176-178 °C. ΛM (DMSO, 10^{-3} M): 28.84 Ω^{-1} cm^2 mol^{-1}. Anal. Calcd. For C21H30Cl2N4Os: C 42.06; H, 5.04; N, 9.34. Found: C. 40.45; H, 5.23; N, 9.56%. IR (cm^{-1}): 2928w *ν*(Carom-H), 1558m *ν*(*C*=N + C=C), 1471m, 1423s, 1277s, 1055w, 774vs, 689m, 456w, 401w ν(Os-C), 287s *ν*(Os-Cl), 245m (Os-N). ^{1}H (DMSO): *δ*=1.08 (d, 6H, CH_3-C_6H_4-CH(C*H*$_3$)$_2$), 2.25 (s, 3H, C*H*$_3$-C_6H_4-CH(CH_3)$_2$), 2.50 (s, 6H, C_3-C*H*$_3$ and $C_{3'}$-C*H*$_3$ of L_2), 2.51 (s, 6H, C_5-C*H*$_3$ and $C_{5'}$-C*H*$_3$ of L_2), 2.68 (m, 1H, ^3J = 7.0 Hz, CH_3-C_6H_4-C*H*(CH_3)$_2$), 6.31 (d, 4H, cc' and $H_{4,4'}$ of L_2, ^3J = 6.3 Hz,

CH_3-C_6H_4-$CH(CH_3)_2$), 6.42 (d, 2H, bb', ^3J = 5.8 Hz, CH_3-C_6H_4-$CH(CH_3)_2$), 5.55, 6.58 (d, 2H, AX spin system, $^2J_{AX}$: 15.6 Hz, H_2C-of L_2). ^{13}C (DMSO): δ= 11.13 (s, $C_{5'}$-CH_3 of L_2), 15.73 (s, $C_{3'}$-CH_3 of L_2), 18.31 (s, CH_3-C_6H_4-$CH(CH_3)_2$), 22.86 (s, CH_3-C_6H_4-$CH(CH_3)_2$), 31.79 (s, CH_3-C_6H_4-$CH(CH_3)_2$), 57.98 (s, H_2C- of L_2), 73.85, 76.35, 92.00, 97.40 (s, CH_3-C_6H_4-$CH(CH_3)_2$), 108.61 (s, $C_{4,4'}$ of L_2), 143.26 (s, $C_{5,5'}$ of L_2), 155.33 (s, $C_{3,3'}$ of L_2). ESI-MS (MeCN) (+): m/z (%)) 565 (100) $[Os(cym)(L_2)Cl]^+$.

[Os(cym) (L_3)Cl]Cl (9). Derivative **9** was synthesized according **7**. It is very soluble in water, alcohols, chlorinated solvents, DMSO, acetonitrile and DMF. Yield 77%. Mp 110-114 °C. ΛM (DMSO, 10^{-3} M): 30.25 Ω^{-1} cm^2 mol^{-1}. Anal. Calcd. for $C_{19}H_{26}Cl_2N_4Os$: C. 39.79; H, 4.92; N, 9.77. Found: C. 39.43; H, 4.91; N, 9.65%. IR (cm^{-1}): 2961w *ν*(Carom-H), 1634w *ν*(C=N), 1454m, 1390s, 1317s, 1169s, 1031s, 792m, 639s, 599s, 456w, 418w ν(Os-C), 295s *ν*(Os-Cl), 272m (Os-N). ^{1}H (DMSO): δ= 1.21 (d, 6H, CH_3-C_6H_4-$CH(CH_3)_2$), 1.99 (s, 6H, C_4-CH_3 of L_3), 2.05 (s, 3H, CH_3-C_6H_4-$CH(CH_3)_2$), 2.73 (m, 1H, ^3J = 6.8 Hz, CH_3-C_6H_4-$CH(CH_3)_2$), 6.20, 6.29 (d, 4H, AA'BB' spin system, $^4J_{AA'}$: 5.8 Hz, $^3J_{AB}$: 14.2 Hz, CH_3-C_6H_4-$CH(CH_3)_2$), 6.29 (d, 2H, bb'', ^3J = 5.8 Hz, CH_3-C_6H_4-$CH(CH_3)_2$), 5.93, 7.02 (d, 2H, AX spin system, $^2J_{AX}$: 14.3 Hz, H_2C- of L_3), 7.75 (d, 2H, $H_{3,3'}$ of L_3), 7.94 (d, 2H, $H_{5,5'}$ of L_3).^{13}C (DMSO): δ=18.24 (s, CH_3-C_6H_4-$CH(CH_3)_2$), 22.70 (s, CH_3-C_6H_4-$CH(CH_3)_2$), 30.95 (s, CH_3-C_6H_4-$CH(CH_3)_2$), 63.49 (s, $C_{3,3'}$ of L_3), 75.05, 77.33, 92.02, 95.96 (s, CH_3-C_6H_4-$CH(CH_3)_2$), 108.55 (s, H_2C of L_3), 135.48 (s, $C_{4,4'}$ of L_3), 147.33 (s, $C_{5,5'}$ of L_3). ESI-MS (MeCN) (+): m/z (%)) 537 (100) $[Os(cym)(L_3)Cl]^+$.(not good).

[Os(cym) (L_4)Cl]Cl (10). The synthesized methods of derivative **10** was according to **7**. It is very soluble in water, DMSO, DMF, chlorinated solvents, and acetonitrile. Yield 68%. Mp 70-75 °C. ΛM (DMSO, 10^{-3} M): 29.99 Ω^{-1} cm^2 mol-1. Anal. Calcd. For $C_{19}H_{26}Cl_2N_4Os$: C 39.93; H, 4.58; N, 9.80. Found: C. 38.83; H, 4.87; N, 10.57%. IR (cm^{-1}): 2963w ν(Carom-H), 1634w, 1515w ν(C=N + C=C), 1416s, 1386s, 1313s, 1236s, 1104s, 762vs, 619vs, 455w, 421w ν(Os-C), 284s ν(Os-Cl), 251m (Os-N). ^{1}H (DMSO): δ= 1.24 (d, 6H, CH_3-C_6H_4-$CH(CH_3)_2$), 1.93 (s, 3H, CH_3-C_6H_4-$CH(CH_3)_2$), 2.19, 2.53 (s, 6H, $(CH_3)_2$C- of L_4), 2.77 (m, 1H, 3J = 6.8 Hz, CH_3-C_6H_4-$CH(CH_3)_2$), 6.27, 6.39 (d,

4H, AA'BB' spin system, CH_3-C_6H_4-$CH(CH_3)_2$), 6.69 (d, 2H, $H_{4,4'}$ of L_4), 8.25 (d, 2H, $H_{5,5'}$of L_4), 8.38 (d, 2H, $H_{3,3'}$ of L_4). ^{13}C (DMSO): δ=18.11 (s, (CH_3)$_2$C- of L_4), 22.85 (s, CH_3-C_6H_4-$CH(CH_3)_2$), 26.22, 29.52 (s, CH_3-C_6H_4-$CH(CH_3)_2$), 31.21 (s, CH_3-C_6H_4-$CH(CH_3)_2$), 75.93, 76.48, 90.95, 96.69 (s, CH_3-C_6H_4-$CH(CH_3)_2$), 78.46 (s, $(CH_3)_2C$- of L_4), 108.61 (s, $C_{4,4'}$ of L_4), 134.16 (s, $C_{5,5'}$ of L_4), 151.75 (s, $C_{3,3'}$ of L_4). ESI-MS (MeCN) (+): m/z (%)) 537 (100) [Os(cym) (L_4)Cl] $^+$.

[Os(cym) (L_1)Cl][Os(cym) Cl_3]] (11). [(Os(cym)Cl_2)$_2$] (79.1 mg, 0.1 mmol) was dissolved in methanol (10 mL) under stirring for 30 min. Afterwards, L_1 (14.8 mg, 0.1 mmol) was added to the solution which immediately changed to yellow under stirring for 24 h at room temperature. Finally, the resulting yellow solution was evaporated to dryness and redissolved in dichloromethane (4 mL) and n-hexane (0.1 mL). Slow evaporation afforded a yellow powder, which was washed with *n*-hexane and dried under reduced pressure and denoted as derivative **11**. It is very soluble in water, alcohols, chlorinated solvents, DMSO, and DMF and slight soluble in acetonitrile. Yield 73%. Mp 205-208°C. ΛM (DMSO, 10^{-3} M): 34.06 Ω^{-1} cm^2 mol^{-1}. Anal. Calcd. for $C_{17}H_{22}Cl_2N_4Os$: C. 34.54; H, 3.86; N, 5.97. Found: C. 34.12; H, 3.92; N, 5.67%. IR (cm^{-1}): 2957m ν(Carom-H), 1617w ν(C=N), 1503m ν(C=N + C=C), 1424m, 1407s, 1272s, 1096m, 1066m, 770vs, 608m, 464w, 418w, 292s ν(Os-Cl), 247m (Os-N). ^{1}H (DMSO): δ=1.20, 1.21 (d, 12H, CH_3-C_6H_4-$CH(CH_3)_2$), 2.05, 2.14 (s, 6H, CH_3-C_6H_4-$CH(CH_3)_2$), 2.74 (m, 2H, ^3J = 7.0 Hz, CH_3-C_6H_4-$CH(CH_3)_2$), 6.00, 6.24 (d, 4H, AA'BB' spin system, $^4J_{AA'}$: 6.0 Hz, $^3J_{AB}$: 43.5 Hz, CH_3-C_6H_4-$CH(CH_3)_2$,), 6.25, 6.33 (d, 4H, AA'BB' spin system, $^4J_{AA'}$: 5.2 Hz, $^3J_{AB}$: 7.8 Hz, CH_3-C_6H_4-$CH(CH_3)_2$), 6.04, 6.64 (d, 2H, AX spin system, $^2J_{AX}$: 14.6 Hz, H_2C- of L_1),7.23 (d, 2H, $H_{3,3'}$ of L_1), 7.91 (d, 2H, $H_{5,5'}$ of L_1), 8.18 (d, 2H, $H_{4,4'}$ of L_1).^{13}C (DMSO): δ=18.43 (s, CH_3-C_6H_4-$CH(CH_3)_2$), 22.46, 22.90 (s, CH_3-C_6H_4-$CH(CH_3)_2$), 30.59, 31.16 (s, CH_3-C_6H_4-$CH(CH_3)_2$), 63.46 (s, $C_{3,3'}$- of L_1), 75.21, 77.50, 78.61, 78.81, 92.21, 93.62 (s, CH_3-C_6H_4-$CH(CH_3)_2$), 108.78 (s, H_2C of L1), 135.53 (s, $C_{4,4'}$ of L_1), 147.58 (s, $C_{5,5'}$ of L_1). ESI-MS (MeCN)

(+): *m/z* (%)) 508 (100) [Os(cym) (L_1)Cl]$^+$. ESI-MS (MeCN) (-): m/z (%) = 430 (20) [Os(cym)Cl_3]$^-$.

[Os(cym)(L_2)Cl][Os(cym)Cl_3]] (12).

Derivative **12** was synthesized according to **11**. It is very soluble in water, alcohols, DMSO, DMF, chlorinated solvents, acetone and acetonitrile. Yield 85%. Mp 212-213 ° C. ΛM (DMSO, 10^{-3} M): 30.90 Ω^{-1} cm^2 mol^{-1}. Anal. Calcd. For $C_{31}H_{46}Cl_4N_4Os_2$: C 37.42; H, 4.46; N, 63. Found: C. 37.62; H, 4.45; N, 5.39%. IR (cm^{-1}): 2957m *ν*(Carom-H), 1617w *ν*(C=N), 1503m *ν*(*C*=N + C=C), 1424m, 1407s, 1272s, 1096m, 1066m, 770vs, 608m, 464w, 418w, 292s *ν*(Os-Cl), 247m (Os-N). ^{1}H (DMSO): *δ*, 1.20, 1.34 (d, 12H, CH_3-C_6H_4-CH(C*H*$_3$)$_2$), 2.25, 2.28 (s, 6H, C*H*$_3$-C_6H_4-CH(CH_3)$_2$), 2.50 (s, 6H, $H_{7,7'}$ of L_2), 2.65 (s, 6H, $H_{8,8'}$ of L_2), 3.00 (m, 2H, ^3J = 7.0 Hz, CH_3-C_6H_4-C*H*(CH_3)$_2$), 5.83 (d, H, H_2C- of L_2) , 6.01 (s, 2H, $H_{4,4'}$ of L_2), 5.83, 6.03 (d, 4H, AA'BB' spin system, $^4J_{AA'}$: 5.9 Hz, $^3J_{AB}$: 42.3 Hz, CH_3-C_6H_4-CH(CH_3)$_2$), 6.42, 6.27 (d, 4H, AA'BB' spin system, $^4J_{AA'}$: 5.8 Hz, $^3J_{AB}$: 28 Hz, CH_3-C_6H_4-CH(CH_3)$_2$,), 6.23, 6.88 (d, 2H, AX spin system, $^2J_{AB}$: 15.6 Hz, CH_2- of L_2). ^{13}C (DMSO): *δ,* 11.13 (s, $C_{8,8'}$ of L_2), 15.73 (s, $C_{7,7'}$ of L_2), 18.41, 18.50 (s, *C*H_3-C_6H_4-CH(CH_3)$_2$), 22.45, 23.07 (s, CH_3-C_6H_4-CH(*C*H_3)$_2$), 30.59, 31.99 (s, CH_3-C_6H_4-*C*H(CH_3)$_2$), 58.08 (s, H_2*C*- of L_2), 74.02, 76.54, 78.61, 78.81, 92.19, 93.64,97.52, 98.27 (s, CH_3-*C*$_6$H$_4$-CH(CH_3)$_2$), 108.80 (s, $C_{4,4'}$ of L_2), 143.45 (s, $C_{5,5'}$ of L_2), 155.33 (s, $C_{3,3'}$ of L_2). ESI-MS (MeCN) (+): m/z (%)) 565 (100) [Os(cym)(L_2)Cl]$^+$, ESI-MS (MeCN) (-): m/z (%) = 430 (20) [Os(cym)Cl_3]]$^-$.

[Os(cym)(L_3)Cl][Os(cym) Cl_3]] (13). Derivative **13** was synthesized according **11**. It is very soluble in alcohols, chlorinated solvents, DMSO, acetonitrile and DMF. Yield 57%. Mp 238-242 °C. ΛM (DMSO, 10^{-3} M): 31.10 Ω^{-1} cm^2 mol^{-1}. Anal. Calcd. for $C_{29}H_{40}Cl_4N_4Os_2$: C. 36.02; H, 4.17; N, 5.79%. Found: C. 35.66; H, 3.91; N, 5.45%. IR (cm^{-1}): 2961w *ν*(Carom-H), 1634w *ν*(C=N), 1454m, 1390s, 1317s, 1169s, 1031s, 792m, 639s, 599s, 456w, 418w ν(Os-C), 295s *ν*(Os-Cl), 272m (Os-N). ^{1}H (DMSO): *δ*, 1.21 (d, 12H, CH_3-C_6H_4-CH(C*H*$_3$)$_2$), 2.06 (s, 6H, C*H*$_3$-C_6H_4-CH(CH_3)$_2$), 2.14 (s, 3H, C_7-C*H*$_3$ of L_3), 2.73 (m, 1H, ^3J = 6.8 Hz, CH_3-C_6H_4-C*H*(CH_3)$_2$), 6.04 (d, 4H, 4H, AA'BB'

spin system, $^{4}J_{AA'}$: 5.7 Hz, $^{3}J_{AB}$: 41.5 Hz, CH_3-C_6H_4-$CH(CH_3)_2$), 6.28 (d, 4H, AA'BB' spin system, $^{4}J_{AA'}$: 5.8 Hz, $^{3}J_{AB}$: 42 Hz, CH_3-C_6H_4-$CH(CH_3)_2$,), 5.96, 7.18 (d, 2H, AX spin system, $^{2}J_{AB}$: 12 Hz, CH_2- of L_3),7.74 (d, 2H, $H_{5,5'}$ of L_3), 7.98 (d, 2H, $H_{3,3'}$ of L_3), 8.35 (s, H, H_2C- of L_3).^{13}C (DMSO): δ, 8.89 (s, CH_3-L_3), 18.20, 18.26 (s, CH_3-C_6H_4-$CH(CH_3)_2$), 22.70 (s, CH_3-C_6H_4-$CH(CH_3)_2$), 30.4, 30.95 (s, CH_3-C_6H_4-$CH(CH_3)_2$), 62.82 (s, CH_2-L_3), 75.01, 77.16, 78.41, 78.60, 91.68, 93.37, 96.01, 98.17 (s, CH_3-C_6H_4-$CH(CH_3)_2$), 117.98 (s, $C_{4,4'}$ of L_3), 135.2 (s, $C_{5,5'}$ of L_3), 147.2 (s, $C_{3,3'}$ of L_3). ESI-MS (MeCN) (+): *m*/*z* (%)) 537 (100) $[Os(cym)(L_3)Cl]^+$.

[Os(cym)(L_4)Cl][Os(cym)Cl_3]] (14). The synthesized methods of derivative **14** was according to **11**. It is very soluble in DMSO, DMF, chlorinated solvents, alcohols, acetone and acetonitrile. Yield 78%. Mp 176-178 °C. ΛM (DMSO, 10^{-3} M): 31.39 Ω^{-1} cm^2 mol^{-1}. Anal. Calcd. For $C_{29}H_{40}Cl_4N_4Os$: C 36.02; H, 4.17; N, 5.79. Found: C. 36.01; H, 4.40; N, 5.72%. IR (cm^{-1}): 2959w *ν*(Carom-H), 1635w, 1416s, 1396s, 1313s, 1235s, 1103s, 763vs, 619vs, 279s *ν*(Os-Cl), 247m (Os-N). ^{1}H (DMSO): *δ*= 1.20, 1.23 (d, 12H, CH_3-C_6H_4-$CH(CH_3)_2$), 1.93, 2.14 (s, 6H, CH_3-C_6H_4-$CH(CH_3)_2$), 2.19, 2.53 (s, 6H, $(CH_3)_2C$- of L_4), 2.77 (m, 2H, ^{3}J = 6.8 Hz, CH_3-C_6H_4-$CH(CH_3)_2$), 6.04 (d, 4H, 4H, AA'BB' spin system, $^{4}J_{AA'}$: 5.7 Hz, $^{3}J_{AB}$: 41.5 Hz, CH_3-C_6H_4-$CH(CH_3)_2$), 6.32 (d, 4H, AA'BB' spin system, $^{4}J_{AA'}$: 5.8 Hz, $^{3}J_{AB}$: 42 Hz, CH_3-C_6H_4-$CH(CH_3)_2$,), 6.69 (d, 2H, $H_{4,4'}$ of L_4), 8.25 (d, 2H, $H_{5,5'}$of L_4), 8.38 (d, 2H, $H_{3,3'}$ of L_4). ^{13}C (DMSO): *δ*= 14.39 18.12, 18.20 (s, $(CH_3)_2C$- of L_4), 22.25, 22.85 (s, CH_3-C_6H_4-$CH(CH_3)_2$), 26.23, 29.53 (s, CH_3-C_6H_4-$CH(CH_3)_2$), 30.39, 31.21 (s, CH_3-C_6H_4-$CH(CH_3)_2$), 78.41, 78.60, 90.95, 93.44, 96.70 and 98.16 (s, CH_3-C_6H_4-$CH(CH_3)_2$), 78.46 (s, $(CH_3)_2C$- of L_4), 108.62 (s, $C_{4,4'}$ of L_4), 134.16 (s, $C_{3,3'}$ of L_4), 151.74 (s, $C_{5,5}$ of L_4). ESI-MS (MeCN) (+): m/z (%)) 537 (100) $[Os(cym)(L_4)Cl]^+$, ESI-MS (MeCN) (-): m/z (%) = 430 (20) $[Os(cym)Cl_3]]^-$.

5.1.3 Cell culture and inhibition of cell growth

Cell culture and inhibition of cell growth studies were performed in the College of

Material and Chemical Engineering, Zhengzhou University of Light Industry, Zhengzhou, China.

5.1.3.1 Cells

MCF-7 (human breast cancer), 4T1 (Mouse breast cancer cells), CT26 (Mouse colon cancer cells), and Renca (Mouse Renal Carcinoma) were purchased from Procell Life Science&Technology Co.,Ltd in China.

Cell lines were cultured in Dulbecco's modified Eagle's medium (DMEM) and Roswell Park Memorial Institute (RPMI) medium (Beijing Soleibao Technology Co., Ltd) supplemented with 10% bovine serum albumin (BSA). Cell lines were maintained at 37 °C with 5% CO_2 and 95% humidity.

The MTT assay was used to assess cytotoxicity. Cells were seeded as monolayers in 96-well plates with 100 L of cell suspension (approximately 10000 cells) per well and pre-incubated for 24 hours in medium supplemented with 10% FBS. Compounds were prepared as DMF solutions, then dissolved in culture medium and serially diluted to the desired concentration, resulting in a final DMF concentration of 0.5 percent. Each well received 100 L of the drug solution, and the plates were incubated for another 72 hours. MTT (5 mg mL^{-1} solution) was then added to the cells, and the plates were incubated for another 2 hours. The medium was aspirated and the purple formazan crystals formed by the mitochondrial dehydrogenase activity of living cells were dissolved in DMF. Optical density proportional to the number of viable cells was quantified at 570 nm using a multi-well plate reader, and the fraction of viable cells was calculated based on the absorbance of untreated control cells. Evaluations are based on mean values from at least two independent experiments, each experiment including quadruplicates for each concentration level.

5.2 Results and discussion

5.2.1 Synthesis and spectroscopic characterization of ruthenium complexes

Complexes **7-10** were prepared in a single step by the interaction of 1 equiv of the

dinuclear $[(cym)OsCl(\mu\text{-}Cl)]_2$ with 2 equiv of bis(pyrazol-1-yl)alkanes L′ (**Figure 15**) in methanol at room temperature as shown in **Scheme 13**.

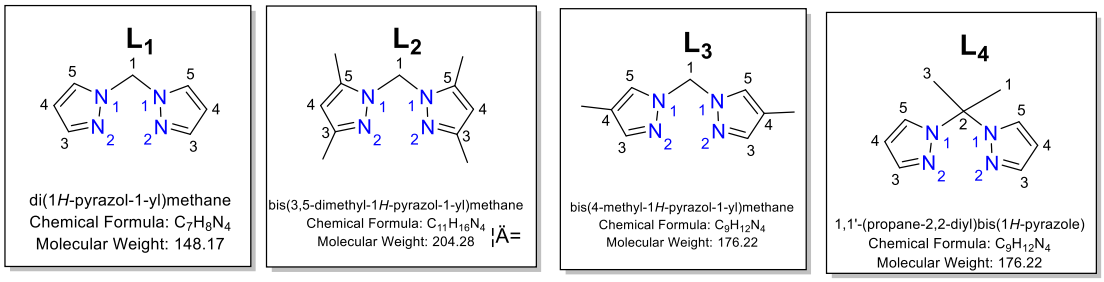

Figure 15 the structure of bis(pyrazol-1-yl)alkanes L′.

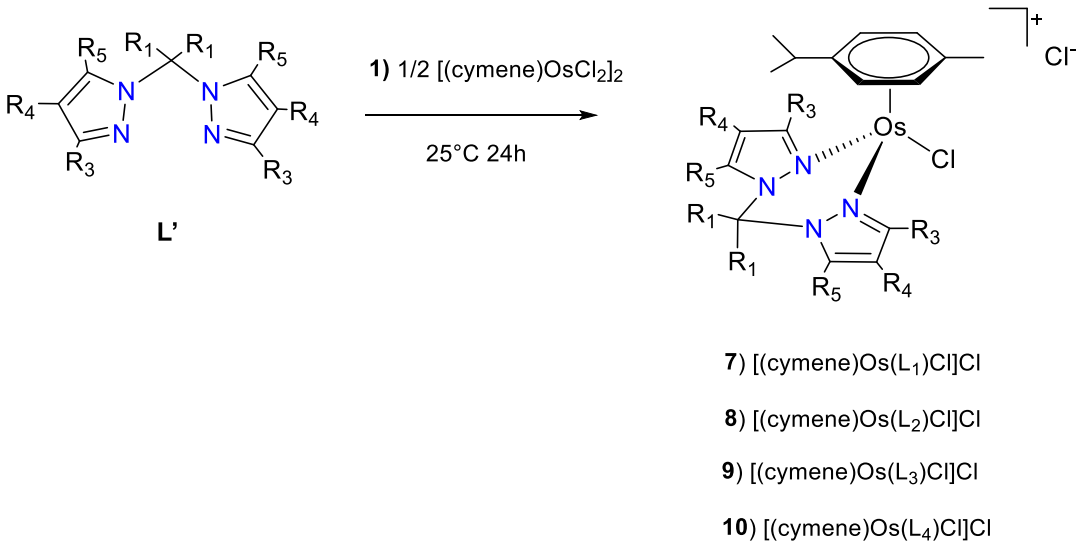

Scheme 13. Synthesis of complexes **7-10**.

Complexes **7-10** are air and moisture stable and are soluble in alcohols, acetone, acetonitrile, DMF and DMSO. In addition, these complexes can also dissolve in water, which is very important for the study of cytotoxicity of complexes.

A strong and sharp absorption due to ν(Os−Cl) has always been found in the range 270−295 cm^{-1} in the far-IR spectra of **7-10**, indicating the presence of single Os-Cl bonds. The IR spectra of **7-10** show broad bands above 1500-1600 cm^{-1} due to the *C*=N + C=C of pyrazole[79].

In DMSO-d_6, the ^1H and ^{13}C NMR spectra of **7-10** (**Figure 16** and **17**) show all of the expected signals due to the bis(pyrazol-1-yl)alkanes L′ ligands, as well as the arene rings after coordination.

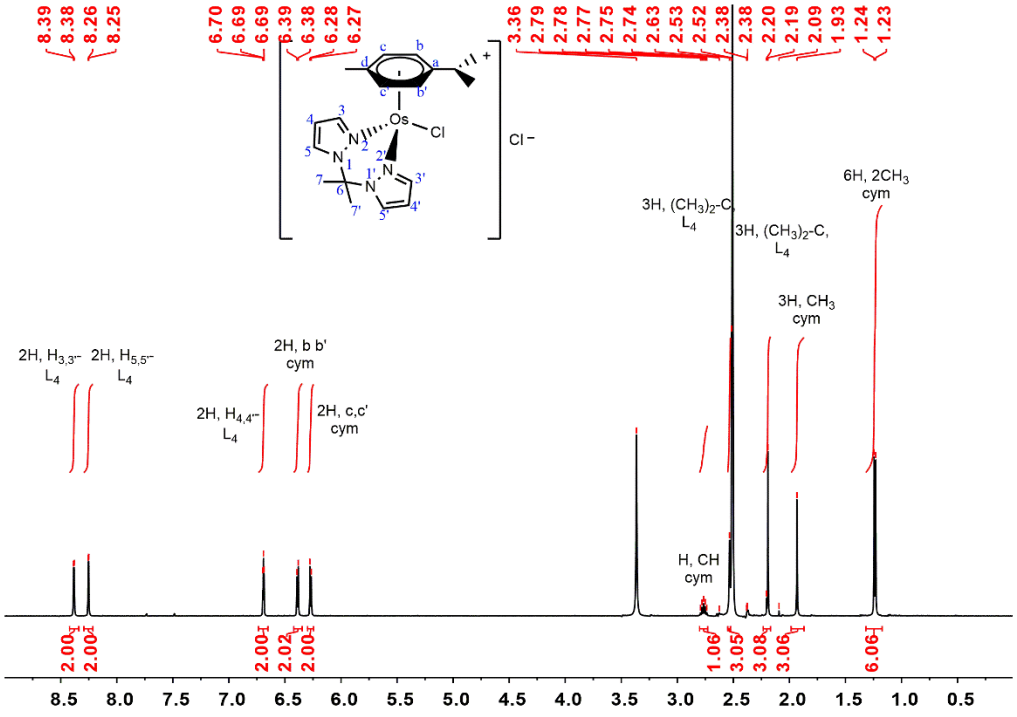

Figure 16. ^{1}H NMR spectrum of [Os(cym) (L_4)Cl]Cl, **10**, in DMSO-d_6.

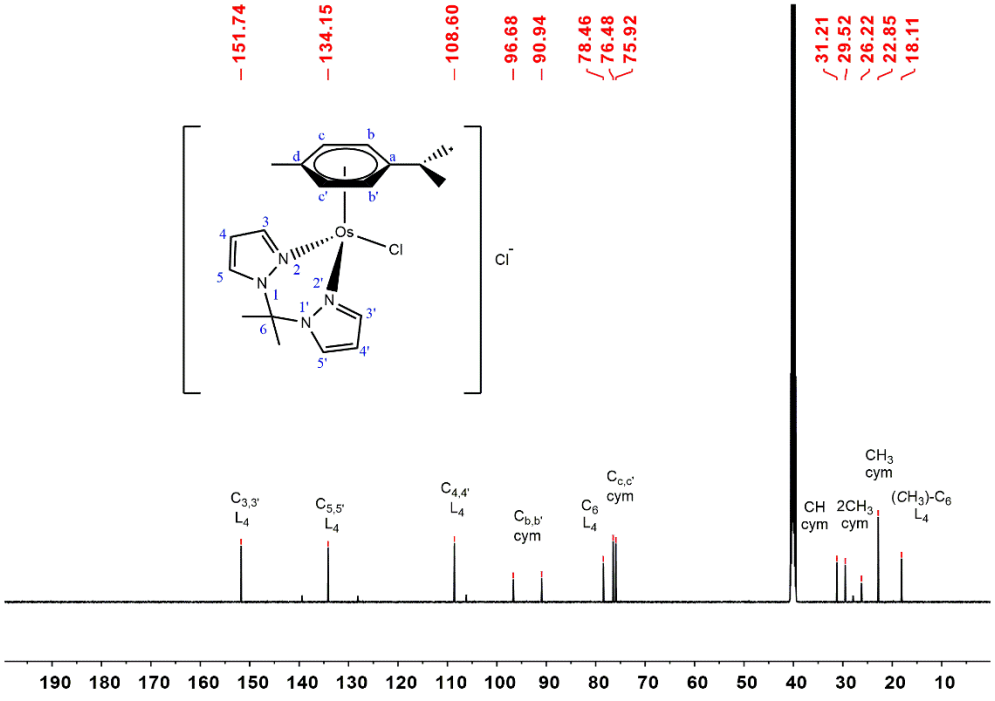

Figure17. ^{13}C NMR spectrum of [Os(cym)(L_4)Cl]Cl, **10**, in DMSO-d_6.

Complexes **11-14** were also synthetized in methanol by the interaction of 1 equiv of the dinuclear [Os(cym)Cl(μ-Cl)]$_2$ with 1 equiv of bis(pyrazol-1-yl)alkanes L′ in methanol at room temperature as shown in **Scheme 14**.

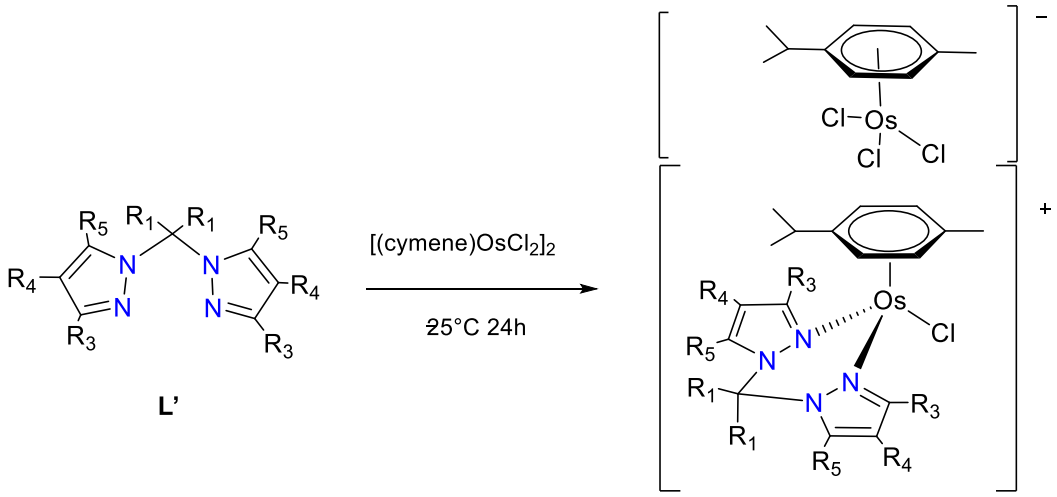

11) [(cymene)Os(L_1)Cl][$OsCl_3$]

12) [(cymene)Os(L_2)Cl][$OsCl_3$]

13) [(cymene)Os(L_3)Cl][$OsCl_3$]

14) [(cymene)Os(L_4)Cl][$OsCl_3$]

Scheme 14. Synthesis of complexes **11-14**.

Complexes **11-14** are soluble in alcohols, acetone, acetonitrile, DMF, chlorinated solvents, DMSO and considerably soluble in water.

The far-IR spectra of **11-14** show a very strong but broad absorption below 300 cm^{-1} , due to overlapped ν(Os-Cl) stretching modes of the cationic $[(arene)Os(L')Cl]^+$ and anionic $[(arene)OsCl_3]^-$ fragments. The IR spectra of **11-14** show broad bands above 2900 cm^{-1} due to the Carom-H stretching of pyrazole.

The ^1H and ^{13}C NMR spectra of **11-14** (**Figure 18** and **19**) display all the expected signals due to the coordinated arene rings and bis(pyrazol-1-yl)alkanes L′ ligand. Comparing with complex **10**, the ^1H NMR of complex 14 display other peaks at 5.99, 6.08, 2.14 ppm belonged to [Os(cym) Cl_3], while the new peaks at 90-98 ppm attributed to the ^{13}C NMR spectra of **14.**

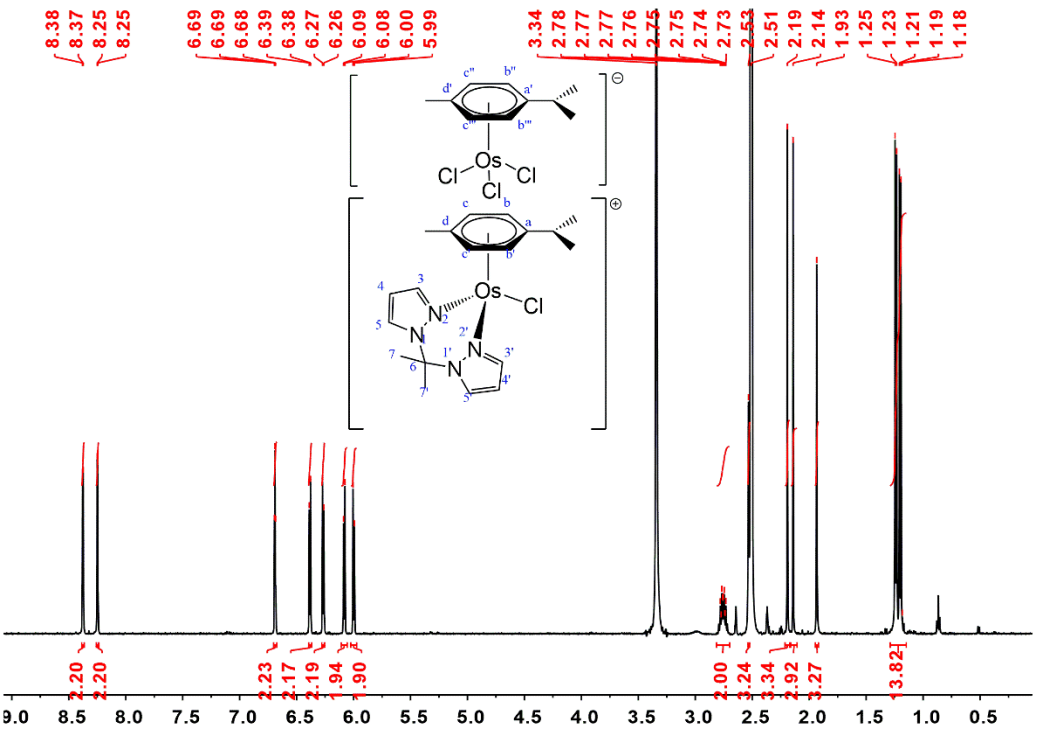

Figure 18 ^{1}H NMR spectrum of [Os(cym)(L_4)Cl][Os(cym)Cl_3]], **14**, in DMSO-d_6.

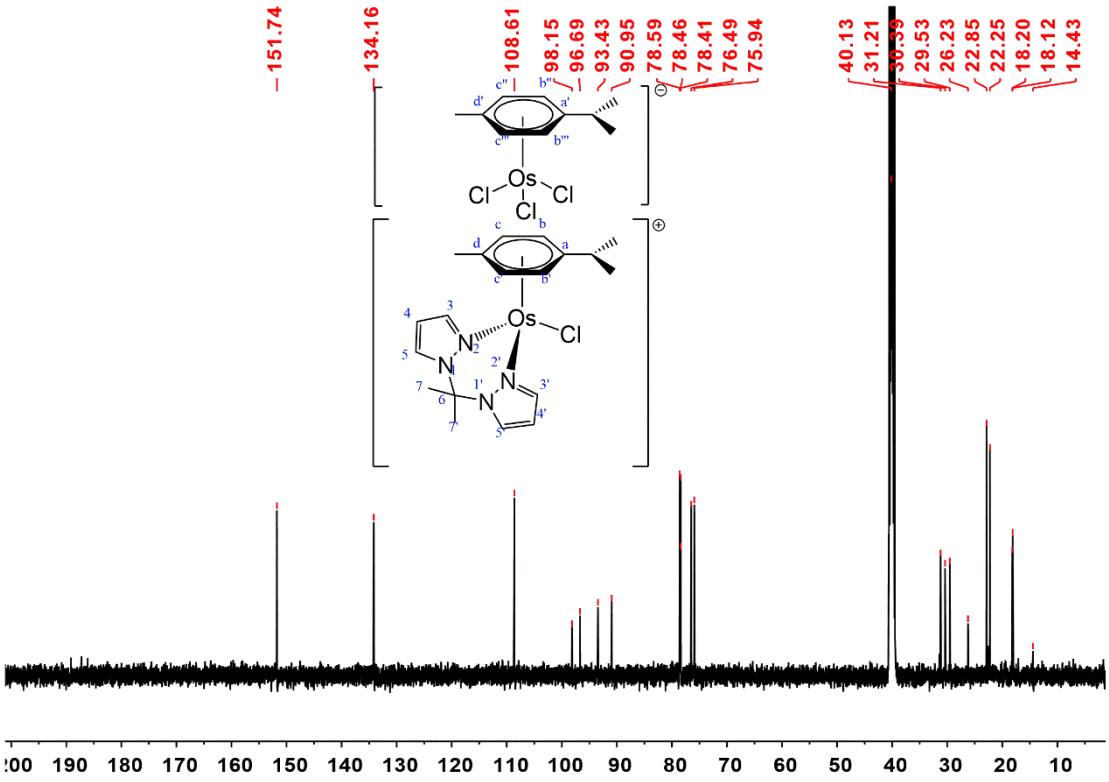

Figure 19. spectrum of [Os(cym)(L_4)Cl][Os(cym)Cl_3]], **14**, in DMSO-d_6.

The electrospray ionization (ESI) mass spectra of **7-14** display peaks corresponding to the appropriate $[Os(cym)(L^{'})Cl]^{+}$ ion that is generated by the dissociation of the chloride ligand or [Os(cym)Cl_3].

5.2.2 Stability of the complexes in DMSO

Since DMSO is the common solvent used to solubilize the complexes in order to perform cytotoxicity assays, the stability of all the compounds in DMSO-d_6 was investigated. Solutions of the complexes (c = 20.0 mM) in DMSO-d_6 were prepared and their stability was monitored for 5 days by ^{1}H NMR spectroscopy. Complex **9** proved to be unstable in DMSO in fact it was possible to detect immediately a dissociation of the ligand from the metal center when the complex is dissolved in DMSO (**Figure 20**). On the contrary, the other complexes were proved to be stable in DMSO. **Figure 21** and **22** is reported the comparison of the spectra of compound **10** and **14** in DMSO at t = 0, 1, 2, 3, 4, and 5 days, respectively. Complexes **7, 8, 11, 12,** and **13** also have the same property. It is possible to observe that these stable compounds can be used for cytotoxic assays.

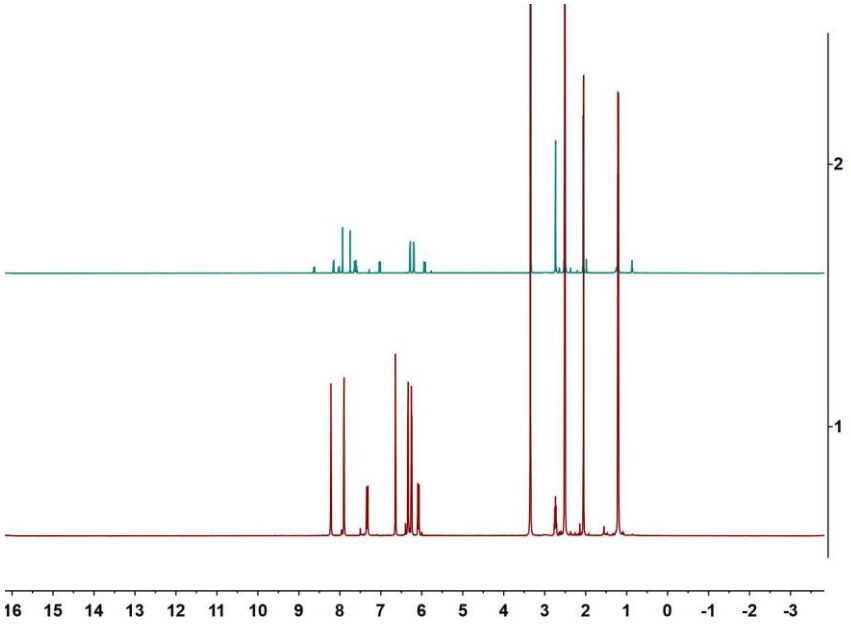

Figure 20. ^{1}H NMR spectrum of [Os(cym)(L_3)Cl]Cl, **9**, in DMSO at t = 0 day (bottom) and t = 2 day (top).

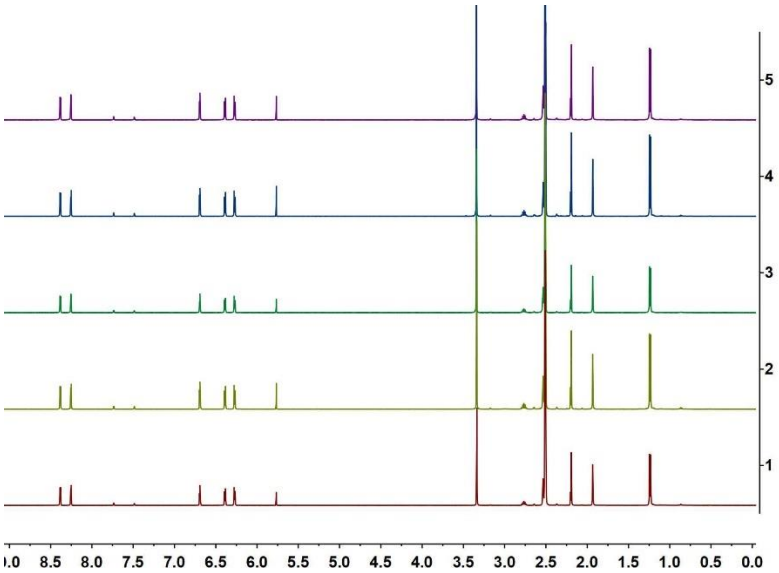

Figure 21. ^{1}H NMR spectrum of [Os(cym)(L_4)Cl]Cl, **10**, in DMSO at t = 0 day (bottom), 1, 2, 3, 4, and 5 day (top).

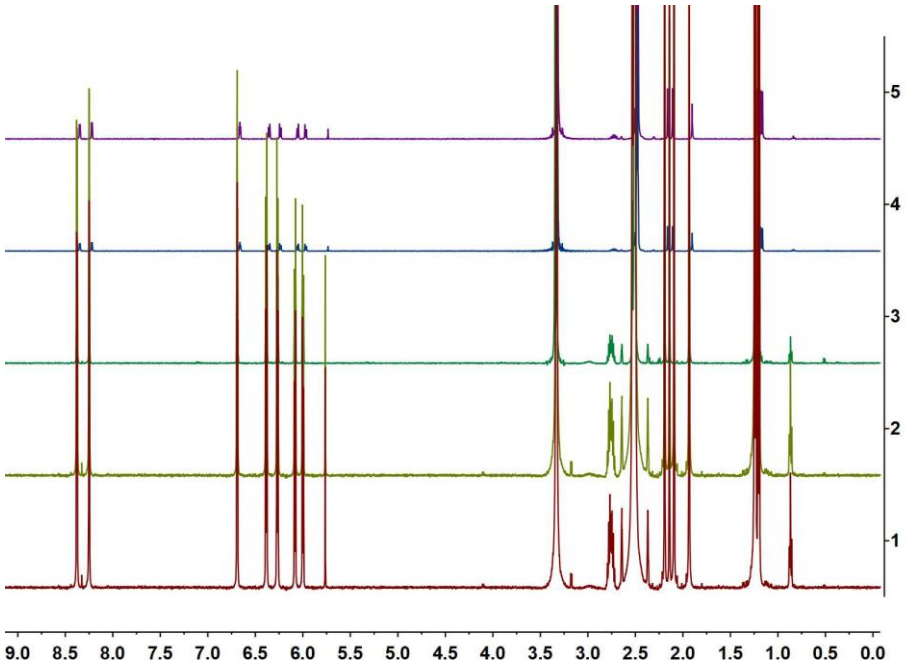

Figure 22. ^{1}H NMR spectrum of [Os(cym)(L_4)Cl][Os(cym)Cl_3]], **14**, in DMSO at t = 0 day (bottom), 1, 2, 3, 4, and 5 day (top).

5.2.3 Cytotoxic activity

In vitro, the cytotoxicity of complexes **7, 8, 10, 11, 12, 13, and 14** were assessed by determining the IC_{50} concentration against cisplatin-resistant cancer cells (MCF-7, 4T1, CT26, and Renca). After 72 hours of drug exposure, IC_{50} values of the compound were determined and are listed in **Table 3**.

Owing to unstable, the cytotoxicity of complexes **9** was not evaluated.

Complexes **7** and **8** have been found to be moderately cytotoxic at micromolar concentrations against MCF-7 with IC_{50} values 37.81 and 2.935 μM, respectively. On the contrary, the IC_{50} values of complexes **11-14** against MCF-7 are in the range of 65.25-227.6 μM, which is higher than that of complexes **7** and **8**. It is indicated that [Os(cym)(L')Cl]Cl is more conducive to apoptosis of cancer cells compared with [Os(cym)(L')Cl][Os(cym)Cl_3].

It is interesting to note that the IC_{50} values of complex **11** against 4T1 cells and complex **14** against Renca cells are 30.87 and 23.96, respectively. The result indicated that complex **11** shows moderately cytotoxic at micromolar concentrations against 4T1 cells as well as complex **14** shows moderately cytotoxic at micromolar concentrations against Renca cells, which may operate through a different mechanism.

Table 3. Cytotoxicity (IC_{50}, μM) of **7-14** and cis-Pt following incubation for 72 h with cancer cell lines.

Complex	MCF-7 **IC_{50} [μM]**	4T1 IC_{50} [μM]	CT26 **IC_{50} [μM]**	Renca **IC_{50} [μM]**
cis-Pt	8.40 ± 2.11	0.178 ± 0.009	0.045 ± 0.002	11.94 ±2.10
7	37.81 ± 3.54	180.15 ± 4.89	>500	244.79 ± 3.01
8	2.93 ± 0.35	166.31 ± 9.01	>500	152.69 ±4.68
10	>500	>500	>500	>500
11	113.77 ± 10.52	30.87 ± 2.67	>500	139.37 ± 3.89
12	105.76 ± 13.14	>500	>500	>500
13	65.25 ± 5.59	>500	>500	>500
14	227.6 ± 19.01	113.86 ± 4.56	>500	23.96 ± 2.35

5.3 Conclusions

The novel Os complexes such as [Os(cym)(L')Cl]Cl and [Os(cym)(L')Cl][Os(cym)Cl_3] containing bis(pyrazolyl)alkane were synthesized.

These [Os(cym)(L')Cl]Cl and [Os(cym)(L')Cl][Os(cym)Cl_3] complexes possess a higher water solubility and most of them are stable in solventst, which make them more advantageous in antitumor applications. Furthermore, we found that the [Os(cym)(L')Cl]Cl complexes has excellent anti-tumor properties via MTT assy.

.

Chapter 6. Ruthenium(II) 1,4,7-Trithiacyclononane Complexes of Curcumin and Bisdemethoxycurcumin: Synthesis, Characterization, and Biological Activity

Two kind of ruthenium(II) 1,4,7-Trithiacyclononane complexes were synthesized and characterized by IR, ESI-MS, and ^{1}H and ^{13}C NMR, elemental analysis, and X-ray crystallography. The cytotoxicity of the proligands and metal complexes was evaluated in vitro against cancer cells. In general, the cationic PTA-containing complexes are more cytotoxic than their neutral precursors with a chloride ligand in place of the PTA. The relatively high stability of these complexes is most likely responsible for their moderate pharmacological activity.

6.1 Experimental

6.1.1 General procedures

The dimers $[(arene)RuCl_2]_2$ (arene = p-cymene) was obtained from Aldrich and used exactly as received. All other materials were obtained commercially and used exactly as received. PTA was purchased from Aldrich. Other characterization methods are the same as that of Chapter 5.1.1.

6.1.2 Synthesis and characterization of the complexes

[Ru(curc)(dmso-S)([9]aneS$_3$)]Cl (15). 0.76 mmol Curcumin (280 mg) was dissolved in methanol (20 mL) contained CH_3ONa (40.0 mg, 0.76 mmol) under stirring for 1 h at room temperature. After that, $[RuCl_2(dmso\text{-}S)([9]aneS_3)]$ (328 mg, 0.76 mmol) was added into the mixture and stirred under reflux for 5h. Next, the mixture continue to stirred for 24h at room temperature. Under reduced pressure, the solvent was removed, and 10 mL of dichloromethane was added

before the mixture was filtered to remove the sodium chloride. The solution was concentrated to approximately 2 mL and stored at 4°C, resulting in orange crystals (160 mg, 0.208 mmol, yield 27 %). Compound **15** is soluble in alcohols, DMSO, DMF, water and partially soluble in chlorinated solvents, acetonitrile and acetone. Crystals of **15** suitable for X-ray diffraction were grown…. Mp: 194°C. Anal. Calcd for $C_{29}H_{37}ClO_7RuS_4$: C, 45.69; H, 4.89; S, 16.82. Found: C, 45.56; H, 4.79; S, 16.68. Λ_m (DMSO, 293 K, 10^{-4} mol/L): 38 S cm^2 mol^{-1}. IR (cm^{-1}): 3009mbr, 1617m, 1593m, 1582m, 1491s ν(C=C; C=O), 1393m, 1271s, 1162s, 1123s, 1079s ν(S=O_{dmso-S}), 966m, 834m, 805m, 681s, 558s, 450 w, 424s ν(S=O_{dmso-S}), 389s. ^{1}H NMR (DMSO, 293 K): δ, 2.66-2.92 (m, 12H, CH_2[9]aneS_3), 3.81 (s, 6H, OCH_3 of curc), 5.83 (s, 1H, C(1)*H* of curc), 6.71 (d, 2H, C(4, 4')*H* of curc), 6.78 (d, 2H, C(10, 10')*H* of curc), 7.08 (d, 2H, C(9, 9')*H* of curc), 7.24 (s, 2H, C(6, 6')*H* of curc), 7.31 (d, 2H, C(3, 3')*H* of curc), 9.57 (br, 2H, O*H* of curc). ^{13}C NMR (DMSO, 293 K): δ, 30.6, 33.1, 35.1 (s, *C*H_2 [9]aneS_3), 41.1, 43.3 (s, *C*H_3), 56.7 (s, O*C*H_3 of curc), 102.3 (s, *C*(1) of curc), 111.6 (s, *C*(6, 6') of curc), 116.3 (s, *C*(9, 9') of curc), 122.9 (s, *C*(10, 10') of curc), 125.9 (s, *C*(5, 5') of curc), 127.6 (s, *C*(3, 3') of curc), 139.1 (s, *C*(4, 4') of curc), 148.6 (s, *C*(7, 7') of curc), 149.3 (s, *C*(8, 8') of curc), 179.9 (s, *C*(2, 2')=O of curc). ESI-MS (+) CH_3OH (*m/z*, relative intensity %): 727 [100], [Ru(curc)(dmso-S)([9]aneS_3)]$^+$, 649, [Ru(curc)([9]aneS_3)]$^+$..

[Ru(bdcurc)(dmso-S)([9]aneS_3)]Cl (16). First, 0.76 mmol of bisdemethoxycurcumin (bdcurcH) was dissolved in methanol solution, and then 0.76 mmol of CH_3ONa was added. The mixture was stirred at room temperature for 1 h, following by added 0.76 mmol of [$RuCl_2$(dmso-S)([9]aneS_3)]. The resulting solution was stirred first at reflux for 5 hours and then at room temperature for 24 hours. After completion of the reaction, the solvent was removed under reduced pressure, dichloromethane (10 mL) was added, and the mixture was filtered to remove sodium chloride. The solution was concentrated to about 2 mL and stored at 4°C to obtain orange crystals (140 mg, 0.199 mmol,

26% yield). Compound **16** is soluble in alcohols, DMSO, DMF, water and partially soluble in chlorinated solvents, acetonitrile and acetone. Crystals of **16** suitable for X-ray diffraction were grow. Mp: 206°C. Anal. Calcd for $C_{27}H_{33}ClO_5RuS_4$: C, 46.18; H, 4.74; S, 18.26. Found: C, 46.06; H, 4.69; S, 18.09. Λ_m (DMSO, 293 K, 10^{-4} mol/L): 37 S cm^2 mol^{-1}. IR (cm^{-1}): 3118mbr, 1621m, 1600m, 1500sν(C=C; C=O), 1421m, 1393m, 1270m, 1165s, 1069m, 983m, 834m, 681m, 551s, 522s, 487s, 456m, 425s (Ru-S), 390s. ^{1}H NMR (DMSO, 293 K): δ, 2.63-2.89 (m, 12H, C*H*$_2$[9]aneS$_3$), 5.78 (s, 1H, C(1)*H* of bdcurc), 6.63 (d, 2H, C(4, 4')*H* of bdcurc), 6.77 (d, 4H, C(6, 6')*H* e C(10, 10')*H* of bdcurc), 7.30 (d, 2H, C(3, 3')*H* of bdcurc), 7.48 (d, 4H, C(7, 7')*H*e C(9, 9')*H* of bdcurc), 9.97 (br, 2H, O*H* of bdcurc). ^{13}C NMR (DMSO, 293 K): δ, 30.7, 31.5, 33.1, 34.5, 34.9, 35.1 (s, *C*H$_2$[9]aneS$_3$), 43.3, 44.5 (s, *C*H$_3$), 103.4 (s, *C*(1) of bdcurc), 116.5 (s, *C*(6, 6') e *C*(10, 10') of bdcurc), 125.6 (s, *C*(5, 5') of bdcurc), 127.1 (s, *C*(3, 3') of bdcurc), 130.4 (s, *C*(7, 7') e *C*(9, 9') of bdcurc), 138.9 (s, *C*(4, 4') of bdcurc), 159.8 (s, *C*(8, 8') of bdcurc), 179.8 (s, *C*(2, 2')=O of bdcurc). ESI-MS (+) CH$_3$OH (*m*/*z*, relative intensity %): 667 [100], [Ru(bdcurc)(dmso-S)([9]aneS^3)]$^+$, 588, [Ru(bdcurc)([9]aneS^3)]$^+$.

[Ru(curc)(PTA)([9]aneS$_3$)]Cl (**17**). PTA (20.6 mg, 0.131 mmol) and compound **15** (100 mg, 0.131 mmol) were added to methanol (10 mL) under stirring at room temperature for 24 hours. The solution was then dried by rotary evaporation and dichloromethane (2 mL) and excess n-hexane were added. The mixture was store at 4°C until a yellow precipitate formed. The powder was recovered by filtration and air dried. Compound **17** (38.6 mg, 0.046 mmol, yield 35%), is soluble in alcohols, acetone, acetonitrile, chlorinated solvents, DMF, DMSO and water. Mp: 219-221°C. Anal. Calcd for $C_{33}H_{43}ClN_3O_6PRuS_3$: C, 47.11; H, 5.15; N, 4.99; S, 11.43. Found: C, 46.97; H, 5.07; N, 4.85; S, 11.30. Λ_m (DMSO, 293 K, 10^{-4} mol/L): 40 S cm^2 mol^{-1}. IR (cm^{-1}): 3356mbr, 1621m, 1588m, 1503s ν(C=C; C=O), 1402m, 1279m, 1239m, 1160m, 1124m, 1012m, 969m, 948m, 808m, 742m, 574m, 478m, 451m, 397m. ^{1}H NMR (DMSO, 293 K): δ, 2.49-2.91 (m, 12H, C*H*$_2$ [9]aneS$_3$), 3.81 (s,

6H, OC*H₃* di curc), 3.96 (s, 6H, P-*C*H₂-N, PTA), 4.39 (s, 6H, N-*C*H₂-N, PTA), 5.80 (s, 1H, C(1)*H* of curc), 6.65 (d, 2H, C(4, 4')*H* of curc), 6.78 (d, 2H, C(10, 10')*H* of curc), 7.06 (d, 2H, C(9, 9')*H* of curc), 7.19 (d, 2H, C(3, 3')*H* of curc), 7.22 (s, 2H, C(6, 6')*H* of curc), 9.51 (s, 2H, O*H* of curc). ^{13}C NMR (DMSO, 293 K): δ, 30.4, 33.1, 34.9 (s, *C*H₂ [9]aneS₃), 54.2 (d, PCH₂N, PTA), 56.8 (s, O*C*H₃ of curc), 76.3 (d, NCH₂N, PTA), 104.3 (s, *C*(1) of curc), 112.9 (s, *C*(6, 6') of curc), 118.1 (s, *C*(9, 9') of curc), 125.4 (s, *C*(10, 10') of curc), 126.8 (s, *C*(5, 5') of curc), 127.5 (s, *C*(3, 3') of curc), 140.3 (s, *C*(4, 4') of curc), 149.9 (s, *C*(7, 7') of curc), 151.2 (s, *C*(8, 8') of curc), 181.2 (s, *C*(2, 2')=O of curc).^{31}P{^{1}H} NMR (DMSO, 298 K): δ= -27.5. ESI-MS (+) CH₃OH (m/z, relative intensity %): 806 [100][Ru(curc)(PTA)([9]aneS3)]$^{+}$.

[Ru(bdcurc)(PTA)[([9]aneS3)]Cl (18). The reaction procedure is similar to that of **compound 17**, except that the reactants are replaced by compound **16**. The powder was recovered by filtration and air-dried. Compound **18** (37.7 mg, 0.048 mmol, yield 34%) is soluble in alcohols, acetone, acetonitrile, chlorinated solvents, DMF, DMSO and water. Mp: 237-238°C. Anal. Calcd for $C_{31}H_{39}ClN_3O_4PRuS_3$: C, 47.65; H, 5.03; N, 5.38; S, 12.31. Found: C, 47.21; H, 4.91; N, 5.31; S, 12.23. Λ_m (DMSO, 293 K, 10^{-4} mol/L): 38 S cm^2 mol^{-1}. IR (cm^{-1}): 2933mbr, 1622m, 1602m, 1580m, 1500sν(C=C; C=O), 1401m, 1277m, 1238m, 1163s, 1100m, 1012m, 966s, 947s, 826m, 741m, 689m, 599m, 575s, 548m, 517s, 481s, 451m, 391m, 381m, 336m. ^{1}H NMR (DMSO, 293 K): δ, 2.52-2.89 (m, 12H, C*H₂*[9]aneS₃), 3.95 (s, 6H, P-*C*H₂-N, PTA), 4.37 (s, 6H, N-*C*H₂-N, PTA), 5.75 (s, 1H, C(1)*H* of bdcurc), 6.59 (d, 2H, C(4, 4')*H* of bdcurc), 6.77 (d, 4H, C(6, 6')*H* e C(10, 10')*H* of bdcurc), 7.17 (d, 2H, C(3, 3')*H* of bdcurc), 7.46 (d, 4H, C(7, 7')*H*e C(9, 9')*H* of bdcurc), 9.96 (br, 2H, O*H* of bdcurc). ^{13}C NMR (DMSO, 293 K): δ, 33.5, 38.7, 42.7 (s, *C*H₂[9]aneS₃), 55.8 (d, P-*C*H₂-N, PTA), 77.4 (d, N-*C*H₂-N, PTA), 107.9 (s, *C*(1) of bdcurc), 121.2 (s, *C*(6, 6') e *C*(10, 10') of bdcurc), 130.6 (s, *C*(5, 5') of bdcurc), 131.9 (s, *C*(3, 3') of bdcurc), 134.9 (s, *C*(7, 7') e *C*(9, 9') of bdcurc), 142.6 (s, *C*(4, 4') of bdcurc), 164.3 (s, *C*(8, 8') of bdcurc), 184.4 (s, *C*(2, 2')=O of

bdcurc).).^{31}P NMR (DMSO, 298 K): δ= -22.8. ESI-MS (+) CH_3OH (m/z, relative intensity %): 746 [100][Ru(bdcurc)(PTA) ([9]aneS_3)]$_+$.

6.1.3 X-ray diffraction structural analysis

The test steps are like those in the previous chapter.

6.1.4 Mass spectrometry research

Each complex (3×10^{-4} M) was incubated in 20 mM ammonium acetate buffer (pH = 6.8) contained HEWL (3:1 complex/protein molar ratio) at 37 °C for 24 h, and then ESI was used to record the MS spectrum. After 20-fold dilution with water, ESI MS spectra were measured by direct introduction at a flow rate of 5 μL min^{-1} in an Orbitrap high-resolution mass spectrometer (Thermo, San Jose, CA, USA) equipped with a conventional ESI source. Spray voltage was 3.1 kV, capillary voltage was 45 V, capillary temperature was 220 °C, and tube lens voltage was 230 V. Sheath gas and auxiliary gas are both set to 17 (arbitrary units) and 1, respectively. Xcalibur 2.0 is used for acquisition. The software (Thermo) and the integrated Xtract tool were used to obtain monoisotopic and mean deconvoluted masses. A nominal resolution of 100,000 (m/z 400) was used for spectral acquisition.

6.1.5 Cell culture

Dr. R. Danesi, University of Pisa, Pisa, Italy, kindly provided human type II alveolar epithelial cells (A549, American Type Culture Collection, CCL-195). Dr. Tania Gamberi, Department of Experimental and Clinical Biomedical Sciences "Mario Serio", University of Florence, kindly provided MCF-7, American Type Culture Collection, HTB-22) and human colorectal carcinoma cells (HCT116, American Type Culture CollectionCCL-247).

6.1.6.1 MTT assay

The experimental steps are the same as the chapter 4.1.4.2.

6.2 Results and discussion

6.2.1 Synthesis and spectroscopic characterization of ruthenium complexes

As shown in **Scheme 15**, [Ru(curc)(dmso-S)([9]aneS$_3$)]Cl (**15**) and [Ru(bdcurc)(dmso-S)([9]aneS$_3$)]Cl (**16**) were synthesized by reacting [RuCl$_2$(dmso-S)([9]aneS^3)] with the curc or bdcurc proligands, respectively, in methanol with potassium hydroxide as deprotonating agent.

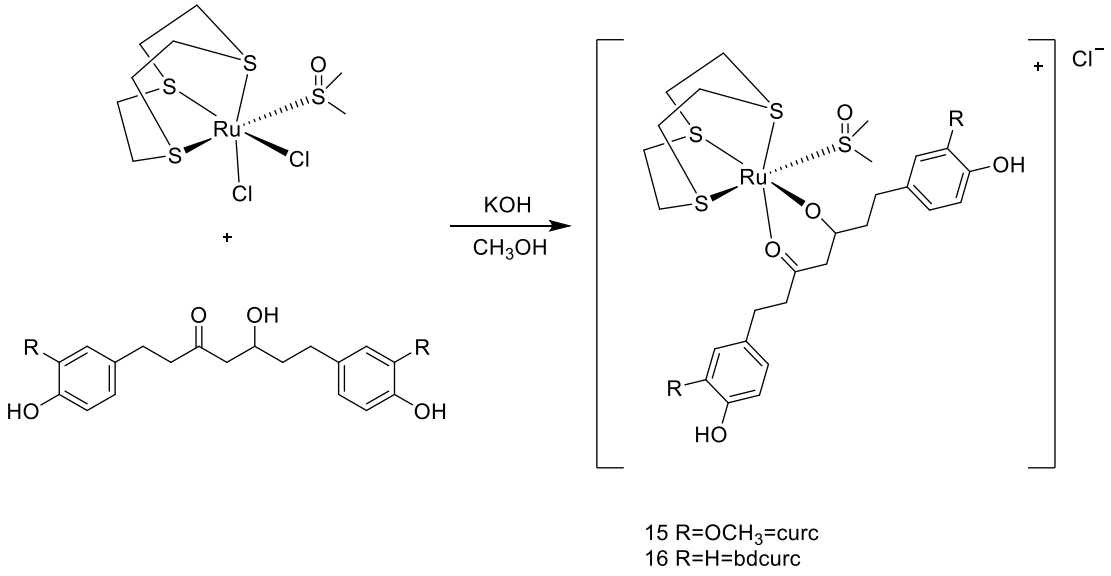

Scheme 15. Synthesis of complexes **15** and **16**.

From the IR spectra of complexes **15** and **16,** the ν(C=O) absorption bands of the curcuminoid ligand was shift to lower wavenumbers, indicating confirms coordination to the ruthenium(II) center in the O,O'-bidentate chelating mode. In positive ion mode, the peaks in ESI mass spectra of **15** and **16** are the cation fragments [Ru(curc)(dmso-S)([9]aneS$_3$)]$^+$ and [Ru(bdcurc)(dmso-S)([9]aneS$_3$)]$^+$, respectively. The ^{1}H and ^{13}C NMR spectra of **15** and **16** were recorded in DMSO-d$_6$. In comparison to the equivalent protons in the free proligands, complexes **15** and **16** exhibit the expected distinct changes in frequency for the resonances of the free proligands. The proton and carbon assignments were made based on previous studies on analogous complexes. Complexes **15** and **16** react with PTA in acetone to form complexes [Ru(curc)(dmso-S)([9]aneS$_3$)]Cl (**17**) and [Ru(bdcurc)(dmso-S)([9]aneS$_3$)]Cl (**18**), respectively.

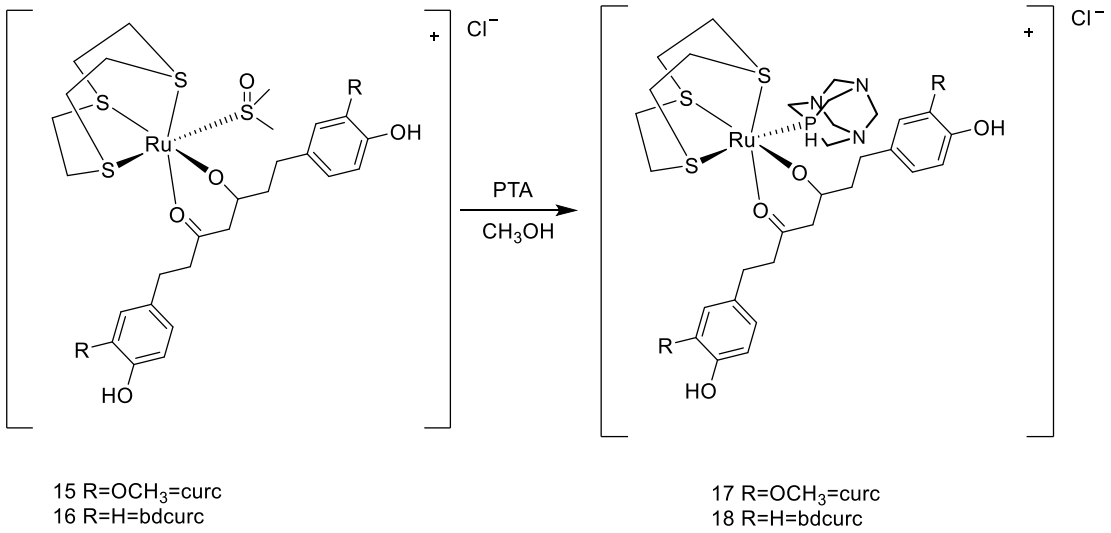

Scheme 16. Synthesis of complexes **17** and **18**.

Complexes **17** and **18** are soluble in the majority of organic solvents and are also very soluble in water. The expected signals in the ^{1}H NMR spectra of **17** and **18** attributed to the coordinated [9]aneS3, curcuminoids, and PTA ligands. Moreover, in the ^{31}P NMR spectra of **17** and **18**, the phosphorus of PTA affords a singlet at –27.5 and –22.8 ppm, respectively, which are consistent with previous reports [80]. Ions corresponding to the cationic species $[Ru(curc)(PTA)([9]aneS_3)]^+$ and $[Ru(bdcurc)(PTA)([9]aneS_3)]^+$ can be found in the positive ion ESI mass spectra of **17** and **18**, respectively.

6.2.2 Molecular structures.

According to the Single crystal X-ray structure analysis, the molecular structures of $[Ru(curc)(PTA)([9]aneS_3)]Cl$ (**15**, **Figure 23**) and $[Ru(bdcurc)(PTA)([9]aneS_3)]Cl$ (**16**, **Figure 24)** were confirmed by single crystal X-ray structure analysis (see the structure refinement parameters in **Table 4**).

Complexes **15** and **16** has a similar coordination environment of ruthenium atom. Despite the different nature of the face-capping ligand, the Ru–O distances (2.088/2.066 and 2.068/2.098 for complexes 15 and 16) are similar to those observed for half-sandwich Ru-curcuminoid complexes previously reported ([9]aneS3 *vs* η6-arene) [76,81,82].

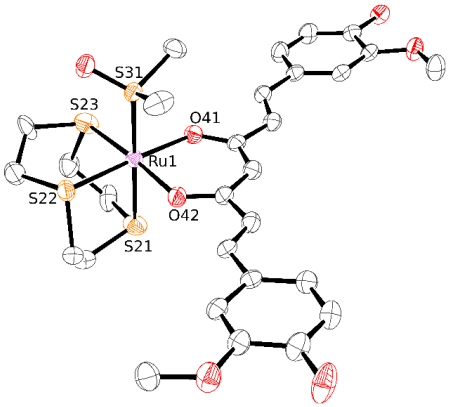

Figure 23. ORTEP representation (50% probability ellipsoids) of the molecule of complex 1 in the crystal structure.

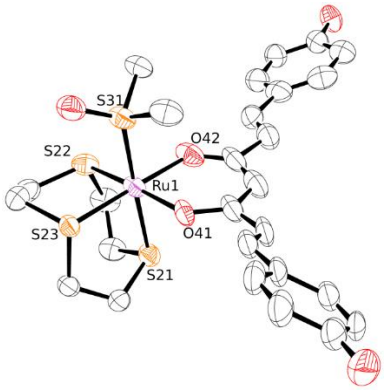

Figure 24. ORTEP representation (50% probability ellipsoids) of the molecule of complex 2 in the crystal structure.

Table 4. Crystallographic data and refinement details for complexes [Ru (curc)(dmso-S)([9]aneS^3)]Cl·2H$_2$O (15·2H$_2$O) and [Ru (bdcurc)(dmso-S)([9]aneS$_3$)]Cl (16).

Compound	15	16
Chemical formula	$[RuC_{29}H_{37}S_4O_7]Cl{\cdot}2H_2O$	$[RuC_{27}H_{33}S_4O_5]Cl$
M/gmol^{-1}	798.38	702.29
T (K)	173(2)	173(2)
Crystal system	triclinic	monoclinic
Space group	P –1	$P2_1/c$
a (Å)	10.048(3)	17.153(2)
b (Å)	12.7060(8)	7.5090(9)
c (Å)	14.316(2)	23.549(2)
β (°)	93.51(1)	93.210(2)
V (Å3)	1784.7(5))	3028.4(5)
Z	2	4
ρ (g cm^{-3})	1.486	1.540

μ (mm^{-1})	0.753	0.867
Unique reflections	23986	99238
R_{int}	0.0365	0.0658
Goodness-of-fit (GOF) on F^2	1.025	1.051
$R1$ [$I > 2\sigma(I)$][a]	0.0492	0.0632
$wR2$ [$I > 2\sigma(I)$][a]	0.1316	0.1711

Multiple adducts with stoichiometry up to 1:4 was discovered (protein to metal ratio). Furthermore, the presence of a peak at 14583.7 Da attributed to the cationic species $[Ru([9]aneS^3)]^{2+}$ indicates the release of the curcumin ligand, albeit in very small quantities. Despite this, the native protein has the most intense peak (**Figure 25**). In contrast to compound 1, compound 2 is less reactive, with only a single detectable peak at 14892.8 Da, which is assigned to a monoadduct of the type $[Ru(bdcurc)([9]aneS^3)]^{+}$ (**Figure 26**). Complexes 17 and 18 are even more resistant to HEWL. The peak at 14952.8 Da attributable to the coordination of the fragment $[Ru(curc)([9]aneS^3)]^{+}$ (**Figure 27**) after release of the PTA moiety shows that 17 coordinates the protein. However, the intensity of this peak is very low, and in the case of 18 no adducts are formed.

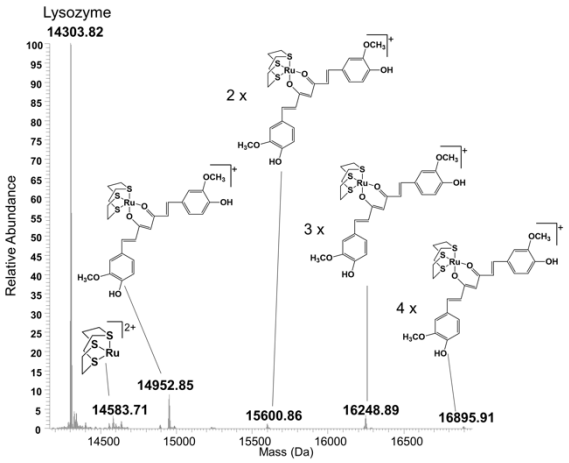

Figure 25. Deconvoluted ESI-MS spectrum of 1 recorded after 24 h incubated at 37° C with HEWL (10-4 M). Metal to protein ratio 3:1, ammonium, acetate buffer pH 6.8.

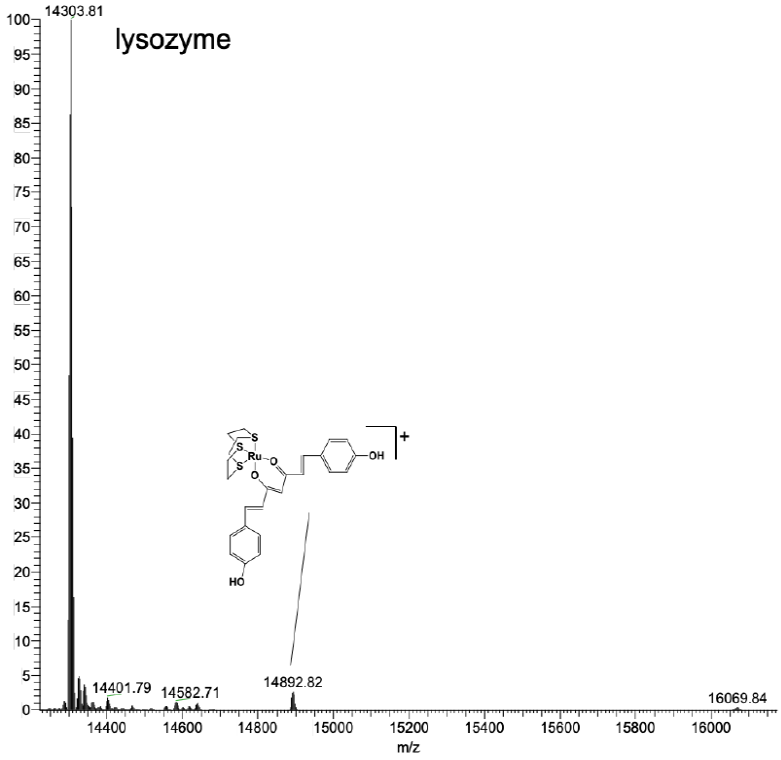

Figure 26. Deconvoluted ESI-MS spectrum of 16 recorded after 24 h incubated at 37° C with HEWL (10-4 M). Metal to protein ratio 3:1, ammonium, acetate buffer pH 6.8..

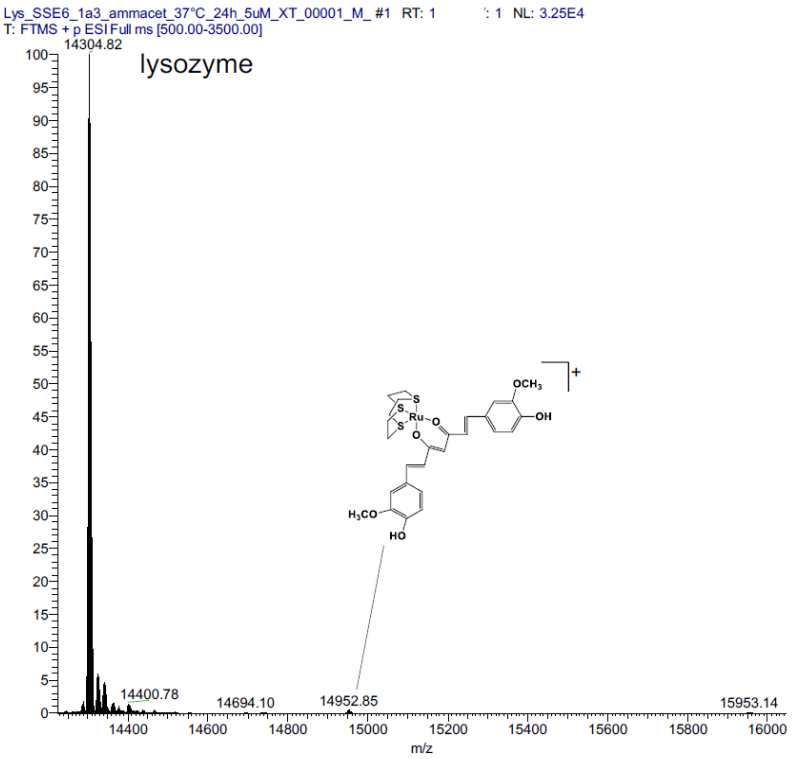

Figure 27. Deconvoluted ESI-MS spectrum of 17 recorded after 24 h incubated at 37° C with HEWL (10-4 M). Metal to protein ratio 3:1, ammonium, acetate buffer pH 6.8.

6.2.3 Cellular actions.

The cytotoxicity of complexes **15-18** to three different cancer cell lines: A549, adenocarcinoma human alveolar basal epithelial cells (NSCLC); MCF7, adenocarcinoma breast cancer cell line (ER+, PR^{+}, HER^{2-}) and HCT116, colorectal cancer cell line was assessed via MTT assay.

As described in **Table 5**, curcH and bdcurcH were used as references, which affect significantly the A549 cell viability (IC_{50} = 32.7 ± 5.0, 21.6 ± 9.8 μM, respectively)[83,84]. **Table 5** indicates that the Ru complexes show poor effect to decrease the breast cancer cells MCF-7 viability with IC_{50} values falling in the high micromolar range. Similarly, the IC_{50} values against the HCT116 remained in the 50-200 micromolar range. According to the literature, the cytotoxic activities of curcH and bdcurcH were in the low micromolar range [85]. These results implied that coordination to the ruthenium(II) centre decrease cytotoxic activity of curcH and bdcurcH. Notably, the cytotoxicity of curc-containing complexes **15** and **16** is lower than that of the correspondent bdcurc-containing complexes **17** and **18**.

Table 5. IC_{50} Values (μM) determined for complex **15-18**, curcH and bdcurcH[a]

Complex	A549	MCF-7	HCT116
1	> 500	165.9 ± 7.8	116.1 ± 18.2
2	> 500	233.7 ± 41.0	191.3 ± 11.1
3	> 500	84.7 ± 12.8	68.0 ± 7.6
4	> 500	198.7 ± 19.4	170.6 ± 47.1
curcH	32.7 ± 5.0	10.5 ± 0.4	7.1 ± 3.2
bdcurcH	21.6 ± 9.8	8.4 ± 3.3	11.5 ± 1.8

[a] Results are reported as the mean ± SD of three independent experiments.

6.3 Conclusions

In summery, two neutral half-sandwich Ruthenium(II) complexes [Ru(curc)(dmso-S)([9]aneS$_3$)]Cl (**15**) and [Ru(bdcurc)(dmso-S)([9]aneS$_3$)]Cl (**16**) and the related ionic complexes [Ru(curc)(PTA)([9]aneS$_3$)]Cl (**17**) and [Ru(bdcurc)PTA([9]aneS$_3$)]Cl (**18**) have been prepared and characterised. The X-ray structures of the complexes **15** and **16** contains both curcumins and a face-capping ligand. The interactions of the aforementioned complexes with the model protein lysozyme were then investigated using ESI MS (HEWL). Overall, there was a rather limited reactivity with lysozyme, accompanied by a generally modest cytotoxic potency against three representative cancer cell lines.

Chapter 7. Electrochemical aptasensing strategy based on a multivariate polymer-titanium-metal-organic framework for zearalenone analysis

Food safety issues have received increasing attention along with the progress and development of society. Sensitive determination of mycotoxins, antibiotics, pesticides, pathogens, or heavy metal ions in foodstuffs is essential for market supervision and food safety inspection.. As a well-known mycoestrogen, ZEN in various grains can lead to a widespread food contamination because it will cause the acute toxic effects, including embryotoxicity, immunotoxicity, genotoxicity, and carcinogenicity, as well as induce oxidative stress and apoptosis [86]. The maximum residue levels of ZEN are 0.5 μg kg^{-1} established by the World Health Organization (WHO), 60 μg kg^{-1} in wheat or corn by China, and 100 μg kg^{-1} in all cereals and products derived from cereals by European Union (EU) [87]. Considering the low permissible limit and extensive presence of ZEN, it should be quantitatively determined for food safety. Over the past decades, diverse approaches have been developed for sensitive analysis of ZEN in foods, such as enzyme-linked immunosorbent assay, liquid chromatography-mass spectrometry, colorimetric method, high-performance liquid chromatography, surface-enhanced Raman scattering immunoassay, electrochemical biosensors, electrochemiluminescence, surface plasmon resonance, and fluorescence sensors [88]. In spite of the advantages of conventional techniques, some shortcomings, such as fussy sample pretreatment procedure, expensive instruments, and need of skilled technicians remarkably hamper their applications. Hence, developing new sensing strategies is required for sensitive monitoring of ZEN in foodstuffs or environments.

Aptamers, which are short nucleic acid (DNA or RNA) sequences, were first synthesized in vitro in 1990 and exhibit enhanced affinity toward diverse targets, such as cancer markers, antibiotics, heavy metal ions, or hazardous analytes in foodstuffs

(typical mycotoxins, antibiotics, pesticides, pathogens, or metal ions). In contrast to antibodies, aptamers show the merits of feasible synthesis, low cost, and high selectivity toward different analytes. A number of aptasensors have been developed by combining different determination techniques, such as electrochemical, electrochemiluminescence, fluorescence, and surface plasmon resonance methods for analysis of food contaminants [89]. Electrochemical aptasensors afford the advantages of simplicity, easy miniaturization, high sensitivity, and economy and have received wide attention for detecting mycotoxins. The development of diverse electrochemical aptasensors for efficient analysis of ZEN is an excellent alternative to conventional methods. For instance, a "signal-on" electrochemical aptasensor was constructed by using the hollow cubic platinum@gold nanoframes functionalized with polyethyleneimine-reduced graphene oxide (hcPt@AuNFs/PEI-rGO) for analysis of ZEN with a limit of detection (LOD) of 0.105 pg mL^{-1} [90].

Most MOFs exhibit inferior electrochemical activity and limited network spaces; in this condition, several strategies have been exploited to develop MOF-based electrochemical aptasensors by integrating MOFs with conductive materials, annealing MOFs to inorganic compounds and mesoporous carbon, and synthesizing semiconductive MOFs [91]. Despite the low detection limit and outperformed sensing performances of these MOFs-based sensors, disadvantages, such as complex preparation for MOF-based derivatives and harsh synthesis conditions for conductive MOFs, restrict their uses. An amorphous polyMOF was firstly synthesized by Zhang et al. using a symmetrical polymer as ligand, with coordination moieties on the main polymer chain [92]. As a new class of organic–inorganic hybrid materials, polyMOFs can be developed by combining organic polymers and metal–organic materials. Compared with MOFs synthesized using small molecules as ligands, polyMOFs can integrate the advantages of polymers and MOFs, such as good processability, facile fabrication of films, high chemical stability, well-determined structures, and permanent porosity. However, the applications of polyMOFs have not been fully studied and most reports focus on the synthesis and characterizations of polyMOFs. Notably, titanium (Ti)-based MOFs (Ti-MOFs) are believed to be excellent sensing platforms [93], because they

possess not only rigid framework but also excellent redox activity. Given that poly-MOF(Ti) can combine the advantages of Ti-MOF and polyMOF, such as strong bioaffinity toward biomolecules, good biocompatibility, and feasible film forming ability, polyMOF(Ti) can be employed as a superior platform for constructing electrochemical aptasensors.

This work aims to build a novel bioplatform based on multivariate (MTV) polyMOF(Ti) network for electrochemical ZEN aptasensor. MTV polyMOF(Ti) was prepared (**Figure 28**) by polyether polymer ligands with 1,4-benzenedicarboxylic acid units (L_8) and terephthalic acid (L_0) as building blocks and tetrabutyl titanate as precursor (MTV polyMOF(Ti)-$L_{8,0}$). The MTV hierarchical MOFs, synthesized by using mixed ligands, contain multiple regions arranged in ordered structures [94] and show potential applications as biosensors. Owing to the high heterogeneity of MTV MOFs, they exhibit superior performance compared with their "simple" counterparts. Compared with Ti-MOFs synthesized using the single ligand of L_8 and L_0, denoted as polyMOF(Ti)-L_8 and MIL-125, respectively, MTV polyMOF(Ti) shows nanosheet-like shape, good electrochemical activity and more active sites for anchoring the ZEN-targeted aptamer. Thus, the MTV polyMOF(Ti)-$L_{8,0}$-based aptasensor has ultralow LODs of 7 and 3.5 fg mL^{-1} using electrochemical impedance (EIS) and differential pulse voltammetry (DPV), respectively, in a wide ZEN concentration from 10 fg mL^{-1} to 10 ng mL^{-1}. The sensor also exhibits good selectivity, stability, reproducibility, and regeneration in aqueous media as well as applicability in diverse samples.

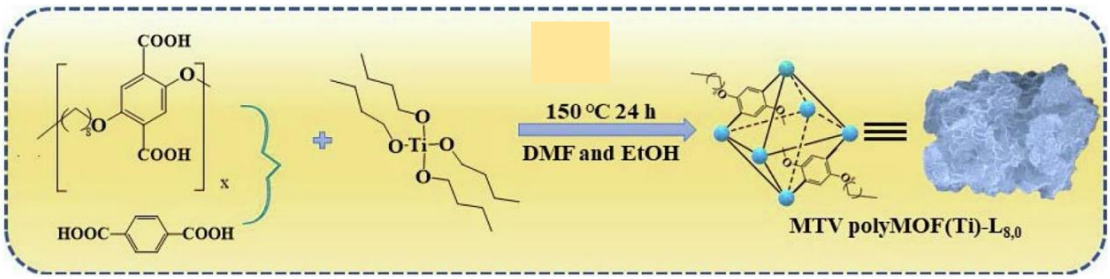

Figure 28 Multivariate polyMOF(Ti) (*MTV polyMOF(Ti)*) was prepared by using mixed linkers of polyether polymer (L_8) and 1,4-benzenedicarboxylic acid (H_2bdc or L_0) as well as tetrabutyl titanate as nodes (MTV polyMOF(Ti)-$L_{8,0}$).

7.1 Experimental

7.1.1 Chemicals

2,5-Dihydroxyterephthalic acid, methanol, $NaHCO_3$, CH_2Cl_2, 1,8-dibromooctane, K_2CO_3, NaOH, tetrabutyl titanate (TNBT), terephthalic acid (TPA), zearalenone (ZEN), aflatoxins (AFs), ochratoxin A (OTA), fumonisin B 1 (FB 1), bovine serum albumin (BSA), deoxynivalenol (DON), oxytetracycline (OTC), chlortetracycline (CTC), and tetracycline (TET) were purchased from Aladdin Reagent Co. Ltd. Tetrahydrofuran (THF), N,N-dimethylformamide (DMF), sulfuric acid, HCl, and ethanol were ordered from Sinopharm Chemical Reagent Co., Ltd. The sequence of ZEN-targeted aptamer is as follow: 5'-GGA ATT CTT GAT GTT GCC TGG GAT TGT TTG GGC CTT GTG TTT TCT TCC GTT CCA ACT TAG TAG GAT CCC GAA-3', which was ordered from Solarbio Life Sciences Co. Ltd. In addition, all solutions were prepared with Milli-Q water. All reagents were of analytical grade and used without further purification.

7.1.2 Preparation of solutions

The phosphate buffer solution (PBS, 0.01 M) was prepared by dissolving KH_2PO_4 (0.242 g), KCl (0.200 g), Na_2HPO_4 (1.445 g), and NaCl (8.003 g) in Milli-Q water (1 L). The pH value of PBS was modulating to 7.4 using NaOH (0.1 M) or HCl (0.1 M). The electrolyte was obtained by dissolving $K_3Fe(CN)_6$ (1.65 g) and $K_4Fe(CN)_6$ (2.111 g) in 1 L PBS.

7.1.3 Pre-treatment of Au electrode (AE)

The bare AE was pre-treated in prior to each electrochemical test. The AE becomes smooth through immersing into a mixed solution of H_2O_2 and H_2SO_4 (v/v = 3/7) for 30 min and washing several times by water. Subsequently, the AE was soaked in 10.0 mL solution of water and ethanol (v/v = 1/1) for another 30 min.

7.1.4 Characterizations

A Bruker TENSOR27 spectrophotometer was used to record the Fourier transform infrared (FT-IR) spectra. Field emission scanning electron microscopy (FE-SEM) using the JSM-6490LV scanning electron microscope and transmission electron microscopy

(TEM) by JEOL JSM-6490L V system were taken to study the morphology. A Thermo Fisher ESCALAB 250Xi photoelectron spectrometer was applied to investigate X-ray photo-electron spectroscopy (XPS). The Rigaku D/Max-2500 X-ray diffractometer with Cu Kα radiation diffractometer was used to record the powder X-ray diffraction (PXRD) pattern. An ASAP 2010 physisorption analyzer was employed to analyze the Brunauer-Emmett-Teller (BET) surface areas, pore size distributions, and pore volumes of MOFs. The Renishaw in Via Raman spectrometer with a solid-state laser (excitation at 532 nm) was executed to Raman spectra at room temperature in 200–3000 cm^{-1} region.

7.1.5 Electrochemical measurements

All electrochemical measurements, including electrochemical impedance (EIS), cyclic voltammetry (CV), and differential pulse voltammetry (DPV) were carried out on a CHI660D electrochemical workstation (Shanghai Chenhua, China). The traditional three-electrode system was applied, including modified electrode (working electrode); Ag/AgCl (saturated KCl) electrode (reference electrode), and platinum wire (counter electrode). CV curves were measured in 5.0 mM $K_3[Fe(CN)_6]/K_4[Fe(CN)_6]$ (1: 1) as a redox probe dissolved in 0.01 M PBS at –0.2 to 0.8 V *vs.* Ag/AgCl (saturated KCl) at the scan rate of 100 mV s^{-1}. DPV curves were collected in the same mixture at potentials ranging from –0.2 to 0.6 V *vs.* Ag/AgCl (saturated KCl) at the scan rate of 50 mV s^{-1}.

7.1.6 Synthesis and characterization of the ligands and the complexes

7.1.6.1 Synthesis of L8

The ligand L_8 was prepared according to the previous work [95].

7.1.6.2 Synthesis of MTV polyMOF(Ti)-$L_{8,0}$ (19)

0.338 g L_8, terephthalic acid (0.083 mg), and 0.204 g tetrabutyl titanate were added into the mixed solvent of N,N-dimethylformamide (DMF, 0.4 mL) and ethanol (0.4 mL). Then, such a mixed solution was poured into a reaction kettle and heated at 150 ℃ for 24 h. After cooling to the room temperature, the product was filtrated and washed successively with methanol and DMF. Orange powder of MTV polyMOF(Ti)-$L_{8,0}$ was

obtained after dried in vacuum for 24h.

7.1.6.3 Fabrication of electrochemical aptasensors

AE was used as the working electrode for all tests. First, 100 mg of MTV polyMOF(Ti)-$L_{8,0}$ was dispersed into 100 mL Milli-Q water and ultrasonically agitated for 1 h, gaining a homogeneous MTV polyMOF(Ti)-$L_{8,0}$ suspension (1 mg mL^{-1}). MTV polyMOF(Ti)-$L_{8,0}$ suspensions of 0.2, 0.5, 1, and 2 mg mL^{-1} were obtained by a similar way. The homogeneous suspensions of polyMOF(Ti)-L_8 and MIL-125 were also obtained by the similar way, but dispersing polyMOF(Ti)-L_8 and MIL-125 into Milli-Q water, respectively.

10 μL of the MTV polyMOF(Ti)-$L_{8,0}$ suspension was coated on the clean AE surface and naturally dried to room temperature for 4 h (MTV polyMOF(Ti)-$L_{8,0}$/AE). Subsequently, MTV polyMOF(Ti)-$L_{8,0}$/AE was immersed in the ZEN-targeted aptamer solution (200 nM) for 2 h to immobilize aptamer (Apt/MTV polyMOF(Ti)-$L_{8,0}$/AE). Then, Apt/MTV polyMOF(Ti)-$L_{8,0}$/AE was rinsed with phosphate buffer solution (PBS, 0.01 M, pH 7.4) to remove unanchored aptamer strands. Subsequently, Apt/MTV polyMOF(Ti)-$L_{8,0}$/AE was immersed in BSA (1%) for 30 min to block residual active sites, following by rinsed with PBS to afford BSA/Apt/MTV polyMOF(Ti)-$L_{8,0}$/AE), which was incubated with ZEN solution (1 pg mL^{-1}) for 1 h to produce ZEN/BSA/Apt/MTV polyMOF(Ti)-$L_{8,0}$/AE). For comparison, the aptasensors based on polyMOF(Ti)-L_8 and MIL-125 were also constructed for ZEN detection. All developed electrochemical aptasensors were stored in a refrigerator at −4 °C when not in use.

7.1.6.4 Evaluation of LOD, selectivity, stability, reproducibility, and regeneration of aptasensor

To assess the LOD of sensor, the BSA/Apt/MTV polyMOF(Ti)-$L_{8,0}$/AE was immersed in different concentrations of ZEN for 1 h, following by washed with PBS several times to remove loosely physical adsorbed ZEN molecule. After that, DPV and EIS measurements were taken in 0.01 M PBS containing 5 mM $[Fe(CN)_6]^{3-/4-}$. Taking EIS response (resistance of charge transfer, R_{ct}) and the current density of DPV as the function of logarithm of ZEN concentration, the calibration curves can be deduced. As

a result, the LOD of the gained aptasensor was calculated for detecting ZEN was evaluated in accordance with the IUPAC criterion [96].

To evaluate the selectivity of aptasensor, aflatoxins (AFs), ochratoxin A (OTA), fumonisin B 1 (FB 1), BSA, deoxynivalenol (DON), tetracycline (TET), oxytetracycline (OTC), and chlortetracycline (CTC) were used as interferents, which are possibly exist in foodstuffs containing ZEN. The aptasensor was then applied to detect diverse interferents and the mixture of ZEN and interferents (100 pg mL^{-1}), whose concentration is set as 100-fold of that of the ZEN solution (1 pg mL^{-1}).

Five developed aptasensors were independently used to detect ZEN (1 pg mL^{-1}) for probing the reproducibility. Moreover, the developed aptasensor was continuously used to detect ZEN (1 pg mL^{-1}) for measuring the stability for 15 days. To assess the regenerability of aptasensor, ZEN/BSA/Apt/MTV polyMOF(Ti)-$L_{8,0}$/AE was dipped in 25 mM glycine-hydrochloric acid (pH ~ 2.4) solution for 5 min, followed by rinsed with excess PBS, resulting in the dissociation of ZEN from aptamer-ZEN complex. As such, the aptasensor was regenerated to BSA/Apt/MTV polyMOF(Ti)-$L_{8,0}$/AE. Then, the refreshed aptasensor was incubated with the ZEN solution (1 pg mL^{-1}) for 1 h. The same procedure was repeated by 10 cycles.

7.1.6.5 Analysis of real samples

Three kinds of real samples, including beer, corn, and peanut obtained from the local supermarket, were used to explore the practical applications of aptasensor. Before used, beer sample was pre-treated by standard addition method [97]. The sample (10 mL) was ultrasonically degassed for 1 h to remove foaming followed by centrifuged for 5 min at 10000 r min^{-1}. According to previous work, corn and peanut samples (20 g) were separately crushed into powder. Then, 2 g NaCl was solved in 50 mL of mixed solvent (acetonitrile: water = 9: 1, v: v), following by added the sample under stirring for 30 min. After that, the mixture was filtered by 0.22 μm organic filtering membrane and 15 mL of filter solution was diluted with 45 mL of water to prepare the sample solution. The ZEN solution (5 mL, 1μg mL^{-1}) was separately added to real samples and used as the stock solution. All the stock solutions were further diluted to diverse concentrations

by PBS and analyzed using the developed aptasensor.

7.2 Results and discussion

7.2.1. Design of the electrochemical aptasensor for ZEN detection

Three types of MOFs networks (**Scheme 17**), i.e., MTV polyMOF(Ti)-$L_{8,0}$, polyMOF(Ti)-L_8, and MIL-125, have been prepared and used as bioplatforms for constructing aptasensors for detecting ZEN. In view of nano-scaled size and van der Waals force [98], the MOFs can be uniformly coated on the bare AE surface. Given outstanding chemical stability, large specific surface areas, good redox activity and strong bioaffinity of Ti-MOFs [93], the ZEN-targeted aptamers can be adsorbed over these bioplatforms via various interactions. Moreover, bovine serum albumin (BSA) was used as the blocking agent for avoiding nonspecific adsorption between ZEN and platforms. In presence of ZEN, G-quadruplex can be formed between ZEN and aptamers immobilized over Ti-MOFs in view of specific recognition by changing the aptamer conformations to combine with ZEN [99]. Any change at the interface of electrolyte and electrode can be monitored by electrochemical approaches.

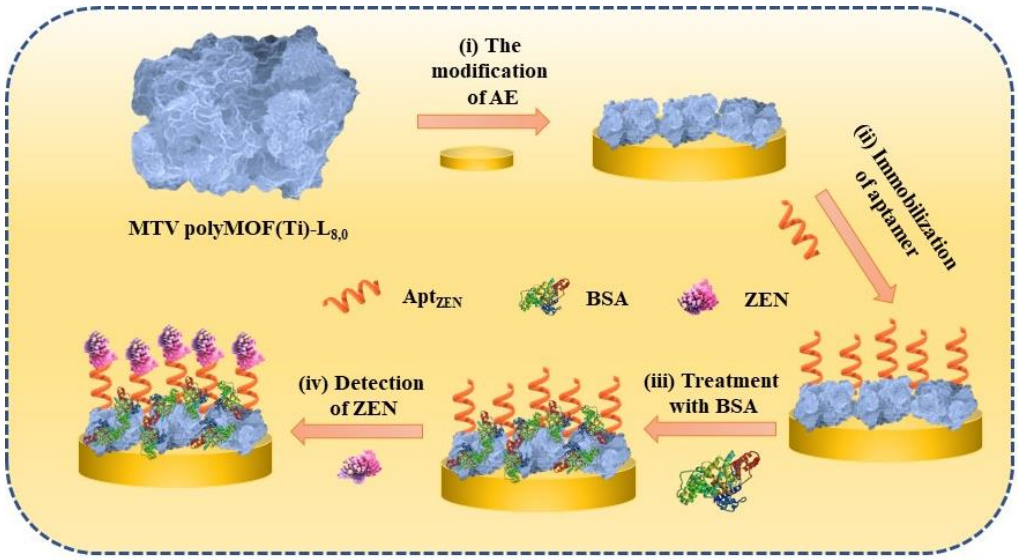

Scheme 17 Schematic illustration of the constructing steps of MTV polyMOF(Ti)-$L_{8,0}$-based aptasensor for detecting ZEN, including (i) the modification of Au electrode (AE) with MTV polyMOF(Ti)-$L_{8,0}$, (ii) the anchoring of ZEN-targeted aptamer, (iii) the blocking of Apt/MTV polyMOF(Ti)-$L_{8,0}$/AE, and (iii) the detection of ZEN using bovine serum albumin (BSA)/Apt/MTV

polyMOF(Ti)-$L_{8,0}$/AE.

7.2.2. Characterizations

The field-emission scanning electron microscopy (FE-SEM) image (**Figure 29**) indicates that MTV polyMOF(Ti)-$L_{8,0}$ has a nanoflower-like shape, which accumulates a large number of homogeneous, corrugated, and layered nanosheets. The resembled nanosheet structure is observed in the transmission electron microscopy (TEM) image of MTV polyMOF(Ti)-$L_{8,0}$ (**Figure 29b**), in which ultrathin nanosheets are folded together. The high-resolution TEM (HR-TEM) image of MTV polyMOF(Ti)-$L_{8,0}$ (**Figure 29c**) reveals clear interplanar spacings of 0.198 and 0.207 nm, which can be ascribed to the (200) facets of anatase TiO_2 crystals [100] and the (101) facets of graphite [101], respectively. This finding indicates that ultrasmall TiO_2 nanocrystals are embedded within the carbon network. The ultrathin and porous structure of MTV polyMOF(Ti)-$L_{8,0}$ benefit the immobilization of ZEN-targeted aptamers. The elemental mapping spectroscopy (EDS) of MTV polyMOF(Ti)-$L_{8,0}$ shows that C, O, and Ti are homogeneously distributed (**Figure 29d**). MIL-125 [102] shows a disk-like plate morphology with smooth surface (**Figure 30a**). The Ti, C and O elements are distributed evenly (**Figure 30b**). As shown in the HR-TEM images (**Figure 30c** and **30d**), the dark parts are mainly the morphology of MIL-125(Ti) and no clear lattice fringe with the interplanar spacing is observed. The FE-SEM image of polyMOF(Ti)-L_8 (**Figure 31a**) reveals large solid shape which is composed of irregular spheres. **Figure 31b** shows a homogeneous distribution of Ti, C, and O in polyMOF(Ti)-L_8. The TEM image (**Figure 31c**) shows that the nanospheres in polyMOF(Ti)-L_8 are loosely assembled together, having an average diameter of ca. 50 nm. No obvious lattice structure is observed in the HR-TEM image (**Figure 31d**).

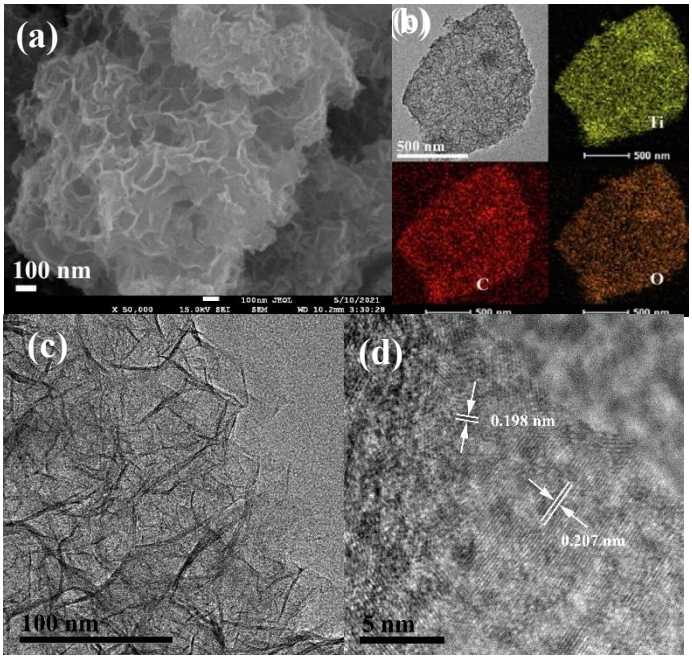

Figure 29 (b) High-magnification FE-SEM image, (c and d) high-magnification and high-resolution TEM images, and (e) dark-field TEM image and corresponding EDS elemental mapping of MTV polyMOF(Ti)-$L_{8,0}$.

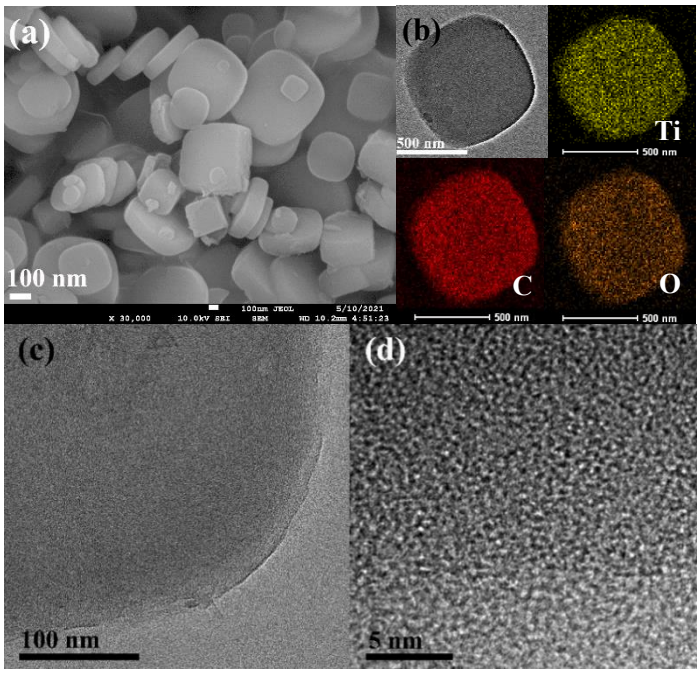

Figure 30 (a) High-magnification FE-SEM images, (b) dark-field TEM image and corresponding EDS elemental mapping, and (c, d) high-magnification and high-resolution TEM images of MIL-125.

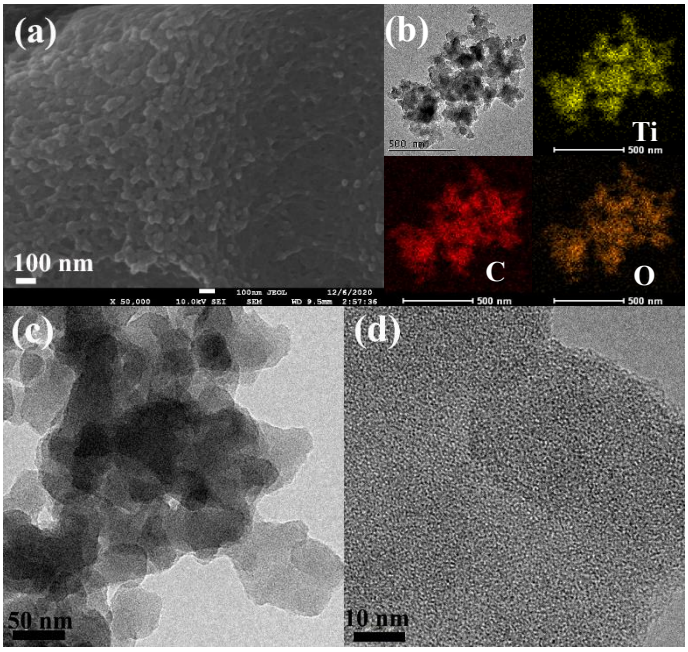

Figure 31 (a) High-magnification FE-SEM images, (b) dark-field TEM image and corresponding EDS elemental mapping of polyMOF(Ti)-L_8, and (c, d) high-magnification, and high-resolution TEM images of polyMOF(Ti)-L_8.

The PXRD pattern (**Figure 32**) of MTV polyMOF(Ti)-$L_{8,0}$ (curve *i*) shows a characteristic diffraction peak at $2\theta = 6.8°$, which is consistent with that of MIL-125(Ti) [103]. Another characteristic diffraction peak is found at $2\theta = 25°$, corresponding to graphite-like structure [104]. Two other peaks emerging at $2\theta = 38.4$ and $48.4°$ are ascribed to the anatase (112) and (200) crystal planes of TiO_2 (JCPDS files Nos. 89-4921), respectively. The PXRD pattern of polyMOF(Ti)-L_8 (curve *ii*) includes the diffraction peaks at $2\theta = 6.8°$ and $26.0°$ that are assigned to MIL-125(Ti) and graphite-like structure,

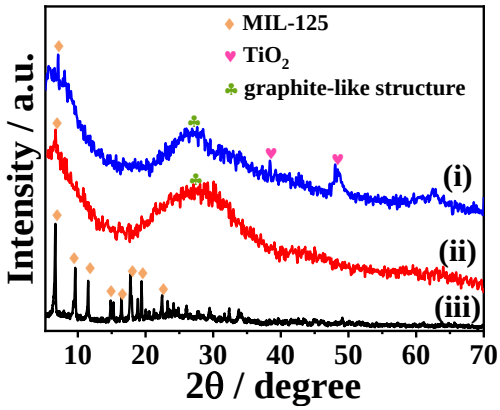

Figure 32 XRD patterns of (i) MTV polyMOF(Ti)-$L_{8,0}$, (ii) polyMOF(Ti)-L_8, and (iii) MIL-125.

respectively. For MIL-125 (curve *iii*), three diffraction peaks at $2\theta = 6.8$, 9.5, and 11.4° are ascribed to anatase MIL-125(Ti). In contrast to Ti-MOFs synthesized using the single ligand, MTV polyMOF(Ti)-$L_{8,0}$ integrates the nanostructure of polymer and MIL-125. This feature can boost the electrochemical activity and enlarge the sensing response of aptasensor.

The FT-IR spectrum of MTV polyMOF(Ti)-$L_{8,0}$ (curve *i*, **Figure 33**) shows a broad and strong peak at 3453 cm^{-1}, which is due to OH group originating from physically adsorbed water. The characteristic peaks at 2926 and 2838 cm^{-1} correspond to the stretching vibration of CH_x [105], which originates from the alkyl chain of polymer ligand. The peak at 1627 cm^{-1} is the symmetrical stretching vibration of C=O. The peaks at 1437 and 1007 cm^{-1} are attributed to the asymmetric and symmetric stretching vibrations of C–O–C, respectively [106]. The peak at ca. 800 cm^{-1} can be assigned to the stretching and bending vibrations of O–Ti–O bond [103], confirming the existence of TiO_2 nanocrystals within polyMOF(Ti)-$L_{8,0}$. PolyMOF(Ti)-L_8 shows similar characteristics peaks in FT-IR spectrum (curve *ii*), indicating analogous chemical components to polyMOF(Ti)-$L_{8,0}$. In terms of MIL-125 (curve *iii*), except for the characteristic peaks at 3453 and 1627 cm^{-1}, the vibration peaks in 1365–1540 cm^{-1} are observed, due to the C=C bonds in terephthalic acid. The peak at 1261 cm^{-1} is assigned to C–O vibration [107].

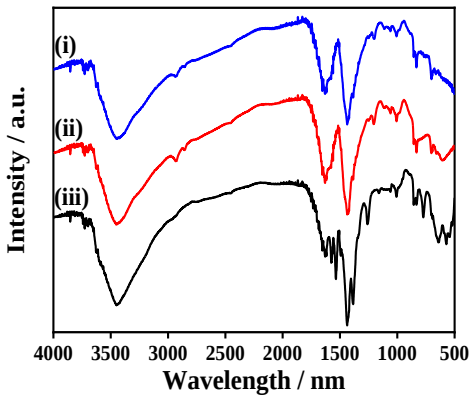

Figure 33 FT-IR spectra of (i) MTV polyMOF(Ti)-$L_{8,0}$, (ii) polyMOF(Ti)-L_8, and (iii) MIL-125.

Figure 34 presents the Raman spectra of the three samples. Three distinct peaks are observed in the similar Raman spectra of MTV-Ti-polyMOF-L8-L0 (curve *i*) and polyMOF(Ti)-L_8 (curve *ii*), in which two peaks at 1300 and 1603 cm^{-1} are due to the

D-band and G-band of carbon structures, respectively. The peak at 633 cm^{-1} is the in-plane bending vibration of C−C bands of the polymer ligand, while the band at 231 cm^{-1} reveals the formation of TiO_2 [100,108]. The intensity of characteristic peaks of MIL-125 (curve *iii*) is lower than those of MTV polyMOF(Ti)-$L_{8,0}$ and polyMOF(Ti)-L_8. The values of I_D/I_G are 0.99, 0.99, and 0.96, for MTV polyMOF(Ti)-$L_{8,0}$, polyMOF(Ti)-L_8, and MIL-125, respectively, revealing their similar defects and disordered structures. The coexistence of strong D- and G-bands reveals a graphene-like nanostructure of MTV polyMOF(Ti)-$L_{8,0}$, which not only improve the electrochemical performance but also boosts the aptamer immobilization via π–π^* stacking interaction.

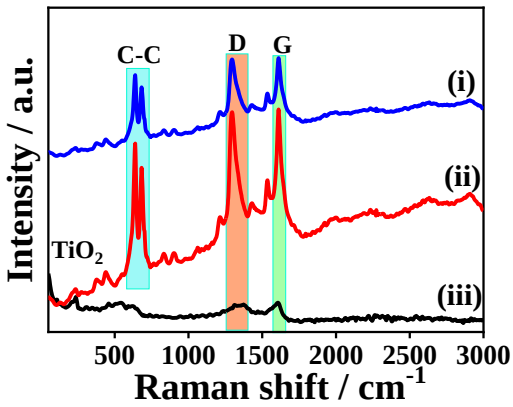

Figure 34 Raman spectra of (i) MTV polyMOF(Ti)-$L_{8,0}$, (ii) polyMOF(Ti)-L_8, and (iii) MIL-125.

The specific surface areas were determined by Brunauer-Emmett-Teller (BET) approach. **Figure 35a** shows the N_2 isotherms of MTV polyMOF(Ti)-$L_{8,0}$, polyMOF(Ti)-L_8, and MIL-125 at 77 K, with BET surface areas of 315, 126, and 380 $m^2\ g^{-1}$, respectively. MTV polyMOF(Ti)-$L_{8,0}$ and MIL-125 exhibit type IV hysteresis loops, while MIL-125 displays type I N_2 sorption isotherm (**Figure 35a**). According to the IUPAC classification, MTV polyMOF(Ti)-$L_{8,0}$ shows the monolayer loading of nitrogen [109]. The pore sizes of MTV polyMOF(Ti)-$L_{8,0}$, polyMOF(Ti)-L_8 and MIL-125 are 0.59, 1.39, and 0.61 nm, respectively (**Figure 35b**). This verifies that mixing polymers and small ligands can modulate the nanostructures of MOFs, thereby affecting the sensing performances of the constructed aptasensors.

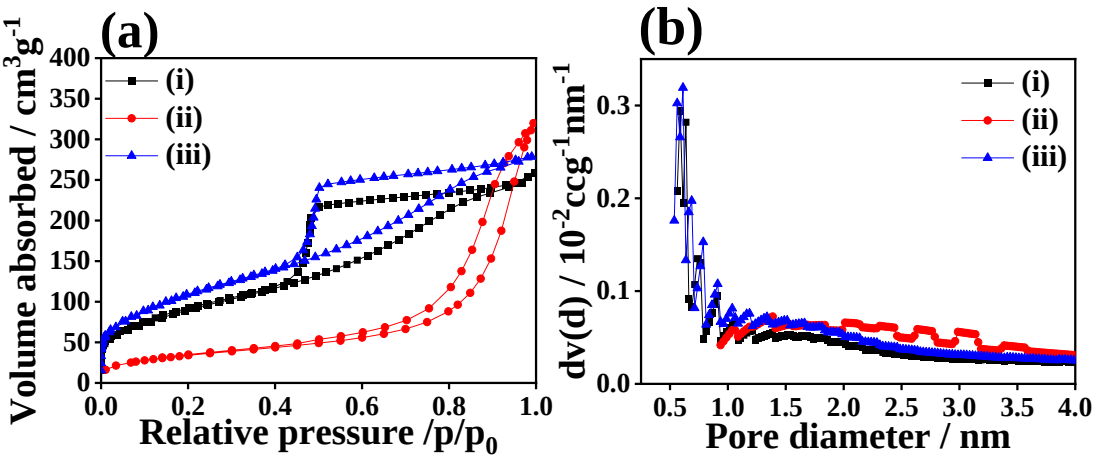

Figure 35. (a) N_2 adsorption-desorption isotherms and (b) pore distribution of (i) MTV polyMOF(Ti)-$L_{8,0}$, (ii) polyMOF(Ti)-L_8, and (iii) MIL-125.

Thermal gravimetric analysis (TGA) was carried out to evaluate their thermal stability (**Figure 36**). The guest and coordinated solvents in the pores of MTV polyMOF(Ti)-$L_{8,0}$ (curve *i*) and polyMOF(Ti)-L_8 (curve *ii*) are evaporated at lower temperatures in 25 to 300 °C compared with MIL-125 (curve *iii*) (249 to 344°C). Furthermore, polyMOF(Ti)-L_8 and MTV polyMOF(Ti)-$L_{8,0}$ are degraded within 300–466 °C. The weights of polyMOF(Ti)-L_8 and MTV polyMOF(Ti)-$L_{8,0}$ remain unchanged, whereas the mass of MIL-125 decreases with increasing the temperature. Also, the weight loss of polyMOF(Ti)-L_8 or MTV polyMOF(Ti)-$L_{8,0}$ is lower than that of MIL-125, revealing their higher thermal stability. The integration of polymer ligand into MIL-125 can cause missing of linker defects in MTV polyMOF(Ti)-$L_{8,0}$ [110], thus enhancing the structural stability.

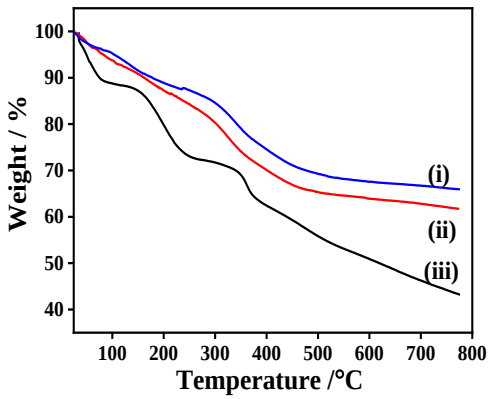

Figure 36 TGA curves of (i) MTV polyMOF(Ti)-$L_{8,0}$, (ii) polyMOF(Ti)-L_8, and (iii) MIL-125.

XPS analysis was performed to determine the chemical structures and components

of MOFs. **Figure 37** illustrates the XPS survey scan spectra, verifying the clear signals of Ti 2*p* (457.5 eV), C 1*s* (284.3 eV), and O 1*s* (529.1 eV).

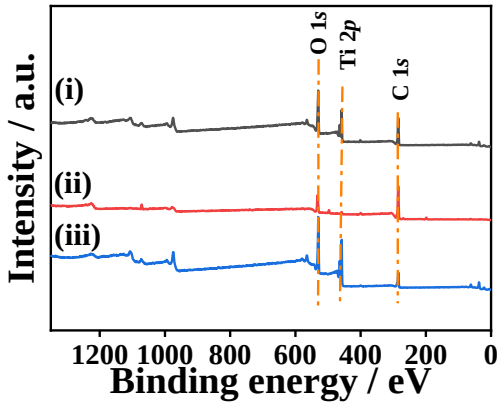

Figure 37 XPS survey spectra of (i) MTV polyMOF(Ti)-$L_{8,0}$, (ii) polyMOF(Ti)-L_8, and (iii) MIL-125.

The atomic% values of each element are summarized in **Table 6**. Based on the comparison of the three samples, the atomic% of C 1*s* of polyMOF(Ti)-L_8 is the largest (54.33%) due to the polymer ligand containing a long carbon chain. The atomic% of Ti 2*p* of MTV-Ti-polyMOF-$L_{8,0}$ is 36.04%, comprising the Ti components of polyMOF(Ti)-L_8 and Ti-MOF. The high-solution XPS spectra were analyzed by Gaussian fitting to indicate the chemical structures and valence states of each element in MOFs. Two apparent peaks are found in the high-resolution Ti 2*p* XPS spectra of the three samples at the binding energies (BEs) of 464.3 and 458.6 eV, corresponding to Ti $2p_{1/2}$ and Ti $2p_{3/2}$, respectively (**Figure 38a1-a3**). The peak is assigned to Ti^{4+} state in titanium-oxo cluster [111]. The high-resolution C 1*s* XPS spectra (**Figure 38b1-b3**) can be separated into three peaks located at the BE levels of 284.6, 286.2, and 288.6 eV, which are due to C–C, C–O, and O–C=O, respectively. The high-resolution O 1*s* XPS spectra (**Figure 38c1**) are deconvoluted into three peaks at the BE levels of 529.7, 531.7, and 533.31 eV, which are attributed to lattice oxygen from Ti–O bond in titanium-oxo clusters, C=O, and C–O=C, respectively [112]. The peak areas of C=O and COO groups in the O 1*s* XPS spectra of polyMOF(Ti)-L_8 (**Figure 38c2**) are the largest among the three s amples, which originate from the polymer ligand. The peak area of the Ti–O bond of polyMOF(Ti)-L_8 and MIL-125 (**Figure 38c3**) indicates that it is dominant in

Ti 2*p* signal, suggesting a high content of TiO_2 nanocrystals in polyMOF network. MTV polyMOF(Ti)-$L_{8,0}$ integrates the chemical components of MTV polyMOF(Ti)-$L_{8,0}$ and MIL-125 and thus exhibits improved electrochemical activity and bioaffinity.

Table 6. Atomic% of elements in MIL-125, polyMOF(Ti)-L_8, and MTV polyMOF(Ti)-$L_{8,0}$.

Samples	Atomic%			
	C 1*s*	O 1*s*	Ti 2*p*	P 2*p*
MIL-125	11.68	44.60	43.72	-
polyMOF(Ti)-L_8	54.33	37.51	8.16	-
MTV polyMOF(Ti)-$L_{8,0}$	23.25	40.71	36.04	-

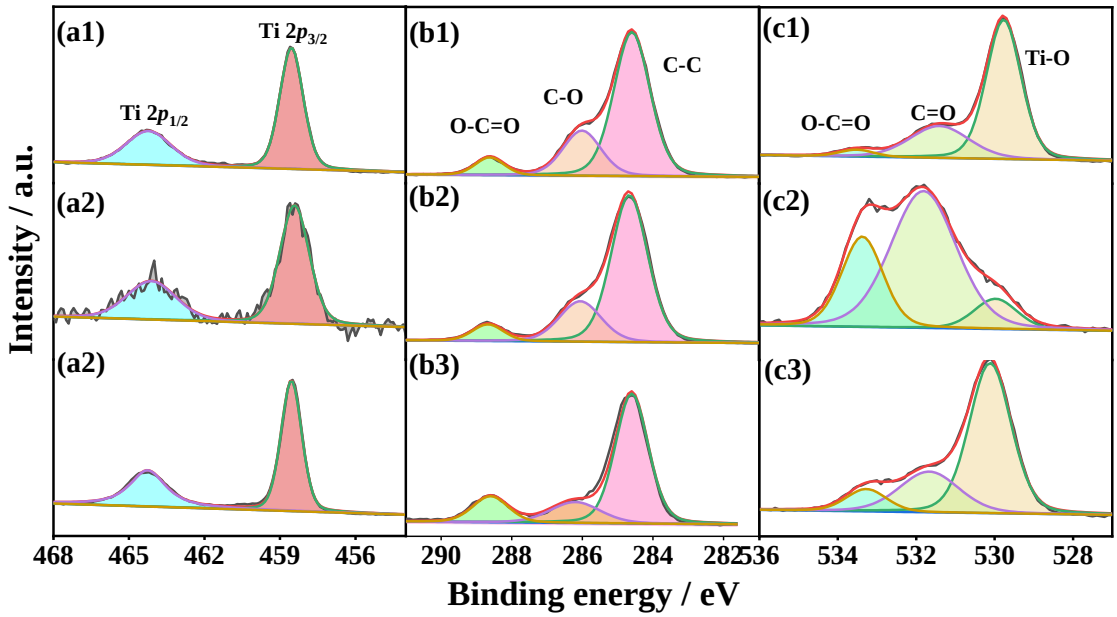

Figure 38 High-resolution XPS spectra of (a) Ti 2*p*, (b) C 1s, and (c) O 1s of (a1, b1, and c1) MTV polyMOF(Ti)-$L_{8,0}$, (a2, b2,and c2) polyMOF(Ti)-L_8, and (a3, b3,and c3) MIL-125.

XPS analysis suggests the anchoring of aptamer on surface of MTV polyMOF(Ti)-$L_{8,0}$. The XPS survey spectrum (**Figure 39**) shows the clear signals of Ti 2*p* (457.5 eV), C 1*s* (284.3 eV), O 1*s* (529.1 eV), and P 2*p* (133.6 eV). The atomic% of each element

in the three samples are summarized in **Table 6**.

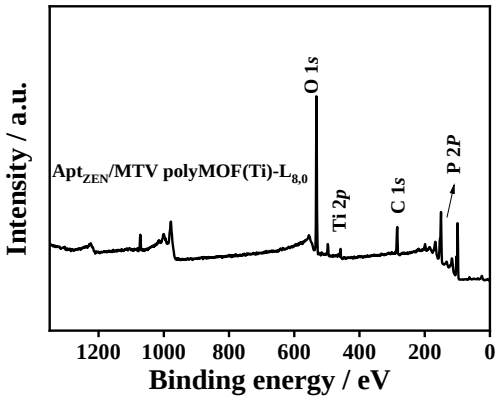

Figure 39 XPS survey spectrum of Apt/MTV polyMOF(Ti)-$L_{8,0}$.

As shown in **Figure 40a**, the Ti 2*p* XPS spectrum of Apt/ MTV polyMOF(Ti)-$L_{8,0}$ can be deconvoluted into two peaks at 458.5 and 464.2 eV originated from Ti $2p_{3/2}$ and Ti $2p_{1/2}$, respectively. The C 1*s* spectrum of Apt/ MTV polyMOF(Ti)-$L_{8,0}$ contains three peaks at 284.5, 286.2 and 288.8 eV (**Figure 40b**), which originate from the C–C, C–O and O–C=O groups, respectively. The O 1*s* spectrum of Apt/MTV polyMOF(Ti)-$L_{8,0}$

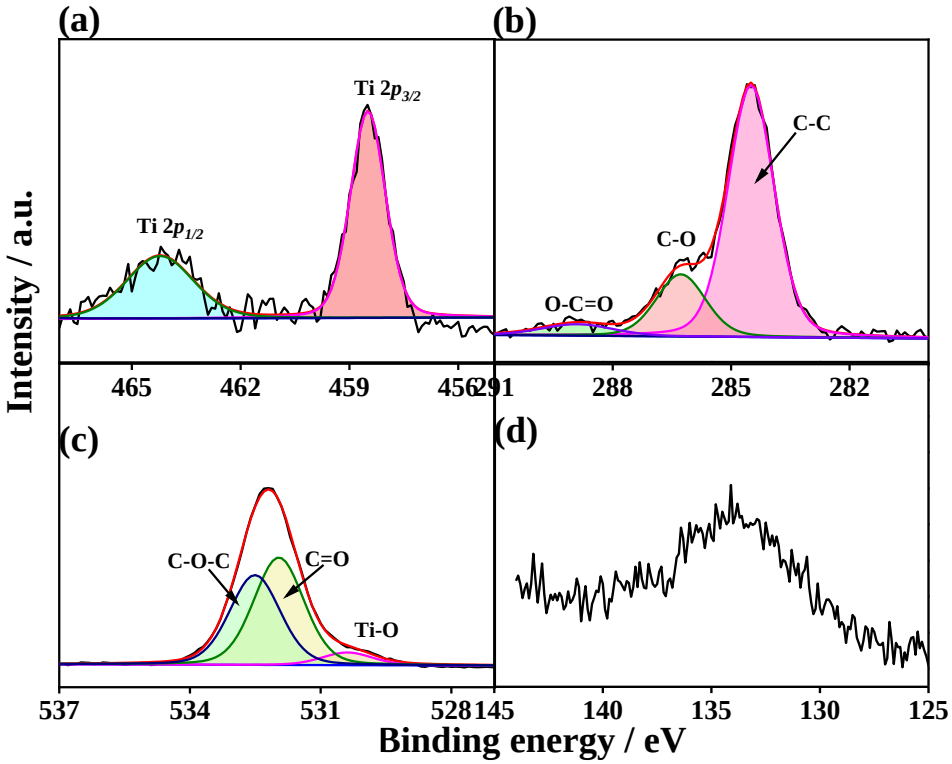

Figure 40 High-resolution (a) Ti 2*p*, (b) C 1*s*, (c) O 1*s* and (d) P 2*p* XPS spectra of Apt/MTV polyMOF(Ti)-$L_{8,0}$.

includes three peaks at 530.4, 531.8 and 532.5 eV (**Figure 40c**), which are attributed to

lattice oxygen from in titanium-oxo cluster, C=O, and C–O–C groups in carboxyl groups, respectively [113]. Furthermore, the P 2*p* signal is observed after immobilizing aptamer. The P 2*p* core-level XPS spectrum (**Figure 40d**) reveals that the aptamer is adsorbed onto MTV polyMOF(Ti)-$L_{8,0}$.

7.2.3 Electrochemical performances

Various electrochemical approaches, including EIS, DPV, and cyclic voltammetry (CV), were used to assess the performances of aptasensors based on Ti-MOFs (**Figure 41. 42**, and **43**). All measurements were carried out in 0.01 M PBS containing 5 mM $[Fe(CN)_6]^{3-/4-}$ (pH = 7.4). All EIS Nyquist plots were fitted and analyzed using the Randles equivalent circuit gained from Zview2 software (inset, **Figure 44**). As described in **Figure 41a** (curve *i*), the resistance of charge transfer (R_{ct}) of bare AE is as small as 98.1 Ω, verifying the rapid electron transfer at the electrode/electrolyte interface. After separate coating of Ti-MOFs, the electrochemical activity of modified electrode declines substantially with regard to the enlarged semicircle of the EIS Nyquist plot. This can be ascribed to the reduced electroconductivity of Ti-MOFs. Among the three MOFs, the R_{ct} of MTV polyMOF(Ti)-$L_{8,0}$/AE (218.1 Ω) is lower than those of the polyMOF(Ti)-L_8/AE (351.4 Ω) and MIL-125/AE (314.5 Ω). The use of polymer ligand for the preparation of polyMOF(Ti)-L_8 (**Figure 41b**) can hamper electron transfer at the interface of electrolyte/electrode, and the electrochemical activity of MTV MOF is superior to the reported MOFs [such as Al-MOF (750 Ω) [114] and Zr-MOF (2.716 kΩ) [115]], MOFs-based composites [gold-palladium-modified Fe-MOFs (1212 Ω) [116] and Fe-MOF@mFe_3O_4@mC (528 Ω) [117]], and MOFs-based derivatives [CeO_2/CuO_x@mC (529 Ω) [118] and CuO_x-C-550 N (605 Ω) [119]]. The MTV polyMOF(Ti)-$L_{8,0}$ network is composed of highly regular carbon lamellar and TiO_2 nanocrystals, showing porous nanosheet-like structure with large specific surface area, thus resulting in excellent electrochemical activity.

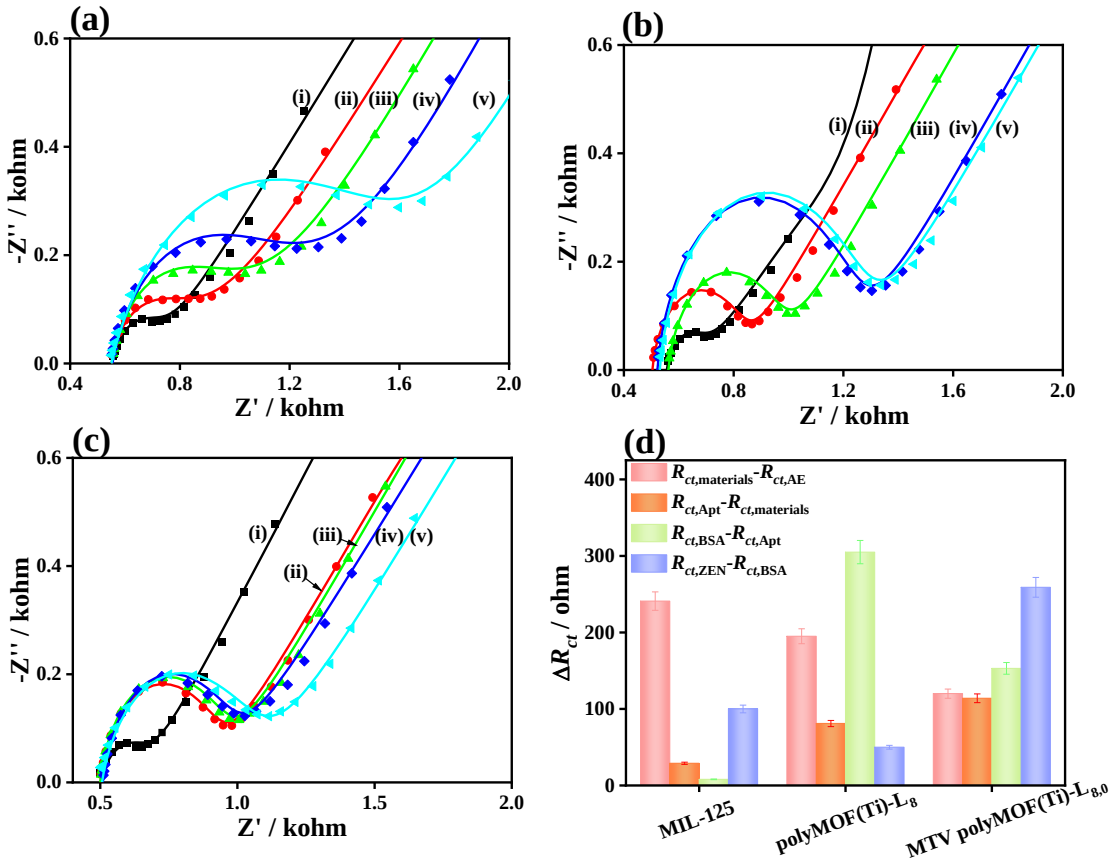

Figure 41 EIS responses of electrodes after different modifications in 5 mM $[Fe(CN)_6]^{3-/4-}$ containing 0.1 mol L^{-1} KCl: (a) MTV polyMOF(Ti)-$L_{8,0}$, (b) polyMOF(Ti)-L_8, and (c) MIL-125. (b) Variations in R_{ct} for each stage in fabrication procedure of aptasensors based on MIL-125, polyMOF(Ti)-L_8, and MTV polyMOF(Ti)-$L_{8,0}$.

As shown in **Figure 42**, the typical EIS Nyquist plots and equivalent circuit of current system were taken. In Nyquist diagram, R_{ct} is directly related to the semicircle diameter and the real and imaginary parts of EIS spectra represent Nyquist plots (Z′ vs –Z″) using 5 mM $[Fe(CN)_6]^{3-/4-}$ as electrolyte. All EIS experimental data were fitted by the Randles equivalent circuit model, in which R_s, R_{ct}, CPE1 and W represent electrolyte resistance, charge transfer resistance, constant-phase element, and Warburg impedance. The charge transfer process was determined by measuring the charge transfer resistance (R_{ct}) at the electrode/electrolyte interface under different conditions and calculating the equivalent circuit elements from the model.

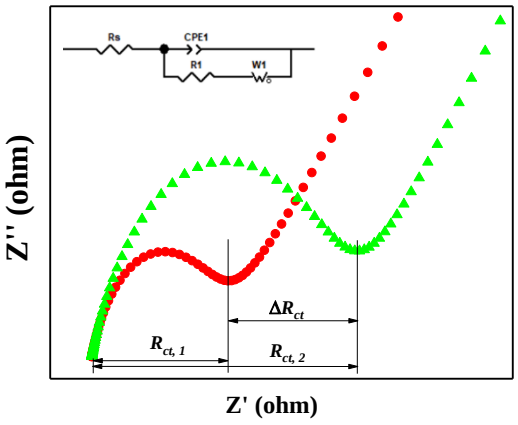

Figure 42 EIS Nyquist plots and equivalent circuit.

After immobilizing ZEN-targeted aptamer (200 nM), the R_{ct} of Apt/MTV polyMOF(Ti)-$L_{8,0}$/AE significantly increases to 332.4 Ω (curve *iii*). The repulsion interaction between the negatively charged phosphate backbone of probe and $[Fe(CN)_6]^{3-/4-}$ in water solution will prevent electron transfer at the electrode/electrolyte interface. Further, the coverage of insulated aptamer layer decreases the electrode conductivity. Based on the impedance data, the fractional electrode coverage (θ) of aptamer over MTV polyMOF(Ti)-$L_{8,0}$/AE can be calculated using the following equation

$$\theta = (R_{ct} - R_{ct,0})/R_{ct}$$

where $R_{ct,0}$ and R_{ct} are the charge-transfer resistance at Materials/AE and Apt/Materials/AE electrodes, respectively [120]. The coverage of aptamer strands over the MTV polyMOF(Ti)-$L_{8,0}$ layer is 52.3%, which is substantially larger than those of polyMOF(Ti)-L_8 (9.3%) and Ti-MOF (23%). BSA is first adsorbed over the gained MTV polyMOF(Ti)-$L_{8,0}$/AE, leading to a further increase in R_{ct} (486.0 Ω) (curve *iv*). This finding is ascribed to a small amount of BSA adsorbed over substance. After incubation with ZEN solution (1 pg mL^{-1}), the R_{ct} increases to 745.2 Ω (curve *v*) due to efficient binding of aptamers with ZEN, thus forming G-quadruplex to further hamper the electron transfer at interface of electrolyte/electrode [121]. For polyMOF(Ti)-L_8- and MIL-125-based aptasensors, the R_{ct} values for each step increase relative to that of the previous step (**Figure 41**), which is similar to that of MTV polyMOF(Ti)-$L_{8,0}$-based

aptasensor. **Table 7** shows the R_{ct} values of electrode in each step for the two aptasensors. As a result, the θ values over the modified electrode are 9.3% and 23% for the polyMOF(Ti)-L_8- and MIL-125-based aptasensors, respectively, which reveals an improved bioaffinity to aptamer and thus superior sensing performance toward ZEN for polyMOF(Ti)-$L_{8,0}$.

Table 7. Deduced R_{ct} values for each step in fabrication procedure of aptasensors based on MTV polyMOF(Ti)-$L_{8,0}$, polyMOF(Ti)-L_8, and MIL-125.

Electrode materials	R_{ct} (Ω)				
	Bare AE	Modified AE	Aptamer immobilization	BSA blocking	ZEN detection
polyMOF(Ti)-L_8	155.8	351.4	432.4	737.7	788.4
MIL-125	72.6	314.5	343.9	352	452.2
MTV polyMOF(Ti)-$L_{8,0}$	98.1	218.1	332.4	486	745.2

Table 8. Variations of R_{ct} values for each step in fabrication procedures of aptasensors based on MTV polyMOF(Ti)-$L_{8,0}$, polyMOF(Ti)-L_8, and MIL-125.

Electrode materials	ΔR_{ct} (Ω)			
	$R_{ct,\ materials} - R_{ct,\ bare\ AE}$	$R_{ct,\ Apt} - R_{ct,\ materials}$	$R_{ct,\ BSA} - R_{ct,\ Apt}$	$R_{ct,\ ZEN} - R_{ct,\ BSA}$
polyMOF(Ti)-L_8	195.6	81.0	305.3	50.7
MIL-125	241.9	29.4	8.1	100.2
MTV polyMOF(Ti)-$L_{8,0}$	120.0	114.3	153.6	259.2

Detection efficiency of aptasensor can be obtained from the changes in EIS response for detecting targets. The detection efficiency can be represented by ΔR_{ct} ($\Delta R_{ct} = R_{ct,i+1} - R_{ct,i}$)/$R_{ct,i}$, in which ΔR_{ct} is the difference in R_{ct} values before ($R_{ct,i}$) and after the detection of analyte ($R_{ct,i+1}$) [98]. **Table 8** shows the ΔR_{ct} values for each step based on MTV polyMOF(Ti)-$L_{8,0}$, polyMOF(Ti)-L_8, and MIL-125. The results reveal that MTV polyMOF(Ti)-$L_{8,0}$ can act as sensitive bioplatform for detection of ZEN because it not only adsorbs aptamer but also stabilizes the formed G-quadruplex.

DPV technique was used to validate the aptasensor in electrolyte (**Figure 43a-c**)

and the results are consistent with those of EIS. The bare AE shows a significant peak (curve *i*) and high peak current (I_p = 52.6 μA) due to its high conductivity (**Figure 43a**). When MTV polyMOF(Ti)-$L_{8,0}$ was coated on AE (curve *ii*), a decreased I_p (48.9 μA) is found. The I_p of Apt/MTV polyMOF(Ti)-$L_{8,0}$/AE continuously declines (46.2 μA, curve *iii*) in comparison with MTV polyMOF(Ti)-$L_{8,0}$/AE. After blocking with BSA, the I_p further decreases to 43.8 μA. The incubation with ZEN solution causes a further decrease in I_p (39.8 μA) due to the G-quadruplex formed between aptamer and ZEN. Moreover, **Figure 43d-f** present the CV curves for ZEN detection using the Ti-MOFs-based aptasensor. The bare AE has a well-defined pair of redox peaks with a peak potential difference (ΔE_p) of 254.0 mV (curve *i*) (**Figure 43d**). After the modification with MTV polyMOF(Ti)-$L_{8,0}$ (curve *ii*), the ΔE_p of modified electrode increases to

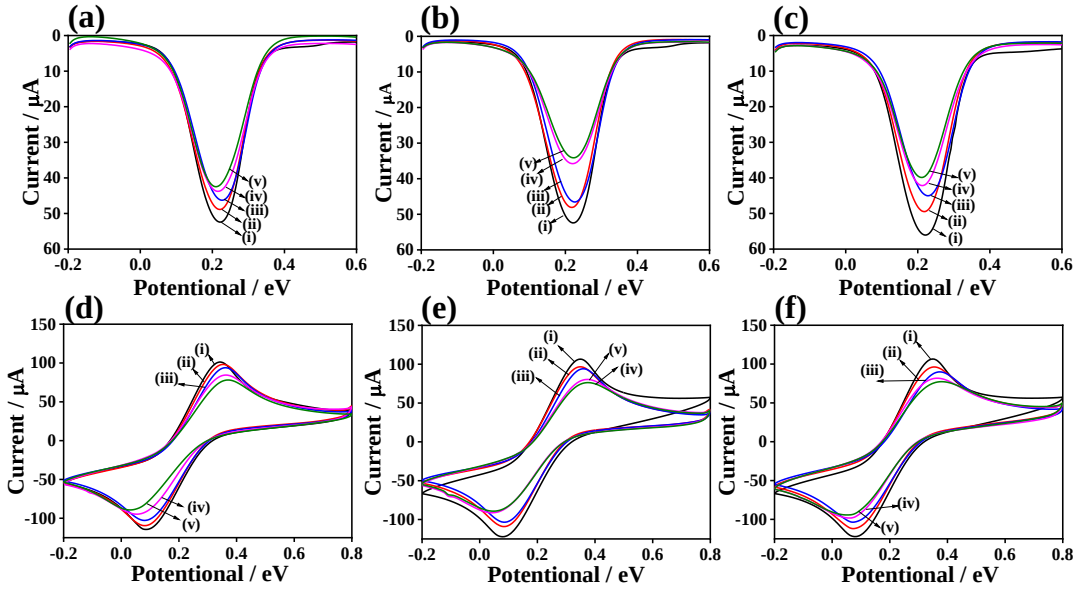

Figure 43 DPV and CV curves of aptasensors based on MTV polyMOF(Ti)-$L_{8,0}$ (a, d), polyMOF(Ti)-L_8 (b, e), and MIL-125 (c, f) for detection of ZEN at various steps in 0.01 M PBS containing 5 mM $[Fe(CN)_6]^{3-/4-}$, including (i) AE, (ii) Material/AE, (curve iii) Apt/Material/AE, (curve iv) BSA/Apt/Material/AE, and (curve v) ZEN/BSA/Apt/Material/AE.

270.1 mV, confirming that MTV polyMOF(Ti)-$L_{8,0}$ hinders electron transfer at electrode/electrolyte interface. After the immobilization of aptamers on Apt/MTV polyMOF(Ti)-$L_{8,0}$, the ΔE_p continuously increases to 285.2 mV (curve *iii*). The ΔE_p increases to 305.3 mV after incubation in BSA (curve *iv*) and in the presence of ZEN, the ΔE_p further increases (337.6 mV, curve *v*). These results are consistent with the EIS

and DPV data.

7.2.4 Optimization of the parameters for constructing aptasensor

To obtain the optimal experimental condition of the MTV polyMOF(Ti)-$L_{8,0}$-based aptasensor, dosage of MTV polyMOF(Ti)-$L_{8,0}$, concentration of aptamer, and binding time of ZEN were optimized, respectively. The optimal dosage of MTV polyMOF(Ti)-$L_{8,0}$ can be achieved by modifying AE surface with MTV polyMOF(Ti)-$L_{8,0}$ suspension at different concentrations (0.2, 0.5, 1, and 2 mg mL^{-1}). After aptamer immobilization, blocking with BSA, and detection of ZEN, the ΔR_{ct} values were collected (**Figure 44a**). The results indicates that the thick layer hinders the electron transfer, which leads to the increases of ΔR_{ct} value with the increased dosage of MTV polyMOF(Ti)-$L_{8,0}$ (from 0.2 to 1.0 mg mL^{-1}). After the dosage of MTV polyMOF(Ti)-$L_{8,0}$ exceeds 1 mg mL^{-1}, the ΔR_{ct} values of Apt/MTV polyMOF(Ti)-$L_{8,0}$/AE decrease due to the release of Apt/MTV polyMOF(Ti)-$L_{8,0}$ from AE surface. Thus, MTV polyMOF(Ti)-$L_{8,0}$ at a concentration of 1 mg mL^{-1} was used for aptasensor fabrication. To find the optimal concentration of aptamer, MTV polyMOF(Ti)-$L_{8,0}$/AEs were incubated in aptamer solutions at different concentrations (50, 100, 200, 300 and 500 nM) and then used to detect ZEN (**Figure 44b**). The aptamer concentration is changed from 50 to 100 nM with MTV polyMOF(Ti)-$L_{8,0}$ solution of 1 mg mL^{-1} as a model. The ΔR_{ct} values increase and then leveled off after 200 nM. As a result, the aptamer solution of 200 nM is enough for further analysis. **Figure 44c** shows the optimal binding time between ZEN and BSA/Apt/MTV polyMOF(Ti)-$L_{8,0}$/AE. The ΔR_{ct} values increase for detecting ZEN with the increase of binding time due to the formation of G-quadruplex. After 60 min, the ΔR_{ct} value is stabilized to reveal the completeness of the reaction. Thus, the binding time was set to 60 min.

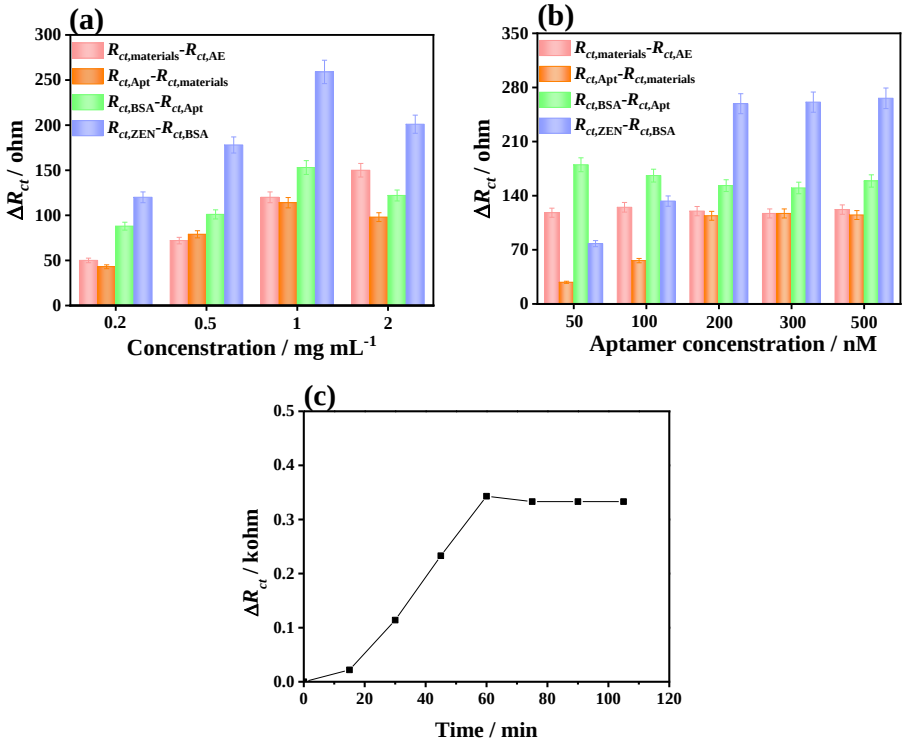

Figure 44 Optimization of fabrication conditions for ZEN aptasensor. (a) Effect of the different amounts of MTV polyMOF(Ti)-$L_{8,0}$; (b) effect of the aptamer concentration; and (c) effect of the binding time between the aptamer and ZEN (1 pg mL^{-1}).

7.2.5 Sensing performances of the MTV polyMOF(Ti)-L8,0-based aptasensor

The performance of MTV polyMOF(Ti)-$L_{8,0}$-based aptasensor was quantitatively evaluated under the optimized experimental conditions. Different concentrations of ZEN solutions were detected using EIS and DPV techniques. **Figure 45a** indicates that the semicircles of EIS responses gradually expand with increasing ZEN concentration in the range from 10 fg mL^{-1} to 10 ng mL^{-1}. This result shows that large amounts of ZEN molecules can be recognized and bound to aptamer strands immobilized on the MTV polyMOF(Ti)-$L_{8,0}$ matrix. The difference in EIS response is represented by ΔR_{ct} values ($\Delta R_{ct} = R_{ct,ZEN} - R_{ct,BSA}$), which can precisely interpret the quantitative analysis of ZEN using the MTV polyMOF(Ti)-$L_{8,0}$-based aptasensor. The ΔR_{ct} for ZEN detection (**Figure 45b**) increases with increasing concentration of ZEN within 10 fg mL^{-1} to 10 ng mL^{-1}. As described in **Figure 45b** inset, the ΔR_{ct} value is linearly positively correlated with the logarithm of ZEN concentrations from 10 fg mL^{-1} to 10 ng mL^{-1} with the following equation: ΔR_{ct} (kΩ) = 1.58 log (C_{ZEN}) – 0.298 (R^2 = 0.9903).

The LOD is 7 fg mL^{-1} with the signal-to-noise ratio (S/N) of 3 according to 3σ/slope (σ is standard deviation of blank signal). The proposed aptasensor shows lower LOD on ZEN detection compared with the reported examples (**Table 9**). The excellent detection performance aptasensor can be due to the following points: (i) MTV polyMOF(Ti)-$L_{8,0}$ contains uncoordinated ligands, leading to abundant defects to facilitate immobilization of aptamer via π-π stacking between nucleotide bases on aptamer and electron-rich surface of MTV polyMOF(Ti)-$L_{8,0}$; (ii) the multi-ligand strategy used for synthesis of MTV polyMOF(Ti)-$L_{8,0}$ can improve the structural stability; (iii) the porous nanosheet structure and multiple components of MTV polyMOF(Ti)-$L_{8,0}$ benefit to promote the electrochemical performance. Thus, MTV polyMOF(Ti)-$L_{8,0}$ can afford fast electron transfer and mass transmission, high aptamer immobilization ability and good biocompatibility. Notably, the MTV polyMOF(Ti)-based aptasensor can also be applied to detect other targets by replacing the corresponding aptamer.

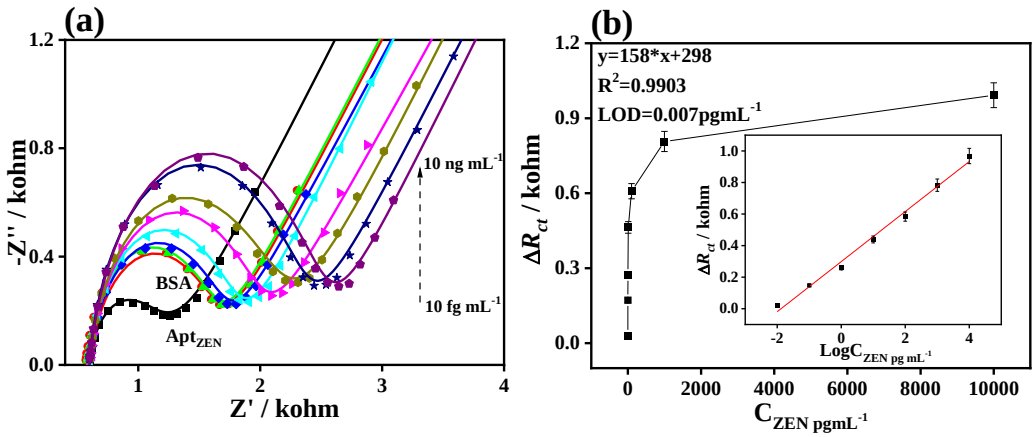

Figure 45 (a) EIS Nyquist for detection of ZEN at different concentrations (0.00001, 0.0001, 0.001, 0.01, 0.1, 1, and 10 ng mL^{-1}) by using the MTV polyMOF(Ti)-$L_{8,0}$-based aptasensor. (b) Calibration curves between ZEN concentrations and ΔR_{ct} (inset: the linear fit plot of ΔR_{ct} as a function of the logarithm of ZEN concentration, where the error bars are standard deviations for n = 3).

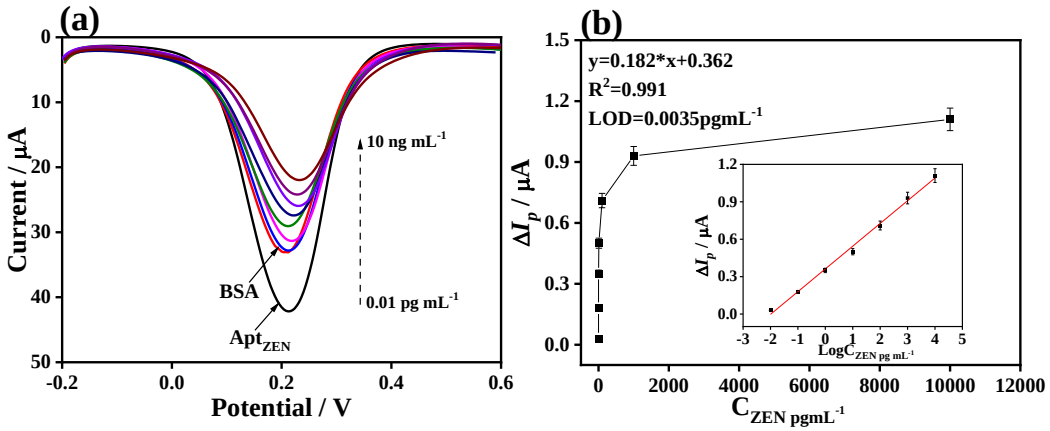

Figure 46 (a) DPV Nyquist for detection of ZEN at different concentrations (0.00001, 0.0001, 0.001, 0.01, 0.1, 1, and 10 ng mL^{-1}) by using the MTV polyMOF(Ti)-$L_{8,0}$-based aptasensor. (b) Calibration curves between ZEN concentrations and ΔI_p (inset: the linear fit plot of ΔI_p as a function of the logarithm of ZEN concentration, where the error bars are standard deviations for $n = 3$).

Figure 46a shows the DPV curves for detection of ZEN at different concentrations using the proposed MTV polyMOF(Ti)-$L_{8,0}$-based aptasensor. The peak current decreases with increased concentration of ZEN from 10 fg mL^{-1} to 10 ng mL^{-1}. The calibration plot for ZEN is shown in **Figure 46b** inset. A linear calibration curve with a regression equation of ΔI_p (μA) = 0.182 log C_{ZEN} + 0.362 was obtained. Thus, the LOD of 3.5 fg mL^{-1} (S/N = 3) was obtained using the method similar to EIS approach. The LODs obtained from DPV and EIS are similar, further proving the excellent sensing ability of aptasensor.

Table 9. Comparison of the ZEN aptasensors based on different electrode materials.

Electrode materials	Methods	Detection range	LOD	Refs.
hcPt@AuNFs/PEI-rGO	DPV	0.5 pg mL^{-1} – 50 ng mL^{-1}	0.105 pg mL^{-1}	90
rMoS_2-Au	CV and DPV	1 pg mL^{-1}–10 ng mL^{-1}	0.5 pg mL^{-1}	122
PEI-MoS_2-MWCNTs	CV	0.5 pg mL^{-1} –50 ng mL^{-1}	0.17 pg mL^{-1}	123
BSA synthesized AuNCs	fluorescence	0 – 100 ng mL^{-1}	0.53 pg mL^{-1}	124
Cysteamine-hydrochloride and 1,4-phenylene diisocyanate	DPV	0.01 – 1000 ng mL^{-1}	0.017 ng mL^{-1}	125
Carboxy-functionalized multi-walled carbon nanotubes and chitosan	DPV	10 pg mL^{-1} – 1000 ng mL^{-1}	4.7 pg mL^{-1}	126
MTV polyMOF(Ti)-$L_{8,0}$	**EIS** **DPV**	**0.01 pg mL^{-1} – 10 ng mL^{-1}**	**7 fg mL^{-1}** **3.5 fg mL^{-1}**	**this work**

7.2.6 Selectivity, stability, reproducibility and regeneration of aptasensor

Selectivity is an indicator used to assess quantitatively the analytical ability of an aptasensor. **Figure 47** depicts the remarkable EIS response of the developed aptasensor when detecting ZEN (1 pg mL^{-1}); only insignificant detection signals were found for the detection of interferents (100 pg mL^{-1}). The EIS response to detection of mixture is comparable to that of ZEN. Thus, the proposed aptasensor illustrates high selectivity in the complex environment.

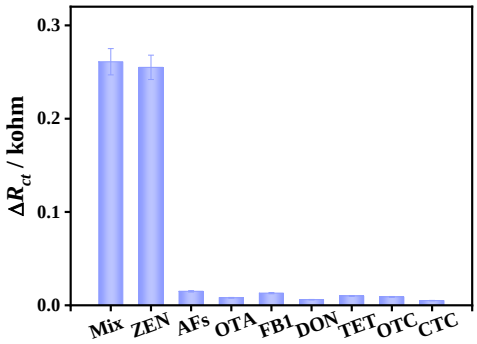

Figure 47 (a) ΔR_{ct} values of MTV polyMOF(Ti)-$L_{8,0}$-based aptasensor by adding the interference (AFs, OTA, FB1, DON, TET, OTC, and CTC with the concentration of 100 pg mL^{-1}) and their mixture.

The reproducibility of sensor was assessed by detecting ZEN (1 pg mL^{-1}) using five independent electrodes prepared under the same conditions (**Figure 48**). The relative standard deviation (RSD) of ΔR_{ct} for the simultaneous analysis of ZEN using five electrodes is as low as 1.43%, thus indicating the good reproducibility.

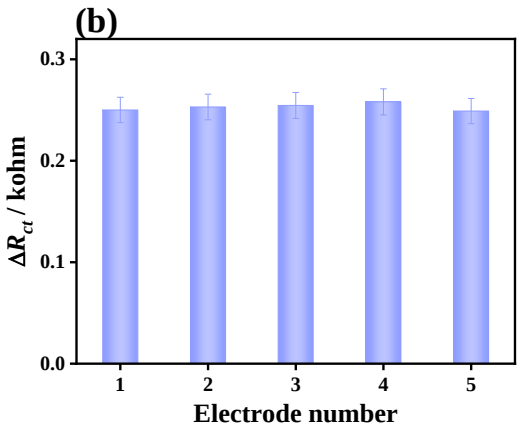

Figure 48 Reproducibility for ZEN detection at a concentration of 1 pg mL^{-1}

The MTV polyMOF(Ti)-$L_{8,0}$-based aptasensor was stored at 4 °C for 15 days, and EIS response was continuously recorded every day to confirm its stability. The EIS responses are listed in **Figure 49**. The ΔR_{ct} value only increases by 0.81% of the initial sensing capacity for detection of ZEN (1 pg mL^{-1}), revealing the good stability of aptasensor in 15 days.

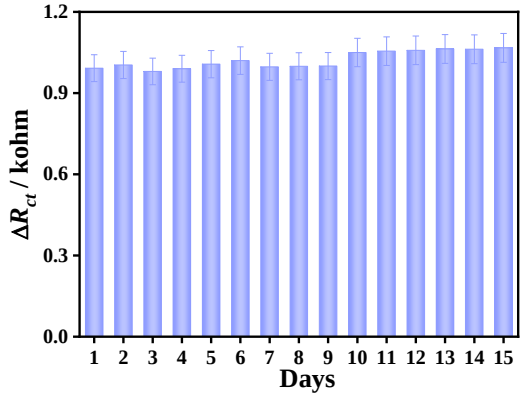

Figure 49 Stability of the proposed aptasensor for detection of ZEN at a concentration of 1 pg mL^{-1}.

The regeneration ability of the proposed aptasensor is also important for detecting ZEN. The used aptasensor was regenerated by immersing in 25 mM glycine-hydrochloric acid (pH ~ 2.4) solution for 5 min and rinsed thoroughly. The treated sensor was re-measured by EIS. **Figure 50** shows the EIS results for detection of ZEN (1 pg mL^{-1}) and regeneration cycles. The entire procedure can be regenerated for 10

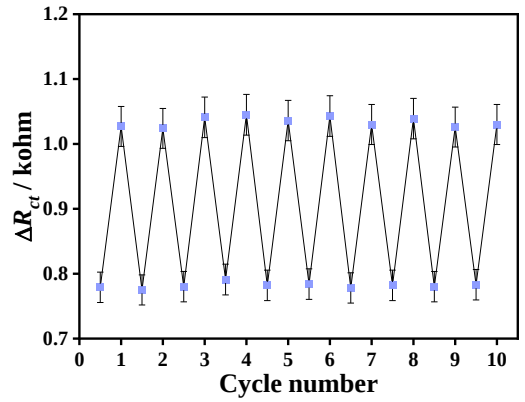

Figure 50 Regenerability of the proposed aptasensor for detection of ZEN at a concentration of 1

pg mL^{-1}.

cycles at least and the same result was obtained. This finding suggests the good regeneration ability of aptasensor. In brief, the aptasensor has good selectivity, stability, reproducibility, and regeneration for ZEN detection.

7.2.7 Detection of ZEN in real samples

The proposed aptasensor was used to determine ZEN in real samples (beer, corn, and peanut) to assess its applicability. The real sample solutions with certain concentrations of ZEN were determined using the proposed aptasensor by EIS. According to the linear regression equations of EIS technique for ZEN, the concentrations of analytes can be obtained (**Table 10**). The apparent recovery of beer, corn, and peanut is in the range of 95.72%–104.50%, 96.50%–104.47%, and 97.13–106.32%, respectively. Further, the RSD of beer, corn, and peanut samples is less than 3.89%, 4.01%, and 4.21%, respectively. Hence, the proposed aptasensor shows good recovery and precision for ZEN detection in real foodstuffs.

Table 10 Determination of ZEN with the MTV polyMOF(Ti)-$L_{8,0}$ aptasensor in sample.

Sample	Spiked amount (pg mL^{-1})	Found amount (pg mL^{-1})	ΔR_{ct} (ohm)	Apparent recovery (%)	RSD (%)
beer	0.1	0.103	142	103	2.11
	1	0.965	295	96.5	1.37
	10	10.44	459	104.4	1.24
	100	102.11	615	102.1	3.89
	1000	1045	775	104.5	1.21
	10000	9572	927	95.72	2.76
	100000	104469.62	1091	104.47	2.11

corn	0.1	0.097	138	103	2.11
	1	1.044	295	96.5	1.37
	10	10.296	458	102.96	1.41
	100	104.47	617	104.47	3.15
	1000	10029.58	774	100.3	4.01
	10000	10034	930	100.34	3.06
	100000	98553.03	1087	98.55	1.3
peanut	0.1	0.102	141	101.5	1.05
	1	1.03	300	103	2.45
	10	9.713	454	97.13	1.13
	100	106.32	616	106.32	4.21
	1000	985.53	771	98.55	3.34
	10000	10295.8	932	102.95	0.98
	100000	101468	1089	101.47	2.56

7.3 Conclusions

A superior aptasensing strategy was developed by the ingenious design of a MTV polyMOF(Ti)-$L_{8,0}$ for the sensitive analysis of ZEN. The prepared MTV polyMOF(Ti)-$L_{8,0}$ shows ultrathin sheet-like nanostructures, comprising TiO_2 nanocrystals and polymeric layers, and rich functionality. Compared with the Ti-MOFs prepared using the single ligand, MTV polyMOF(Ti)-$L_{8,0}$ is highly porous and can act as an efficient scaffold for anchoring a large number of ZEN-targeted aptamers. Under the optimal experimental conditions, a linear relationship is established between ΔR_{ct} and the concentration of ZEN from 10 fg mL^{-1} to 10 ng mL^{-1}, leading to LODs of 7 fg mL^{-1} and 3.5 fg mL^{-1} determined by EIS and DPV techniques, respectively. Moreover, the MTV-Ti-polyMOF-based aptasensor has high selectivity, stability, and reproducibility, also showing practical applications for ZEN detection in diverse samples.

Chapter 8. Chromium-based metal-organic framework embedded with cobalt phthalocyanine for the sensitively impedimetric cytosensing of colorectal cancer (CT26) cells and cell imaging

Very recently, MOFs have been also explored as sensitive layers for the biosensor development because of controllable structure, large surface area, adjustable aperture, and easy combination with other components [127,128]. The biosensors fabricated with MOFs have been paid increasing attention and applied for detecting various targets, such as biomarkers [129], heavy metal ions [130], hazard molecules [56], and living cancer cells [42]. However, the absence of fluorescence performance of some MOFs results in that the determination procedure also cannot be determined by cell imaging [131]. At moment, preparing nanosized and integrated MOFs with other electrochemically active components have become efficient methods to exploit novel MOF-based cytosensors. Bimetallic TbFe-MOFs have been designed using MOF-on-MOF strategy and utilized as a platform for anchoring the carbohydrate antigen 125 aptamer and for detecting living Michigan Cancer Foundation-7 (MCF-7) cells [132]. Moreover, the bimetallic ZrHf-MOF doped with carbon dots was applied as scaffold for immobilizing the aptamer strands and for the determination of human epidermal growth factor receptor-2 (HER2) and living HER2-overexpressed MCF-7 cells [42]. Multicomponent Zr-MOFs were applied for the detection of MCF-7 cells and showed extremely low detection limit of 31 cell mL^{-1} [133]. Although these cytosensors demonstrate superior sensing performances for determining living cancer cells, the preparation of MOF-on-MOF nanostructures requires multiple steps and time-consuming, thereby limiting their applications.

Combining MOFs with other kinds of nanomaterials, such as metal nanoparticles,

metal oxide, and carbon-based nanomaterials, can produce new multifunctional composites/hybrids, which can greatly boost the electrochemical activity of MOFs and be widely applied in biosensors [134,135]. As a versatile class of organic compounds, metallophthalocyanines (MPcs) (e.g., CoPc, CuPc, FePc, and NiPc) demonstrate good electrocatalysis for the oxidation of biological compounds [134]. Therefore, MPcs have good electrochemical sensing properties for detecting different analytes. Some examples include the CoPc/MWCNT composite for the determination of uric acid [136], polyacrylic acid/rGO/vinyl substituted polyaniline/LuPc2 for the detection of glucose oxidase [137], PcFe/Zn-based MOF (ZIF-8) for analyzing trichloroacetic acid [138], FePc/nitrogen-doped graphene for the determination of NO release from living cells [139], and nanoCoPc-graphene for detecting H_2O_2 [140]. Therefore, integrating Pc and MOFs can provide excellent electrochemical performances and remarkable sensing activity to the composite. FePc/Zn-based MOF (ZIF-8) has been prepared for sensitively detecting trichloroacetic acid [138]. Among many MOFs, Cr(III)-based clusters are strong candidates to act as an inorganic node for supporting mesoporous MOFs compared with other trivalent metal species due to the kinetic inertness of Cr(III) [141]. As a promising mesoporous Cr-MOF, Material Institut Lavoisier-101 (MIL-101) has been synthesized using Cr_3O clusters with six connectivity and linear 1,4-benzenedicarboxylate (BDC) linkers [135]. MIL-101 is thermally and chemically stable and can be applied in gas adsorption and catalysis. [142]. Considering its large specific surface area and nanosized scale [143], MIL-101 (Cr-MOF)-based electrochemical biosensors should be developed for detecting living cells.

Since CT26 cells are present in biological tissue of colorectal cancer (CRC) [144], it is essential to sensitively and selectively detect living CT26 cells for the early diagnosis of CRC. In this work, we have designed and developed a series of nanohybrids of Cr-MOF and CoPc nanoparticles (represented by Cr-MOF@CoPc) and explored them as the platforms for immobilizing the living cell-targeted aptamer strands for detecting living cancer cells (**Scheme 18**). Given intrinsic features of MOFs (large specific surface area and several active sites) and excellent electrochemical activity of CoPc,

the Cr-MOF@CoPc-based cytosensor exhibited remarkably high sensing sensitivity for CT26 cells compared with the individual components of Cr-MOF and CoPc. The electrochemical impedance spectroscopy (EIS) and differential pulse voltammetry (DPV) results showed that this cytosensor had extremely low limit of detection (LOD) of 36 and 8 cells·mL^{-1}, respectively, along with other good sensing performances, such as selectivity, reproducibility, stability, and acceptable applicability. This sensing strategy clearly demonstrates the four following novelties: (i) the extremely high specific surface area and microporous structure of Cr-MOF [145] allow a large amount of CoPc NPs to be embedded within the pores of the MOF skeleton, thus enhancing electrochemical activity and improving aptamer immobilization; (ii) the pyrolysis-free *in situ* preparation of Cr-MOF@CoPc nanohybrids and non-use of electrochemically active indicator greatly reduce the cost of cytosensor fabrication, shorten the development procedure, and remarkably boost the detection sensitivity; (iii) integrating

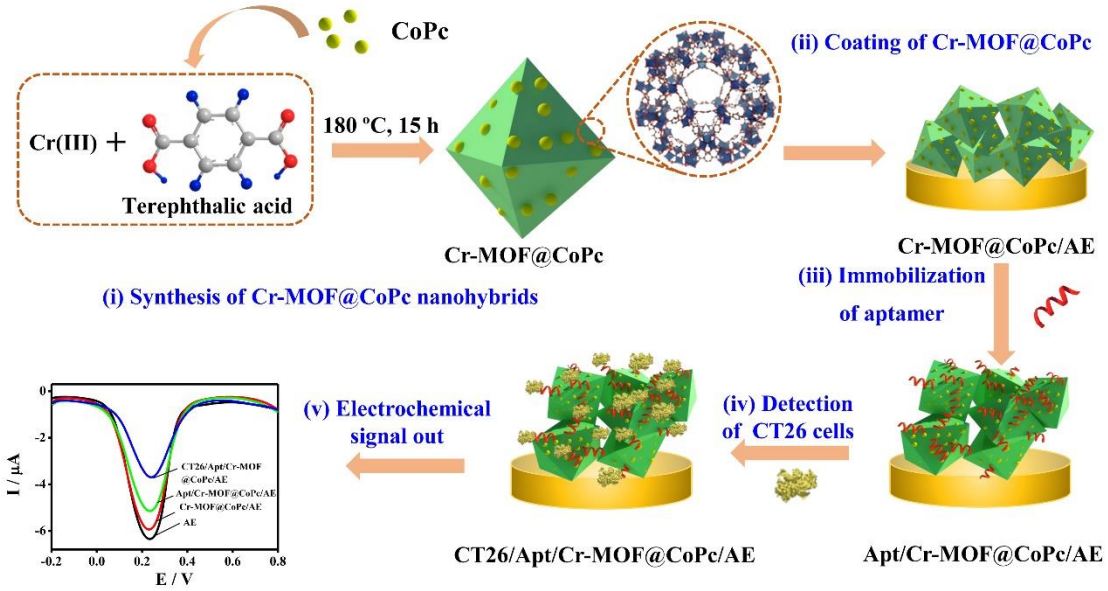

Scheme 18 Schematic diagram of the construction of the electrochemical cytosensor based on the Cr-MOF@CoPc nanohybrid.

electrochemically active CoPc into the Cr-MOF network is a potential strategy for modifying MOF-based nanomaterials and extending the applications of MOFs in the biosensor fields, and (iv) good cells imaging can be achieved by integrating CoPc with strong fluorescence and small size and excellent biocompatibility of Cr-MOF. The

prepared cytosensor can be extensively explored for the detection of other living cancer cells when anchored their corresponding aptamer strands, providing great potential applications in the biosensor and biomedical fields.

8.1 Experimental

8.1.1 Chemicals

Chromium nitrate ($Cr(NO)_3$•$9H_2O$) and 1,4-benzenedicarboxylic acid (H_2BDC) were obtained from Aladdin Biotechnology Co., Ltd. Cobalt(II) phthalocyanine ($C_{32}H_{16}CoN_8$) was from Deen Chemical Reagent Co., Ltd. (Tianjin, China). Colorectal cancer (CT26) and normal L929 cells were purchased from Henan United Limin Biotechnology Co., Ltd. The CT26-targeted aptamer consensus sequence is 5'-GAAGTGAAAATGACAGAACACAACA-3'. KCl, NaCl, KH_2PO_4, Na_2HPO_4, $K_3[Fe(CN)_6]$ and $K_4[Fe(CN)_6]$•H_2O were ordered from Sinopharm Chemical Reagent Co., Ltd. (Beijing, China). All chemicals used were of analytical reagent grade and used without further purification. All solutions were prepared with Milli-Q water (≥18.2 MΩ·cm).

8.1.2 Preparation of solutions

Phosphate buffered solution (PBS, 0.01 M, pH 7.4) was prepared by mixing 0.24 g KH_2PO_4, 1.44 g Na_2HPO_4•$12H_2O$, 0.20 g KCl, and 8.0 g NaCl. And the electrolyte solution for electrochemical measurements was prepared immediately before use by dissolving 1.65 g $K_3[Fe(CN)_6]$, 2.11 g $K_4[Fe(CN)_6]$, 8.0 g and 7.45 g KCl in 1.0 L of PBS. The stock aptamer solution (1 μM) was prepared with 0.01 M PBS (pH 7.4) and diluted to diverse concentrations for electrochemical measurements. The suspension of CT26 cells were also prepared by dispersion CT26 cells in 0.01 M PBS (pH 7.4) and diluted to different concentrations (50, 10^2, 10^3, 10^4, 10^5, 10^6, 5×10^6 and 10^7 cell·mL^{-1}). All solutions were prepared immediately before each experiment and stored at 4°C until use.

8.1.3 Pre-treatment of Au electrode (AE)

The produced same as the chapter 7.1.3.

8.1.4 Characterizations

Powder X-ray diffraction measurements were recorded on a Rigaku D/Max-2500 X-ray diffractometer using Cu Kα as a radiation. X-ray photoelectron spectroscopy (XPS) was performed on a Thermo Fisher ESCALAB 250Xi photoelectron spectrometer equipped with an Al anode (Al-Kα 1486.6 eV). Fourier transform infrared (FT-IR) spectra were recorded from samples in KBr pellets using a Bruker TENSOR27 FTIR instrument within the range of 400−4000 cm^{-1}. Field emission scanning electron microscopy (FE-SEM) was conducted using a JSM-6490LV scanning electron microscope. Transmission electron microscopy (TEM) investigations were performed using a JEOL JSM-6490L V system, respectively. UV-Vis spectra of the samples were recorded with a UV U3900 spectrophotometer (Hitachi Ltd., Japan) in the range of 200-800 nm. Photoluminescence spectra of the samples were obtained using a fluorescence spectrophotometer (F-7000, Hitachi Ltd., Japan) with the excitation wavelength of 360 nm. The specific surface area of the samples was measured by Brunauer-Emmett-Teller (BET) using a Micromeritics ASAP2022 instrument at the temperature of liquid nitrogen. All of the samples were degassed at 573 K for 8 h before measuring. Cellular uptake and intracellular distribution were researched using a confocal laser scanning microscopy (CLSM, LSM710, ZEISS, Germany).

8.1.5 Electrochemical measurements

All electrochemical measurements are same as the chapter 7.1.5.

8.1.6 Cell lines and cell culture

Human normal L929 cells and CT26 cancer cells were obtained from First Affiliated Hospital of Zhengzhou University and grown in Roswell Park Memorial Institute 1640 (RPMI 1640) medium with 10% heat inactivated fetal bovine serum and antibiotics (50 units mL^{-1} penicillin and 50 units mL^{-1} streptomycin). The cells were maintained at 37 °C in 5% CO_2 until use.

8.1.7 MTT assay and in vitro cell uptake

The *in vitro* cytotoxicity of Cr-MOF@CoPc against CT26 cells was evaluated by 3-(4,5-dimethylthiazol-2-yl)-2,5-diphenyltetrazolium bromide (MTT) assay. Prior to treatment with Cr-MOF@CoPc, CT26 cells were seeded in 96-well plates with a density of 8000 cells·well-1 and incubated. After 24 h, the medium was replaced by fresh medium containing the Cr-MOF@CoPc dispersion with different concentrations (0, 20, 50, 80, 100, and 200 g mL^{-1}), and incubated for another 2 h. Subsequently, the medium was discarded, whereas the CT26 cells were washed with PBS for twice. After incubation in medium for 24 h, MTT (5 mg·mL^{-1}, 20 μL) was added, followed by adding the culture of cells and standing for another 4 h. Finally, Dimethyl sulfoxide (150 μL) was added to the plate wells, followed by shaking the plate for 15 min. The absorbance values at 488 nm were measured with a microplate reader.

Since CoPc NPs can endow Cr-MOF@CoPc nanohybrids with excellent fluorescence, it is possible to investigate the *in vitro* cell uptake behaviors of the series of Cr-MOF@CoPc nanohybrids immobilized with aptamer strands against L929 and CT26 cells. L929 and CT26 cells were separately cultured in laser confocal culture dish for 12 h in a humidified atmosphere (5% CO_2, 37 °C) with a medium containing the series of Cr-MOF@CoPc nanohybrids. For comparison, the blank experiments of the cell uptake behaviors of Cr-MOF and CoPc NPs were also carried out. After the media were removed, the cells were softly rinsed with PBS (pH=7.4) twice and fixed with 4% paraformaldehyde solution for 15 min. The nuclei were then stained with Hoechst 33342 (20 μg mL^{-1} in PBS) for 20 min and washed with PBS thrice. Finally, the fluorescence images of cells were observed using a confocal laser scanning microscope (CLSM).

8.1.8 Synthesis and characterization of the ligands and the complexes

8.1.8.1 Synthesis of Cr-MOF

Cr-MOF was synthesized by solvothermal synthesis in according to a reported literature.

8.1.8.2 Synthesis of the series of Cr-MOF@CoPc nanohybrids

In brief, $Cr(NO)_3$•$9H_2O$ (250.1 mg, 0.625 mmol) and H_2BDC (103.8 mg, 0.625 mmol) were thoroughly dissolved in 10 mL of Milli-Q water, followed by ultra-sonicating for 30 min. Afterward, it was transferred into a 25 mL Teflon-lined stainless. Then, the steel autoclave was sealed and heated in an oven at 180 °C for 15 h. After cooling to room temperature, the resultant precipitate was collected by centrifugation and washed with absolute ethanol for 3 times. Finally, the product was dried under vacuum at 60 °C for 12 h. Moreover, the series of Cr-MOF@CoPc nanohybrids were prepared in the similar method with Cr-MOF except adding CoPc NPs with different dosages. According to the dosages of CoPc NPs (10, 20, and 40 mg), the corresponding Cr-MOF@CoPc nanohybrids were denoted as Cr-MOF@CoPc-1(**22**), Cr-MOF@CoPc-2 (**23**), and Cr-MOF@CoPc-3 (**24**), separately.

8.1.8.3 Cytosensor fabrication based on Cr-MOF and the series of Cr-MOF@CoPc nanohybrids

The pristine Cr-MOF (**25**) and the series of Cr-MOF@CoPc nanohybrids were concurrently used to construct cytosensors for determination CT26 cells. Taking the fabrication of the Cr-MOF@CoPc-2-based cytosensor as an example, it is described as below. The Cr-MOF@CoPc-2 powder (1 mg) was added to 1 mL of Milli-Q water and sonicated thoroughly to form a homogeneous suspension with concentration of 1 mg mL^{-1}. For optimizing the dosage of the sensitive layer, the Cr-MOF@CoPc-2 dispersion with different concentrations (0.1, 0.2, 0.5, 1, and 2 mg mL^{-1}) were prepared using the same approach.

Then, 5.0 μL of the Cr-MOF@CoPc-2 dispersion was dropped onto the pre-treated bare AE surface and dried under air atmosphere at room temperature (denoted by Cr-MOF@CoPc-2/AE). Subsequently, the modified AE was separately immersed in the aptamer solution (100 nM) for 4 h at 4 °C, followed by rinsed with phosphate buffer solution (PBS, pH 7.4, 0.01 M) (represented by Apt/Cr-MOF@CoPc-2/AE). Furthermore, to achieve the optimal aptamer concentration for determining CT26 cells,

the Cr-MOF@CoPc-2/AE was also separately incubated with the aptamer solution with different concentrations (10, 20, 50, 100, and 200 nM).

Finally, the Apt/Cr-MOF@CoPc-2/AE was incubated with CT26 cell solution (1000 cell mL^{-1}) at 37 °C for 2 h (denoted by CT26/Apt/Cr-MOF@CoPc-2/AE). Then, the non-specific bound cells were removed by washing the modified electrode with PBS for five times. Similarly, the Cr-MOF-, Cr-MOF@CoPc-1-, and Cr-MOF@CoPc-3-based cytosensors were developed by the same method. Cr-MOF and the series of Cr-MOF@CoPc nanohybrids were used for the determination of CT26 cells in order to obtain the optimal sensitive layer for immobilizing aptamer strands.

8.1.8.4 Electrochemical performances for the Cr-MOF@CoPc-2-based cytosensor towards CT26 cells

EIS and CV measurements were performed on a CHI760E electrochemical workstation equipped with the traditional three-electrode system in 0.01 M PBS (pH 7.4) containing $[Fe(CN)_6]^{3-/4-}$ and KCl. The detailed description for electrochemical measurements were supplied in the **S1.5** part (See the **Supplementary Material**). Three parallel experiments were carried out for each measurement, and error bar represents the standard deviation of the three parallel experiments. Moreover, to obtain excellent sensing performance toward CT26 cells, the experiment conditions were considered to be optimized, including the dosage of Cr-MOF@CoPc (0.1, 0.2, 0.5, 1, and 2 mg mL^{-1}), the concentration of aptamer solution (10, 20, 50, 100, and 200 nM), and the incubation time of the suspension of CT26 cells.

Additionally, the LOD of the proposed Cr-MOF@CoPc-based cytosensor was assessed by measuring electrochemical responses (EIS responses and peak current densities of DPV) of the Apt/Cr-MOF@CoPc/AE when incubating with the CT26 cell suspension with different concentrations (50, 10^2, 10^3, 10^4, 10^5, 10^6, 5×10^6 and 10^7 cell mL^{-1}) under optimal conditions. Thus, the calibration plot was obtained by taking electrochemical responses as the function of the logarithm of the concentration of the CT26 cells suspension. As such, according to the criterion of IUPAC recommendation [146], the LOD for determining CT26 cells was deduced from these calibrations.

Moreover, to assess the specificity of the proposed cytosensor for analyzing CT26 cells, mouse normal cells (L929 cells) were explored as the interferent. For testing the reproducibility of the cytosensor for analyzing CT26 cells, five constructed independently Apt/Cr-MOF@CoPc/AEs were applied to determine CT26 cells with different concentrations (50, 100, and 1000 cells mL^{-1}) by comparing their obtained electrochemical responses. The cytosensor stability was measured by storing the CT26/Apt/Cr-MOF@CoPc/AE which was fabricated with CT26 cells with different concentrations (50, 100, and 1000 cell mL^{-1}) for 15 days at 4 °C and continuously testing by electrochemical technique once per day.

8.1.8.5 Analysis of real samples

For the assessment of the applicability of the proposed cytosensor, human serum samples were obtained from The First Affiliated Hospital of Zhengzhou University after permission and obtaining informed consent of the patient. The study protocol was in accordance with the ethical standards of the 1964 Declaration of Helsinki and its later amendments, and it was approved by the ethics committee of the First Affiliated Hospital of Zhengzhou University. After collection of the whole blood, it was left undisturbed at room temperature for 30 min and centrifuged at 2000 r min^{-1} for 10 min. The resultant supernatant serum was separated and stored at -20 °C. Considering the limited amount of the sample and also the detection range of the cytosensor, the serum sample was diluted 100-folds with PBS solution before use. The diluted human serum was spiked with CT26 cell suspension with different concentrations (50, 100, 1000, 10^4, 10^5, 10^6, 5×10^6 and 10^7 cell mL^{-1}) and recorded by electrochemical measurements. The concentration of CT26 cell suspension was determined by the proposed cytosensor in according to the calibration plot and compared with the real added values.

8.2 Results and discussion

8.2.1. Design of the electrochemical aptasensor for ZEN detection

Since CT26 cells are present in biological tissue of CRC [44], it is essential to sensitively and selectively detect living CT26 cells for the early diagnosis of CRC. In this work,

we have designed and developed a series of nanohybrids of Cr-MOF and CoPc nanoparticles (represented by Cr-MOF@CoPc) and explored them as the platforms for immobilizing the living cell-targeted aptamer strands for detecting living cancer cells (**Scheme 18**). Given intrinsic features of MOFs (large specific surface area and several active sites) and excellent electrochemical activity of CoPc, the Cr-MOF@CoPc-based cytosensor exhibited remarkably high sensing sensitivity for CT26 cells compared with the individual components of Cr-MOF and CoPc. The electrochemical impedance spectroscopy (EIS) and differential pulse voltammetry (DPV) results showed that this cytosensor had extremely low limit of detection (LOD) of 36 and 8 cells·mL^{-1}, respectively, along with other good sensing performances, such as selectivity, reproducibility, stability, and acceptable applicability. This sensing strategy clearly demonstrates the four following novelties: (i) the extremely high specific surface area and microporous structure of Cr-MOF [45] allow a large amount of CoPc NPs to be embedded within the pores of the MOF skeleton, thus enhancing electrochemical activity and improving aptamer immobilization; (ii) the pyrolysis-free *in situ* preparation of Cr-MOF@CoPc nanohybrids and non-use of electrochemically active indicator greatly reduce the cost of cytosensor fabrication, shorten the development procedure, and remarkably boost the detection sensitivity; (iii) integrating electrochemically active CoPc into the Cr-MOF network is a potential strategy for modifying MOF-based nanomaterials and extending the applications of MOFs in the biosensor fields, and (iv) good cells imaging can be achieved by integrating CoPc with strong fluorescence and small size and excellent biocompatibility of Cr-MOF. The prepared cytosensor can be extensively explored for the detection of other living cancer cells when anchored their corresponding aptamer strands, providing great potential applications in the biosensor and biomedical fields.

8.2.2. Characterizations

8.2.2.1 Surface morphologies and nanostructures of Cr-MOF and the Cr-MOF@CoPc nanohybrids

FE-SEM images (**Figure 51a** and 5**1b)** illustrated a multifaceted morphology of Cr-MOF with a uniform size of around 100 nm. As for the Cr-MOF@CoPc nanohybrids (**Figure 51c-51h**), the addition of CoPc NPs changed the Cr-MOF nanostructure into irregular shapes. This finding showed that the existence of CoPc NPs had a negative effect on the crystallinity of Cr-MOF. In particular, the Cr-MOF@CoPc-3 nanohybrid failed to maintain its original shape due to the large dosage of CoPc NPs. Furthermore, the surfaces of the Cr-MOF@CoPc nanohybrids appeared much rougher than that of the pristine Cr-MOF.

The TEM image of Cr-MOF (**Figure 52a**) indicated a typical octahedral morphology accompanied with smooth surface, whereas Cr-MOF displayed the irregular edge (**Figure 52b**). The HR-TEM image (**Figure 52c**) demonstrated a lattice spacing of 0.36 nm, which belonged to the (012) plane of Cr_2O_3 [147].The TEM image of Cr-MOF@CoPc-1 (**Figure 52d**) demonstrated a similar structure with that of Cr-MOF, but showing different particle sizes. As indicated in the HR-TEM image (**Figure 52e**), the appearance of some dark spots suggested that CoPc units [148] were embedded within the Cr-MOF network, which can be proved by the results of Brunauer-Emmett-Teller of all samples. Furthermore, no substantial lattice spacing was observed in the HR-TEM image (**Figure 52f**). The TEM image of Cr-MOF@CoPc-2 clearly demonstrated a uniform particle size (about 82 nm), rough surface and most irregular edge comparing with the other materials (**Figure 52g**). As shown in **Figure 52h,** large amounts of CoPc NPs were loaded in the interior of Cr-MOF. CoPc units and a lattice spacing attributed to Cr_2O_3 were also found in the HR-TEM image (**Figure 52i**). The Cr-MOF@CoPc-3 nanohybrid had the largest size and an irregular shape (**Figure 52j**). However, the Cr-MOF@CoPc-3 nanohybrid exhibited the regular edge, for which large amounts of CoPc

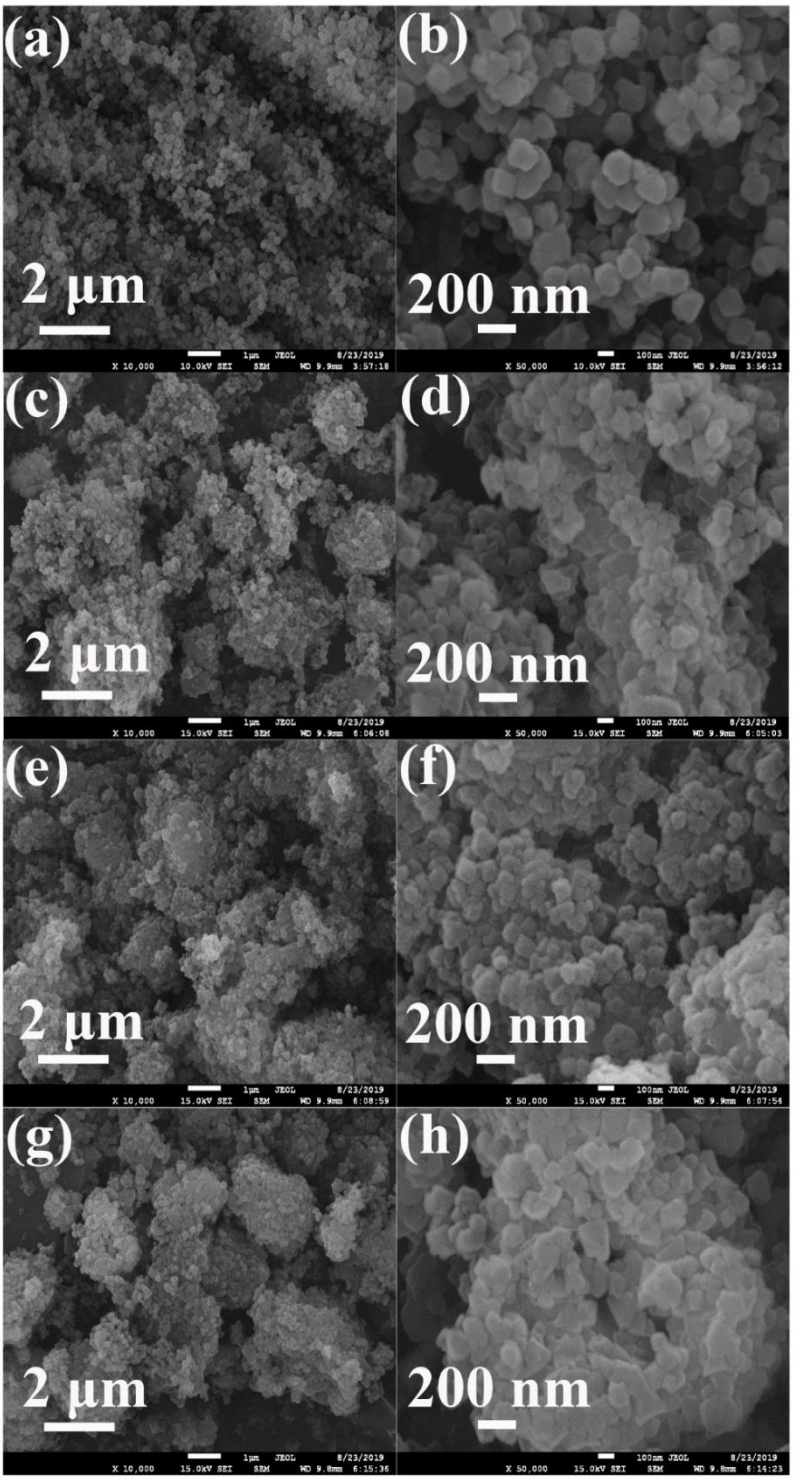

Figure 51. Low- and high-magnification images of (a, b) Cr-MOF, (c, d) Cr-MOF@CoPc-1, (e, f) Cr-MOF@CoPc-2, and (g, h) Cr-MOF@CoPc-3 nanohybrids.

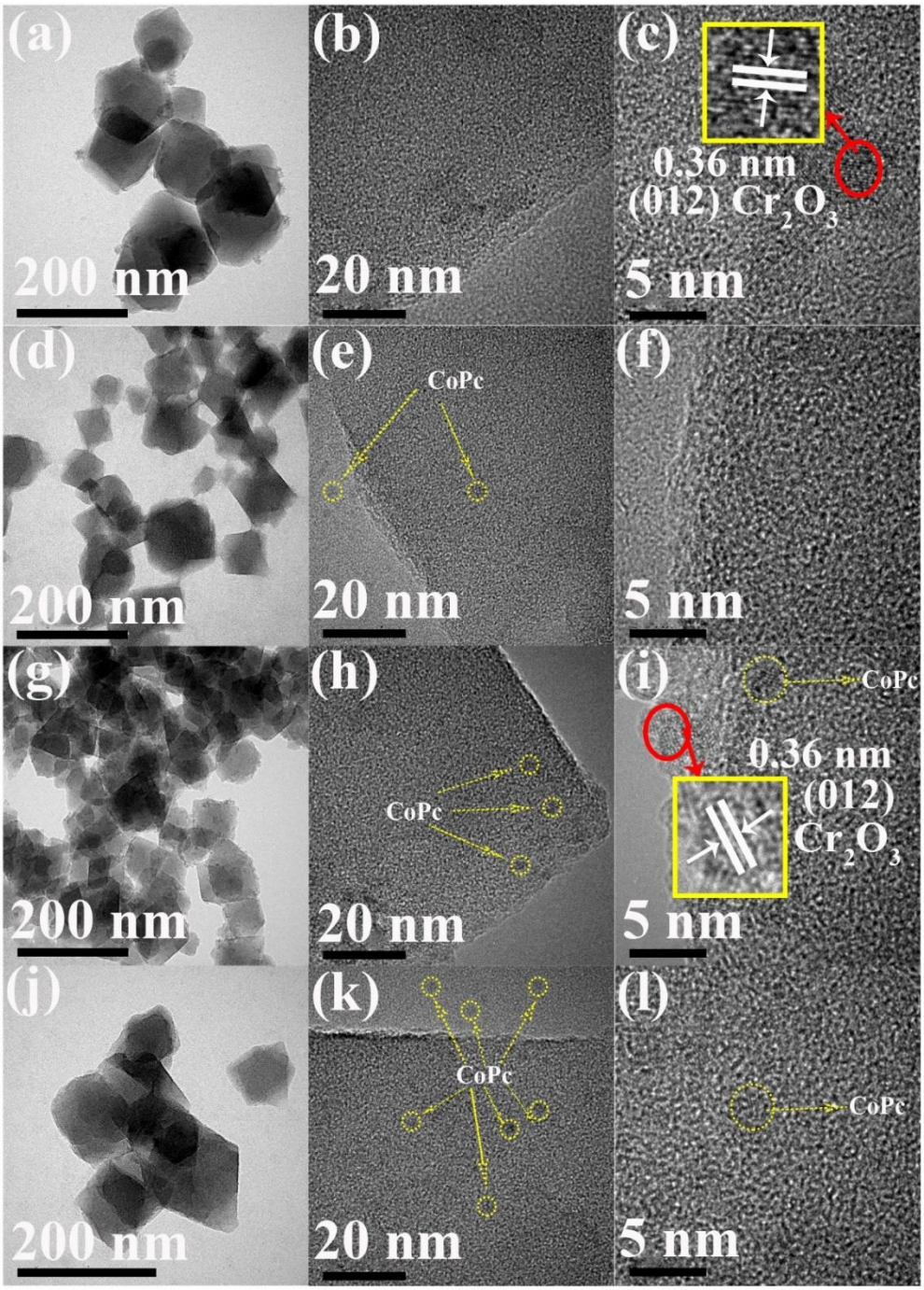

Figure 52 Low-magnification, high-magnification, and high-resolution TEM images of (a, b, c) Cr-MOF, (d, e, f) Cr-MOF@CoPc-1, (f, g, h) Cr-MOF@CoPc-2, and (i, j, k) Cr-MOF@CoPc-3 nanohyhybrids.

NPs were embedded within the nanohybrid network (**Figure 52j**). Moreover, no substantial lattice spacing was observed in the HR-TEM image (**Figure 521**), in which few CoPc nanoparticles appeared. In summary, a suitable amount of CoPc NPs were homogeneously embedded within the skeleton channels of Cr-MOF and induce Cr-

MOF to retain its polyhedron nanostructure and small particle size. The small size and homogeneous distribution of nanoparticles can improve the dispersion degree in the aqueous solution of Cr-MOF, further enhancing its adhesive interaction with the electrode surface.

Further, N_2 adsorption/desorption isotherms of Cr-MOF and the series of Cr-MOF@CoPc nanoparticles were measured. As shown in **Figure 53a,** N_2 sorption isotherms of all the samples exhibited type I isotherm with a hysteresis loop at high relative pressure (p/p_0>0.5). The Brunauer-Emmett-Teller (BET) surface areas and average BJH pore diameters of all four samples are shown in **Table 11**. The BET surface areas of Cr-MOF, Cr-MOF@CoPc-1, Cr-MOF@CoPc-2, and Cr-MOF@CoPc-3 were 4272.73, 4100.72, 3445.09, and 2657.05 m^2 g^{-1}, respectively. This finding suggested that CoPc NPs were embedded within the pore of Cr-MOF and partly occupied the pore volume of Cr-MOF [149]. Further, the Barrett–Joyner–Halenda (BJH) pore size distribution diagrams of all samples showed that the pore size of all samples was around between 2–3 nm. These results hinted that all samples were composed of microporous structures and a small amount of mesoporous structure. The extremely high BET surface areas and large pore size of the nanohybrid can provide more active sites, further greatly boosting the aptamer strand immobilization and improving the sensing performance the corresponding cytosensor.

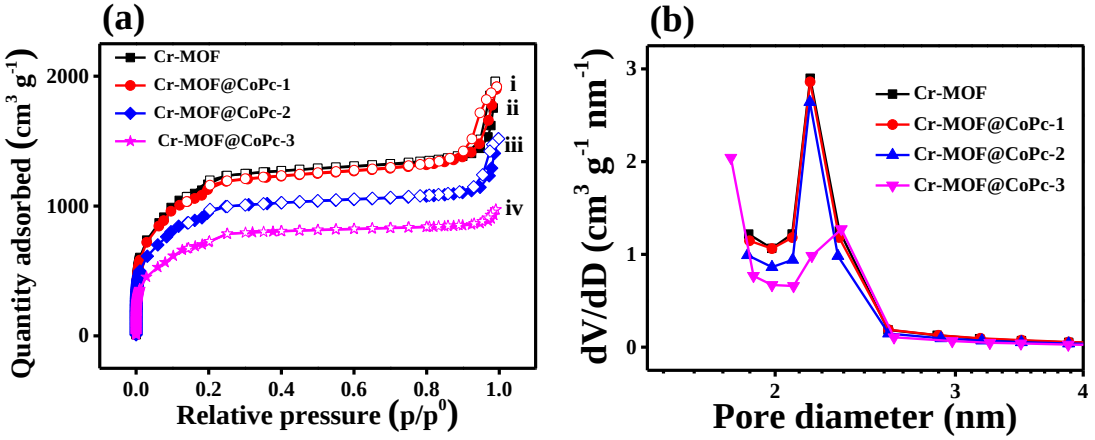

Figure 53 (a) N_2 adsorption/desorption isotherms and (b) pore distribution curves of Cr-MOF and the series of Cr-MOF@CoPc nanohybrids.

Table 11 BET surface area and average pore sizes of Cr-MOF and the series of Cr-MOF@CoPc

Samples	BET surface area (m^2 g^{-1})	average pore size (nm)
Cr-MOF	4272.73	2.84
Cr-MOF@CoPc-1	4100.72	2.89
Cr-MOF@CoPc-2	3445.09	2.68
Cr-MOF@CoPc-3	2657.05	2.25

8.2.2.2 Crystal and chemical structures of Cr-MOF and the series of Cr-MOF@CoPc nanohybrids

The crystal and chemical structures of Cr-MOF and the series of Cr-MOF@CoPc nanohybrids were investigated by powder X-ray diffraction (PXRD) patterns, Fourier transform infrared (FT-IR), Raman spectrum, and X-ray photoelectron spectroscopy (XPS).

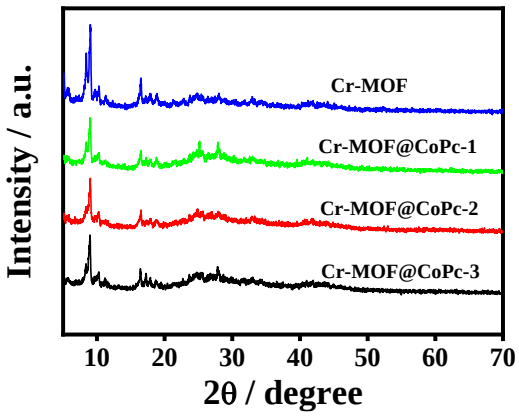

Figure 54 PXRD patterns of Cr-MOF, Cr-MOF@CoPc-1, Cr-MOF@CoPc-2, and Cr-MOF@CoPc-3 composites.

As illustrated in **Figure 54**, the PXRD patterns of Cr-MOF indicated that the peaks and corresponding reflection planes agreed well with the reported standard cubic structure of MIL-101 (Cr-MOF) [150]. The PXRD peak positions of the Cr-MOF@CoPc nanohybrids showed similar diffraction peaks with those of MIL-101 (Cr-MOF). All samples were soaked in 0.01 M PBS (pH = 7.4) for 15 days to estimate the stability of

Cr-MOF and Cr-MOF@CoPc nanohybrids in aqueous solution.

FT-IR analysis was performed to identify the functional groups present in Cr-MOF and their status after integrating CoPc into Cr-MOF. As shown in **Figure 55**, the FT-IR spectrum of Cr-MOF showed a broad band at 3430 cm^{-1}, which corresponded to stretching (ν) vibrations due to the adsorbed water on the surface of the particles. The band at 1400 cm^{-1} was assigned to the symmetric (O–C–O) vibrations of dicarboxylate, whereas that at 1520 cm^{-1} corresponded to the asymmetric stretching (C=O) vibrations of dicarboxylate, thus confirming the presence of the H_2BDC linker within the Cr-MOF [151]. The bands observed between 600 and 1600 cm^{-1} were due to the benzene ring, including the stretching vibrations (C=C) at 1620 cm^{-1}, the bending vibrations (C=C) at 1240 cm^{-1}, and the deformation vibrations (C–H) at 1104, 1018, 890, and 750 cm^{-1}.

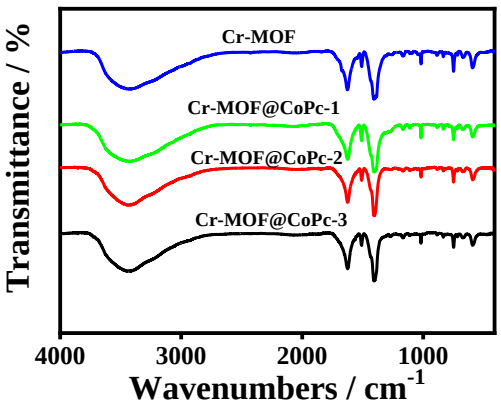

Figure 55 FT-IR spectra of Cr-MOF, Cr-MOF@CoPc-1, Cr-MOF@CoPc-2, and Cr-MOF@CoPc-3 composites.

Figure 56 illustrated the characteristic Raman peaks located at 871, 1146, 1447, and 1615 cm^{-1} [152]. A new band at 1314 cm^{-1} was observed in the Cr-MOF@CoPc nanohybrids due to the breathing modes of sp^2-hybridized carbon [153].

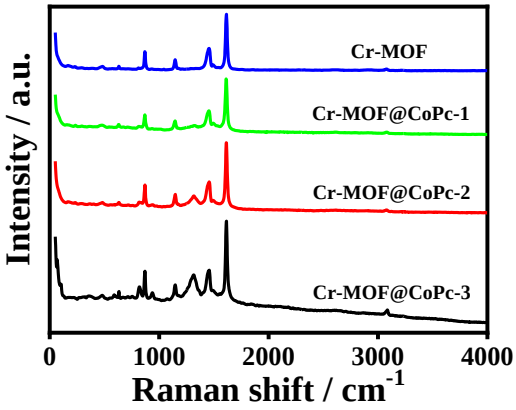

Figure 56 Raman spectra of Cr-MOF, Cr-MOF@CoPc-1, Cr-MOF@CoPc-2, and Cr-MOF@CoPc-3 composites.

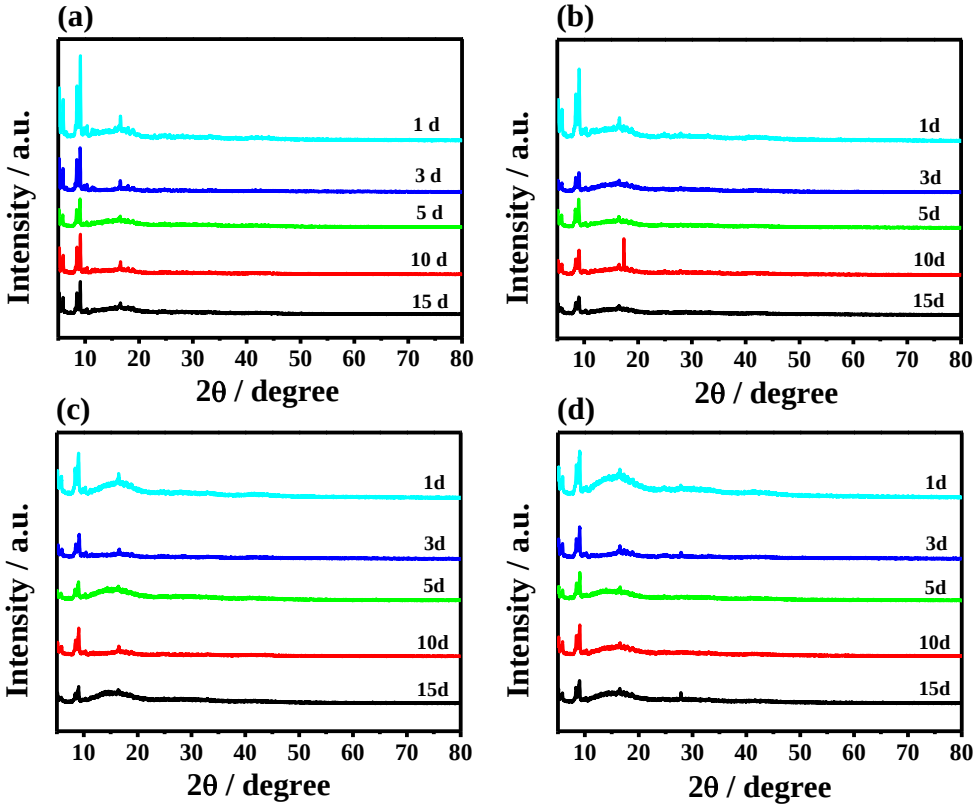

Figure 57 The variations in the PXRD patterns of (a) Cr-MOF, (b) Cr-MOF@CoPc-1, (c) Cr-MOF@CoPc-1, and (d) Cr-MOF@CoPc-1 nanohybrids in 0.01 M PBS (pH = 7.4) for different durations

The results revealed that no clear change was observed among the Fourier transform infrared (FT-IR) and Raman spectra of Cr-MOF and the Cr-MOF@CoPc nanohybrids, suggesting a small dosage of CoPc NPs into the Cr-MOF network. Additionally, PXRD patterns of all samples before and after immersed in 0.01 M PBS

(pH = 7.4) for 15 days revealed good stability in the crystal structure of the series of Cr-MOFs@CoPc nanohybrids (**Figure 57**), thereby ensuring excellent sensing performance of the corresponding electrochemical cytosensors.

All samples were subjected to XPS to probe the change before and after combining CoPc NPs with Cr-MOF. The XPS survey spectra of all samples (**Figure 58**) demonstrated clear signals of C 1*s* (285 eV), N 1*s* (400.1 eV), O 1*s* (531 eV), and Cr 2*p* (578 eV). An additional signal of Co 2*p* (780 eV) was observed in the Cr-MOF@CoPc nanohybrids, demonstrating the successful integration of CoPc and Cr-MOF.

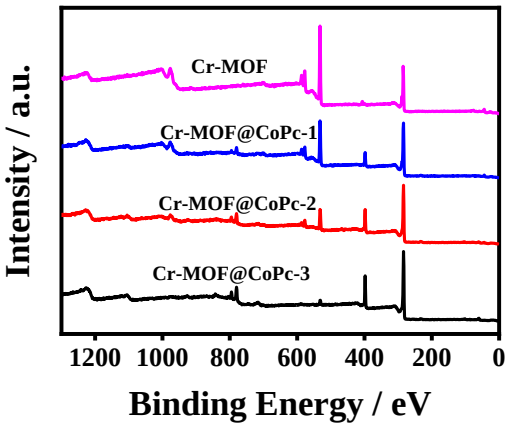

Figure 58 XPS survey scan spectra of Cr-MOF, Cr-MOF@CoPc-1, Cr-MOF@CoPc-2, and Cr-MOF@CoPc-3 composites.

As for XPS characterizations of all samples, an additional signal of Co 2*p* (780 eV) was observed in the Cr-MOF@CoPc nanohybrids, demonstrating the successful integration of CoPc NPs and Cr-MOF. The high-resolution XPS spectra of all elements were analyzed through fitting by using the XPSPEAK1 software to investigate the variation in the chemical valence states of each element in the Cr-MOF@CoPc nanohybrids. Briefly, the deconvoluted XPS peaks of Cr 2*p* XPS for all samples (**Figure 59a1, 59b1**, and**59c1**) hinted its coexisted metal valences of $Cr^{2+}/Cr^{3+}/Cr^{5+}$ [154]. No substantial change appeared in the Cr 2*p* XPS spectra containing the three kinds of Cr-MOF@CoPc nanohybrids, revealing that the doping of CoPc NPs cannot alter the chemical structure of Cr-MOF. As for the C 1*s* XPS spectra (**Figure 59a2, 59b2**, and **59c2**) of all sample, C-C, C-O, and COO groups were obtained, accompanying with the

weak π–π* bond. The apparent Co 2*p* XPS spectra obtained from the Cr-MOF@CoPc nanohybrids (**Figure 59a3, 59b3**, and **59c3**) were composed of Co^{3+}/Co^{2+} species. Multiple metal valence states of $Cr^{3+}/Cr^{4+}/Cr^{5+}$ and Co^{2+}/Co^{3+} coexisted in the developed nanohybrids, which can greatly improve electrochemical activity [155] and modify the sensing performance of aptasensors.

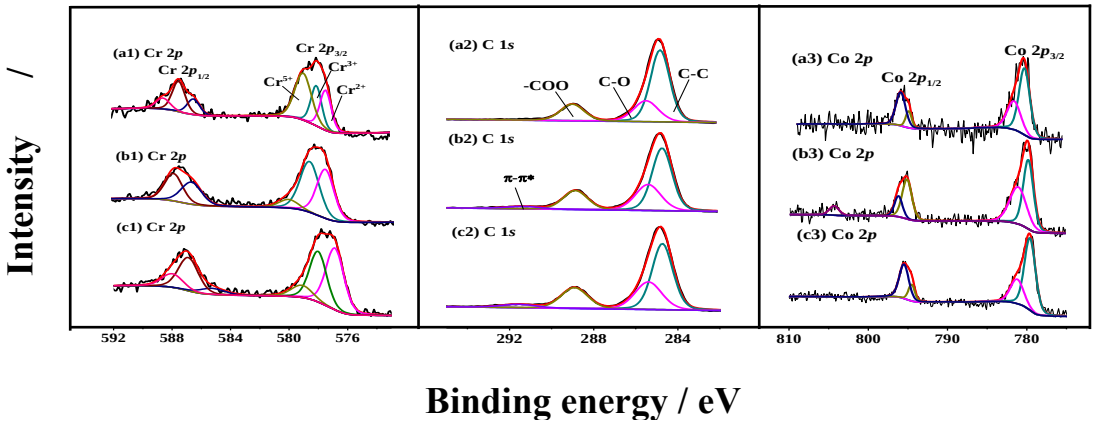

Figure 59 The high-resolution Cr 2*p*, C 1*s*, and Co 2*p* XPS spectra of (a) Cr-MOF@CoPc-1, (b) Cr-MOF@CoPc-2, and (c) Cr-MOF@CoPc-3 nanohybrids.

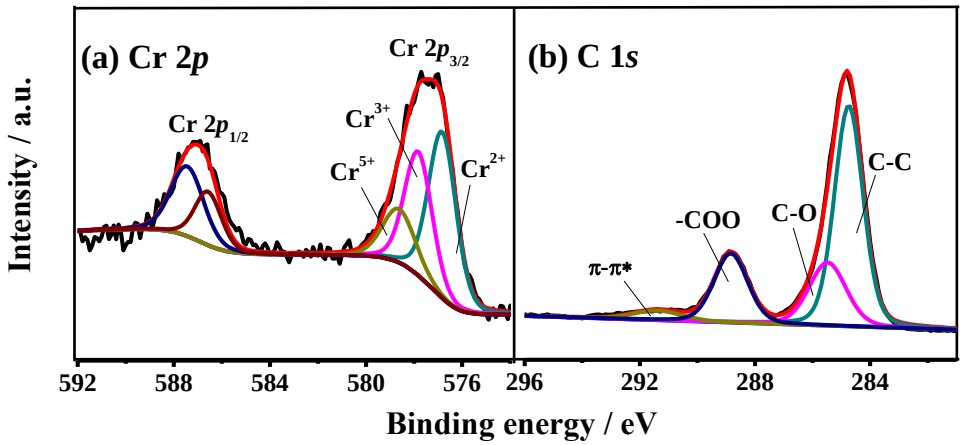

Figure 60 Cr 2*p* and C 1*s* XPS spectra of Cr-MOF.

Similar deconvolutions for the Cr 2*p* and the C 1*s* XPS spectra for Cr-MOF were obtained (**Figure 60**). These results verified that the combination of CoPc and Cr-MOF retained the intrinsic chemical performances of Cr-MOF.

Moreover, the XPS characterization for the Cr-MOF@CoPc nanohybrid immobilized with aptamer was also tested, for which the detailed explanation was

provided in **Figure 61**. Moreover, the Cr-MOF@CoPc immobilized with aptamer strands was subjected to XPS. Given the limited determination capability of XPS [156], the weak Cr 2*p* and Co 2*p* signals (**Figure 61a** and **b**) revealed that the Cr-MOF@CoPc nanohybrid was fully covered by the aptamer strands. The clear C 1*s*, N 1*s*, and O 1*s* XPS signals originated from oligonucleotide strands. As for the C 1*s* XPS spectrum (**Figure 61c**), the appearance of C-N and N-C=O groups were fitted out. The C-N and C=N groups were deconvoluted from the N 1*s* XPS spectrum (**Figure 61d**). These functional groups originated from the base bearing on the aptamer strands. The presence of P 2*p* also confirmed this observation (**Figure 61e**).

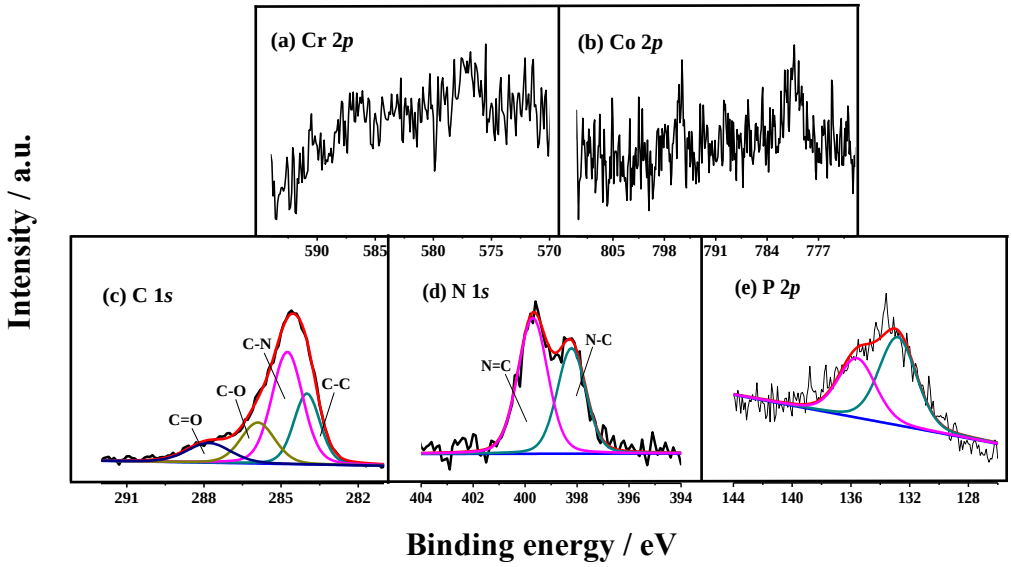

Figure 61 C 1*s*, N 1*s*, and P 2*p* XPS spectra of the Cr-MOF@CoPc-2 immobilized with aptamer strands.

UV–vis spectra and the fluorescence performances of Cr-MOF and the series of Cr-MOF@CoPc nanohybrids were also investigated (**Figure 62**). The analysis of the UV-Vis spectra for the series of Cr-MOF@CoPc nanohybrids verified that CoPc and Cr-MOF interacted in Cr-MOF@CoPc nanohybrids and further affected the π–π* electronic transition in the CoPc fragments. The fluorescence spectra revealed that the pristine Cr-MOF did not display any fluorescence emission. After integrating Cr-MOF with CoPc, the fluorescence spectra of the obtained Cr-MOF@CoPc nanohybrids

showed maximum emission at 520 nm at an excitation wavelength of 355 nm, which was clearly caused by CoPc nanoparticles. The illuminescence intensity of Cr-MOF@CoPc increased with increasing the dosage of CoPc used, showing the maximum emission peak remained at 520 nm.

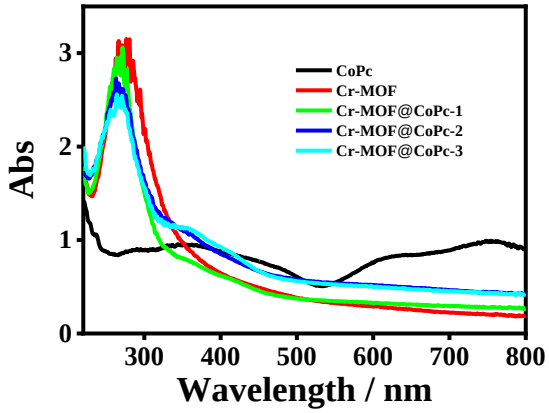

Figure 62 UV of Cr-MOF and the series of Cr-MOF@CoPc nanohybrids.

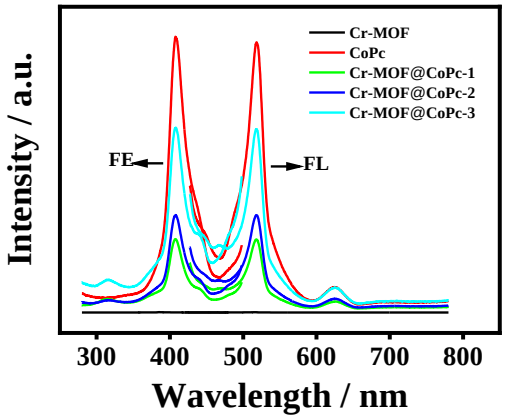

Figure 63 PL of Cr-MOF and the series of Cr-MOF@CoPc nanohybrids.

The fluorescence spectra at an excitation wavelength of 355 nm showed maximum emission at 520 nm for the CoPc (**Figure 63**). No fluorescence emission was observed for Cr-MOF at the excitation wavelength of 355 nm, hinting it does not exhibit fluorescence performance, which is consistent with the previously work [157]. In terms of the series of Cr-MOF@CoPc nanohybrids, the luminescence intensity of Cr-MOF@CoPc also increased along with the increase of the amount of CoPc, showing the maximum emission peak remained at 520 nm.

The hydrodynamic sizes of Cr-MOF, Cr-MOF@CoPc-1, Cr-MOF@CoPc-2, and Cr-MOF@CoPc-3 were 69.6, 113.0, 88.2, and 89.4 nm, respectively (**Figure 64**). The

small size of the series of MOFs ensures that the nanohybrids can be uptaken by cells and detected by the cell imaging.

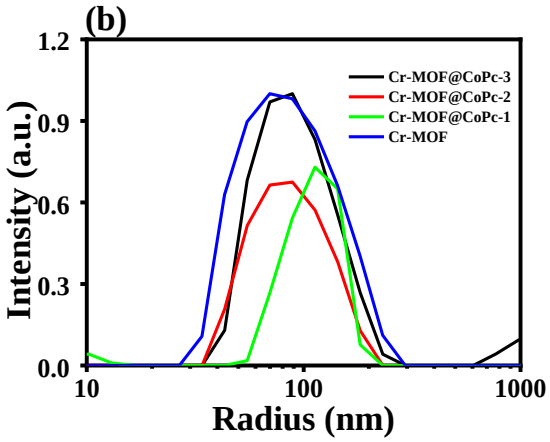

Figure 64 DLS of Cr-MOF and the series of Cr-MOF@CoPc nanohybrids.

8.2.2.3 Cell images of Cr-MOF and the Cr-MOF@CoPc nanohybrids

Probing the biocompatibilities of all samples is vital in prior to the investigation of the cell uptake behavior to ensure that the synthesized Cr-MOF@CoPc nanohybrid can be used as scaffold for anchoring the aptamer to detect CT26 cells. When the dosages of the samples were as high as 200 μg mL^{-1}, the cell viabilities for the Cr-MOF@CoPc nanohybrids were around 59.6%–68.7%, suggesting that most of the cancer cells were alive when attached to the electrode nanomaterials. The cell uptake behavior of Cr-MOF, CoPc, and the Cr-MOF@CoPc nanohybrids immobilized with aptamer strands were observed using (CLSM). The cell uptake behaviors of Apt/CoPc and Apt/Cr-MOF against L929 and CT26 cells are illustrated in **Figure 65a, 65b, 66a,** and **66b**. Because the pristine Cr-MOF does not exhibit the fluorescence performance [157], there is no fluorescence signal for Apt/Cr-MOF against L929 and CT26 cells. When excited by a 400 nm laser, Apt/CoPc was observed with a weak blue fluorescence against L929 cells. Moreover, the Apt/CoPc had stronger blue fluorescence intensity against CT26 cells than against L929 cells. This blue fluorescence originated from CoPc NPs. Owing to the specific recognition of aptamer strands and the nucleolin of cancer cells, the Apt/CoPc NPs were weakly accumulated in cancer cells and directly exhibited the strong fluorescence without using other dyes. By contrast, the Apt/CoPc NPs were not gathered within the cells because no specific recognition occurred between the aptamer

and the L929 cells. This phenomenon resulted in a weak fluorescence signal. Therefore, Apt/Cr-MOF and Apt/CoPc immobilized with aptamer strands can be endocytosed by

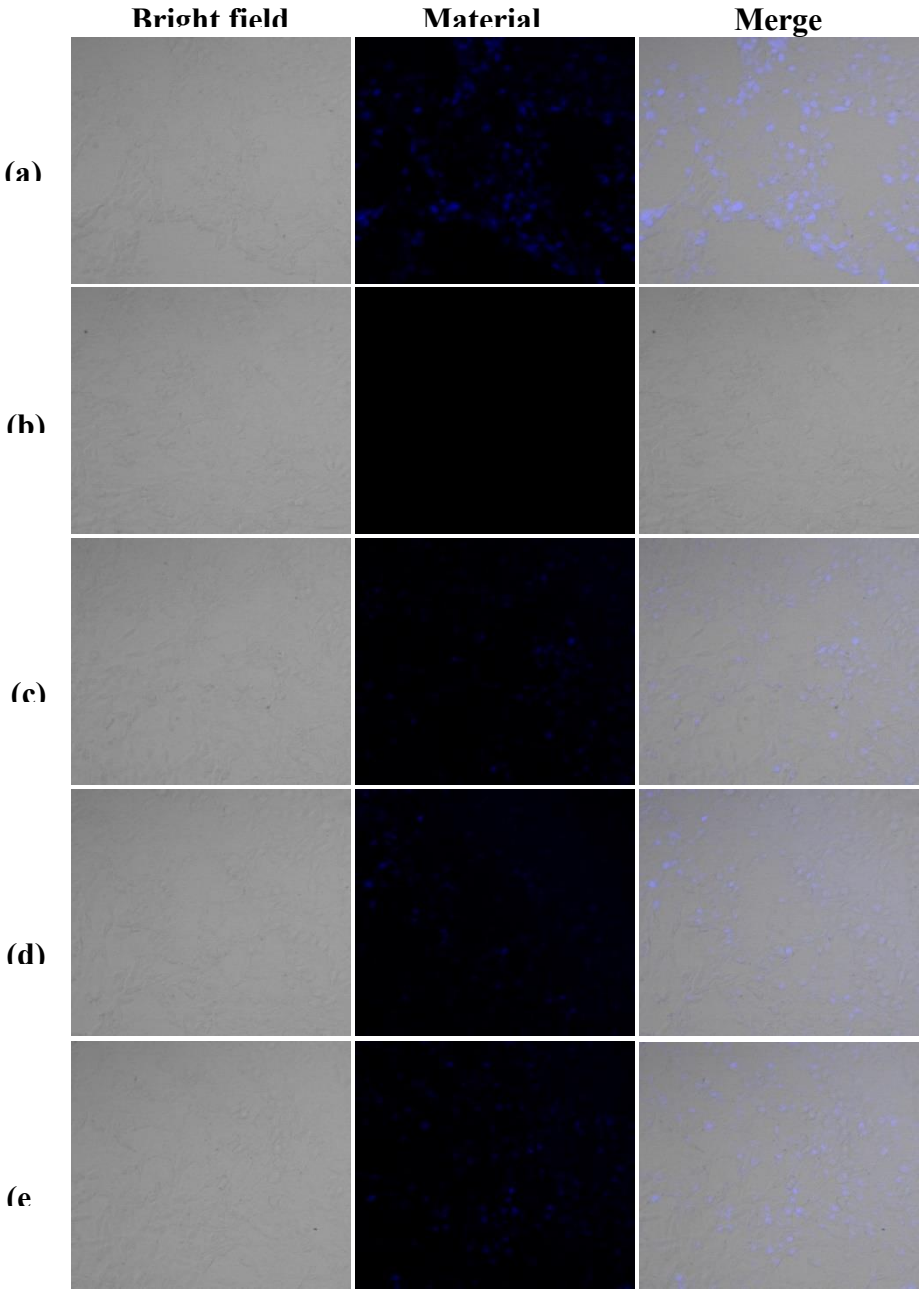

Figure 65 Cell uptake behaviours of (a) CoPc, (b) Cr-MOF, (c) Cr-MOF@CoPc-1, (d) Cr-MOF@CoPc-2 and (e) Cr-MOF@CoPc-3 immobilized with aptamer strands incubated with CT26 cells (1000 cells mL^{-1}) for 2 h. Blue fluorescence: CoPc NPs. The scale bar is 50 μm.

cancer cells. As displayed in **Figs. 65c–65e**, the cell uptake behavior of the Apt/Cr-MOF@CoPc nanohybrids against L929 cells also demonstrated a weak blue fluorescence signal. The relatively strong fluorescence signal was observed for CT26

cells (**Figs. 66c–66e**), which increased with increasing the dosage of CoPc NPs

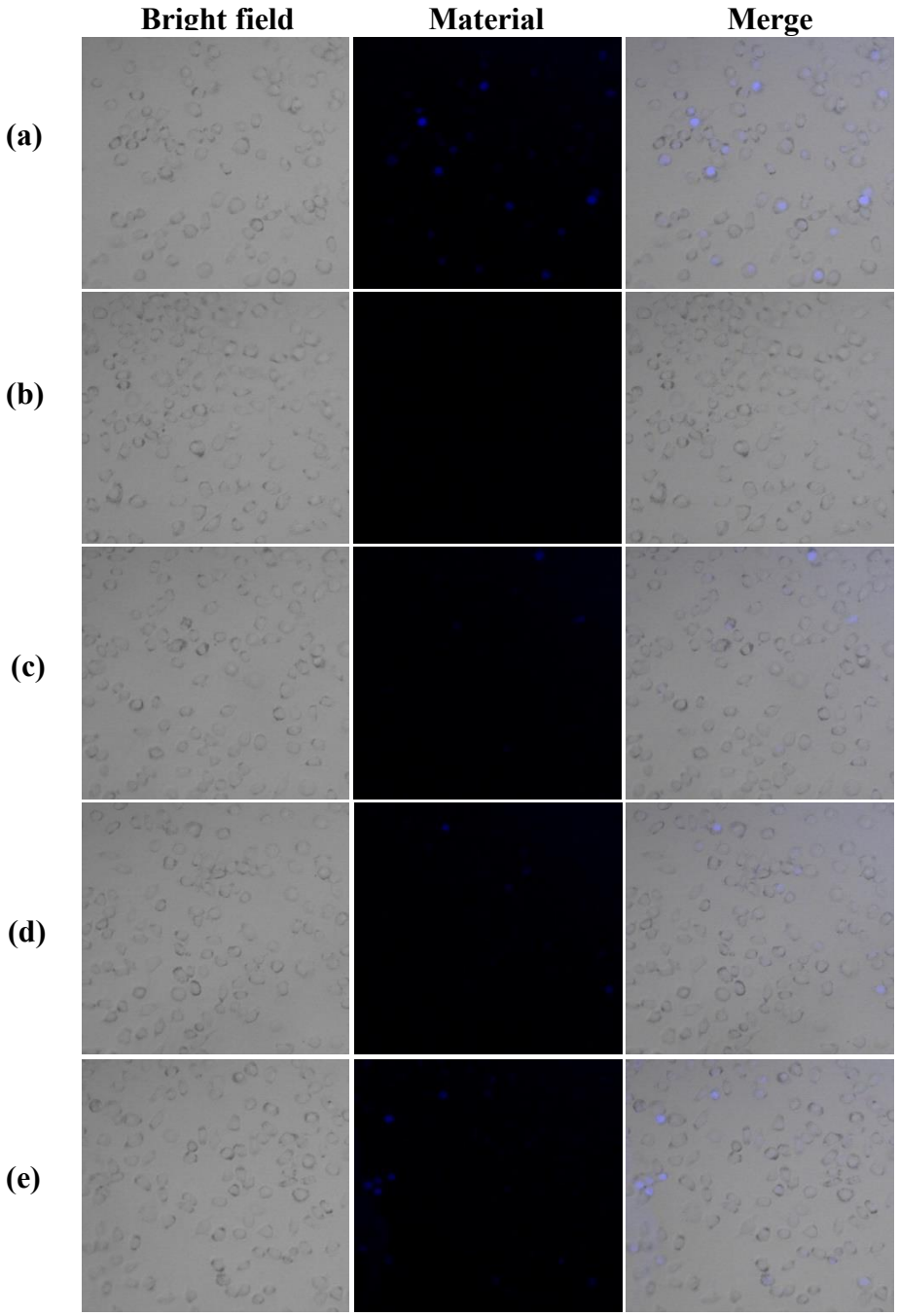

Figure 66 Cell uptake behaviours of (a) CoPc, (b) Cr-MOF, (c) Cr-MOF@CoPc-1, (d) Cr-MOF@CoPc-2 and (e) Cr-MOF@CoPc-3 incubated with L929 cells (1000 cells mL^{-1}) for 2 h. Blue fluorescence: CoPc NPs. The scale bar is 50 μm.

containing in Cr-MOF@CoPc nanohybrids, thereby following the order: Apt/Cr-MOF@CoPc-1 > Apt/Cr-MOF@CoPc-2 > Apt/Cr-MOF@CoPc-3. As compared, the blue fluorescence signal of Apt/CoPc NPs against CT26 cells displayed stronger

fluorescence intensity than those of Apt/Cr-MOF@CoPc. It is mainly due to the relatively weak fluorescence performance of the Cr-MOF@CoPc nanohybrids, which contain low amount of CoPc in comparison with the pure CoPc nanoparticles with the same dosage. Notably, it should be mentioned that no fluorescence quenching occurs between Cr-MOF and CoPc due to the absence of fluorescence performance of Cr-MOF. Therefore, the Apt/Cr-MOF@CoPc NPs were preferred to be endocytosed by cancer cells. These results showed that the proposed Cr-MOF@CoPc NPs can act as a sensitive layer for the electrochemical cytosensor in determining CT26 cells.

8.2.3 Electrochemical sensing performances of Cr-MOF and the Cr-MOF@CoPc nanohybrids toward CT cells

In this work, EIS and CV techniques were employed to study the sensing performances toward CT26 cells by using the Cr-MOF@CoPc- and the Cr-MOF-based cytosensors. As displayed in **Figure 67**, the EIS Nquist curves for developing diverse cytosensors and analyzing CT26 cells showed similar appearances. This result revealed that the semicircles of the EIS spectra became larger and larger along with the order of the AE modification with different Cr-MOFs, aptamer anchoring, and CT26 cell determination (50 cells·mL^{-1}). The R_{ct} values obtained from the equivalent circuit (inset of **Figure 67a**) for diverse cytosensors are summarized in **Table 12**. All the bare AEs showed small R_{ct} values, which were attributed to the excellent electrochemical activity of AEs in aqueous solution [56]. The R_{ct} values of the modified AE increased when modified with Cr-MOF and Cr-MOF@CoPc nanohybrids because of the relatively poorer electrochemical conductivity of these nanomaterials than that of the bare AE, thus leading to slow electron transfer at the electrode/electrolyte interface [129]. The variation in R_{ct} values before and after the AE modification with different Cr-MOF-related nanomaterials ($\Delta R_{ct} = R_{ct,material} - R_{ct,AE}$) represents the real electrochemical

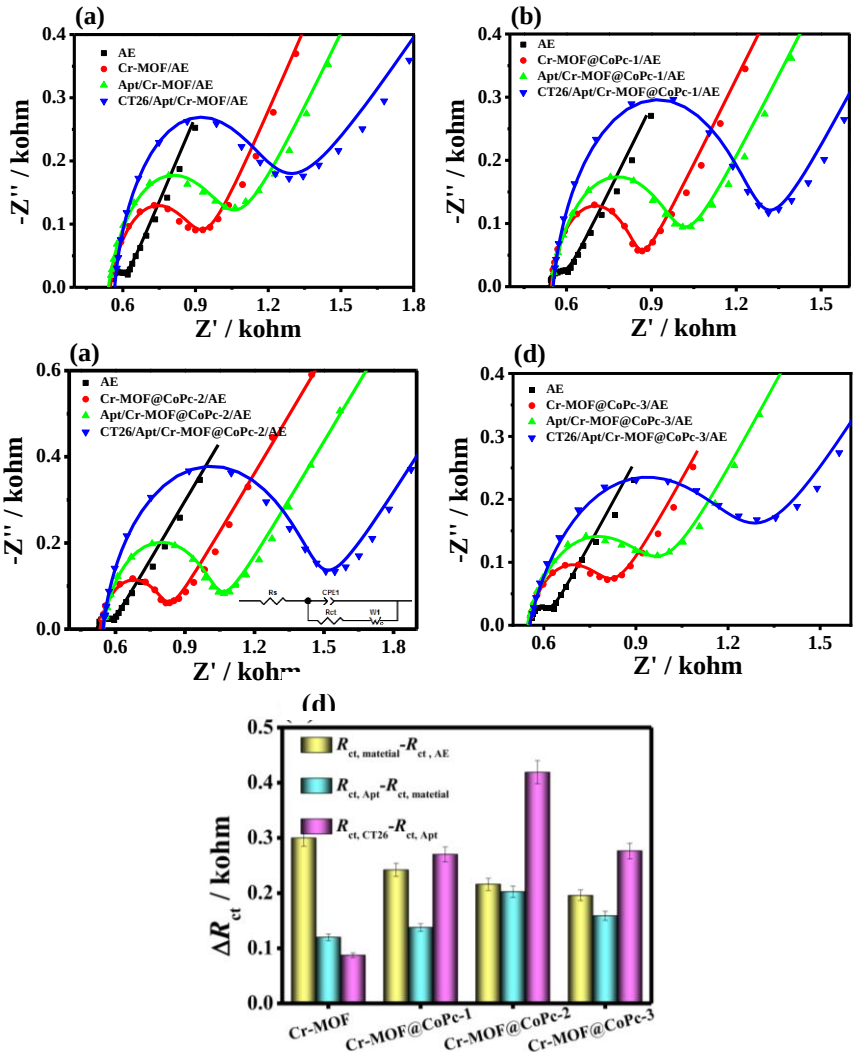

Figure 67 EIS Nquist plots of the procedures of CT26 cell detection using the electrochemical cytosensors based on (a) Cr-MOF, (b) Cr-MOF@CoPC-1, (c) Cr-MOF@CoPC-2 and (c) Cr-MOF@CoPC-3 nanohybrids; (d) Variations in R_{ct} values for each stage in the fabrication procedure of the aptasensors based on Cr-MOF, Cr-MOF@CoPc-1, and Cr-MOF@CoPc-2, and Cr-MOF@CoPc-3 nanohybrids for detecting CT26 cells.

activity of electrodes [158]. The pristine Cr-MOF showed a large R_{ct} value of 355.7 Ω, whereas the Cr-MOF@CoPc electrodes exhibited small R_{ct} values. These results indicated that the integration of CoPc NPs with Cr-MOF can greatly enhanced the electrochemical activity. As the dosage of CoPc NPs increased, the R_{ct} value of the modified electrode decreased from 292.5 Ω to 251.8 Ω. Compared with the other bulk MOF-based electrode materials (**Table 12)** that acted as sensitive layers for the construction of cytosensors, the constructed Cr-MOF@CoPc nanohybrids displayed

small EIS responses, thereby showing their superior electrochemical performances. The R_{ct} values increased after the aptamer strands were immobilized, which was ascribed to the repulsion force between the negative charges of PO_4^{3-} bearing on the aptamer strands and $[Fe(CN)_6]^{3-/4-}$ redox [42]. As illustrated in **Table 13** and **Figure 67d**, the four kinds of electrodes exhibited comparable aptamer anchoring ability. Among these electrodes, the obtained ΔR_{ct} value for the Apt/Cr-MOF@CoPc-2/AE was the largest (202.3 Ω), reflecting its strong adsorption toward aptamer strands. The Cr-MOF@CoPc-2 nanohybrid exhibited uniform NP distribution and small NP size, thereby showing high stability on the electrode surface in aqueous solution. Thus, this nanohybrid can enhance the immobilization ability toward aptamer strands to a certain extent. Subsequently, the R_{ct} values of all electrodes continuously increased when the proposed cytosensors were explored to determine CT26 cells. In the presence of the CT26 cells, the aptamer strands would change their conformation to specifically bond with the nucleolin of cancer cells [159], thus increasing the difficulty of electron transfer at the electrolyte/electrode interface. The electrochemical results demonstrated the highest variation for determining CT26 cells due to the strong anchoring of the aptamer strands of Cr-MOF@CoPc-2/AE, giving a large ΔR_{ct} value (418.9 Ω). The EIS responses of the proposed cytosensors toward CT26 cells were consistent with their CV and DPV curves measured in 0.01 M PBS (pH 7.4) containing $[Fe(CN)_6]^{3-/4-}$ (**Figure 68** and **69**).

Table 12 R_{ct} values of each step during the detection procedures of CT26 using the cytosensors based on different MOFs.

Electrode materials	R_{ct} (Ω)			
	The bare AE	The modified electrode	Immobilization of aptamer	Detection of CT26 cells
Cr-MOF	55.86	355.7	475.6	562.8
Cr-MOF@CoPc-1	50.44	292.5	430	700.2
Cr-MOF@CoPc-2	56.66	272.5	474.8	893.7

Cr-MOF@CoPc-3	55.99	251.8	410.6	687

Table 13 Comparison with the electrochemical activity of other reported MOFs.

Samples	R_{ct}(ohm)	Refs.
PPy/Cu-MOF	345.3	[160]
MnFe-PBA	407.3	[161]
Zr-MOF	523	[162]
NiCo-PBA	370	[163]
ZnNi-MOF	370.8	[164]
Cr-MOF@CoPc-2	272	This work

The CV results verified that similar electrochemical behavior was achieved for all cytosensors when determining CT26 cells (**Figure 68**). Any change in the electrode, including the modification of different Cr-MOFs, aptamer adsorption, and CT26 cell determination, continuously hampered electron transfer, resulting in decreased peak current densities of the CV curves. Among these cytosensors, the Cr-MOF@CoPc-2-based cytosensor illustrated the most substantial variation in the peak current densities for determining CT26 cells. As indicated in **Figure 69**, the DPV curves of the four kinds of cytosensors for analyzing CT26 cells demonstrated a similar appearance. The peak current densities of the electrode also continuously decreased with the order of the electrode modification, aptamer anchoring, and CT26 cell determination. The variation in the peak current density of the Cr-MOF@CoPc-2/AE for determining CT26 cells was the largest among the four kinds of cytosensors. Therefore, the Cr-MOF@CoPc-2 nanohybrid was chosen as the sensitive layer for further analysis of CT26 cells.

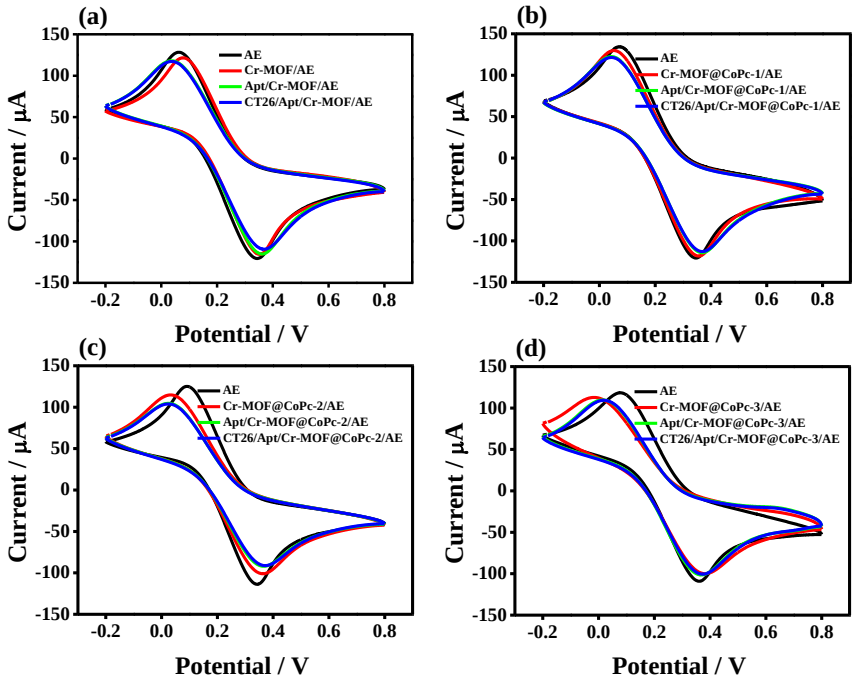

Figure 68 CV curves of the procedures of CT26 cell detection using the electrochemical cytosensors based on (a) Cr-MOF, (b) Cr-MOF@CoPc-1, and (c) Cr-MOF@CoPc-2, and (d) Cr-MOF@CoPc-3 nanohybrids in 0.01 M PBS (pH 7.4) containing 5 mM $[Fe(CN)_6]^{3-/4-}$.

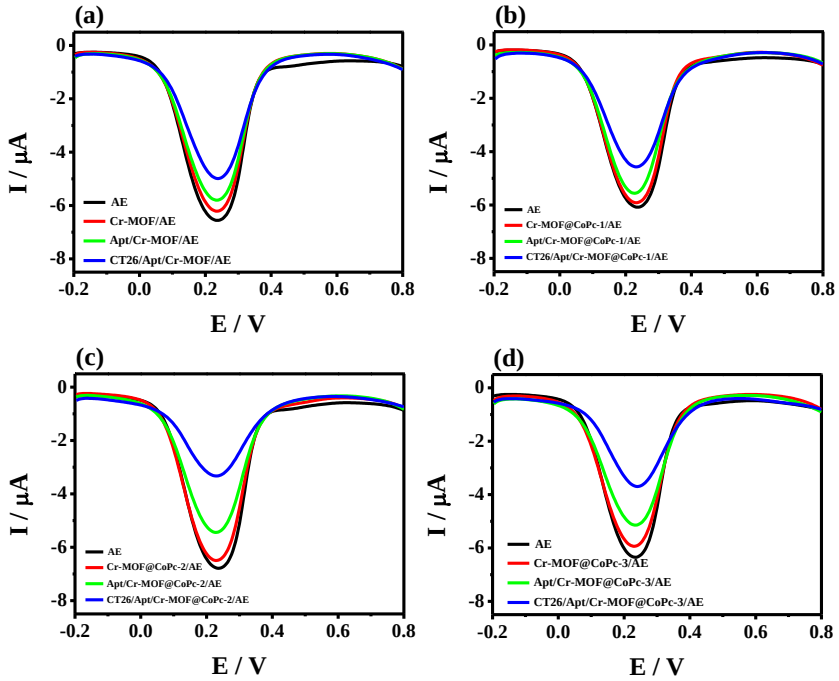

Figure 69 DPV curves of the procedures of CT26 cell detection using the electrochemical cytosensors based on (a) Cr-MOF, (b) Cr-MOF@CoPC-1, and (c) Cr-MOF@CoPc-2, and (d) Cr-MOF@CoPc-3 nanohybrids in 0.01 M PBS (pH 7.4) containing 5 mM $[Fe(CN)_6]^{3-/4-}$.

8.2.4 Quantitative analysis of CT26 cells

The proposed cytosensor was incubated with different concentrations of CT26 cell suspensions and recorded using EIS and DPV techniques, as displayed in **Figure 70** and **71**, respectively. **Figure 70a** showed that the EIS responses increased with the increase in the concentration of the CT26 cell suspension. The obtained ΔR_{ct} values also remarkably increased within the concentration of the CT26 cell suspension ranging from 50 cells·mL^{-1} to 10^7 cells·mL^{-1}. The signal approached a platform and remained consistent when the concentration was larger than 10^7 cells·mL^{-1}. At the very beginning, CT26 cells were rapidly recognized by aptamer strands, leading to their conformation change and increment in the EIS response (**Figure 70b**). Along with the ongoing recognition, more active sites of aptamer strands were occupied by living CT26 cells. Thus, the binding between aptamer strands and CT26 cells reached equilibrium, resulting in a slight change in EIS responses. Taking the ΔR_{ct} value as the function of the logarithm of the concentration of CT26 cell suspension, a linear relationship was found within the range of 50–1.0×10^7 cells·mL^{-1} (inset of **Figure 70b**). After the simulation, the regression equation is: ΔR_{ct} (kΩ) = 0.23logCon_{CT26} – 0.2, with a correlation coefficient (R^2) of 0.9868 and extremely low LOD of 31 cells·mL^{-1}. A wide detection range was also obtained based on 3σ/slope calculation.

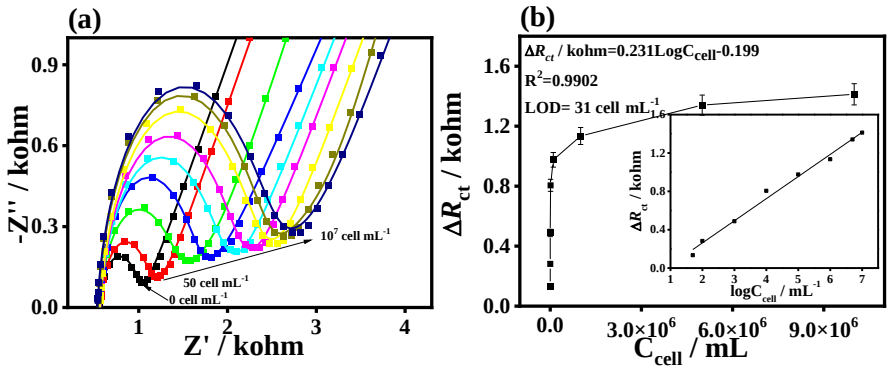

Figure 70. (a) EIS Nyquist plots using the Cr-MOF@CoPc-2-based aptasensor; (b) the calibration curves between ΔR_{ct} and the concentration of CT26 cell (inset: the linear fit plot of ΔR_{ct} as function of the logarithm of the concentration of the CT26 cell suspension, the error bars are standard deviations for n = 3);

Meanwhile, DPV technique was applied to investigate the sensitivity of the cytosensor in detecting CT26 cells. As demonstrated in **Figure 71**, the peak current

densities decreased with the increase in the concentration of the CT26 cell suspension, indicating the continuous interception of electron transfer at the interface along with more CT26 cells. A similar appearance was observed as the variations in peak current density (ΔI) dramatically increased with the increase in the concentration of the CT26 cell suspension (**Figure 71b**). A good linear relationship was also achieved between the ΔI values and logarithm of the concentration of the CT26 cell suspension (inset of **Figure 71b**), with a regression equation of ΔI (μA) = 0.81logCon_{CT26} − 0.94 and R^2 of 0.9868. Thus, an extremely low LOD of 8 cells·mL^{-1} was calculated, which was slightly lower than that obtained from the EIS technique. As compared with other cytosensors for detecting living cancer cells, the detection limit of the Cr-MOF@CoPC-2-based cytosensor is lower (**Table 14**). The outstanding sensing performance of the Cr-MOF@CoPc-2-based cytosensor can be attributed to the following intrinsic features of the Cr-MOF@CoPc nanohybrid: (i) the extremely large specific surface area and microporous structure of Cr-MOF [145] allow large amounts of CoPc NPs to stably embed within the pore channels of Cr-MOF, thus resulting in good electrochemical activity,

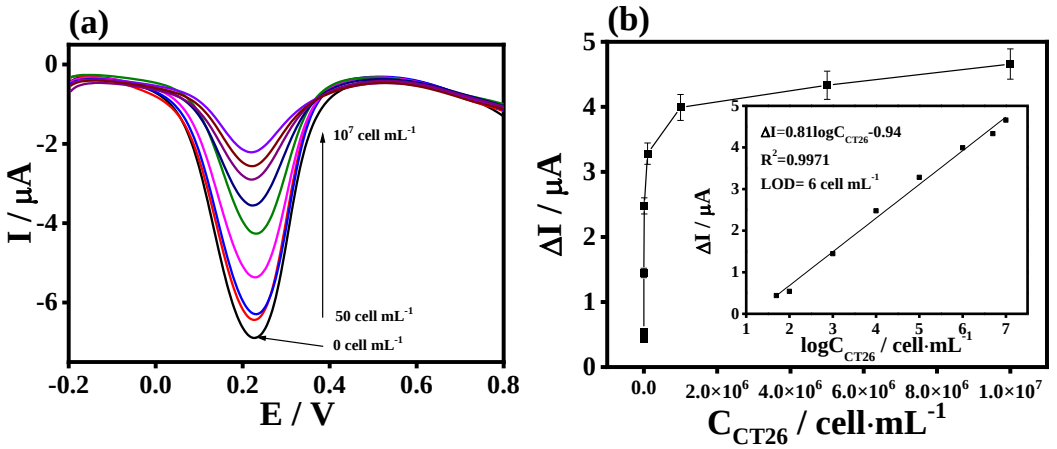

Figure 71. (a) DPV Nyquist plots using the Cr-MOF@CoPc-2-based aptasensor; (b) the calibration curves between ΔI_p and the concentration of CT26 cell (inset: the linear fit plot of ΔI_p as function of the logarithm of the concentration of the CT26 cell suspension, the error bars are standard deviations for n = 3);

high thermostability, and improved detection sensitivity of the proposed cytosensor. (ii) The strong interaction between CoPc can remarkably boost the DNA aptamer

immobilization [165] and stabilize the formed aptamer–cell complex. (iii) The excellent biocompatibility of the Cr-MOF carrier helps in anchoring the aptamer strands and detecting the living cancer cells [166]. The synergistic effect among these factors enhanced the sensing performance of Cr-MOF.

Table 14 Comparison with other reported techniques for CT26 cell detection.

Type of cells	Materials	Detection method	Detection range (cell·mL^{-1})	LOD (cell·mL^{-1})	Refs.
CT26	Au nanoparticles	EIS	$10 – 1.0\times10^5$ and $1.0\times10^5 – 6\times10^6$	2	[167]
CT26	Graphene-peptide-based	Fluorescent	$10 – 1.2\times10^5$	1000	[168]
MCF-7	NiO nanoparticles	Surface plasmon resonance (SPR)	$5.0\times10^2 – 4.0\times10^3$	136	[169]
A549	Silane self-assembled monolayer (SAM)	CV and DPV	$1.0 \times 10^3 – 1.0 \times 10^7$	1000	[170]
CTCs	Porous anodic alumina (PAA)	Linear sweep voltammetry (LSV)	$1.0\times10^2 – 1.0\times10^6$	100	[171]
Ramos	AuNP probe	Chemiluminescence	$0 – 2.0\times10^3$	163	[172]
MDA-MB-231	Carbon dots and AuNPs	FRET immunosensing	$1.0\times10^3 – 4.0\times10^4$	300	[173]
CT26	**Cr-MOF@CoPc-2**	**EIS** **DPV**	**$50 - 10^7$** **$50 - 10^7$**	**31** **6**	**This work**

8.2.5 Selectivity, reproducibility, and stability of the proposed cytosensor

The proposed cytosensor was incubated in human normal L929 cells (1000 cells·mL^{-1}) and tested using EIS and CV to determine its selectivity (**Figure 72**). **Figure 72a** showed the EIS Nquist plots of the Cr-MOF@CoPc-2-based cytosensor for determining L929 cells. No substantial change in the EIS signals was found before and after the determination of CT26 cells. A similar result was obtained from the CV curves for determining L929 cells using the Cr-MOF@CoPc-2-based cytosensor (**Figure 72b**). This finding revealed that no substantial recognition occurred between the aptamer and the L929 cells, thus verifying the high selectivity of the proposed cytosensor.

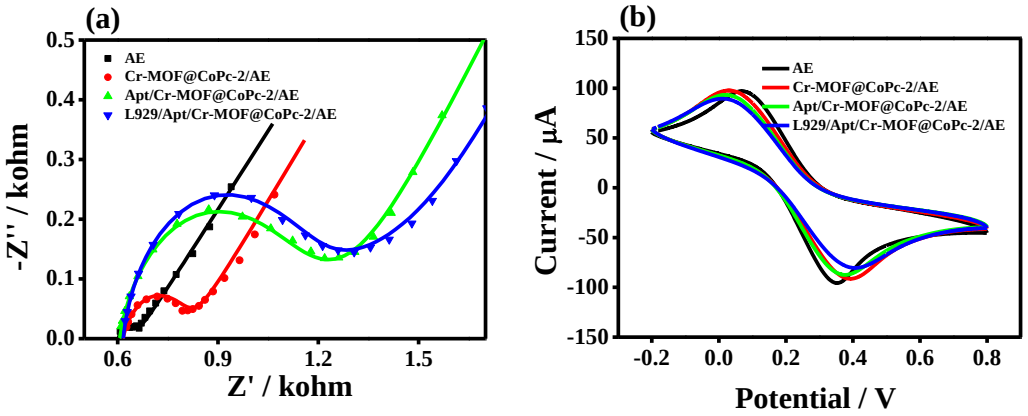

Figure 72 (a) EIS Nquist plots and (b) CVs curve of the procedure of L929 cell detection using the electrochemical cytosensors based on Cr-MOF@CoPc-2 nanohybrids in 0.01 M PBS (pH 7.4) containing 5 mM $[Fe(CN)_6]^{3-/4-}$.

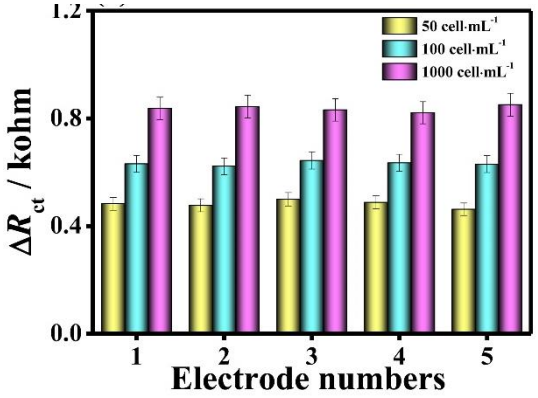

Figure 73. Reproducibility of the proposed aptasensor for detecting CT26 cells (n = 3).

The reproducibility of the proposed cytosensor was probed using five electrodes, which were prepared for the individual detection of CT26 cells by EIS. As indicated in **Figure 73**, the obtained EIS responses demonstrated comparable ΔR_{ct} values and low relative standard deviations (RSD) of 2.86%, 1.24%, and 1.36% for determining CT26 cells at concentrations of 50, 100, and 1000 cells·mL^{-1}, respectively.

The stability of the cytosensor was studied when detecting CT26 cells with the concentrations of 50, 100, and 1000 cells·mL^{-1} once every day for 15 days (**Figure 74**). The results indicated that more than 109.9%, 106.2%, and 104.3% of the initial response ($n = 5$, RSD = 3.54%, 1.98%, and 1.45%, respectively) remained constant after storage at 4 °C. These findings suggested that the Cr-MOF@CoPc-2-based cytosensor had high selectivity, good reproducibility, and excellent stability, thus providing considerable applicability in clinical diagnosis.

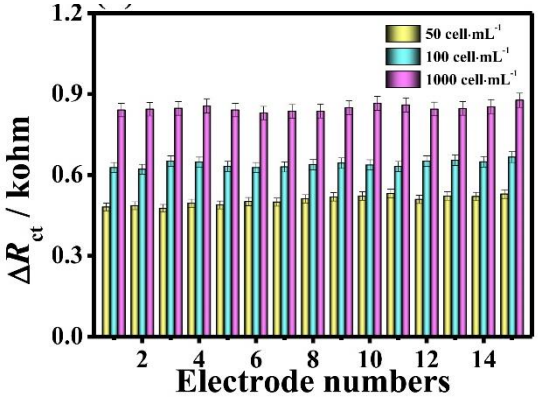

Figure 74. Stability of the proposed aptasensor for detecting CT26 cells ($n = 3$).

8.2.6 Real samples

The reliability and feasibility of the proposed cytosensor in real serum were also investigated by adding various concentrations of the CT26 cell suspension to pretreated human serum, measured using EIS, and analyzed on the basis of the calibration plot. All recoveries listed in **Table 15** confirmed that the Cr-MOF@CoPc-2-based cytosensor can achieve good performances for CT26 cell detection in human serum samples with RSD of 1.29%–4.53%. Therefore, the proposed strategy and the developed cytosensor showed high accuracy for practical applications.

Table 15 Determination of CT26 cells in human serum sample using the developed electrochemical

Cr-MOF@CoPc-2-based cytosensor.

Added amounts (cells·mL^{-1})	**Found amounts (cells·mL^{-1})**	**Apparent recovery (%)**	**RSD (%)**
50	52	104	2.21
100	110	110	1.32
1000	1130	113	4.11
10^4	10745	107.5	4.10
10^5	105320	105.3	4.53
10^6	1022172	102.2	1.29
5×10^6	516500	103.3	2.18
10^7	1052000	105.2	3.41

8.3 Conclusions

In summary, a novel electrochemical cytosensor based on the Cr-MOF@CoPc nanohybrids was constructed for the detection of living CT26 cells. Owing to the large specific surface area and big pore size of the Cr-MOF skeleton, large amounts of CoPc NPs were embedded within the Cr-MOF network via in situ hydrothermal method. The presence of CoPc NPs in the nanohybrid greatly enhanced the fluorescence intensity, electrochemical activity, thermostability, and biocompatibility, as well as the immobilization ability toward the aptamer strands compared with the individual component. As compared, the Cr-MOF@CoPc nanohybrid with the dosage of CoPc NPs of 20 mg exhibited homogenous nanoparticle distribution and small nanoparticle size, thus providing the superior sensing performance. The constructed Cr-MOF@CoPc-2-based cytosensor exhibited superior sensing performance for detecting CT26 cells; extremely low LOD values of 36 and 8 cells·mL^{-1} were obtained using EIS and DPV, respectively, within a wide linear concentration range of the CT26 cell

suspension from 50 cells mL^{-1} to 1×10^7 cells mL^{-1}; high selectivity; good stability; and acceptable reproducibility. It also had an outstanding applicability for the detection of CT26 cells from the human serum samples. This work has a considerable potential for the early diagnosis of living cancer cells and other cancer biomarkers.

Chapter 9. Preparation of CuPc-bTDC-COF-based agents for Photodynamic Therapy and Photothermal Therapy (PTT) against breast cancer

Photodynamic therapy (PDT) and photothermal therapy (PTT) have the advantages of less invasiveness, less side effects, less damage to surrounding tissues, and ability to overcome drug resistance, resuliting widely used in basic research and preclinical applications of tumor treatment. The PDT and PTT synergistic therapy is necessary due to each individual therapy cannot completely cure the cancer. In general, photosensitizers with both PDT and PTT effects are generally complexes of multiple components. Therefore, the preparation of a simple-component photosensitizer with PDT and PTT effects under a single NIR laser irradiation has more potential in tumor phototherapy. Two-dimensional covalent organic framework (COFs) materials are emerging crystalline materials with the ability to control the ordered spatial arrangement of building units for precise assembly. In recent years, it has been reported that COFs is used to achieve drug release, in vitro drug loading, and in vivo drug delivery. Therefore, COF materials are very promising candidates for the construction of ordered spatially arranged photoactive agents in the combined PDT and PTT for tumors therapy. Unfortunately, most synthetic COFs materials are too bulky to be used in vivo, so size issues need to be addressed if COFs materials are to be used as photosensitizers. Herein, a nanoscale Cu-phthalocyanine-containing COFs (CuPc-bTDC-COF) were synthesized and then evaluated the performance of the CuPc-bTDC-COF for cancer treatment by PDT and PTT under NIR (808 nm) irradiation. The resulting nanoparticles have a high photothermal conversion efficiency of 57% and a good photodynamic effect. For the first time, in vitro and in vivo tests revealed that

CuPc-bTDC-COF s with combined PDT and PTT had improved antitumor efficacy.

9.1 Experimental

9.1.1 Chemical and materials

4-Nitrophthalonitrile, 2,2′-bithiophenyl-5,5′-dicarbaldehyde (bTDC) $CuCl_2$, polyethylene glycol (PEG-NH_2), triphenylphosphine, and 1,3-diphenylisobenzofuran (DPBF) were purchased from Shanghai Aladdin Biotechnology Co., Ltd. Dimethyformamide (DMF), anhydrous methanol, dimethyl sulfoxide (DMSO) were obtained from Tianjin Fuyu Fine Chemical Co., Ltd. Methylene blue and triethanolamine were from Tianjin Fengchuan Chemical Reagent Co., Ltd. 3-(4,5)-dimethylthiahiazo(-z-y1)-2,5-di-phenytetrazoliumromide (MTT) assay, AS1411 aptamer with the sequence of 5′-GGTGGTGGTGGTTGTGGTGGTGGTGG-3′, 2′,7′-dichlorofluorescein diacetate (DCFH-DA) reactive oxygen fluorescent probe, Hoechst 33342 solution, calcein-AM/PI Double Staining Kit, Dulbecco's modified Eagle's medium (DMEM) and phosphate buffered saline (PBS) were gained from Beijing Soleibao Technology Co., Ltd. In addition, all solutions were prepared with Milli-Q water (18.2 MΩ cm). All reagents were of analytical grade and used without further purification.

9.1.2 Synthesis of CuPc-bTDC-COF

Herein, the used CuPc-bTDC-COF was synthesized according to the previous work [174], but with slight modification. Briefly, CuPc-TA (0.05 mmol) and bTDC (0.1 mmol) were dispersed in 8 mL of DMSO and 0.2 mL aqueous acetic acid (6.0 M), following by sonicating until forming the homogenous dispersion. After degassed using three freeze-pump-thaw cycles, the mixture was heated to 120 °C and reacted for 3 days. Subsequently, atrovirens precipitate was produced, following by filtrating, and washing with DMF and DMSO for three times. Then, the powder was dried in vacuum (80 °C) for 24 h. As such, the resulting was named as CuPc-bTDC-COF.

9.1.3 Preparation of CuPc-bTDC-COF@PEG and CuPc-bTDC-COF@PEG@AS1411

The preparation of CuPc-bTDC-COF@PEG was referred to the reported literature [175]. Typically, PEG-NH_2 (M_w = 3000) (30 mg) and CuPc-bTDC-COF (15 mg) was dispersed in 50 mL of DMSO. After that, 1 mL of aqueous acetic acid (6 M) was added under stirring. The reaction mixture was continuously stirred at room temperature for 24 h. Finally, the product was collected by filtration and washed with water and ethanol couples of times, separately. The resultant was dried at room temperature.

According to the reference [176], CuPc-bTDC-COF@PEG was incubated with the aptamer AS1411 solution (1 mL, 3 M) at 4 °C for 2 h. The suspension was centrifuged at 8000 rpm for 3 min to remove the unabsorbed AS1411 strands, following by washing with phosphate buffered saline (PBS) three times. Due to π-π* stacking and electrostatic interaction caused by the highly conjugated nanostructure and rich amino group of CuPc-bTDC-COF@PEG, AS1411 strands would be tightly immobilized. due to. The resulted CuPc-bTDC-COF@PEG@AS1411 hybrid was stored in a refrigerator (4 °C) for further experiments.

9.1.4 Preparations of all suspensions

For evaluating the PTT and PDT effects, the as-prepared nanomedicines should be dispersed in advances. Typically, CuPc-bTDC-COF@PEG (10 mg) was dispersed in 10 mL of Milli-Q water and ultrasonically agitated for 5 min to obtain the CuPc-bTDC-COF@PEG aqueous dispersion (1 mg mL^{-1}), which was used as stock suspension. As compared, the homogeneous CuPc-bTDC-COF suspension (100 μg mL^{-1}) was prepared in the same way, but dispersing using CuPc-bTDC-COF in Milli-Q water.

9.1.5 Basic characterizations

Powder X-ray diffraction measurements (PXRD) were collected with a Rigaku D/Max-2500 X-ray diffractometer using Cu Kα radiation (λ = 0.15406 nm). Chemical structure and components were analyzed via Fourier transform infrared spectroscopy (FT-IR) by using a Bruker TENSOR 27 spectrometer (32 scans at 4 cm^{-1} resolution) and X-ray photoelectron spectroscopy (XPS) collected on an ESCALAB 250Xi spectrometer (Thermo Fisher Scientific, Manchester, UK) with an Al Kα X-ray source (1486.6 eV photons). The surface morphology was performed with JSM-6490LV field

emission scanning electron microscope (FE-SEM, Japan) and JEOL JEM-2100 high-resolution transmission electron microscopy (HR-TEM, Japan) with a field emission gun of 200 kV. Photoluminescence spectra of the samples were obtained using a fluorescence spectrophotometer (F-7000, Hitachi Ltd., Japan) with the excitation wavelength of 360 nm. UV-Vis spectra of the samples were recorded with a UV U3900 spectrophotometer (Hitachi Ltd., Japan) in the range of 200–800 nm. Cell cytotoxicity was quantified by measuring the absorbance at 490 and 630 nm, using a microplate reader (Thermo Fisher Scientific, Inc., U.S.A.). Cellular uptake and intracellular distribution were studied using a confocal laser scanning microscopy (CLSM, LSM710, ZEISS, Germany) Electron spin resonance (ESR) spectra were recorded on a Burker A200 spectrometer with a modulation frequency of 100 kHz.

9.1.6 In vitro photothermal effect

The CuPc-bTDC-COF and CuPc-bTDC-COF@PEG suspensions (1 mL) with diverse concentrations were transferred to a 1.5 mL of centrifugal tube and irradiated under a NIR 808 nm laser for 10 min, separately. To test the photothermal performance, the heat distribution and the system temperature were recorded by a thermal imaging camera and electronic thermometer, respectively. Different laser power densities (0.3, 0.5, 1, 1.3, and 1.5 W cm^{-2}) of the laser light were also adopted to modulate the temperature of the catalyst.

The temperature variation of the prepared suspensions during the laser on and laser off experiment was used to assess the Photothermal conversion efficiency (PCE). Typically, an 808 nm laser (1 W cm^{-2}) was used to irradiate the sample suspension (100 g mL^{-1}) for 15 min. The laser was then turned off, allowing the solution to naturally cool. Throughout the process, the temperature was recorded every 1 min. After that, the PCE was calculated using the following formula:

$$\eta = \frac{Qs - Qw}{I(1-10^{-A^{808}})} \quad (1)$$

$$hS = \frac{mc}{\tau} \quad (2)$$

$$Q_S = hS\Delta T_{s,h} \quad (3)$$

$$\tau = -\frac{dt}{dln\ \theta} \quad (4)$$

$$Q_W = hS\Delta T_{w,h} \quad (5)$$

$$\theta = \frac{T_{t,c} - T_{min,c}}{\Delta T_{s,c}} \quad (6)$$

, where η is photothermal conversion efficiency; A^{808} is the absorption of solution at 808 nm; I is the power of the laser; $\Delta T_{s,h}$ is the changed temperature of solution in the heating curve; $\Delta T_{w,h}$ is the changed temperature of water in the heating curve; c is specific heat capacity of water; m is solution mass; τ is slope of t–(-ln θ) graph; t is time in the cooling curves; $\Delta T_{s,c}$ is the changed temperature of solution in the cooling curve; $T_{min,c}$ is the final temperature of solution in the cooling curve; and $T_{t,c}$ is the temperature of solution at different times in the cooling curve.

9.1.7 In vitro degradation and response test

9.1.7.1 Detection of $^1O_2$ species

To probe the generated efficiency of $^1O_2$ of the obtained samples, 1,3-diphenylisobenzopyran (DPBF) was employed as a probe. DPBF (1mg mL^{-1}, 20 μL) in water was freshly prepared, followed by adding each of the sample suspension (2 mL, 100 μg mL^{-1}), including CuPc-bTDC-COF and CuPc-bTDC-COF@PEG with stirring for 15 min in dark. After that, the produced $^1O_2$ level was evaluated by monitoring the UV−vis absorption at 414 nm with time intervals of 1 min during the irradiation under NIR 808 nm laser (1 W cm^{-2}). To further study the degradation rate of DPBF, the reaction kinetics was fitted well into the first-order kinetic equation

$$ln(C_0/C) = k_a t \quad (7)$$

, where k_a, t, C_0, and C_t are the pseudo-first-order reaction rate constant, reaction time (min^{-1}), and initial concentration and the concentration during the reaction time of degradation product (mg L^{-1}), respectively.

9.1.8 Intracellular ROS measurements

The generation of intracellular ROS was detected by 2',7'-dichlorodiacetate (DCFH-DA) in mouse melanoma 4T1 cells. Typically, 4T1 cells were seeded into cell culture dish at a density of 1×10^5 per well and incubated with 2 mL 1640 medium for 24 h. After that, each of the fresh 1640 medium containing CuPc-bTDC-COF@PEG (100 μg mL^{-1}) was added and incubated for 6 h, followed by washing with PBS thrice. DCFH-DA (20 μM) was incubated with 4T1 cells with or without stimulating factors,

including (1) control, (2) control + NIR, (3) CuPc-bTDC-COF@PEG, and (4) CuPc-bTDC-COF@PEG + NIR, for further incubation at 37 °C for 20 min. Finally, confocal laser scanning microscopy (CLSM) was used for measuring the intracellular ROS generation in each well when excited at 488 nm.

9.1.8.1. Cytotoxicity measurements

The cytotoxicity of CuPc-bTDC-COF, CuPc-bTDC-COF@PEG, CuPc-bTDC-COF@PEG@AS1411 were measured by typical MTT assay against L929 and mouse breast 4T1 cells, separately. Typically, 4T1 cells (1×10^5) were seeded into 96-well plates and cultured for 24 h (37 °C, 5% CO_2), and then separately incubated with different concentrations of CuPc-bTDC-COF, CuPc-bTDC-COF@PEG, CuPc-bTDC-COF@PEG@AS1411 suspensions for 24 h. The cells were rinsed gently with PBS to remove incompletely internalized materials, and 200 μL Roswell Park Memorial Institute (RPMI-1640) was added to each well. After further incubation for 12 h at 37 °C, 20 μL of MTT (5 mg mL^{-1} in PBS) was added into per well and cultured in the incubator for 4 h. At last, the medium was removed, following by added 150 μL of DMSO to per well. The cell viability was monitored by measuring the absorbance at 490 and 600 nm using a microplate reader (WD-2102A).

9.1.9 Intracellular PTT/PDT performances

To study the in vitro PTT/PDT efficiency, 4T1 cells were seeded into 96-well plates and separately incubated with different concentrations of CuPc-bTDC-COF, CuPc-bTDC-COF@PEG, CuPc-bTDC-COF@PEG@AS1411 suspensions (0, 20, 50, 80, 100 and 200 μg mL^{-1}). After 24 h, to evaluate the therapy performance, four groups of 4T1 cells were cultured with different treatments, including (i) materials and (ii) materials + NIR (1 W cm^{-2}, 15 min) for 24 h. Then, 4T1 cells were washed with PBS and cultured for another 12 h. Subsequently, MTT solution (20 μL, 5 mg mL^{-1} in PBS) was introduced in each well and incubated for 4 h at 37 °C. The formed formazan crystals were dissolved by adding 150 μL of DMSO into per well. The PTT/PDT efficacy were calculated by detecting the absorbance of each well solution at 490 nm and 600 nm with a microplate reader.

9.1.10 Evalution of the target ability of CuPc-bTDC-COF@PEG@AS1411 with 4T1 cells

4T1 cells and L929 cells were migrated from the culture flasks to the bottom of cell culture dishes, respectively. Cells were seeded 20 mm glass-bottom culture dishes

with 1 mL of medium and cultured for 24 h. After removing the medium, CuPc-bTDC-COF@PEG@AS1411@5' Cy3-labeled AS1411(100 μg mL^{-1}, 1 mL) was added in every 20 mm glass-bottom culture dishes and cultured for 4 h. After rinsing three times by PBS, the nucleus was stained with 20 μL of Hoechst 33258 (2 μg μL^{-1}) at 37 °C for 15 min and then rinsing with PBS additional thrice. Finally, the cells fixed with 4% cold paraformaldehyde for 15 min, followed by rinsing with PBS thrice. The targeting effect of AS1411 in the cellular uptake of CuPc-bTDC-COF@PEG@AS1411 was evaluated by CLSM (excited at 532 nm).

9.1.11 In vivo antitumor treatment study

Female BALB/C mice (4-6 weeks) were purchased from Hunan Slaccas Jingda Laboratory Animal Co., Ltd (Hunan, China), and raised in the SPF animal room. All animal procedures were approved by the Animal Research Ethics Committee of Medical School, Henan University. (Document HZYX-2021-010). The 4T1 tumor-bearing nude mice models were successfully established when the tumor volume was about 70 mm^3. The mice were divided into four groups by the random allocation, including PBS, PBS + NIR, CuPc-bTDC-COF@PEG@AS1411, CuPc-bTDC-COF@PEG@AS1411 + NIR. Typically, CuPc-bTDC-COF@PEG@AS1411 (200 μL, 200 μg mL^{-1}) or PBS were administrated into the mice by intravenous injection. After 2 h, the groups of PBS + NIR and CuPc-bTDC-COF@PEG@AS1411 + NIR were treated with NIR irradiation (0.8 W cm^{-2}, 10 min). Then, the body weight and tumor volume of all mouse groups were measured every other day. After two weeks, all dissected tumors were collected for photography.

9.1.12 Histological examinations

After the treatments were finished, the main organs and tumors for each group were collected and washed with PBS for further hematoxylin-eosin (H&E) and TUNEL staining analysis under an optical microscope.

9.1.13 Statistical analysis

All statistical analysis were performed using GraphPad Prism 7 (GraphPad Software Inc., USA) and Origin 2021 software. All data were expressed as mean ± standard error of the mean (SEM, $n \geqq 3$). The differences among groups were analyzed using two-tail Student's t-test. P-values < 0.05 were significant (* $P < 0.05$, * * $P < 0.01$, and * * * $P < 0.001$).

9.2 Results and discussion

9.2.1 Basic characterizations of CuPc-bTDC-COF and CuPc-bTDC-COF@PEG

As indicated in **Scheme 19**, CuPc-bTDC-COF was prepared using bTDC and CuPc-TA as building blocks via Schiff-base condensation by the solvothermal method (**Scheme 19**). Subsequently, to enhance the biocompatibility and dispersion ability of the as-prepared CuPc-bTDC-COF, the amino-modified PEG can be linked with the reserved carbonyl group bearing on CuPc-bTDC-COF also via Schiff-base condensation. **Figure 75a** and **75b** shows CuPc-bTDC-COF is composed of loosely stacked nanospheres with the size of ~ 80 nm. The CuPc-bTDC-COF@PEG hybrid illustrates the adjoined structure with even rough surface (**Figure 75c** and **75d**). The TEM image of CuPc-bTDC-COF (**Figure 76a-c**) illustrates that it is accumulated with multiple nanosheets. No clear lattice spring can be observed in the high-resolution TEM image (**Figure 76c**), revealing its amorphous structure. Further, the typical the elemental mapping with the energy-dispersive X-ray spectroscopy (EDS) spectrum of CuPc-bTDC-COF shows the homogeneous dispersion of Cu, S, C, N, and O within the selected region. The resemble nanosheet-like structure is observed in the TEM and HR-TEM images of CuPc-bTDC-COF@PEG (**Figure 76e-g**), also clarifying its amorphous structure. Also, the even distribution of Cu, S, C, N, and O elements of the whole region in CuPc-bTDC-COF@PEG can be found in the EDX mapping spectra (**Figure 76g**). In addition, the dynamic light scattering (DLS) spectra CuPc-bTDC-COF and CuPc-bTDC-COF@PEG nanospheres (**Figure 77**) were used to determine their nanoparticle sizes. It shows that a broad peak can be found in the DLS spectrum of CuPc-bTDC-COF, manifesting its poor solubility in PBS. As compared, CuPc-bTDC-COF@PEG shows a relatively narrow size distribution with an average size of 73.68 nm, revealing its good dispersion ability. Thereby, CuPc-bTDC-COF@PEG could be ingested by tumor cells due to its small size and good dispersion in aqueous medium.

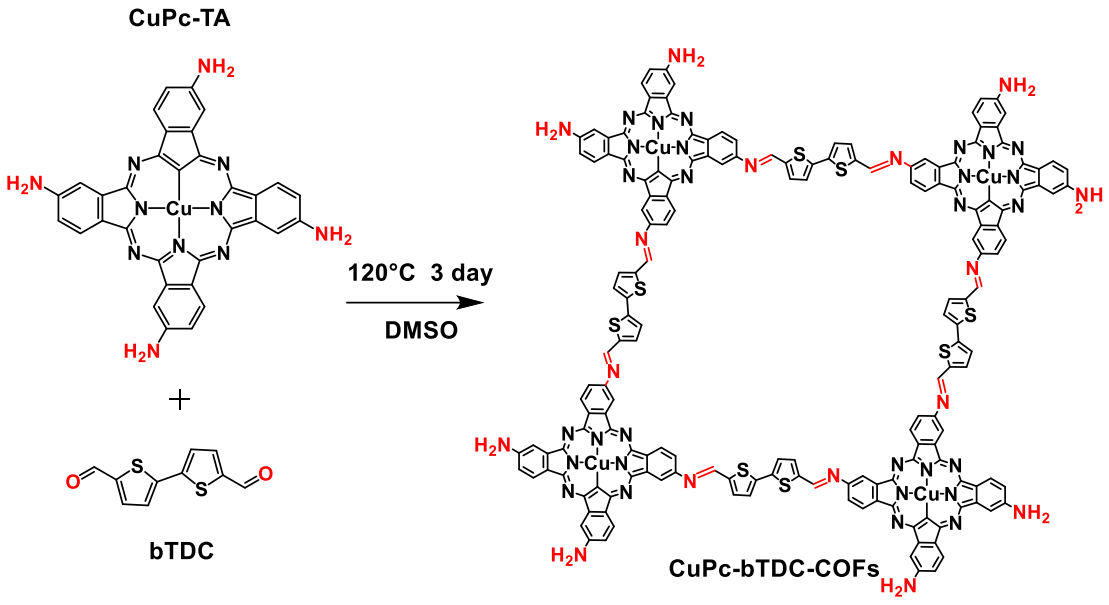

Scheme 19 Schematic illustration of the synthesis procedure of CuPc-bTDC-COF and preparation of CuPc-bTDC-COF@PEG.

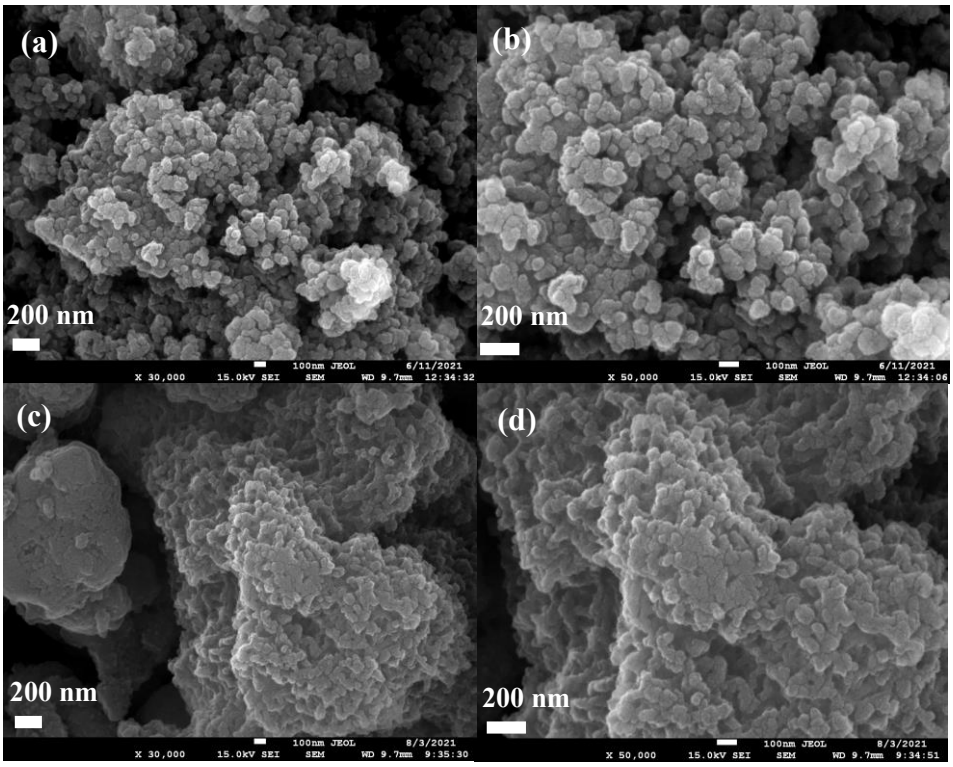

Figure 75 FE-SEM images of (a, b) CuPc-bTDC-COF and (c,d) CuPc-bTDC-COF@PEG.

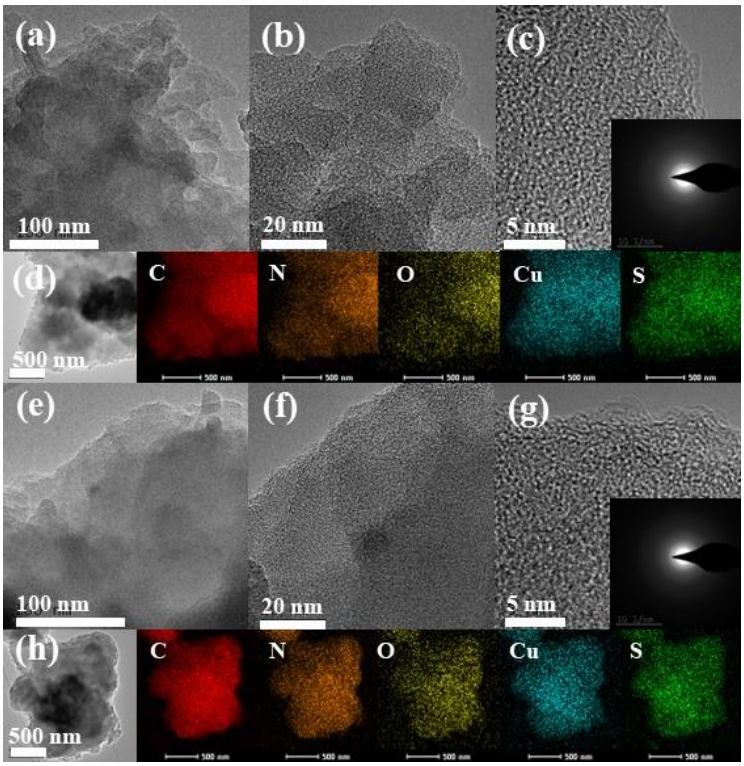

Figure 76 Low-magnification (a), high-magnification (b), and high-resolution (c) TEM images of CuPc-bTDC-COF and (d) dark-field TEM image and corresponding EDS elemental mapping. Low-magnification (e), high-magnification (f), and high-resolution (g) TEM images of CuPc-bTDC-COF@PEG and (h) dark-field TEM image and corresponding EDS elemental mapping.

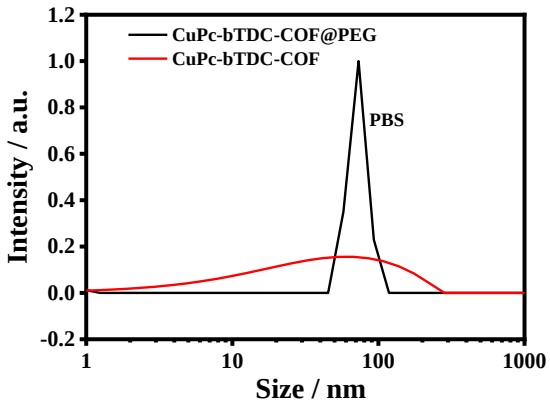

Figure 77. DLS spectra of CuPc-bTDC-COF and CuPc-bTDC-COF@PEG nanospheres in PBS.

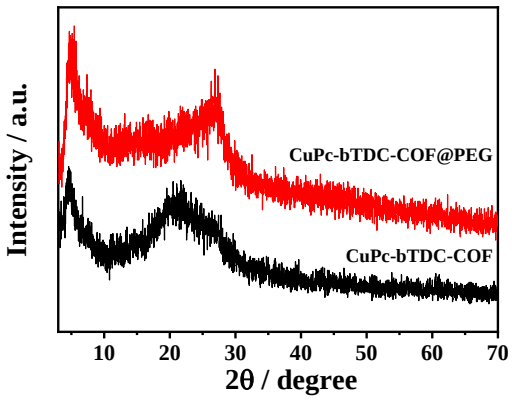

Figure 78 XRD patterns of CuPc-bTDC-COF and CuPc-bTDC-COF@PEG.

The PXRD patterns of CuPc-bTDC-COF (**Figure 78**) show a distinct reflection at 2θ = 4.56°, which is indexed to a primitive tetragonal unit cell similar to other primitive tetragonal reported CoPc-BPDA COF [177]. Further, a broad stacking reflection at 2θ = 25.12° indicates the graphitic carbon [178]. In addition, the resemble PXRD pattern can be observed in CuPc-bTDC-COF@PEG, suggesting the modification with PEG layer cannot change the crystal structure of the obtained COF. Besides, the FT-IR spectra of CuPc-bTDC-COF and CuPc-bTDC-COF@PEG (**Figure 79**) demonstrate the characteristic peak at 1605 cm^{-1} due to –C=N–[179]. It hints the successful condensation between amino moieties bearing on CuPc-TA and aldehyde group of bTDC. Apart from this, CuPc-bTDC-COF@PEG exhibits obvious new characteristic peaks at 1052, 1142, and 1249 cm^{-1}, which ascribed to C−O−C stretching vibration of PEG-NH_2 [180], while the typical characteristic peaks at 941 and 2846 cm^{-1} are assigned to −CH_2 stretching vibration.

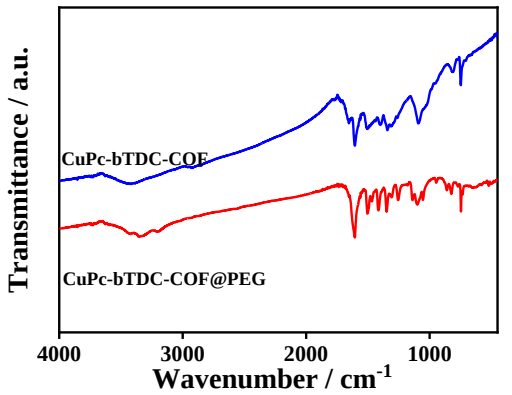

Figure 79 FT-IR spectra of CuPc-bTDC-COF and CuPc-bTDC-COF@PEG.

As indicated in **Figure 80**, the UV-visible (UV-vis) absorption spectra of CuPc-bTDC-COF and CuPc-bTDC-COF@PEG dispersed in Milli-Q water. It illustrates that CuPc-bTDC-COF has the absorbance peak ranging from 248 to 850 nm, revealing its superior photo-adsorption within the range visible light to NIR I region. Notably, CuPc-bTDC-COF also exhibits strong B-band (275-425 nm) absorption and Q-band absorption (590-900 nm), indicating the $\pi \rightarrow \pi^*$ electron transition from the highest occupied molecular orbital to the LUMO of the phthalocyanine ring [181]. In comparison with CuPc-bTDC-COF, the CuPc-bTDC-COF@PEG hybrid illustrates the decreased photo-absorption due to the prescence of PEG layer [182].

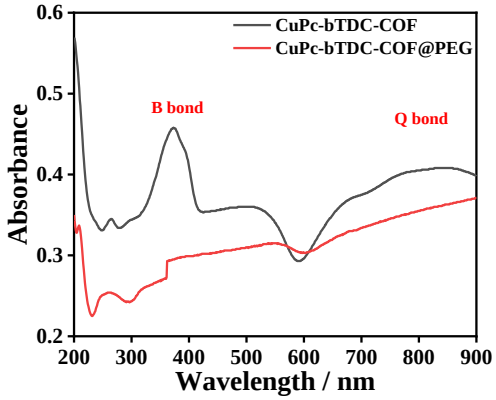

Figure 80 (a) UV-vis absorption of CuPc-bTDC-COF and CuPc-bTDC-COF@PEG.

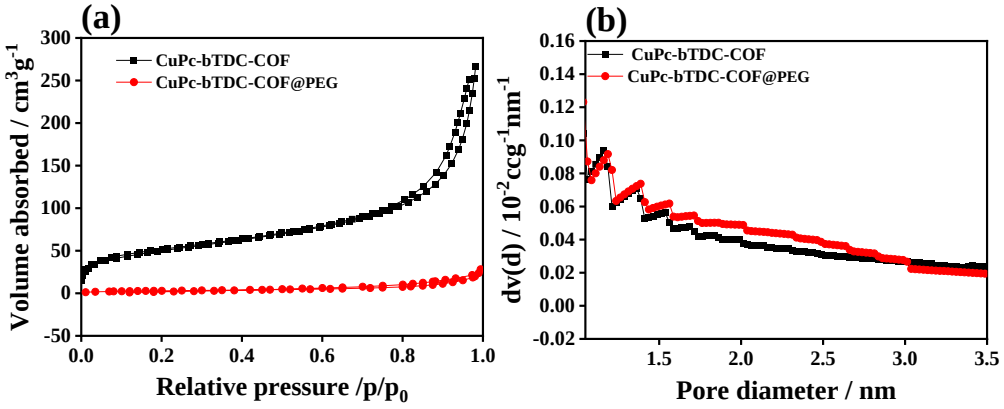

Figure 81 (a) N_2 adsorption-desorption isotherms and (b) pore distribution of CuPc-bTDC-COF and CuPc-bTDC-COF@PEG.

The BET surface area of CuPc-bTDC-COF and CuPc-bTDC-COF@PEG were measured to be 173 $m^3\ g^{-1}$ and 10.30 $m^3\ g^{-1}$, respectively (**Figure 81a**). According to the non-local density functional theory (NLDFT) model, their pore sizes were evaluated

to be 1.17 nm (**Figure 81b**). These results firmly confirmed that CuPc-bTDC-COF are microporous materials and the PEG-NH_2 IS blocking up the access to the pores, which impedes the access of gases into the MOF's interior [183].

For further assessing the change in the chemical structures and components before and after the PEG modification, the XPS analysis of CuPc-bTDC-COF and CuPc-bTDC-COF@PEG were determined. Their XPS survey scan spectra **Figure 82** shows that Cu 2*p* (934.8 eV), S 2*p* (164.0 eV), C 1*s* (284.9 eV), N 1*s* (398.5 eV), and O 1*s* (532.1 eV) signals are co-existed.

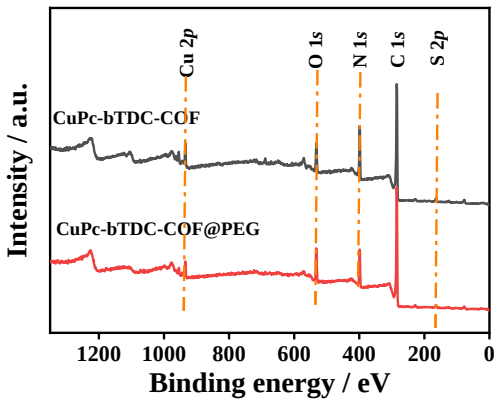

Figure 82. XPS survey scan spectra of CuPc-bTDC-COF and CuPc-bTDC-COF@PEG.

By analyzing the high-resolution XPS spectra of each element in the two samples with Gaussian fitting, the detailed chemical components can be deduced. **Figure 83a** indicates that the high-resolution XPS spectra of Cu 2*p* in the two samples includes two couples of peaks at the centers of the binding energies (BEs) of 935.6 eV and 955.6 eV, which are assigned with the electron states of Cu $2p_{3/2}$ and Cu $2p_{1/2}$, respectively. Distinctly, the Cu $2p_{3/2}$ part can be split into Cu(II) (934.5 eV) and Cu(III) (935.7 eV), as well as their satellite peaks at the BEs of 942 and 944.2 eV. This finding verifies that small partical Cu(II) could be oxidized to its high valcence state during the COF prepation procedure. Further, the C 1*s* XPS spectrum of CuPc-bTDC-COF can be fitted to multiple groups of C=C (284.1 eV), C-C (284.6 eV), C-N (285.5 eV), N-C=O (287.3 eV), COO (289.5 eV), and π–π^* (292.1 eV). Amongst, the presence of C=C indicates the conjugated sp^2 C bearing on Pc rings. As compared, apart from C=C, C-C, and C-N groups, the additional moieties of C-O (286.5 eV) and C=O (288.8 eV) are also

present. However, both N-C=O and π–π^* are absent in the C 1s XPS spectrum of CuPc-bTDC-COF@PEG. This result can be explained by the cover of the PEG layer on CuPc-bTDC-COF. Moreover, three peaks of pyridinic N (398.4 eV), pyrrolic N (398.9 eV), and graphitic N (400.1 eV) are deconvoluted in the N 1*s* XPS spectrum of CuPc-bTDC-COF and CuPc-bTDC-COF@PEG. Additionally, the weak S 2p XPS spectrum of the two samples can be divided the groups of S_2^{2-} $2p_{3/2}$ (163.1 eV), S_2^{2-} $2p_{1/2}$ (164.2 eV), S^{6+} $2p_{3/2}$ (165.5 eV) and S^{6+} $2p_{1/2}$ (167.8 eV). The O 1*s* XPS spectrum of CuPc-bTDC-

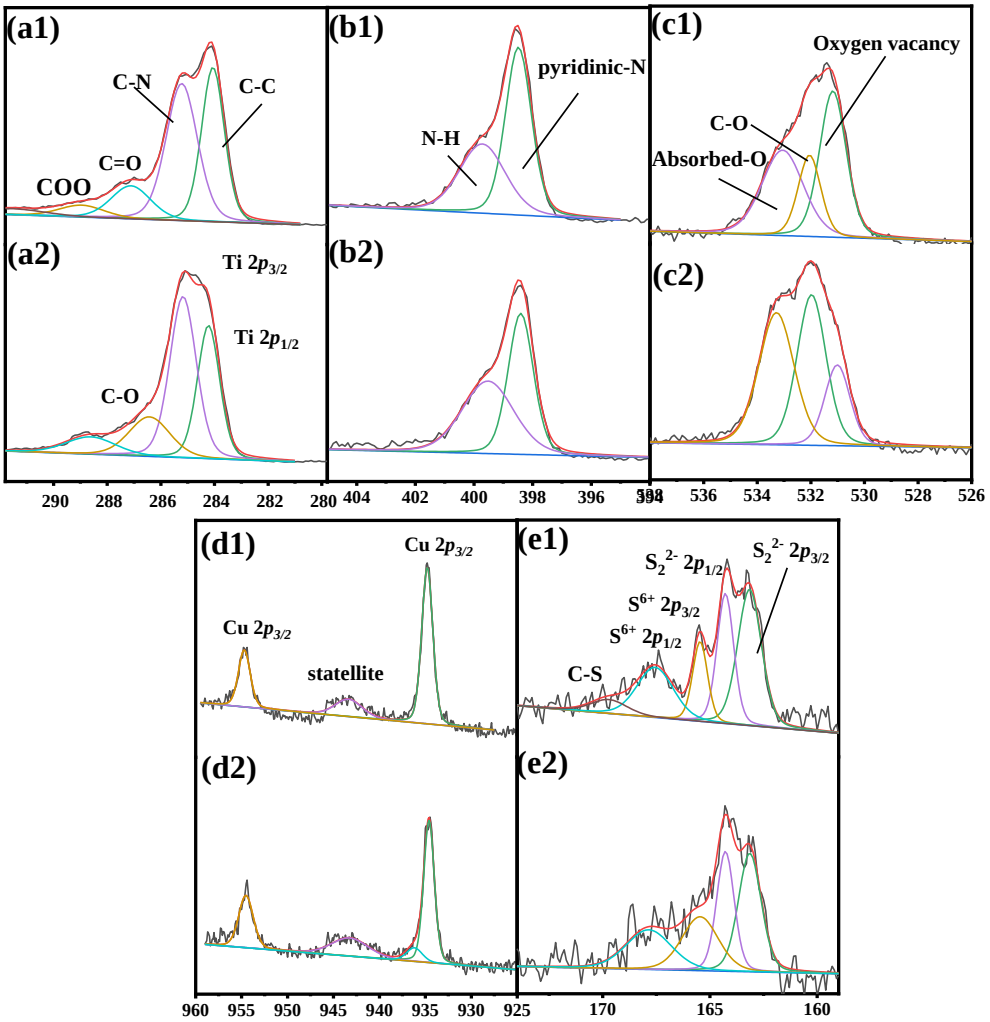

Figure 83. High-resolution C 1*s* (a), N 1*s* (b), O 1*s* (c), Cu 2*p* (d) and S 2*p* (e) XPS spectra of (a1, b1, c1, d1, and e1) CuPc-bTDC-COF and CuPc-bTDC-COF@PEG.

COF (**Figure 83c**) is divided into oxygen vacancy (O_v, 530.1 eV), C-O (531.9 eV), and adsorbed O (533.2 eV). The remarkable O_v could be caused by the incomplete

condensation reaction between the building blocks, further enhancing the catalytic ability of the developed nanomedicine. As compared, the content of O_v in CuPc-bTDC-COF@PEG declines owing to the modification of PEG layer.

Furthermore, electron paramagnetic resonance (EPR) spectra (**Figure 84**) of CuPc-bTDC-COF@PEG were separately evaluated in the dark and under 808 nm NIR irradiation. It demonstrates that a clear signal around g = 1.998 can be found in the EPR spectrum of CuPc-bTDC-COF@PEG, which is attributed to plenty of intrinsic Ovs. Under NIR I irradiation, however, the signal around g = 1.998 is slightly enhanced, which can be assigned to the electron trapped on the oxygen vacancy under 808 nm NIR irradiation.

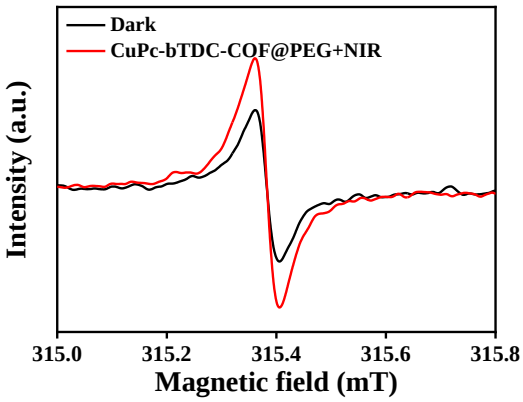

Figure 84 EPR spectra of CuPc-bTDC-COF@PEG (a) in dark and (b) under NIR irradiation.

9.2.2 In vitro photothermal performances

Given that the synthesized CuPc-bTDC-COF is composed of metal Pc rings, the superior PTT ability could be attained. The PTT performances of CuPc-bTDC-COF and CuPc-bTDC-COF@PEG were investigated in water under 808 nm NIR irradiation (1 W cm^{-2}) for 15 min. **Figure 85a** depicts the temperature of the CuPc-bTDC-COF suspension dramatically increases within the initial 6 min. Afterward, the temperature approaches to a platform. Further, the temperature of the suspension increases with increasing the dispersion concentration from 12.5 to 200 μg mL^{-1}. The temperature can be up to 63.2 °C when irradiating the CuPc-bTDC-COF suspension (200 μg mL^{-1}) under 808 nm laser irradiation (1 W cm^{-2}) for 15 min. The similar trend appears in the

plots of the temperature versus the dosages of CuPc-bTDC-COF@PEG under 808 nm irradiation for 15 min (**Figure 85c**). As compared, the maximum temperature of CuPc-bTDC-COF@PEG (100 μg mL^{-1}, 54.8 °C) seems to be slightly lower than that of CuPc-bTDC-COF (56.6 °C) at the same conditions. It reveals the photothermal transfer ability of CuPc-bTDC-COF can be reduced by the modification with the PEG layer. Moreover, the temperature of CuPc-bTDC-COF@PEG (100 μg mL^{-1}) also increases with increasing the laser power density of the NIR light (**Figure 85d**).

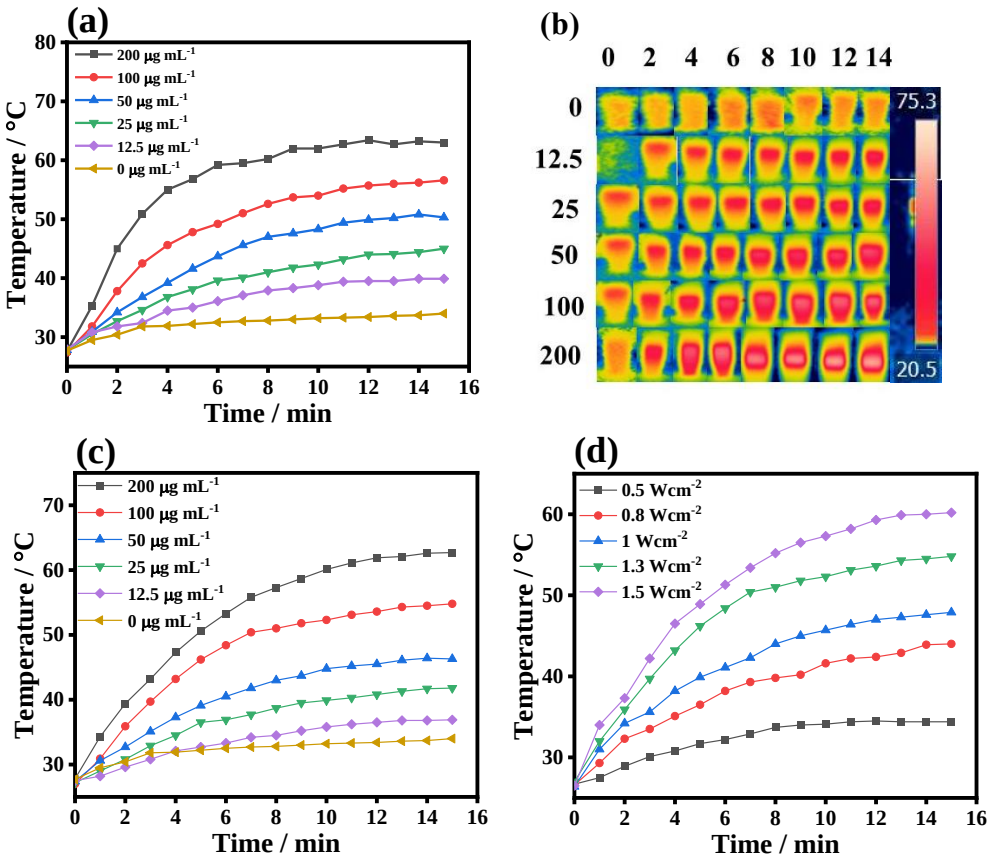

Figure 85 In vitro photothermal performance of CuPc-bTDC-COF and CuPc-bTDC-COF@PEG. Temperature elevation curves of CuPc-bTDC-COF (a) and CuPc-bTDC-COF@PEG (c) at various concentrations under 808 nm laser irradiation for 15 min (0–200 μg mL^{-1}). (b) Infrared thermal images of CuPc-bTDC-COF aqueous solutions at different concentrations when exposing to 808 nm NIR laser for 15 min. (d) Temperature elevation curves of CuPc-bTDC-COF@PEG solutions (100 μg mL^{-1}) irradiated by 808 nm laser with various power densities for 15 min (0.5, 0.8, 1, 1.3, and 1.5 W cm^{-2}).

Moreover, according to the photothermal curves and interrelated time constants

(**Figure 86**), the η of CuPc-bTDC-COF, which was calculated according to the **Eqs. 1-6**, is 63%, fractionally higher than that of CuPc-bTDC-COF@PEG (100 μg mL^{-1}), but substantially higher than those of some Pc-related nanomaterials, such as Pc NPs (31.3%)[71], Pc-based nanodots (ZnPc-NDs) (45.7%)[72], Pc-based polymeric micelles (47.0%)[72], and albumin-iron (II) FePc NPs (HSA-FePc NPs) (44.4%)[44]. Given that the low catalyst dosage of the nanomedicine is beneficial to the reduction of side effects, 100 μg mL^{-1} of CuPc-bTDC-COF@PEG was used for further experiments, which exhibits the maximum temperature of 54.8 °C by irradiation with a laser power density of 1 W cm^{-2}. Further, **Figure 87** demonstrates no obvious change in the η values of CuPc-bTDC-COF and CuPc-bTDC-COF@PEG after five on-off cycles of NIR laser exposure, hinting the excellent photostability of the two samples. Moreover, it also verifies that the PEGylation has no discernible effect on the PTT performance of CuPc-bTDC-COF, affording the ability as an excellent PTT agent for anticancer therapy.

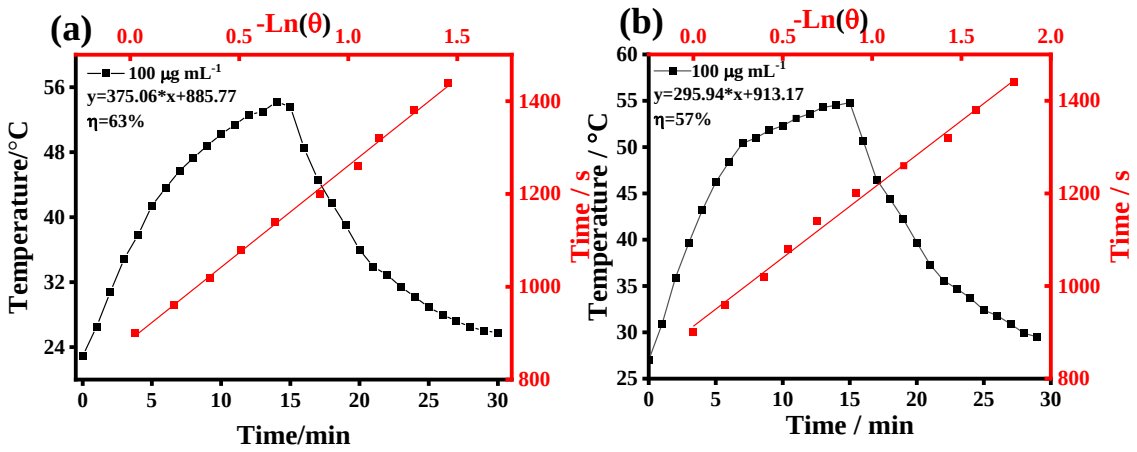

Figure 86 Heating and cooling curves (black) and the t-(-lnθ) diagram (red) obtained during the natural cooling period of (a) CuPc-bTDC-COF and (b) CuPc-bTDC-COF@PEG.

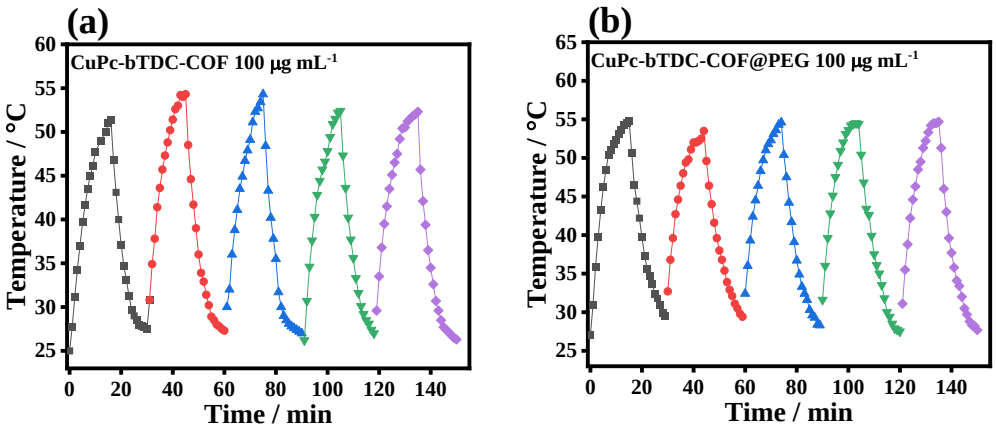

Figure 87 (f) Photothermal profile of CuPc-bTDC-COF and CuPc-bTDC-COF@PEG dispersion over five on/off cycles under the 808 nm laser irradiation (100 μg mL^{-1}, 1 W cm^{-2})

The in vitro PDT effect of one catalyst can be investigated by the determination of the produced $^1O_2$ species, which can cause the dramatic damage to cancer cells under 808 nm laser illumination (**Figure 88)**. Firstly, intersystem crossing (ISC) produces the excited triplet state ^{3}PSs (CuPc-bTDC-COF)* when exposed to 808 laser. Subsequently, the activated CuPc-bTDC-COF would react with the ground state triplet oxygen ($^3O_2$), producing highly active $^1O_2$. Here, DPBF was used to evaluate the $^1O_2$ production rate of one catalyst under NIR irradiation as it can undergo a Diels-Alder 1,4-cycloaddition reaction with $^1O_2$, thus reducing the absorption at ~420 nm. After irradiation with 808 nm NIR laser (1 W cm^{-2}), the DPBF absorbance shows a time-dependent decrease within 24 min at pH 7.4 due to the oxidative decomposition of the generated $^1O_2$. Accordingly, the catalytic reaction belongs to the type II PDT due to energy transfer occurred [91]. As compared, **Figures 88a** and **88b** demonstrate the pure DPBF is hardly degraded in dark with and without the NIR irradiation. On contrast, the peak intensity of the absorption peak decreases significantly within 24 min in the presence of CuPc-bTDC-COF (**Figure 88c**), verifying its superior $^1O_2$ generation ability. As compared, the decrease extent of CuPc-bTDC-COF was marginally higher than that of CuPc-bTDC-COF@PEG. It can be explained by that the long chain of PEG-NH_2 influences molecular aggregation [184]. As a result, the ISC rate of CuPc-bTDC-COF@PEG seems be lowered, resulting in a low concentration of triplet excitons. To further study the

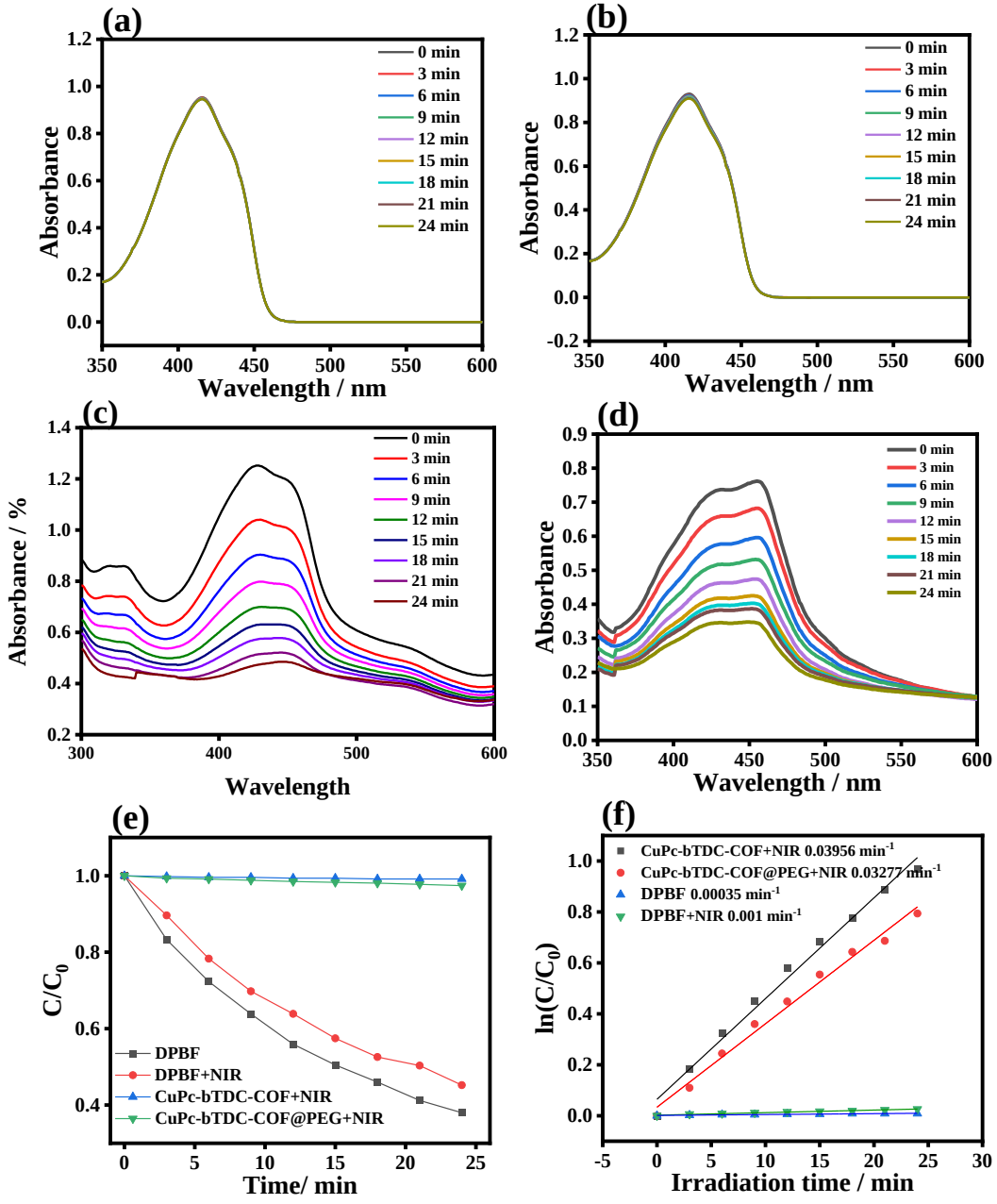

Figure 88. (a) Self-degradation curve of DPBF under dark conditions. (b) Self-degradation curve of DPBF under light irradiation. DPBF absorption of (c) CuPc-bTDC-COF and (d) CuPc-bTDC-COF@PEG (100 μg mL^{-1}) water solution under 808 nm laser irradiation (1 W cm^{-2}). (e) Time-dependent absorbance of DPBF at 420 nm (C/C_0) irradiated with an 808 nm laser without and with the NIR (containing CuPc-bTDC-COF and CuPc-bTDC-COF@PEG for 24 min, respectively. C_0 and C are the initial absorbance of DPBF and the absorbance under definite irradiation time, respectively. (f) The rate constant of DPBF decomposition in the presence of CuPc-bTDC-COF and CuPc-bTDC-COF@PEG under NIR 808 nm laser irradiation (1 W cm^{-2}).

degradation rate of DPBF, time-dependent degradation behaviors of DPBF caused by the two samples within 24 min were assessed (**Figure 88e**). It shows that the reaction kinetics for the DPBF degradation against the two catalysts were fitted well into the first-order kinetic equation (**Eqs. (7)**, **Figure 88c**). The apparent rate constants (k_a) of DPBF photodegradation toward CuPc-bTDC-COF (0.03956 min^{-1}) is larger than that of CuPc-bTDC-COFPEG (0.03277 min^{-1}), consistent with the above degradation analysis of DPBF. Collectively, CuPc-bTDC-COF illustrates the superior and high generation ability of $^1O_2$ species, which would not remarkably affect by the cover of PEG layer, thus showing the great potential as PDT agents.

Furthermore, ESR measurements were carried out to determine the generation of $^1O_2$, for which 2,2,6,6-tetramethylpiperidine (TEMP) was used as the trapping agent. **Figure 89a** depicts no significant peak is observed for the CuPc-bTDC-COF suspension in dark and the pure water, revealing no $^1O_2$ species can be produced. As contrast, obvious peak signals of the two samples recorded in the presence of TEMP with an intensity ratio of 1:1:1 of TEMP-$^1O_2$. In comparison with CuPc-bTDC-COF, the observed peaks for CuPc-bTDC-COF@PEG seems to be lower, hinting the relatively lower content of $^1O_2$ species. Moreover, the ESR spectra against CuPc-bTDC-COF@PEG at various durations (**Figure 89b**). It shows only negligible signal of TEMP-•$^1O_2$ can be observed in dark against CuPc-bTDC-COF@PEG, while the intensity of the three typical characteristic peaks (the intensity ratio of 1:1:1) of TEMP-•$^1O_2$ increases with increasing with the irradiation time going on.

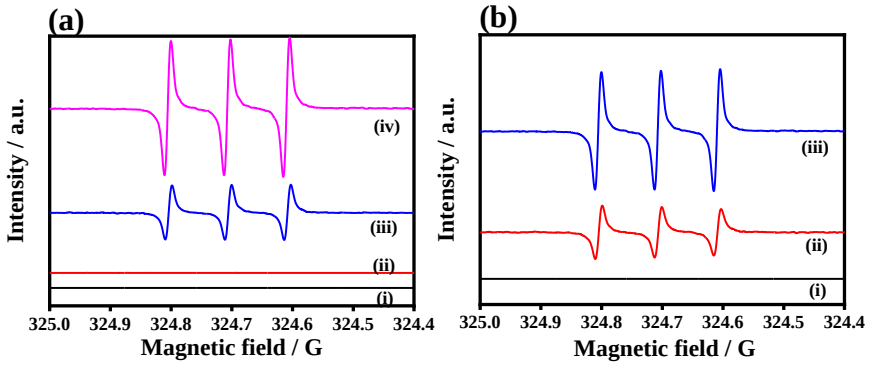

Figure 89 (a) ESR spectra of $^1O_2$ trapped by TEMP• of different materials upon irradiation for 10

min in the presence of TEMP (trapping agent of $^1O_2$). (i) dark, (ii) dark + CuPc-bTDC-COF, (iii) CuPc-bTDC-COF@PEG + NIR, and (iv) CuPc-bTDC-COF + NIR. (b) ESR spectra of $^1O_2$ trapped by TEMP• in CuPc-bTDC-COF@PEG solution (100 μg mL^{-1}) without (i) or with NIR laser irradiation (808 nm, 1 W cm^{-2}, 5 (ii) and 10 min (iii)).

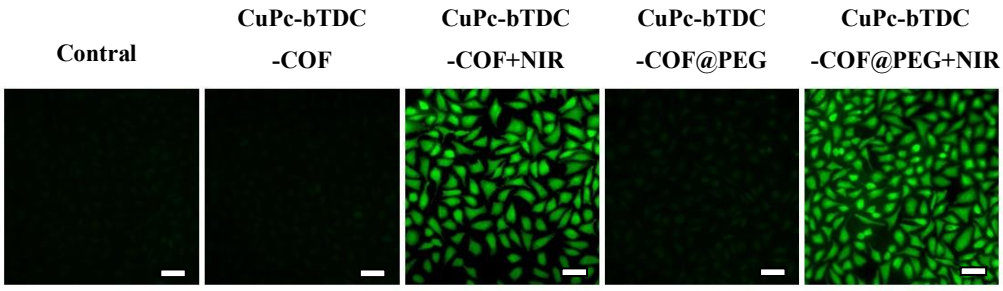

Figure 90 DCF fluorescence images of DCFH-DA-stained 4T1 cells treated with CuPc-bTDC-COF and CuPc-bTDC-COF @PEG (100 μg mL^{-1}) without or with laser irradiation (scale bar: 50 μm).

Given that the as-synthesized CuPc-bTDC-COF@PEG possesses outstanding PTT and PDT properties, as well as excellent dispersion in aqueous solution, it can be served as an effective multimodal agent for cancer therapy. To verify the real level of ROS in 4T1 cells, DCFH-DA was used to determine the change of the fluorescence intensity, which can be oxidized by ROS and transferred to 2,7-dichlorofluorescein (DCF, green fluorescence) (Figure 90a). As indicated in **Figure 90a**, no intracellular green fluorescence signal can be observed is found for both control groups, and CuPc-bTDC-COF in dark. However, the group of CuPc-bTDC-COF@PEG shows weak green fluorescence signal in dark. As aforementioned, the PEGylated CuPc-bTDC-COF exhibits excellent dispersion ability, and can easily endocytosed. The hydroxyl radical (•OH) species can be produced via the Fenton-like reaction mediated by Cu^{2+} ions released from CuPc-bTDC-COF, thus showing the certain content for degrading DCFH-DA. Distinctly, $^1O_2$ species cannot be generated without the NIR irradiation. On contrary, remarkable green fluorescence can be attained for CuPc-bTDC-COF + NIR and CuPc-bTDC-COF@PEG + NIR groups, demonstrating a large amount of ROS can be yielded due to the superior PDT therapy of these nanomedicine with the aid of NIR

I irradiation.

9.2.3 In vitro cytotoxicity of the samples

In prior to the multimodal therapy, the cytotoxicity of CuPc-bTDC-COF, CuPc-bTDC-COF@PEG and CuPc-bTDC-COF@PEG@AS1411 toward L929 and 4T1 cells was assessed by MTT assay. As shown in **Figure 91**, it indicates the substantially high relative viability of L929 cells when incubated with the three samples. Further, the cell viability marginally decreases with increasing the nanomedicine usage. At the large dosage of 200 μg mL^{-1}, the high survival rate of CuPc-bTDC-COF can be attained, 89.9 %, slightly higher than those of CuPc-bTDC-COF@PEG (82.17%) and CuPc-bTDC-COF@PEG@AS1411 (81.2%). **Figure 91b** depicts the analogous appearance for the investigation of the Cell viability of 4T1 cells treated with CuPc-bTDC-COF (200 μg mL^{-1}) is as high as 86.8 %, fractionally larger than those of CuPc-bTDC-COF@PEG (82.7%) and CuPc-bTDC-COF@PEG@AS1411 (79.8 %). Distinctly, the as-prepared CuPc-bTDC-COF demonstrates excellent intrinsic biocompatibility and low cytotoxicity, endowing it with the great potential as nanomedicine for cancer therapy. When irradiated by the NIR I light (880 nm), **Figure 91** shows that the cell viabilities of 4T1 cells incubated with the three samples substantially decrease with increasing the sample dosage from 10 to 20 μg mL^{-1}. When the usage of the sample was set as 50 μg mL^{-1}, cell viability of 4T1 cells dramatically declines to 2.9, 0.5, and 0.45% for the CuPc-bTDC-COF-, CuPc-bTDC-COF@PEG- and CuPc-bTDC-COF@PEG@AS1411-treated group, respectively. It can be ascribed to the PTT/PDT synergistic effect. Apparently, the integrated PDT /PTT therapy strategy for the developed nanomedicine ensures the great specific cytotoxicity against cancer cells, suggesting that it can efficiently act as a potential photosensitizer for cancer therapy.

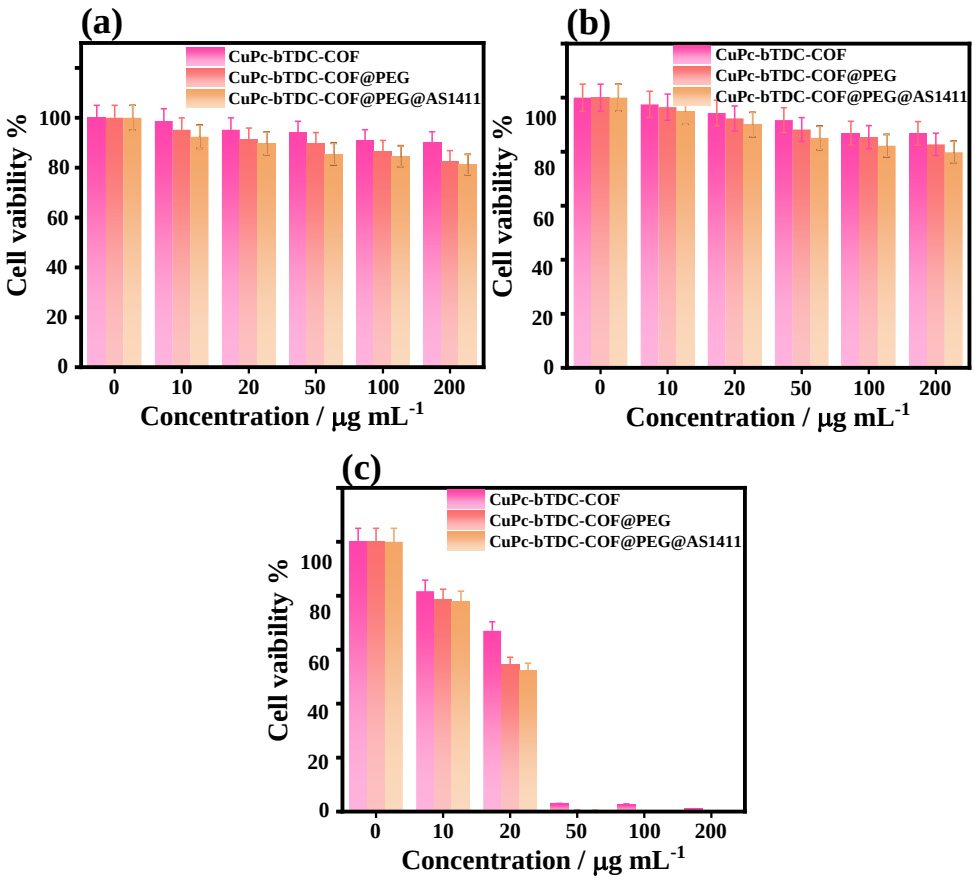

Figure 91 Cytotoxicity of CuPc-bTDC-COF-related nanomedicines. (a) Relative viability of (a) L929 cells and (b) 4T1 cells after separately incubation with CuPc-bTDC-COF, CuPc-bTDC-COF@PEG and CuPc-bTDC-COF@PEG@AS1411 for 24 h. (c) Relative viability of 4T1 cells treated with CuPc-bTDC-COF, CuPc-bTDC-COF@PEG and CuPc-bTDC-COF@PEG@AS1411 (0, 10, 20, 50, 100 and 200 μg mL^{-1}) under the NIR I laser irradiation (808 nm).

Confocal laser scanning microscopy (CLSM) was used to examine the cellular uptake behavior in L9292 and 4T1 cell lines of CuPc-bTDC-COF@PEG, which was modified with 5' Cy3-labeled AS1411. As known, overexpressed nucleolin can be generated within 4T1 cells, which thus can be specifically bind with AS1411 aptamer. **Figure 92** shows that no clear yellow fluorescence signal can be gained in L929 cell lines, revealing that CuPc-bTDC-COF@PEG@AS1411 would not be enriched in normal cells. On contrary, apparent yellow fluorescence signal can be found in 4T1 cell lines, suggesting that yellow fluorescence signal is actively internalized by 4T1 cells.

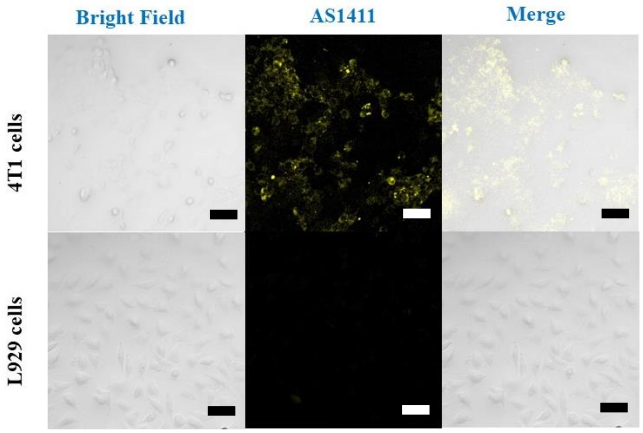

Figure 92 Confocal fluorescence images of (a) 4T1 and (b) L929 cell lines incubated with CuPc-bTDC-COF@PEG@AS1411 for 12 h at 37 °C (scale bar: 50 μm).

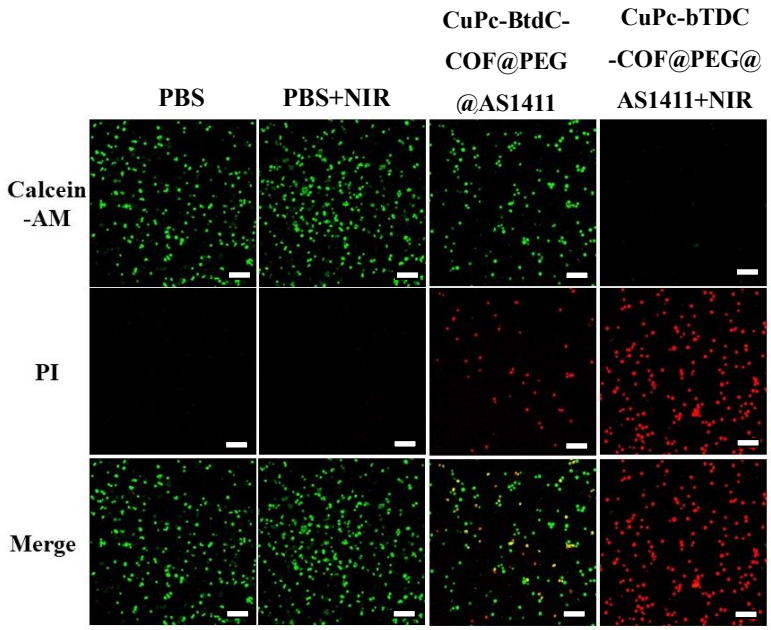

Figure 93 Fluorescence images of Calcein-AM/PI costained 4T1 cells under (a) the pure PBS, (b) PBS + NIR, (c) CuPc-bTDC-COF@PEG@AS1411, and (d) CuPc-bTDC-COF@PEG@AS1411 + NIR (scale bar: 100 μm).

Moreover, to easily comprehend the phototherapeutic performance of CuPc-bTDC-COF@PEG@AS1411, LIVE/DEAD staining kit using the calcein AM/PI were stained with 4T1 cells, in which the cell activity was determined by CLSM (**Figure 93**). It shows that no red fluorescence signal is obtained in the pure PBS and PBS + NIR groups, hinting 4T1 cell cannot be killed in these conditions. However, after 4T1 cells incubated with CuPc-bTDC-COF@PEG@AS1411, a small amount of red fluorescence

signal is clearly present, along with green fluorescence signal. It verifies that the CDT effect caused by the released Cu^{2+} ions from CuPc-bTDC-COF@PEG@AS1411 exhibits an inferior killing effect toward cancer cells. In comparison, the CuPc-bTDC-COF@PEG@AS1411 + NIR group demonstrates the strong red fluorescence signal of 4T1 cells, only remaining extremely low green fluorescence signal. It indicates that all 4T1 cells are withered in light of the integrated effects of PDT and PTT performances.

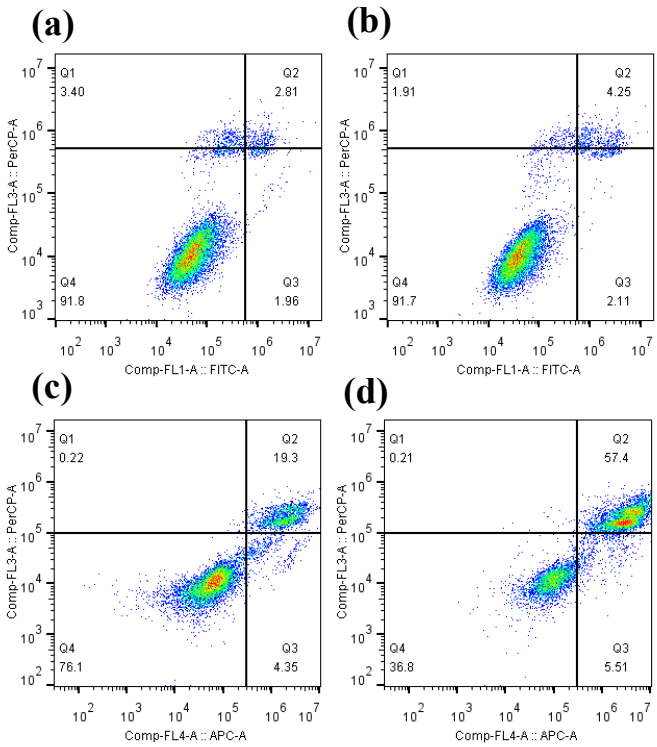

Figure 94 Flow cytometry apoptosis assay of 4T1 cells after different treatments followed by staining with Annexin-FITC and PI. The groups were (1) Control, (2) Control + NIR, (3) CuPc-bTDC-COF@PEG@AS1411, (4) CuPc-bTDC-COF@PEG@AS1411 + NIR. The concentration of CuPc-bTDC-COF@PEG@AS1411 was 100 μg mL^{-1}.

To evaluate the apoptotic and necrotic behaviors, flow cytometry was used to analyze the cell death rate. **Figures 94a** and **b** shows no visible cell apoptosisis present in the control groups treated with 808 nm laser irradiation, revealing that the sole NIR laser light irradiation cannot induce cell damage without any nanomedicine. When 4T1 cells were incubated with the CuPc-bTDC-COF@PEG@AS1411 suspension for 12 h without laser irradiation, the late apoptosis rate increases to 19.3 % (**Figure 94c**). This

finding is consistent with the above analysis, suggesting the low CDT effect can result in the death of few cancer cells. Furthermore, the late apoptosis rate of 4T1 cells under 808 nm irradiation is around 57.4 % for the CuPc-bTDC-COF@PEG@AS1411 + NIR group, illustrating the synergistic PTT/PTT is a preferred approach for cancer treatment. These findings are in line with the results of the live and dead cell staining experiments, demonstrating the superior therapy ability of CuPc-bTDC-COF@PEG@AS1411 under NIR irradiation.

9.2.4 In vivo antitumor treatment study

The in vivo synergistic PTT/PDT/CDT therapeutic efficacy under 808 nm laser irradiation was further assessed on 4T1-tumor-bearing mice model via tail vein injection (**Figure 95a**). Each mouse was intravenously injected with the PBS or CuPc-bTDC-COF@PEG@AS1411 in the first day after the tumor volume reached 70 mm^3, and laser irradiation was executed after 2 h. The mice were randomly divided into four groups (n = 5) and subjected to various treatments, including PBS (0.01 M), PBS + NIR, CuPc-bTDC-COF@PEG@AS1411, and CuPc-bTDC-COF@PEG@AS1411 + NIR. As depicted in **Figure 95b** and **95c,** the temperature of tumor tissues increasing fast at the first 5 min, and approaches an equilibrium slowly, which is consistent with their corresponded infrared thermal images. After 5 min of 808 nm laser irradiation, the local temperature at tumor tissues in the CuPc-bTDC-COF@PEG@AS1411 +NIR group increased to 49.5 °C much higher than that of the PBS + NIR group (34.8 °C). The decrease of tumor volume in the NIR group after 14 days of treatment indicated that laser irradiation had a preferable therapeutic effect on tumors (**Figure 95d**). As illustrated in **Figure 95e**, after 10 days of treatment, no discernible difference in body weight between the mice, indicating the outstanding biocompatibility of CuPc-bTDC-COF @PEG@AS1411.

Comparatively, the mice treated with CuPc-bTDC-COF@PEG@AS1411 without laser irradiation achieved a moderate tumor suppression effect, having a lower tumor growth inhibition (TGI) rate of 95.72 %, which was attributed to the PDT/PTT synergistic threapy of CuPc-bTDC-COF@PEG@AS1411. The photographs of tumor

tissues taken on day 14 are shown in **Figure 96**, which consistent with the tumor growth trend, implying that the tumor size decreases with increasing therapy time in the CuPc-bTDC-COF@PEG@AS1411+NIR groups. Further, main organs and tumors were harvested after treated and stained by H&E, for which no obvious damage and metastases can be found (**Figure 97**). This finding suggests that tumor cells can be remarkably eliminated via the PTT/PDT synergistic treatment. Based on the above results and analysis, the superior therapeutic performance can be ascribed to the CuPc-bTDC-COF@PEG@AS1411-mediated high efficient synergistic PTT/PDT therapeutic efficacy.

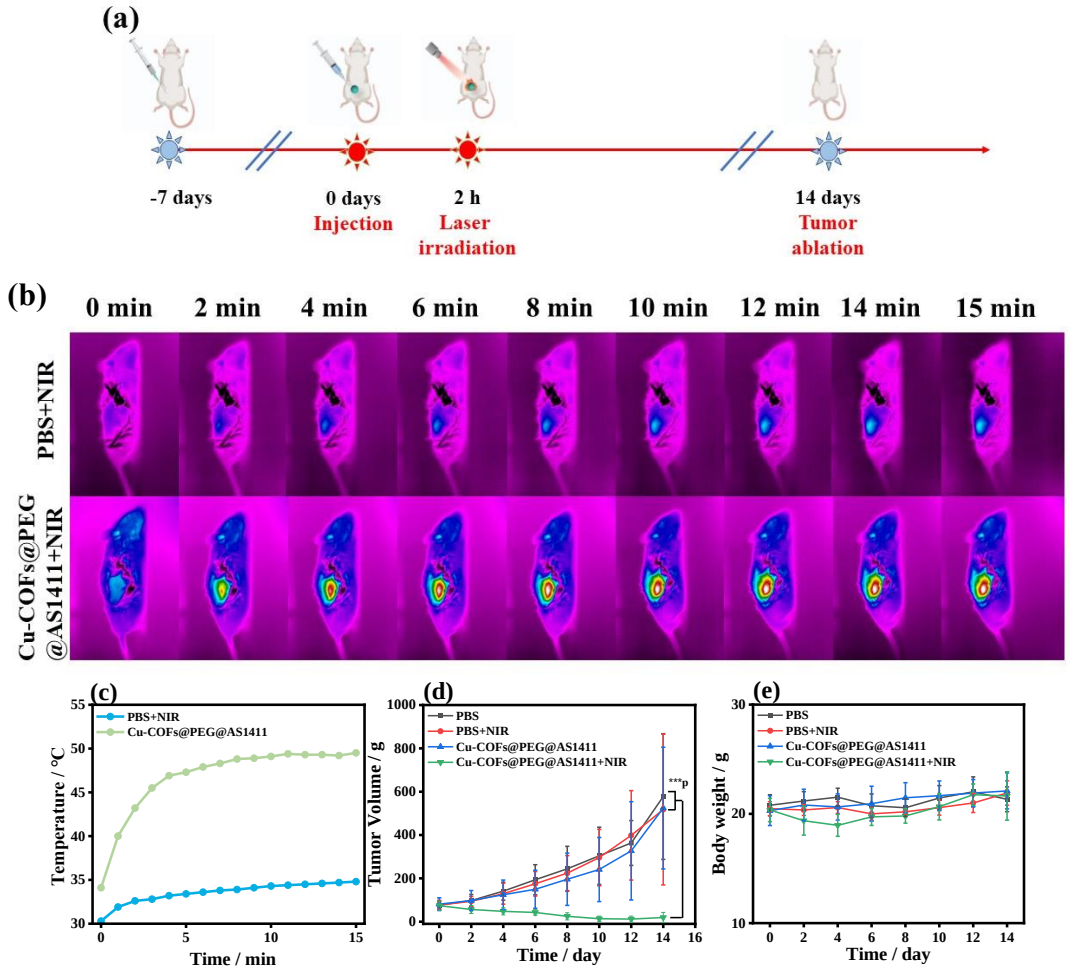

Figure 95 The in vivo synergistic PTT/PDT therapeutic efficacy of CuPc-bTDC-COF@PEG@AS1411 against 4T1-tumor-bearing mice. (a) Treatment schedule of utilizing CuPc-bTDC-COF@PEG@AS1411 for antitumor therapy. (b) Infrared thermal images of tumor when

exposing to 808 nm NIR laser for 15 min. (c) Temperature elevation curves of tumor under 808 nm laser irradiation for 15 min. (d) Tumor volume and (e) Body weight of mice after different treatments. Data are means ± SD (n = 5). *P < 0.05, ** P < 0.01, *** P < 0.001.

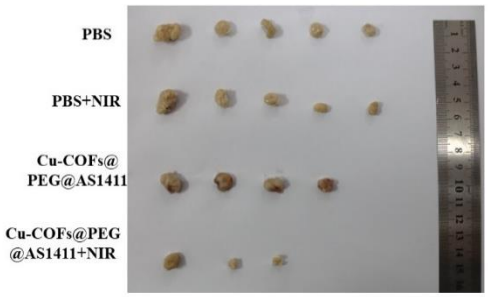

Figure 96 Photographs of tumors collected after the whole treatment were finished.

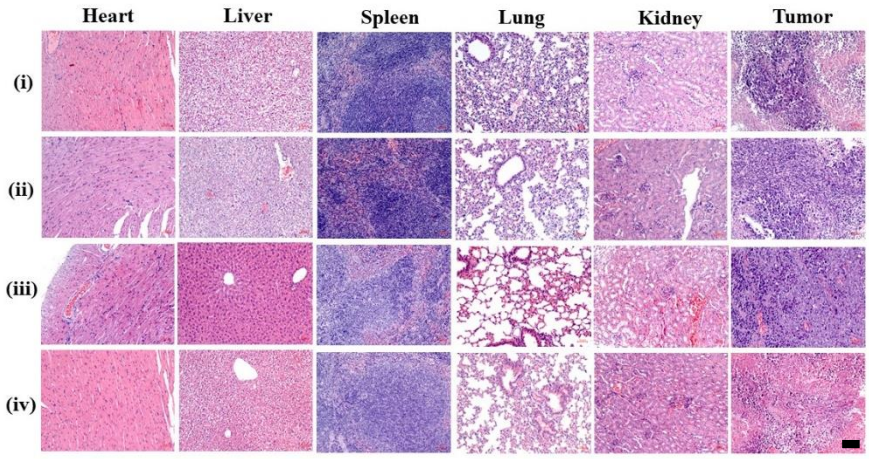

Figure 97 H&E histological staining of the main organs and tumor tissues for different groups. Scale bars: 200 μm.

9.3 Conclusions

In summary, a multimodal cancer therapy platform was provided based on CuPc-bTDC-COF, which demonstrated the efficient NIR-triggered ROS generation ability and excellent performance for cancer cell-targeted PDT/PTT therapeutic efficacy. CuPc-bTDC-COF@PEG@AS1411 were prepared as photoactive agents in the combined PDT and PTT for tumors therapy under 808 nm laser irradiation. The resulting nanoparticles have smaller size and a higher PCE of 57%. Furthermore, the CuPc-bTDC-COF@PEG@AS1411 completely inhibited the large tumor in 4T1 tumor-bearing mice by injecting only once and irradiating with a single wavelength light source. This work would extend the exploration of the COFs as a multifunctional

nanoplatform for synergistic antitumor therapy of solid tumor.

Chapter 10. Achieving integrative type-I and II photosensitizer for photoacoustic imaging-guided multimodal CDT/PTT/PDT upon the Schottky junction nanozyme of manganese-doped cobalt phthalocyanine and $Ti_3C_2T_x$ MXene nanosheets

At moment, various O_2-supplement materials (such as noble metals [185], CaO_2[186], or metal oxides [187]) have been used for reducing the effect of tumor hypoxia, thus promoting the PDT efficiency[188]. However, it could increase the complicacy of these strategies during the treatment process. To conquer this unfavorable situation, the generation of highly cytotoxic ROS [such as superoxide radical ($\bullet O_2^-$) and hydroxyl radicals (•OH)] through the type I PDT path by the NIR light irradiation, which is O_2-less-dependent, with PSs is considered to be a potential alternative [189] .More importantly, these formed $\bullet O_2^-$ and •OH species not only can be served as oxidants for killing tumor cells, but also can yield O_2 for recycling. As such, the type I PDT can overcome the deficiency of traditional type II PDT owing to hypoxic effect in tumors. Apparently, integrating type I and II mechanism for one PS can greatly enhance the treatment efficacy for tumors [190]. Unfortunately, only few PSs have demonstrated the outstanding PDT performances via both the type I and II mechanisms. In addition, PTT is also utilized as an outstanding therapy due to high tumor selectivity by the photo-irradiation, reduced systemic toxicity and stimuli-responsive feature [191] by combining the optical absorbing ability and light irradiation [192]. Meanwhile, materials with high photothermal properties can also be used as contrast agents of PAI for the diagnosis of tumors with deep tissue penetration. Guided by the real-time diagnosis of PAI, PTT could eliminate tumors more accurately, thus enhancing the therapeutic efficacy and

reducing side effects. Generally, the sole cancer therapy method often exhibits the corresponding intrinsically shortcomings, remarkably limiting the wide applications for treating cancers.

Besides phototherapy, with the aid of some metal ions (such as Fe^{2+}, Cu^{2+}, Mn^{2+} and Co^{2+}) released from nanocatalysts, which show the catalytic abilities of bio-enzymes and represented by nanozyme or mimetic enzymes, chemodynamic therapy (CDT) is also widely employed for the efficient anticancer therapy via the decomposition of H_2O_2 to high-toxic hydroxyl radicals (•OH) in tumor tissues by Fenton-type reactions[68]. Some nanomaterials have been utilized as nanozymes to trigger Fenton-like reactions for efficient melanoma therapy. In fact, low H_2O_2 concentration in tumor microenvironment (TME) leads to the limited •OH efficiency. Fortunately, •OH species generated by type I PDT can replenish and increase the H_2O_2 concentration for CDT[36]. In this regard, to improve the treatment effect toward cancer therapy, different therapy methods can be integrated for multimodal imaging-guided synergistic PTT/PDT/CDT. Particularly, to deepen the penetration into tissues and decline the harmful to normal tissue, near-infrared (NIR) light with the wavelengths from 700 to 900 nm (NIR I) is often used for the photocatalytic therapy of tumors [193]. Consequently, seeking novel multifunctional photo-stable PSs with PAI guided-PTT/type I and type II PDT/CDT synergistic therapy effect is a potential way for thorough cancer therapy.

As an important category of photosensitizers, Pc molecules with electronic delocalization of 18-electrons possess the distinct and superior NIR region absorption, low phototoxicity, and high extinction owing to highly conjugated planar structure and coordination ability toward diverse metal ions. Diverse transition metal ions can be cooridinated with nitrogen atoms bearing on Pc rings to form metalophthalocyanine complexes with $M\text{-}N_4$ (e.g. M=Zn, Ni, Fe) structures, which can be considered as outstanding active sites for driving varieties of photocatalytic reactions [The unique features and promises of phthalocyanines as advanced photosensitisers for photodynamic therapy of cancer], especially as PDT and PTT PSs or nanozymes. Like other narrow band gap photocatalysts (such as transition metal compounds, quantum

dots, or polymeric networks, nevertheless, MPcs often illustrate high recombination of photogenerated electron-hole pairs during the photocatalytic process. Under physiological conditions, however, MPcs often show minimal water solubility and serious aggregation tendencies, resulting in low PDT efficacy. To overcome this shortcoming, some MPc-based heterojunctions have been constructed with other semiconductors such as TiO_2 and ZnO. Further, most Pc-related nanomaterials are utilized as PSs via the type II mechanism, rare via the type I mechanism or both of them. Besides, most of MPc-based hybrids demonstrate outstanding PCE, having the promising applications as photocatalysts in cancer therapy when combining the PDT approach. Considering the attractive type I and II PDT ability, superior PTT performances of Pc-based PSs, and enhanced bioenzyme-like features, it is highly desirable to develop MPc-based platforms for efficient cancer therapy via the multi-modal treatment means.

Moreover, MXenes, two-dimensional (2D) transition metal carbides, carbonitrides, and nitrides, have been extensively utilized as PTT agents in the NIR region and employed in the treatment of diverse cancers [194]. As one important MXene, titanium carbide ($Ti_3C_2T_x$) exhibits high PCE for tumor ablation, suggesting a promising application potential in photo-induced cancer therapy. So far, varieties of $Ti_3C_2T_x$ MXene and their composites (such as $Ti_3C_2T_x$-Pt-PEG, 2D Ti_3C_2/g-C_3N_4 heterostructure, Ti_3C_2@chitosan-$MnFe_2O_4$, and CD@$Ti_3C_2T_x$ heterojunctions) have demonstrated remarkable PTT performance in the first near-infrared (NIR I) biowindows for the anticancer therapy. Even some $Ti_3C_2T_x$-based composites or hybrids have been employed as the multimodal anticancer agents [195], the PAI-guided type I and type II PDT with PTT and CDT still cannot be realized. Notably, the Schottky junction, which can be generated at the interface between the two diverse catalysts, has been investigated for the improvement of photocatalytic performances owing that they can effectively inhibit the charge recombination and can improve the multielectron transfer process by accumulating electrons in the cocatalyst. Thereto, different categories of Schottky junctions as excellent photocatalysts have been applied in

varieties of photocatalytic reactions. Cai et al developed a Schottky junction of Ti_3C_2@Chitosan-$MnFe_2O_4$ as a multimodal treatment nanoplatform of CDT/PTT/MRI for efficient anticancer therapy. On account of the excellent photocatalytic therapy ability of Pcs and $Ti_3C_2T_x$ MXene and potential CDT effects, it is reasonable to construct a novel Schottky junction between MPc and $Ti_3C_2T_x$ NSs for the generation of the synergistic effect to efficiently trea tumors.

Herein, we demonstrated the design and construction of a novel Schottky junction hybrid of amino-functionalized CoPc loaded with trace Mn sites and $Ti_3C_2T_x$ NSs (denoted as CoPc-TA/Mn@$Ti_3C_2T_x$) for exploring an "all in one" PAI-guided PTT/PDT/CDT multimodal therapeutic platform under NIR light irradiation (**Scheme 20**). Owing that the ultrathin nanosheet-like structure of CoPc-TA/Mn and $Ti_3C_2T_x$ matrix, the two components were self-assembed together via π–π stacking interaction to generate a Schottky junction, following by modify with PEG (represented by CoPc-TA/Mn@$Ti_3C_2T_x$@PEG) to enhance the water solubility property and biocompatibility. The produced Schottky junction substantially enhanced the electron–hole separation ability and potent redox potentials for self-supplying O_2 via the water splitting. Benefitting from the superior photocatalytic abilities of the two components, the gained CoPc-TA/Mn@$Ti_3C_2T_x$@PEG Schottky junction not only showed substantially photothermal performance under NIR light irradiation and outstanding PAI capability, but also exhibited the synergistic Type I PDT and Type II PDT performance for the production of superoxide radical ($\bullet O_2^-$) and hydroxyl radical (•OH) through electron transfer and the generation of singlet oxygen ($^1O_2$) via energy transfer. Moreover, the enhanced PTT property of the CoPc-TA/Mn@$Ti_3C_2T_x$@PEG Schottky junction also stimulated the production of •OH through Fenton-like reactions via CDT method due to the two redox pairs of Co^{2+}/Co^{3+} and Mn^{2+}/Mn^{3+} active sites. Considering good biocompatibility and high stability of the junction and the tumor-targeting property of AS1411 aptamer strand, the CoPc-TA/Mn@$Ti_3C_2T_x$@PEG@AS1411 hybrid demonstrated excellently therapeutic effect in *vivo*, attaining a high tumor growth

inhibition rate of 100%. Consequently, the developed new Schottky junction at metal phthalocyanine and $Ti_3C_2T_x$ can propose an efficient multifunctional cancer therapeutic nanoplatform.

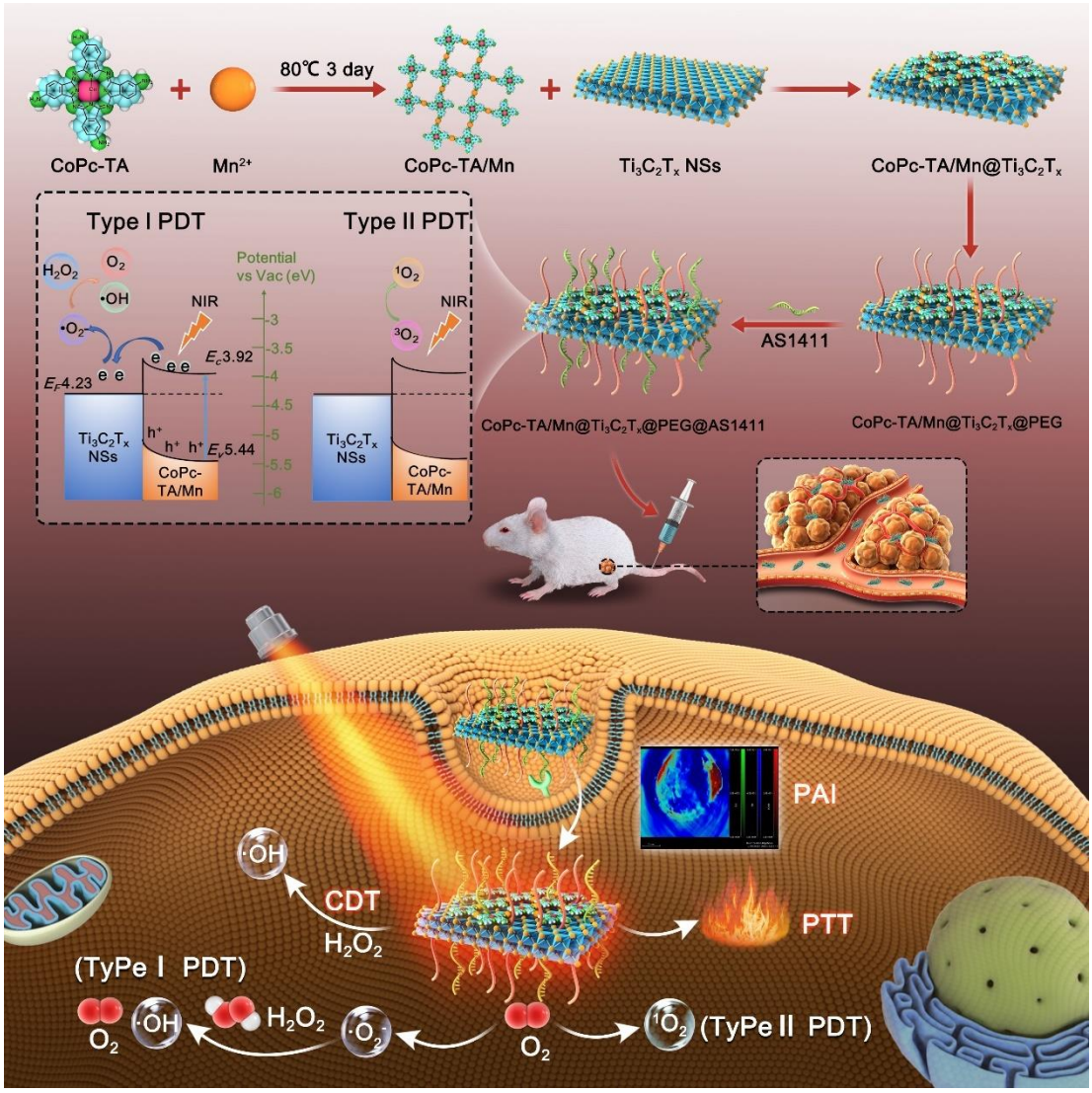

Scheme 20 Schematic illustration of CoPc-TA/Mn@$Ti_3C_2T_x$@PEG@AS1411 for NIR-light triggered synergistic PTT/PDT/CDT cancer therapy. a) Stepwise synthesis of CoPc-TA/Mn@$Ti_3C_2T_x$@PEG@AS1411. b) Schematic diagram of the synergistic anti-tumor effects via CoPc-TA/Mn@$Ti_3C_2T_x$@PEG@AS1411-based PTT/PDT/CDT ablation immunotherapy.

10.1 Experimental

10.1.1 Materials and chemicals.

4-Nitrophthalonitrile, $CoCl_2 \cdot 6H_2O$, $Mn(NO_3)_2 \cdot 6H_2O$, methylene blue (MB),

$Mn(NO_3)_2·6H_2O$, hydrogen peroxide (H_2O_2, 30%), epichlorohydrin, polyethylene glycol, triphenylphosphine, and DPBF were purchased from Shanghai Aladdin Biotechnology Co., Ltd. DMF, anhydrous methanol, and DMSO) were obtained from Tianjin Fuyu Fine Chemical Co., Ltd. Urea, manganese acetate, and epichlorohydrin were gained from Tianjin Komiou Chemical Reagent Co., Ltd. Methylene blue and triethanolamine were from Tianjin Fengchuan Chemical Reagent Co., Ltd. MTT assay, AS1411 aptamer (5′-GGT GGT GGT GGT TGT GGT GGT GGT GG-3′), DCFH-DA reactive oxygen fluorescent probe, Hoechst 33342 solution, calcein-AM/PI Double Staining Kit, DMEM, and PBS were gained from Beijing Soleibao Technology Co., Ltd. In addition, all solutions were prepared with Milli-Q water, while all reagents were of analytical grade and used without further purification.

10.1.2 Preparations of all solutions

For PDT/PTT experiments, CoPc-TA/Mn@$Ti_3C_2T_x$@PEG (10 mg) was dispersed into 10 mL Milli-Q water and ultrasonically agitated for 5 min to obtain a CoPc-TA/Mn@$Ti_3C_2T_x$@PEG aqueous dispersion (1 mg mL^{-1}). After that, the CoPc-TA/Mn@$Ti_3C_2T_x$@PEG aqueous dispersion (1 mg mL^{-1}) was diluted with Milli-Q water to the CoPc-TA/Mn@$Ti_3C_2T_x$@PEG aqueous dispersion with the concentrations of 20, 50, 80, 100, and 200 μg mL^{-1}, respectively. Additionally, CoPc-TA/Mn, $Ti_3C_2T_x$ NSs, and CoPc-TA/Mn@$Ti_3C_2T_x$ homogeneous suspensions (100 μg mL^{-1}) were separately prepared using the similar way.

For CDT experiments, CoPc-TA/Mn@$Ti_3C_2T_x$@PEG (10 mg) was dispersed in 200 mL of DMF and ultrasonically agitated for 5 min to gain the CoPc-TA/Mn@$Ti_3C_2T_x$@PEG dispersion (50 μg mL^{-1}) for the further use.

10.1.3 Preparations of all samples

Preparation of $Ti_3C_2T_x$ NSs (28). Two dimensional $Ti_3C_2T_x$ nanosheets (2D $Ti_3C_2T_x$ NSs) were synthesized according to the previous method [196]. First, LiF (0.6 g) was dissolved in HCl (10 mL, 12 M), followed by adding Ti_3AlC_2 powders (0.8 g) under the vigorous stirring for 30 min at 0 ℃. Then the temperature of the mixture increased

to 40 ℃ for 24 h. Furthermore, mixture was sonicated for 1h. After that, HCl (25 mL, 12 M) was added to the mixture under the vigorous stirring for 40 min at room temperature. The acidic mixture solution was rinsed using Milli-Q water via centrifugation for multiple cycles until a pH of 7 was achieved. Finally, bath sonication was adopted to exfoliate well-dispersed claylike solid suspension (aqueous solution) for 2 h. 2D $Ti_3C_2T_x$ NSs was obtained after centrifugation at 4000 rpm.

Synthesis of PEG-epoxide. PEG (1000 MW, 10 g, 0.01 mol) was dissolved in 20 mL of dehydrated DMF containing 1% (w/v) of triethanolamine at 40 ℃ for 4 h under stirring. Then, 4.5 g epichlorohydrin was added, followed by stirred overnight under reflux to convert the terminal hydroxyl group of PEG into an epoxide. The resulting mixture was precipitated in cold diethyl ether and then washed repeatedly with diethyl ether. The epoxide-derived PEG (PEG-epoxide) was obtained after drying under vacuum.

Preparation of CoPc-TA/Mn (29) and the CoPc-TA/Mn@$Ti_3C_2T_x$ (30) Schottky junction. CoPc-TA was synthesized according to the previous work [197]. Afterward, CoPc-TA suspension (63 mg, 0.1 mmol) was dispersed in 4 mL of Milli-Q water, forming the homogenerous suspension. After mixing with 28 μL of trimethylamine and 2 mL of acetonitrile, $Mn(NO_3)_2{\cdot}6H_2O$ (14.45 mg, 0.05 mmol) was added and thoroughly stirred at 80 °C for 4 days, guaranteeing a certain Mn^{2+} ions were adsorbed into CoPc-TA network. Subsequently, the above suspension was centrifuged, followed by washing with Milli-Q water thrice. After drying in vacuum at 60 °C, the dark green CoPc-TA/Mn powder was obtained. In this case, Mn^{2+} ions can coordinate with abundant amino moieties bearing on CoPc-TA to produce the CoPc-TA/Mn complex.

In addition, CoPc-TA/Mn@$Ti_3C_2T_x$ hybrid was prepared by adding 10 mg exfoliated $Ti_3C_2T_x$ NSs into the CoPc-TA/Mn suspension (1.6 mmol mL^{-1}, 20 mL) and stirred for 24 h. Subsequently, the gained CoPc-TA/Mn@$Ti_3C_2T_x$ mixture was post-treated by the resemble method with CoPc-TA/Mn. Owing to π–π^* stacking interaction between the conjugated CoPc-TA molecules and ultra-thin $Ti_3C_2T_x$ NSs [198], the two components can be closely assembled.

Preparation of CoPc-TA/Mn@$Ti_3C_2T_x$@PEG (31) and CoPc-TA/Mn@$Ti_3C_2T_x$@PEG@AS1411 (32) To improve the dispersion ability and biocompatibility, the PEGylation of CoPc-TA/Mn@$Ti_3C_2T_x$ was carried out according to the reported literature[63]. Typically, CoPc-TA/Mn@$Ti_3C_2T_x$ (50 mg), PEG-epoxide (500 mg), and triphenylphosphine (12.5 mg) were dispersed in DMSO (20 mL) and thoroughly stirred until a transparent homogeneous suspension was obtained. Afterward, the mixture reacted under constant stirring at 190 ºC for 4 h, following by precipitating in cold diethyl ether. Finally, the resulting was rinsed thrice with cold diethyl ether. After dried under vacuum, the CoPc-TA/Mn@$Ti_3C_2T_x$@PEG hybrid was gained.

The CoPc-TA/Mn@$Ti_3C_2T_x$@PEG@AS1411 hybrid was prepared by incubating CoPc-TA/Mn@$Ti_3C_2T_x$@PEG with the aptamer AS1411 solution (1 mL, 3 μM) at 4 °C for 2 h. The resulting suspension was centrifuged at 8000 rpm for 3 min, following by washing with PBS to remove the unabsorbed AS1411 strands. Due to the highly-conjugated nanostructure and rich amino group of CoPc-TA/Mn@$Ti_3C_2T_x$@PEG, AS1411 strands can be immobilized over CoPc-TA/Mn@$Ti_3C_2T_x$@PEG via π–π stacking and electrostatic interaction [199]. The resulted CoPc-TA/Mn@$Ti_3C_2T_x$@PEG@AS1411 was stored in a refrigerator 4 °C for further experiments.

10.1.4 In vitro photothermal effect

In prior to the light irradiation measurements, the CoPc-TA/Mn@$Ti_3C_2T_x$@PEG suspension with diverse concentrations (0, 20, 50, 80, 100, and 200 μg mL^{-1}) and CoPc-TA/Mn, $Ti_3C_2T_x$ NSs, and CoPc-TA/Mn@$Ti_3C_2T_x$ suspension (100 μg mL^{-1}) were separately prepared. The different suspensions (2 mL) were transferred to a 4 mL of centrifugal tube and irradiated under a NIR 808 nm laser for 10 min, separately. The heat distribution and the system temperature were recorded by a thermal imaging camera and electronic thermometer, respectively, to test the photothermal performance. Different laser power densities (0.3, 0.65, and 1 W cm^{-2}) of the laser light were also adopted to modulate the temperature.

10.1.5 In vitro degradation and response test

Detection of •OH and $^1O_2$ species

To evaluate the chemodynamic activity of the developed catalysts, MB was used as an indicator to evaluate the generation of •OH. Firstly, CoPc-TA/Mn@$Ti_3C_2T_x$@PEG (50 μg mL^{-1}, 0.2 mL) and MB (100 μg mL^{-1}, 0.1 mL) were dispersed in DMF (1.5 mL), and stirred for 5 min to form a homogeneous solution. Subsequently, both H_2O_2 (0.1 mL, 50 mM) and $NaHCO_3$ (0.1 mL, 250 mM) were added into the mixed solution. The generation rate of •OH was detected by measuring the absorbance changes of MB at 664 nm at different time points. In addition, the chemodynamic activities of other samples, including CoPc-TA, CoPc-TA/Mn, and CoPc-TA/Mn@$Ti_3C_2T_x$ were also investigated by the same way. Further, the degradation abilities of CoPc-TA/Mn@$Ti_3C_2T_x$@PEG in diverse environments with different pH solutions (pH = 5.4, 6.4, and 7.4) were determined.

Intracellular ROS measurements

The generation of intracellular ROS was detected by DCFH-DA in mouse melanoma B16 cells. Typically, B16 cells were seeded into cell culture dish at a density of 1×10^5 per well and incubated with 2 mL 1640 medium for 24 h. After that, each of the fresh 1640 medium containing CoPc-TA/Mn@$Ti_3C_2T_x$@PEG (100 μg mL^{-1}) was added and incubated for 6 h, followed by washing with PBS thrice. DCFH-DA (20 μM) was incubated with B16 cells with or without stimulating factors, including (1) control, (2) CoPc-TA/Mn@$Ti_3C_2T_x$@PEG, (3) CoPc-TA/Mn@$Ti_3C_2T_x$@PEG + NIR, (4) CoPc-TA/Mn@$Ti_3C_2T_x$@PEG + H_2O_2 (10 μM), and (5) CoPc-TA/Mn@$Ti_3C_2T_x$@PEG + NIR + H_2O_2 (10 μM) for further incubation at 37 °C for 20 min. Finally, CLSM was used for measuring the intracellular ROS generation in each well when excited at 488 nm.

10.1.6 Cytotoxicity measurements

The cytotoxicity of CoPc-TA/Mn, $Ti_3C_2T_x$ NSs, CoPc-TA/Mn@$Ti_3C_2T_x$, and CoPc-TA/Mn@$Ti_3C_2T_x$@PEG were measured by typical MTT assay against L929 and

mouse melanoma cells B16, separately. Typically, B16 cells (1×10^5) were seeded into 96-well plates and cultured for 24 h (37 °C, 5% CO_2), and then separately incubated with different concentrations of CoPc-TA/Mn, $Ti_3C_2T_x$ NSs, CoPc-TA/Mn@$Ti_3C_2T_x$, and CoPc-TA/Mn@$Ti_3C_2T_x$@PEG suspensions for 24 h. The cells were rinsed gently with PBS to remove incompletely internalized materials, and 200 μL Roswell Park Memorial Institute (RPMI-1640) was added to each well. After further incubation for 12 h at 37 °C , 20 μL of MTT (5 mg mL^{-1} in PBS) was added into per well and cultured in the incubator for 4 h. At last, the medium was removed, following by added 150 μL of DMSO to per well. The cell viability was monitored by measuring the absorbance at 490 nm using a microplate reader (WD-2102A).

10.1.7 Intracellular CDT, PTT/PDT, and PTT/PDT/CDT performances

To study the in vitro CDT, PTT/PDT, and PTT/PDT/CDT efficiency, B16 cells were seeded into 96-well plates and separately incubated with different concentrations of CoPc-TA/Mn@$Ti_3C_2T_x$@PEG suspensions (0, 20, 50, 80, 100 and 200 μg mL^{-1}). After 24 h, to evaluate the therapy performance, four groups of B16 cells were cultured with different treatments, including (i) CoPc-TA/Mn@$Ti_3C_2T_x$@PEG, (ii) CoPc-TA/Mn@$Ti_3C_2T_x$@PEG + H_2O_2 (10 μL, 10 μM), (iii) CoPc-TA/Mn@$Ti_3C_2T_x$@PEG + NIR (1 W cm^{-2}, 10 min), and (iv) CoPc-TA/Mn@$Ti_3C_2T_x$@PEG + NIR (1 W cm^{-2}, 10 min) + H_2O_2 (10 μL, 10 μM) for 24 h. Then, B16 cells were washed with PBS and cultured for another 12 h. Subsequently, MTT solution (20 μL, 5 mg mL^{-1} in PBS) was introduced in each well and incubated for 4 h at 37 °C. The formed formazan crystals were dissolved by adding 150 μL of DMSO into per well. The CDT, PTT/PDT, and PTT/PDT/CDT efficacy were calculated by detecting the absorbance of each well solution at 490 nm and 600 nm with a microplate reader.

10.1.8 In vivo and in vitro PA imaging

The suspensions of CoPc-TA/Mn@$Ti_3C_2T_x$@PEG@AS1411 with various concentrations (20, 40, 80, 100, and 200 μg mL^{-1}) were separately prepared for in vitro PAI with NIR 808 nm laser irradiation, in which the PA signals were obtained on mouse

photoacoustic tomographic system (Thera Medical, InVision 256-TF, German). For in vivo PAI, 200 μL of CoTAPc/Mn@Ti_3C_2@PEG@AS1411 (200 μg mL^{-1}) was intravenously injected into B16-tumor-bearing mice. Meanwhile, PA images were taken at different time intervals post-injection (0, 1, 2, 3, 4, 5, and 6 h) after anesthetized with isoflurane.

10.1.9 Evalution of the target ability of CoPc-TA/Mn@$Ti_3C_2T_x$@PEG@AS1411 with B16 cells

B16 cells and L929 cells were migrated from the culture flasks to the bottom of cell culture dishes, respectively. Cells were seeded 20 mm glass-bottom culture dishes with 1 mL of medium and cultured for 24 h. After removing the medium, CoPc-TA/Mn@$Ti_3C_2T_x$@PEG@5' Cy3-labeled AS1411(100 μg mL^{-1}, 1 mL) was added in every 20 mm glass-bottom culture dishes and cultured for 4 h. After rinsing three times by PBS, the nucleus was stained with 20 μL of Hoechst 33258 (2 μg μL^{-1}) at 37 °C for 15 min and then rinsing with PBS additional thrice. Finally, the cells fixed with 4% cold paraformaldehyde for 15 min, followed by rinsing with PBS thrice. The targeting effect of AS1411 in the cellular uptake of CoPc-TA/Mn@Ti_3C_2@PEG@AS1411 was evaluated by CLSM (excited at 532 nm).

10.1.10 In vivo antitumor treatment study

Female BALB/C mice (4-6 weeks) were purchased from Hunan Slaccas Jingda Laboratory Animal Co., Ltd (Hunan, China), and raised in the SPF animal room. All animal procedures were approved by the Animal Research Ethics Committee of Medical School, Henan University. (Document HZYX-2021-011). The B16 tumor-bearing nude mice models were successfully established when the tumor volume was about 70 mm^3. The mice were divided into four groups by the random allocation, including PBS, PBS + NIR, CoPc-TA/Mn@$Ti_3C_2T_x$@PEG@AS1411, CoPc-TA/Mn@$Ti_3C_2T_x$@PEG@AS1411 + NIR. Typically, CoPc-TA/Mn@$Ti_3C_2T_x$@PEG@AS1411 (200 μL, 200 μg mL^{-1}) or PBS were administrated into the mice by intravenous injection. After 2 h, the groups of PBS + NIR and CoPc-

TA/Mn@$Ti_3C_2T_x$@PEG@AS1411 + NIR were treated with NIR irradiation (0.8 W cm^{-2}, 10 min). Then, the body weight and tumor volume of all mouse groups were measured every other day. After two weeks, all dissected tumors were collected for photography.

10.1.11 Histological examinations

After the treatments were finished, the main organs and tumors for each group were collected and washed with PBS for further H&E and TUNEL staining analysis under an optical microscope.

10.1.12 Statistical analysis

All statistical analysis were used the same methods as chapter 9.1.13.

10.2 Results and discussion

10.2.1 FESEM and TEM

SEM images of CoPc-TA/Mn@$Ti_3C_2T_x$ (**Figures 98a** and **98b**) showed that large amounts of NPs are stacked together with larger NSs. **Figures 99a** and **99b** indicated CoPc-TA/Mn NPs were embedded within $Ti_3C_2T_x$ NSs, suggesting the successful integration of the two components. As shown in **Figure 99c**, the high-resolution TEM (HR-TEM) image of CoPc-TA/Mn@$Ti_3C_2T_x$ demonstrated a clear lattice spring of 0.25 nm, corresponding to the crystal planes of (103) of $Ti_3C_2T_x$ NSs [200]. Further, the selective-area electron diffractometry (SAED) pattern of CoPc-TA/Mn@$Ti_3C_2T_x$ (**Figure 99c**, inset) demonstrated a ring pattern, suggesting its low crystallinity. Also, the EDS mapping image of CoPc/TA@Mn@$Ti_3C_2T_x$ (**Figure 99e**) depicted that Co, Mn, C, and N elements were homogeneously dispersed in the whole horizon. However, Ti element was only found within the $Ti_3C_2T_x$ region. According to the EDS spectrum of CoPc-TA@Mn@Ti_3C_2, around 64.45% of C element, 4.90% for Ti, 15.14% for N, and 11.49% for O were found, accompanying with low contents of Co (2.45%) and Mn (1.57%). In addition, CoPc-TA/Mn@$Ti_3C_2T_x$@PEG (**Figures 98c** and **98d**) comprised a large number of NPs with larger size than CoPc-TA@Mn@Ti_3C_2, revealing the successful modification with PEG. Notably, the high-angle annular dark-field scanning

TEM (HAADF-STEM) image of CoPc-TA/Mn@$Ti_3C_2T_x$ (**Figure 99d**) demonstrated some bright dots highlighted by yellow circles, which is possibly due to the atomically dispersed metal sites.

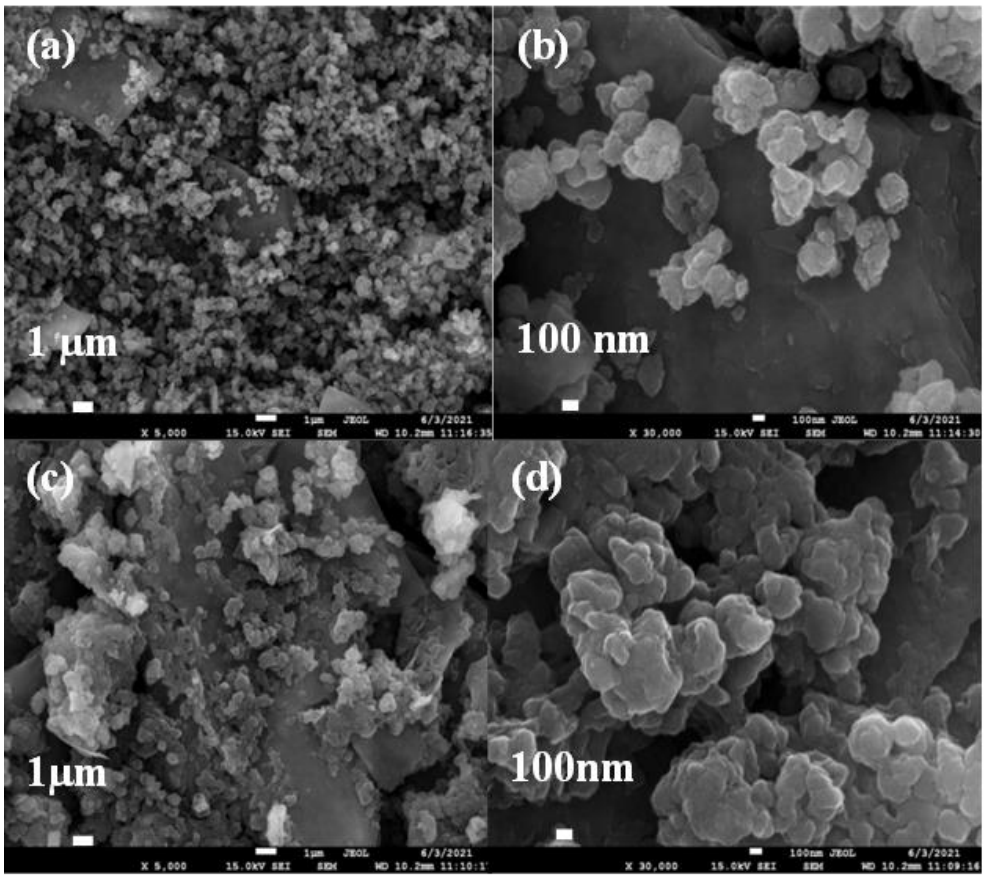

Figure 98. Low and high-magnification SEM images of (a, b) CoPc-TA/Mn@$Ti_3C_2T_x$, and (c, d) CoPc-TA/Mn@$Ti_3C_2T_x$ @PEG.

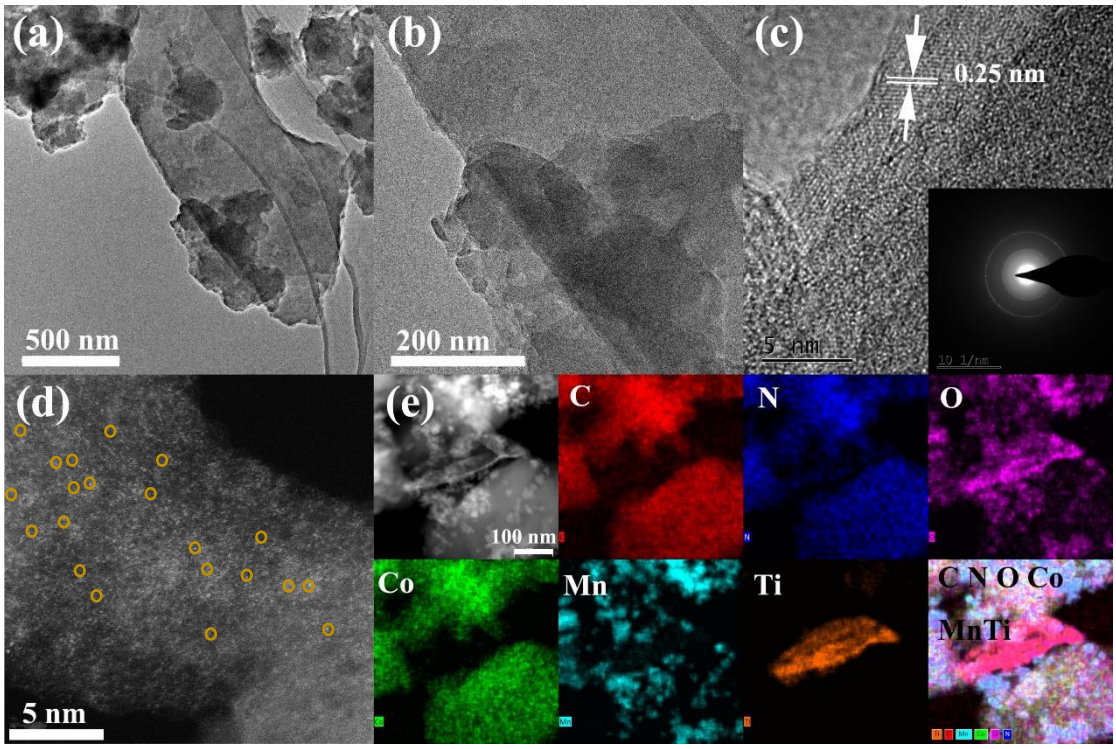

Figure 99. (a,b,c) Low-, high-magnification, and high-resolution TEM images of CoPc-TA/Mn@$Ti_3C_2T_x$ (Inset: SAED pattern of CoPc-TA/Mn@$Ti_3C_2T_x$). (d) HAADF-STEM image of CoPc-TA/Mn@$Ti_3C_2T_x$ and (e) corresponding EDS image of CoPc-TA/Mn@$Ti_3C_2T_x$: C (red), N (blue), O (amaranth), Co (green), Mn (cyan) and Ti (orange).

The SEM image of CoPc-TA (**Figure 100a**) showed that it consists of many irregularly shaped nanoparticles (NPs). It TEM image (**Figure 100b**) demonstrated NPs were accumulated with multilayer NSs. No distinct lattice spring was observed in the high-resolution TEM (HR-TEM) image (**Figure 100c**), revealing its amorphous structure. Further, the high-angle annular dark-field scanning TEM (HAADF-STEM) and energy-dispersive X-ray spectroscopy (EDS) mapping images of CoPc-TA (**Figure 100d**) suggested the homogeneous distribution of Co, C and N elements in the whole selected region. These finding were consistent with the reported literature [201]. In addition, CoPc-TA/Mn complex illustrated the similar surface morphology and nanostructure (**Figure 100e**). The HAADF-STEM and EDS mapping images of CoPc-TA/Mn (**Figure 100h**) also suggested Co, Mn, C, and N were homogeneously dispersed in the whole horizon. According to the EDS spectrum of CoPc-TA/Mn, the atomic contents of Co, Mn, C, O and N were around 4.40, 8.47, 69.72, 7.06 and 10.35 %,

respectively.

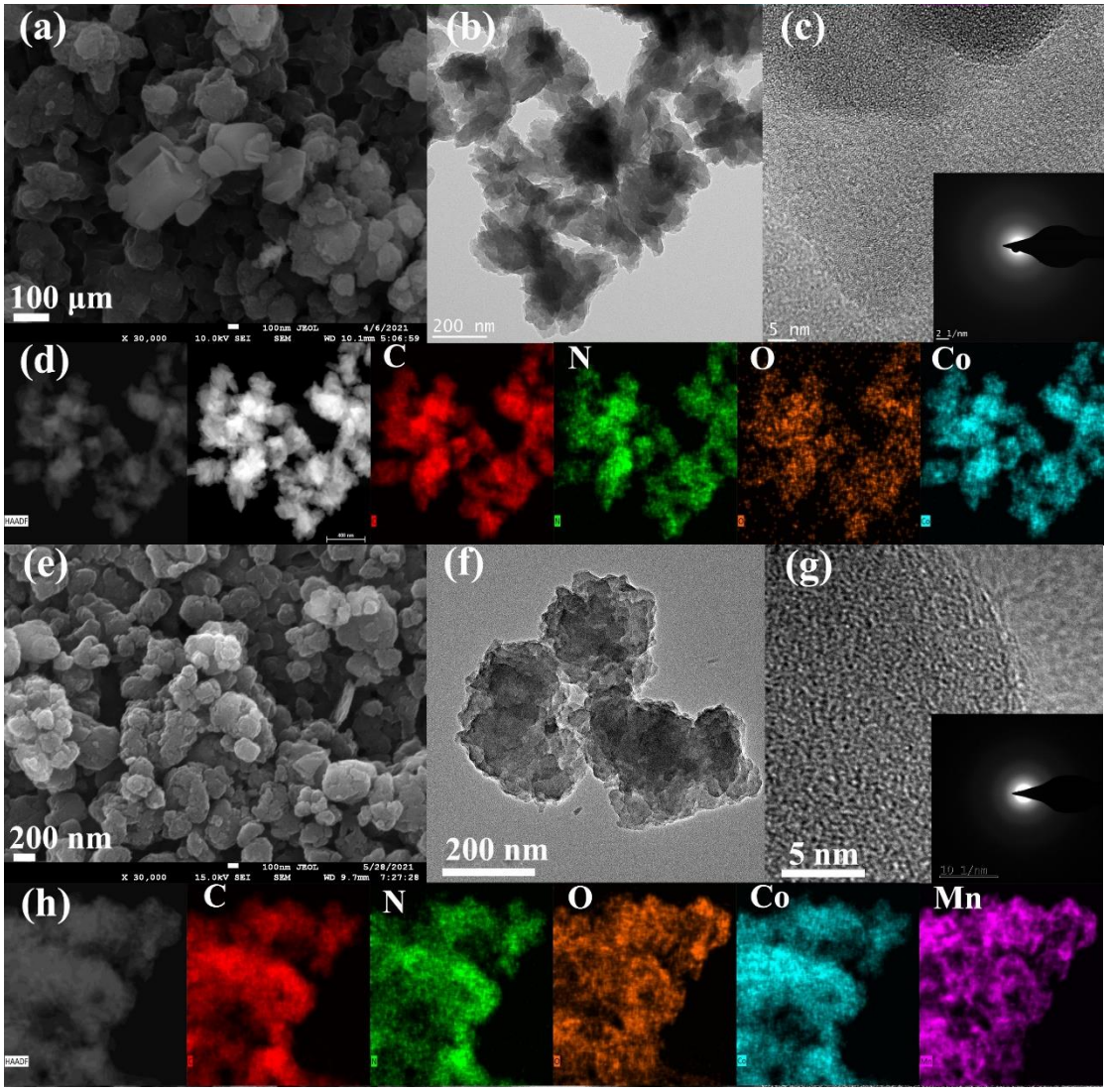

Figure 100. (a) SEM images and (b, c) high-resolution TEM images of CoPc-TA (Insert: SAED pattern of CoPc-TA). (d) HAADF-STEM image and corresponding EDS element maps of CoPc-TA: Co (blue), C (red), O (orange) and N (green). (e) SEM image and (f, g) high-resolution TEM images of CoPc-TA/Mn (Insert: SAED pattern of CoPc-TA/Mn). (h) HAADF-STEM image and corresponding EDS element maps of CoPc-TA/Mn: Co (blue), Mn (amaranth), C (red), O (orange) and N (green)

The SEM image of $Ti_3C_2T_x$ NSs (**Figure 101a**) indicated thin NS-like shape with irregular size, which was consistent with the TEM image (**Figure 101b** and **101c**). Also, $Ti_3C_2T_x$ lamellas were almost transparent, hinting the successful preparation of ultrathin NSs of $Ti_3C_2T_x$ MXene. A clear interplanar spacing of ~1.2 nm was observed in the

HR-TEM image of $Ti_3C_2T_x$ NSs, further proving the observation of NSs. The HAADF-STEM and EDS mapping images of $Ti_3C_2T_x$ NSs (**Figure 101d**) revealed that Ti, C, and N were homogeneously dispersed in the selected area, along with the atomic content of 46.8%, 31.55%, 10.52%, and 11.12%, respectively.

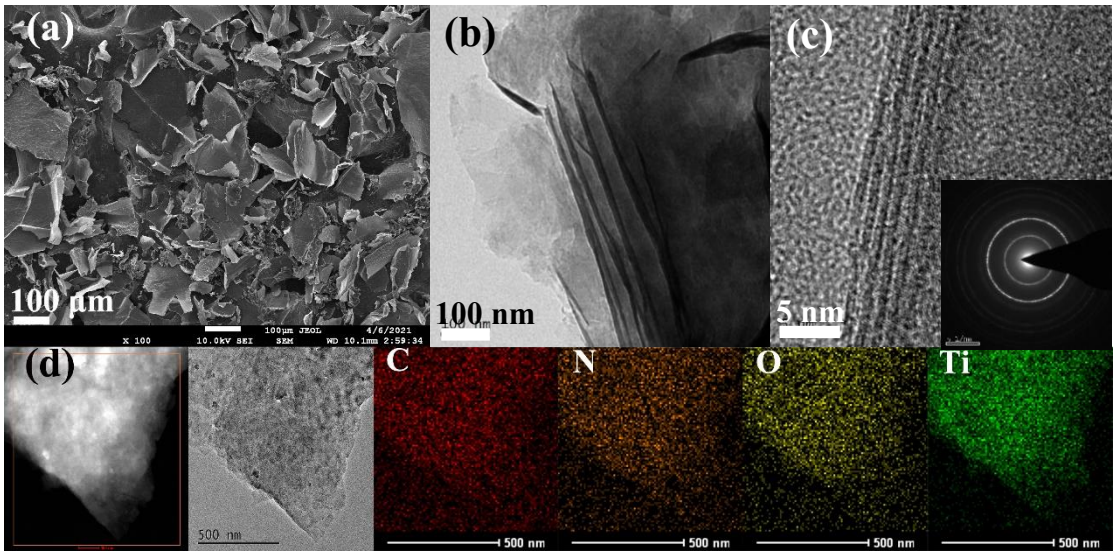

Figure 101. (a) SEM image and (b, c) TEM and high-resolution TEM images of $Ti_3C_2T_x$ NSs (Insert: SAED pattern of MXene). (d) HAADF-STEM image and corresponding EDS element maps of $Ti_3C_2T_x$ NSs: Ti (cyan), C (red), O (yellow) and N (brown).

10.2.2 XRD

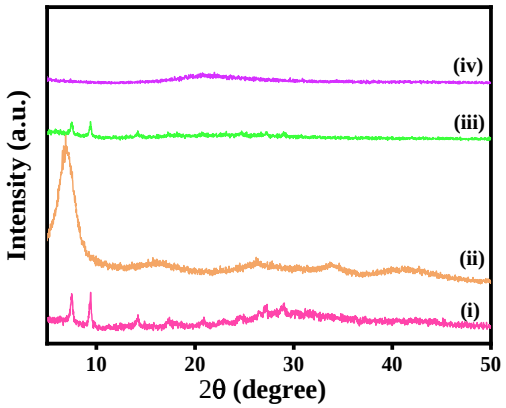

Figure 102. (a) XRD patterns of (i) CoPc-TA/Mn, (ii) $Ti_3C_2T_x$ NSs, (iii) CoPc-TA/Mn@$Ti_3C_2T_x$, and (iv) CoPc-TA/Mn@$Ti_3C_2T_x$@PEG.

The XRD pattern of $Ti_3C_2T_x$ NSs showed the diffraction peaks at $2\theta = 6.94°$, which was assigned to (002) plane of $Ti_3C_2T_x$ NSs. Further, a distinct broad peak shifted from 9.57° to 6.94° compared to $Ti_3C_2T_x$ MXene, indicating the enlargement of interlayer spacing, which make for the intercalation of CoPc-TA/Mn. Besides, the XRD pattern of CoPc-TA/Mn displayed the diffraction peaks at 2θ = 7.54°, 9.45°, 14.24°, 17.42°, 27.17°, and 29.03°, similar with those of CoPc-TA [194]. The resemble characteristic diffraction peaks were observed for CoPc-TA/Mn@$Ti_3C_2T_x$, suggesting the full overlap of $Ti_3C_2T_x$ NSs with CoPc-TA/Mn. After modifying by PEG, the low and relatively broad peaks in the XRD pattern indicated the amorphous feature of CoPc-TA/Mn@$Ti_3C_2T_x$@PEG.

10.2.3 UV-visible (UV-vis) absorption spectra

Figure 103 indicated the UV-visible (UV-vis) absorption spectra of CoPc-TA/Mn, $Ti_3C_2T_x$ NSs, CoPc-TA/Mn@$Ti_3C_2T_x$, and CoPc-TA/Mn@$Ti_3C_2T_x$@PEG in DMF solvent. The absorbance peak ranging from 248 to 850 nm was observed for $Ti_3C_2T_x$ NSs owing to the black color of $Ti_3C_2T_x$ NSs. An obvious absorption of intense B-band (275-500 nm) nm was found for the three CoPc-TA-related samples, accompanying with the Q-band (540-850 nm). As compared, the B-band region of both CoPc-TA/Mn@$Ti_3C_2T_x$ and CoPc-TA/Mn/$Ti_3C_2T_x$@PEG was wider than that of CoPc-TA/Mn, which was mainly attributed to the π-π interaction between CoPc-TA and

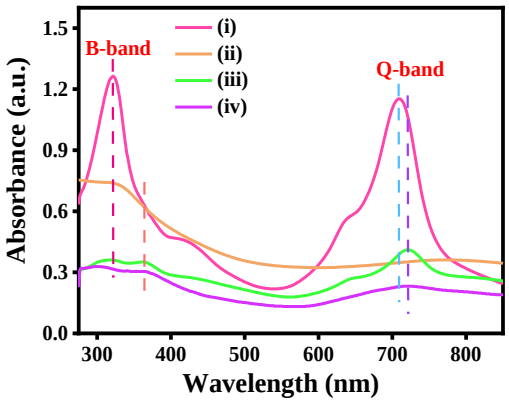

Figure 103 UV-vis absorption of (i) CoPc-TA/Mn, (ii) $Ti_3C_2T_x$ NSs, (iii) CoPc-TA/Mn@$Ti_3C_2T_x$, and (iv) CoPc-TA/Mn@$Ti_3C_2T_x$@PEG.

$Ti_3C_2T_x$. Further, the Q-band of CoPc-TA/Mn@$Ti_3C_2T_x$ and CoPc-TA/Mn@$Ti_3C_2T_x$@PEG had a red-shift of 12 nm compared with CoPc-TA/Mn, which was ascribed to the decrease in the bandgap between the highest occupied molecular orbital (HOMO) and the lowest unoccupied molecular orbital (LUMO).

10.2.4 FT-IR absorption spectra

The FT-IR spectrum of CoPc-TA/Mn (**Figure 104**) illustrates the similar characteristic absorption peaks with CoPc-TA. The peaks 1610, 1358, 830, and 736 cm^{-1} are ascribed to Pc skeletal vibrations. The absorption bands at ~1523, 1421, and 736 cm^{-1} correspond to stretching of aromatic phenyl ring, C-N in-plane, and C–H out-of-plane bending vibrations, respectively. Additionally, the characteristic peaks ranging from 3218 to 3350 cm^{-1} are due to amino moiety. As compared, the analogous FT-IR spectrum of CoPc-TA/Mn@$Ti_3C_2T_x$ is observed, but with two additional weak peaks at ~2928 and 2857 cm^{-1}, which are assigned with g-aliphatic C-H emanated from $Ti_3C_2T_x$ NSs. Moreover, the FT-IR spectrum of CoPc-TA/Mn@$Ti_3C_2T_x$@PEG demonstrate three additional peaks at ~1315, 1024, and 950 cm^{-1}, which are assigned with CH_2 wagging vibration, C-O-C, and CH_2 wagging vibration, respectively, arising from the PEG chain. These appearances hint the successful hybridization of CoPc-TA/Mn@$Ti_3C_2T_x$ with PEG, which not only can greatly enhance water-solubility, but also improve biocompatibility of the developed catalyst.

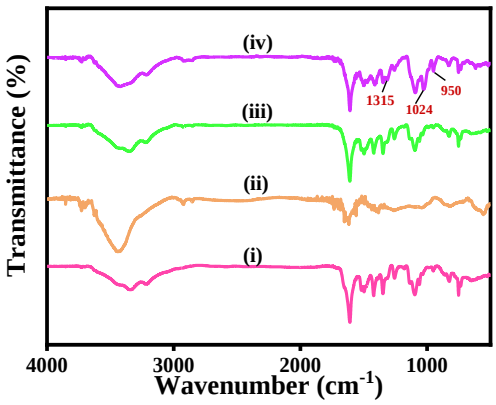

Figure 104 FT-IR spectra of (i) CoPc-TA/Mn, (ii) $Ti_3C_2T_x$ NSs, (iii) CoPc-TA/Mn@$Ti_3C_2T_x$, and (iv) CoPc-TA/Mn@$Ti_3C_2T_x$@PEG.

10.2.5 Photo-luminescence

As depicted in **Figure 105**, a prominent peak is observed in the photo-luminescence (PL) spectrum for CoPc-TA/Mn at 706 nm upon the excitation at 600 nm, which was caused by the photogenerated electron–hole pair recombination of the CoPc-TA/Mn. The emission spectrum for $Ti_3C_2T_x$ NSs exhibited a strong peak at 580 nm under the excitation wavelength of 373 nm. It corresponded to the emission of free and bound excitons produced by oxygen vacancies and surface defects of $Ti_3C_2T_x$ NSs. Owing that the absorption spectrum of $Ti_3C_2T_x$ NSs did not shows any overlap with the emission spectrum of CoPc-TA/Mn (**Figures 103** and **105**), the PL intensity of CoPc-TA/Mn solution was markedly quenched by adding $Ti_3C_2T_x$ NSs. Hence, in terms of CoPc-TA/Mn@$Ti_3C_2T_x$ and CoPc-TA/Mn@$Ti_3C_2T_x$@PEG, the fluorescence emission spectra showed a strong peak at 580 nm under the same excitation wavelength, significantly weaker than that of $Ti_3C_2T_x$ NSs. In other words, the photogenerated electrons of the excited CoPc-TA/Mn transferred to the conduction band (CB) of $Ti_3C_2T_x$ NSs. This result was testified by the relative energy band levels of CoPc-TA/Mn and $Ti_3C_2T_x$ NSs.

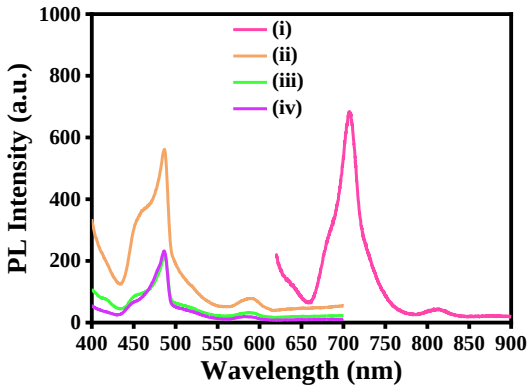

Figure 105 PL spectra of (i) CoPc-TA/Mn, (ii) $Ti_3C_2T_x$ NSs, (iii) CoPc-TA/Mn@$Ti_3C_2T_x$, and (iv) CoPc-TA/Mn@$Ti_3C_2T_x$@PEG.

10.2.6 X-ray photoelectron spectroscopy

The XPS survey scan spectra (**Figure 106**) showed that distinct Co 2*p* (779.8 eV), C 1*s* (284.9 eV), N 1*s* (398.0 eV), and O 1*s* (531.5 eV) signals were co-existed in all

samples, while an additional weak signal of Mn 2*p* (630.0 eV) was present in CoPc-TA/Mn, CoPc-TA/Mn@$Ti_3C_2T_x$, and CoPc-TA/Mn@$Ti_3C_2T_x$@PEG.

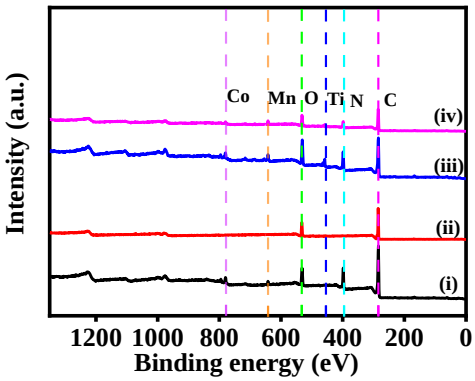

Figure 106. XPS survey scan spectra of (i) CoPc-TA/Mn, (ii) $Ti_3C_2T_x$ NSs, (iii) CoPc-TA/Mn@$Ti_3C_2T_x$, (iv) CoPc-TA/Mn@$Ti_3C_2T_x$@PEG, and (v) CoPc-TA/Mn@$Ti_3C_2T_x$@PEG@AS1411.

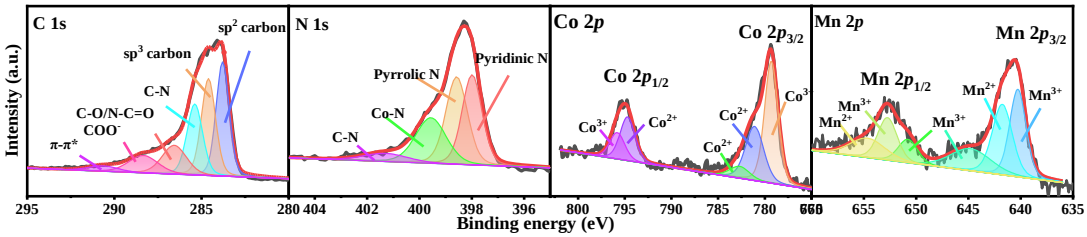

Figure 107 High-resolution XPS spectra of C 1*s*, N 1*s*, Co 2*p*, and Mn 2*p* of CoPc-TA/Mn@$Ti_3C_2T_x$.

As for CoPc-TA/Mn@$Ti_3C_2T_x$ (**Figure 107**) and CoPc-TA/Mn@$Ti_3C_2T_x$@PEG (**Figure 108**), besides of clear C 1*s*, N 1*s*, O 1*s*, and Co 2*p* signals, the clear Ti 2*p* (458.2 eV) signal also appears, hinting the presence of $Ti_3C_2T_x$. **Figure 108a** indicated the C 1*s* XPS spectra of CoPc-TA (curve *i*) and CoPc-TA@Mn (curve *ii*) were deconvoluted into bulk sp^2 carbon (283.7 eV), sp^3 carbon (284.5 eV), C-C (285.3 eV), C-O (286.2 eV), N-C=O (286.7 eV), and COO (288.6 eV). Among them, the presence of sp^2 carbon revealed highly conjugated structure, while C-N was emanated from Pc rings. Both N-C=O and COO groups verified the partial oxidization of CoPc-TA. In terms of CoPc-TA/Mn@$Ti_3C_2T_x$ (**Figure 107**), an additional peak at the BE of 290.6 eV was fitted out, corresponding to π–π^* moiety. As for CoPc-TA/Mn@$Ti_3C_2T_x$@PEG (curve *iii*, **Figure 108a**), the similar deconvoluted groups was obtained, but without π–π^* moiety, indicating the cover of PEG layer. The N 1*s* XPS spectrum of all samples (**Figure 107**

and **108b**), including CoPc-TA, CoPc-TA/Mn, CoPc-TA/Mn@$Ti_3C_2T_x$, and CoPc-TA/Mn@$Ti_3C_2T_x$@PEG, illustrated the similar deconvolutions. Four peaks at the BEs

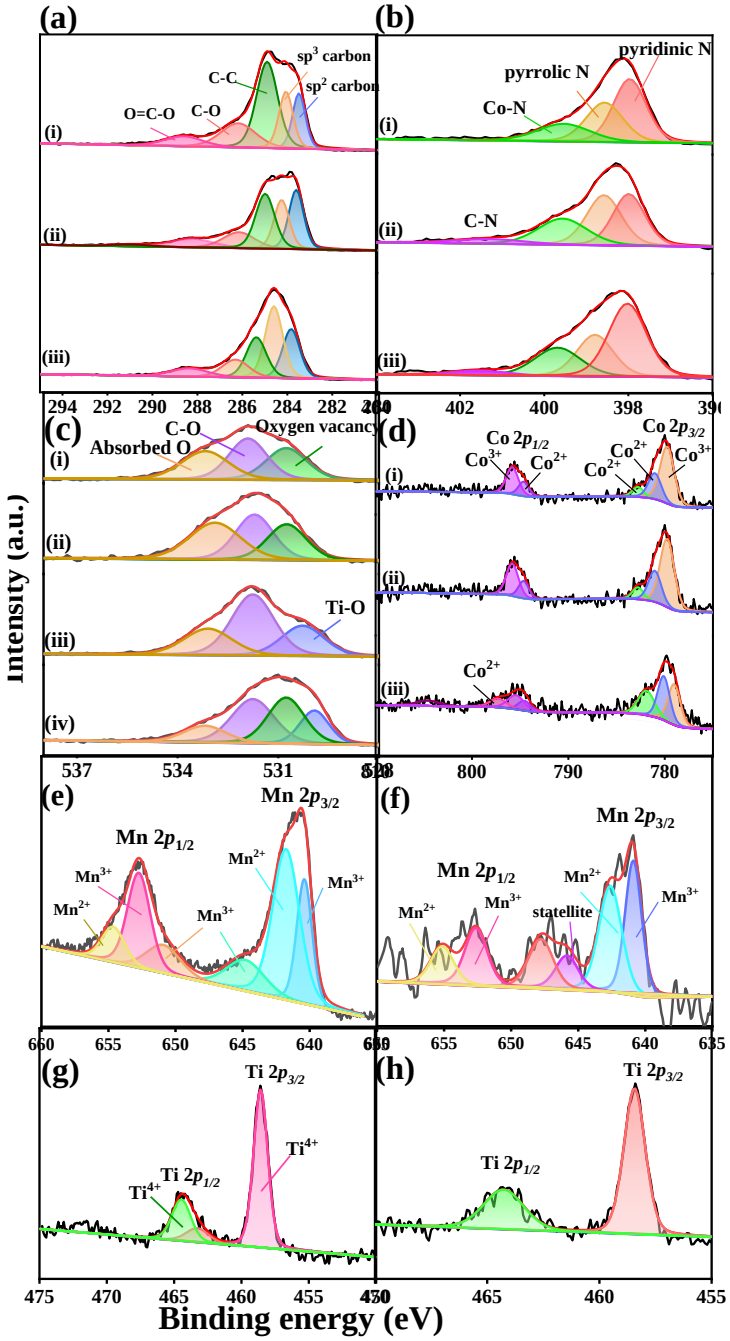

Figure 108. C 1*s* (a), N 1*s* (b), O 1*s* (c) and Co 2*p* (d) high-resolution XPS spectra of (i) CoPc-TA, (ii) CoPc-TA/Mn, CoPc-TA/Mn@$Ti_3C_2T_x$@PEG (iii) and CoPc-TA/Mn@$Ti_3C_2T_x$ (iv); Mn 2*p* high-resolution XPS spectra CoPc-TA/Mn (e) and CoPc-TA/Mn@$Ti_3C_2T_x$@PEG (f); and Ti 2*p* high-resolution XPS spectra CoPc-TA/Mn@$Ti_3C_2T_x$ (g) and CoPc-TA/Mn@$Ti_3C_2T_x$@PEG (h).

of 398.0, 398.6, 399.5, and 401.3 eV are found, cooresponding to pyridinic N, prrolic

N , and C-N, respectively. The O 1*s* XPS spectra of CoPc-TA and CoPc-TA/Mn (curves *i* and *ii*, **Figure 108c**) were fitted to three parts at the BEs of 530.1, 531.9, and 533.2 eV, corresponding to oxygen vacancy, C-O, and adsorbed O, respectively. In case of CoPc-TA/Mn@$Ti_3C_2T_x$ hybrid (curve *iii*) and CoPc-TA/Mn@$Ti_3C_2T_x$@PEG (curve *iv*, Figure S6c), beside of oxygen vacancy, C-O, and adsorbed O, an additional group of Ti-O (529.9 eV) was found. This appearance can be explained by the partical oxidiation of Ti clusters during the preparation of the CoPc-TA/Mn hybrid. As compared, CoPc-TA/Mn@$Ti_3C_2T_x$@PEG showed the larger content of C-O in the O 1*s* XPS spectrum. The similar deconvolutions of Co 2*p* XPS spectra of all samples (**Figure 107** and **108d**) were separated out, including two couples of peaks of Co $2p_{3/2}$ (778.0 eV) and Co $2p_{1/2}$ (795.9 eV). Both Co $2p_{3/2}$ and Co $2p_{1/2}$ parts included the mixed valence states of Co^{3+} and Co^{2+} species at the BEs of 779.4, 781.1, and 782.7 eV, respectively. The Mn 2*p* XPS spectra of all samples was composed of mixed valence states of Mn^{2+} and Mn^{3+} (**Figure 107**, **108e** and **108f**). The redox of Mn^{2+}/Mn^{3+} and Co^{2+}/Co^{2+} containing in the CoPc-TA/Mn@$Ti_3C_2T_x$ can remarkably enhance CDT efficiency for cancer therapy. Further, the Ti 2*p* XPS spectra of CoPc-TA/Mn@$Ti_3C_2T_x$ (**Figure 108g**) and CoPc-TA/Mn@$Ti_3C_2T_x$@PEG (**Figure 108h**) was deconvoluted to two peaks at the BEs of 458.6 and 464.5 eV, owing to Ti^{4+} of Ti $2p_{3/2}$ and Ti $2p_{1/2}$, respectively. These appearances can further prove the multiple components of the developed CoPc-TA/Mn@$Ti_3C_2T_x$@PEG nanozyme, which is expectable to serve as CDT/PDT/PTT agents for anticancer system.

Moreover, for probing whether AS1411 aptamer is immobilized over the CoPc-TA/Mn@$Ti_3C_2T_x$@PEG hybrid, its XPS and FT-IR spectra were investigated (**Figure 109**). part from the C-C (284.4 eV), C-N (285.4 eV), C-O (286.5 eV), and O-C=O (289.0 eV) groups, additional peaks at the BE of 287.8 (C=O) and 288.6 eV (COO) are deconvolved in the C 1*s* XPS spectrum of CoPc-TA/Mn@$Ti_3C_2T_x$@PEG @AS1411. As for N 1*s* XPS spectrum, besides of pyrrolic-N and Co-N, two extra peaks are found at the BEs of 400.4 and 401.4 eV, due to N-H and C-N, respectively, which are originated from the oligonucleotide strand of AS1411 aptamer. In addition, the P 2*p*

XPS spectrum, which can be regarded as the indictor for the aptamer immobilization, can be distinct observed (**Figure 109g**). The P 2*p* XPS spectrum can be divided into two peaks at the BEs of 133.2 and 134.2 eV corresponding to P $2p_{3/2}$ and P $2p_{1/2}$, respectively.

As compared with CoPc-TA/Mn@$Ti_3C_2T_x$@PEG, FT-IR spectrum of CoPc-TA/Mn@$Ti_3C_2T_x$@PEG@AS1411 (**Figure 109h**) shows an absorption peak at 557 cm^{-1} assigned to bending vibrations of PO_4^{3-}. Consequently, combining XPS and FT-IR results findings confirm the AS1411 aptamer can be successfully anchored over CoPc-TA/Mn@$Ti_3C_2T_x$@PEG.

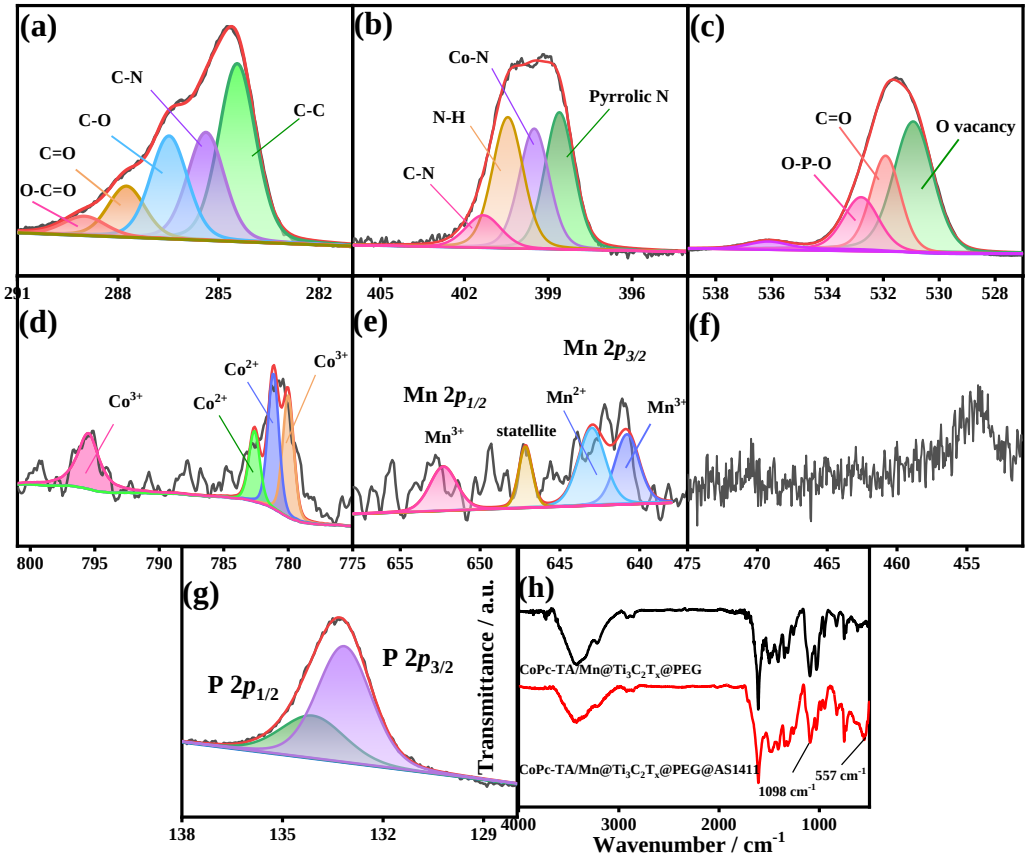

Figure 109 C 1*s* (a), N 1*s* (b), O 1*s* (c), Co 2*p* (d), Mn 2*p* (e), Ti 2*p* (f), and P 2*p* (g) high-resolution XPS spectra of CoPc-TA/Mn@$Ti_3C_2T_x$@PEG@AS1411.

10.2.7 In vitro photothermal performances

Given that the developed catalysts (100 μg mL^{-1}) exhibited characteristic peaks at around 808 nm in the UV-vis absorbance spectra (**Figure 110**), their great potential for

NIR-triggered photothermal therapy can be realized.

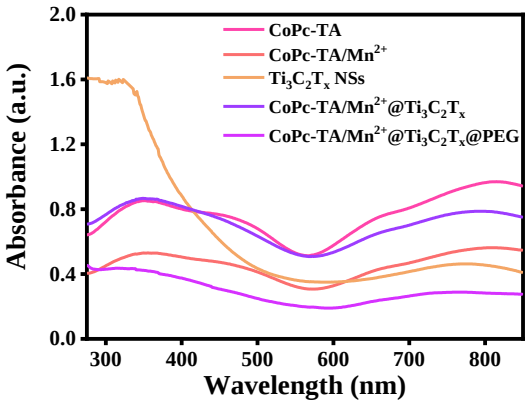

Figure 110 UV spectrum of materials in Milli-Q water.

The PTT performances of CoPc-TA/Mn@$Ti_3C_2T_x$ and CoPc-TA/Mn@$Ti_3C_2T_x$@PEG were investigated in water by irradiating at 808 nm laser (1 W cm^{-2}) for 10 min, while CoPc-TA, CoPc-TA@Mn, and $Ti_3C_2T_x$ NSs were used for comparison. **Figure 111a** showed the temperature of diverse catalysts increased fast at the first 5 min, and approached an equilibrium slowly, which was consistent with their corresponded infrared thermal images (**Figure 111b**). No substantial increase is observed in the temperature of water when irradiating by the NIR laser. Additionally, the temperature of the CoPc-TA/Mn suspension (100 μg mL^{-1}) attained 61.9 °C in 10 min after irradiated by 808 nm laser, close to that of CoPc-TA (66.3 °C), suggesting their comparable photothermal abilities. Further, the temperature of the $Ti_3C_2T_x$ system is as high as 70.2 °C. Further, the temperature of CoPc-TA/Mn@$Ti_3C_2T_x$ is aroud 68.0 °C in 10 min, slightly lower than that of $Ti_3C_2T_x$ NSs, but much higher than CoPc-TA/Mn. Nonetheless, the temperature of CoPc-TA/Mn@$Ti_3C_2T_x$@PEG declined to 53.6 °C when irradiated by 808 nm laser, revealing the cover of PEG layer somehow weakened photothermal transfer.

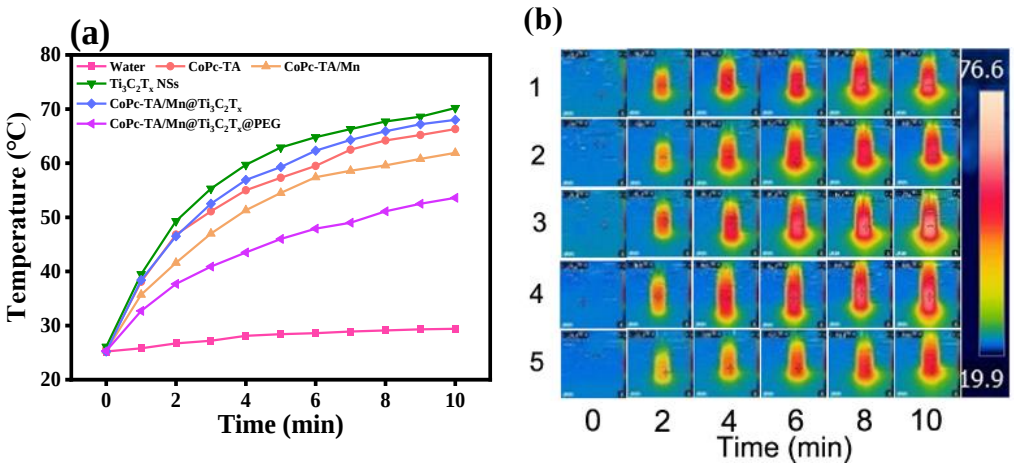

Figure 111. (a) Temperature elevation curves of different materials (100 μg mL^{-1}) under 808 nm laser irradiation for 10 min. (b) Infrared thermal images of different materials aqueous solutions (100 μg mL^{-1}) under 808 nm laser irradiation for 10 min.

The plots of the temperature versus the dosages of CoPc-TA/Mn@$Ti_3C_2T_x$ and CoPc-TA/Mn@$Ti_3C_2T_x$@PEG after 10 min of irradiation were shown in **Figure 112a** and **112b**, respectively. Clearly, the temperatures of the CoPc-TA/Mn@$Ti_3C_2T_x$ and CoPc-TA/Mn@$Ti_3C_2T_x$@PEG systems increased with the catalyst dosage, attaining to the maximum value at 200 μg mL^{-1}.

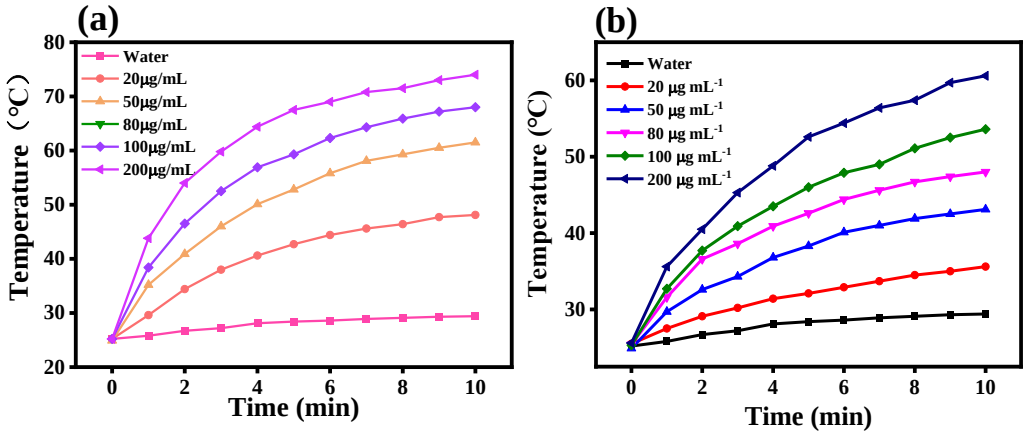

Figure 112. (a) Temperature elevation curves of (a) CoPc-TA/Mn^{2+}@$Ti_3C_2T_x$ and (b) CoPc-TA/Mn^{2+}@$Ti_3C_2T_x$@PEG at various concentrations under 808 nm laser irradiation for 10 min (0–200 μg mL^{-1}).

Moreover, the temperature of these two systems increased with increasing the laser power density (**Figure 113**). Considering the low dosage of catalyst is beneficial to the decline of side effect, 100 μg mL^{-1} of CoPc-TA/Mn@$Ti_3C_2T_x$ and CoPc-

TA/Mn@$Ti_3C_2T_x$@PEG were employed for further experiments, showing the temperature of 68.0 and 53.6 °C, respectively, by irradiated using the NIR laser with the power density of 1 W cm^{-2}.

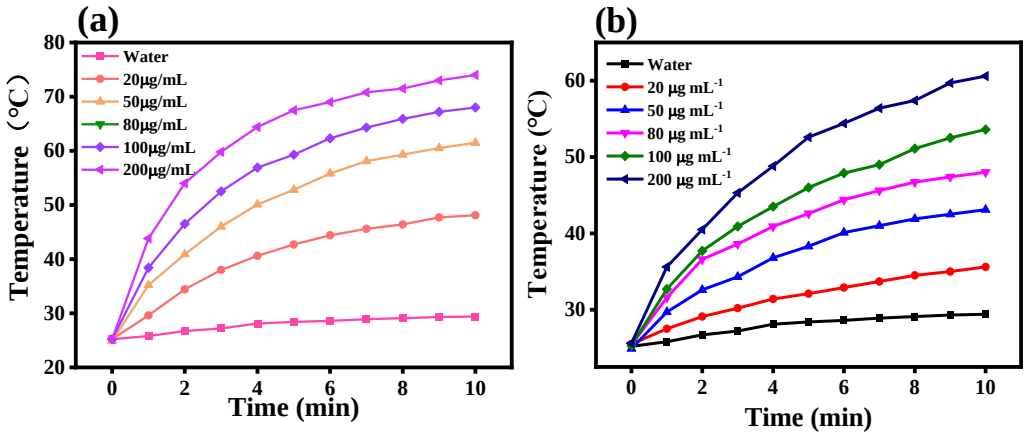

Figure 113. Temperature elevation curves of (a) CoPc-TA/Mn^{2+}@$Ti_3C_2T_x$ and (b) CoPc-TA/Mn^{2+}@$Ti_3C_2T_x$@PEG solutions with different concentrations irradiated by 808 nm laser for 10 min (1 W cm^{-2}).

Moreover, the PTT effect of CoPc-TA/Mn@$Ti_3C_2T_x$ and CoPc-TA/Mn@$Ti_3C_2T_x$@PEG can be deduced in-depth by measuring their PCE, η, which was calculated according to the **Eqs. (1-6)**. The η of CoPc-TA/Mn@$Ti_3C_2T_x$ (**Figure 114a**) is as high as 66.2%, compromising the PTT effects of two components. Further, CoPc-TA/Mn@$Ti_3C_2T_x$@PEG demonstrates a slightly smaller η value of 63.5% (**Figure 114b**) than that of CoPc-TA/Mn@$Ti_3C_2T_x$, meaning the PTT effect is not affected greatly by the covered polymer layer. However, the photothermal efficiency of CoPc-TA/Mn@$Ti_3C_2T_x$@PEG remarkably outperforms to most of reported photothermal agents, such as metallic Mo_2C@N-carbon@PEG nanoparticles (52.7 %), MOFs-derived composited (29.15%) and Ni_3S_2/$Cu_{1.8}S$ nano-heterostructures (49.5%).

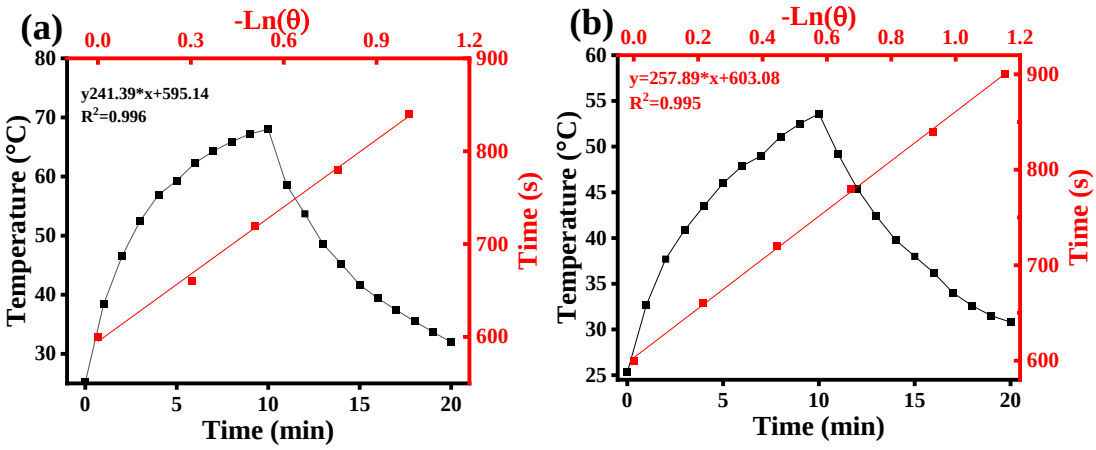

Figure 114. Heating and cooling curves of (a) CoPc-TA/Mn@$Ti_3C_2T_x$ and (b) CoPc-TA/Mn@$Ti_3C_2T_x$@PEG (200 μg mL^{-1}) (black) and the t-(-lnθ) diagram obtained during the natural cooling period of CoPc-TA/Mn@$Ti_3C_2T_x$@PEG (red).

After five on-off cycles of the exposure to the NIR laser, the PCEs of CoPc-TA/Mn@$Ti_3C_2T_x$ and CoPc-TA/Mn@$Ti_3C_2T_x$@PEG remains unchanged (**Figure 115)** verifying their excellent photostability. These results demonstrate that the modification of CoPc-TA/Mn@$Ti_3C_2T_x$ with PEG would not distinctly affect the PTT performance, affording it with potential application as excellent PTT agents for anticancer therapy.

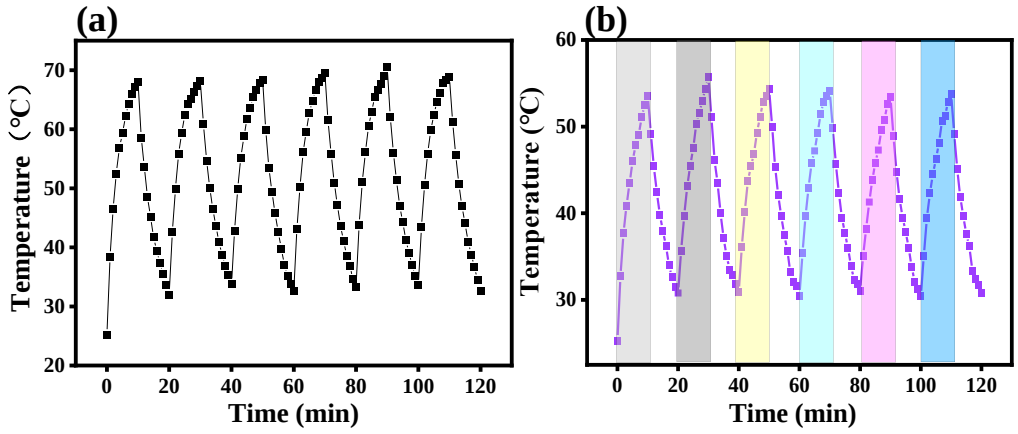

Figure 115. (g) Photothermal profile of the (a) CoPc-TA/Mn@$Ti_3C_2T_x$ and (b) CoPc-TA/Mn@$Ti_3C_2T_x$@PEG solution over five on/off cycles under the 808 nm laser irradiation (100 μg mL^{-1}, 1 W cm^{-2}).

Besides, the strong absorption of CoPc-TA/Mn@$Ti_3C_2T_x$@PEG in the NIR region motivates us to investigate its potential application as a contrast agent for PAI. To probe the capacity of CoPc-TA/Mn@$Ti_3C_2T_x$@PEG as a PAI contrast agent, the

photoacoustic signals from aqueous solution containing different concentrations of CoPc-TA/Mn@$Ti_3C_2T_x$@PEG (**Figure 116a**) show the PA signal linearly increases with increasing the dosage of CoPc-TA/Mn@$Ti_3C_2T_x$@PEG (R^2 = 0.988). Notably, the PA signal of CoPc-TA/Mn@$Ti_3C_2T_x$@PEG still can be detected even at a low dosage of 20 μg mL^{-1} (**Figure 116b**), affording promising application as vivo biological imaging contrast agent.

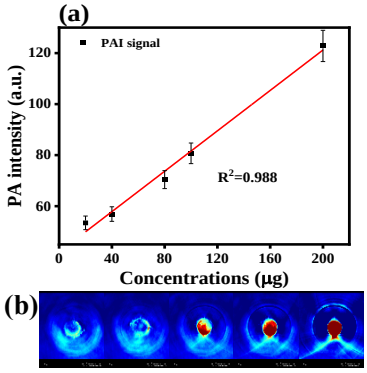

Figure 116 (a) In vitro PA values and (b) PA images of CoPc-TA/Mn@$Ti_3C_2T_x$@PEG with different concentrations (20, 40, 80, 100, and 200 μg mL^{-1}).

10.2.8 Optical and photoelectrochemical properties of CoPc-TA@Mn, $Ti_3C_2T_x$ NSs and CoPc-TA/Mn@$Ti_3C_2T_x$

The UV-vis diffuse reflectance spectra (DRS) of all samples of CoPc-TA@Mn, $Ti_3C_2T_x$ NSs and CoPc-TA/Mn@$Ti_3C_2T_x$ (**Figure 117a**) demonstrate obvious absorption within the region from 200 to 1000 nm. The energy band gaps (E_g) of all samples were calculated from the UV–vis DRS absorption curves by the Kubelka-Munk function transformation (**Eqs. (8)**):

$$(\alpha h\upsilon) = \beta\left(h\upsilon - E_g\right)^{n/2} \qquad (8)$$

, where α, h, υ, β and E_g are absorption coefficient, Planck constant, light frequency, a constant and band gap, respectively. **Figure 117b** depicts the E_g for CoPc-TA/Mn and CoPc-TA/Mn@$Ti_3C_2T_x$ are in the two regions. The obtained E_g (Q band) of CoPc-TA/Mn and CoPc-TA/Mn@$Ti_3C_2T_x$ are 1.50 and 1.52 eV, respectively, while the E_g (B band) of them are 2.08 and 2.22 eV, respectively. As the E_g less than 1.53 eV can be

excited by the NIR light irridation (808 nm laser), the E_g of CoPc-TA@Mn, $Ti_3C_2T_x$

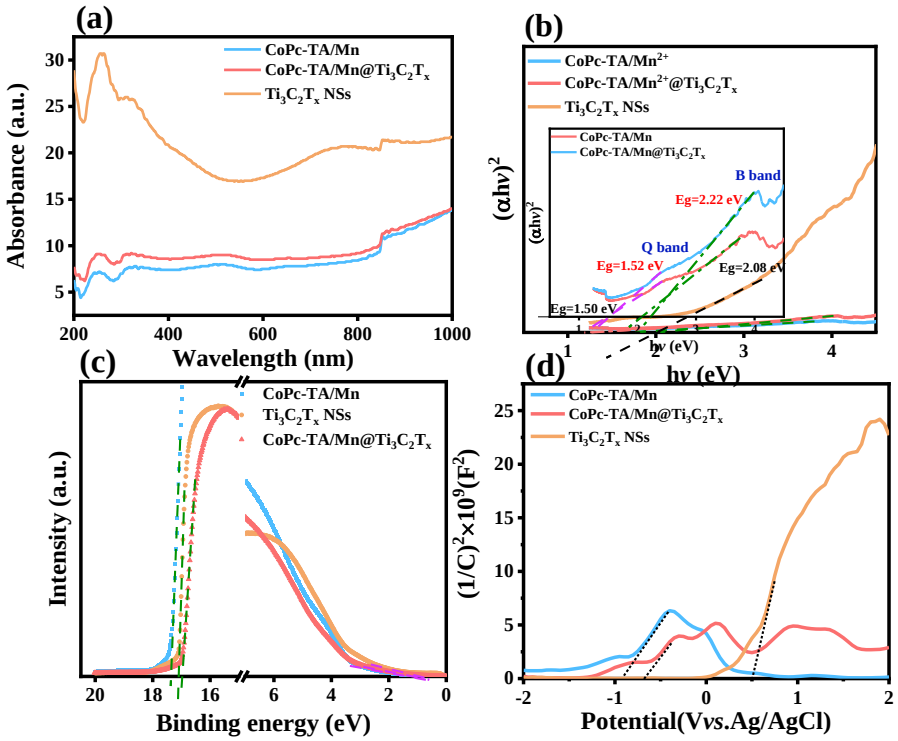

Figure 117 (a) UV–vis DRS absorption spectra, (b) the corresponding $[\alpha hv]^2$ vs hν curves, (c) UPS spectra (d) and Mott-schottky plots of CoPc-TA/Mn, $Ti_3C_2T_x$ NSs, and CoPc-TA/Mn@$Ti_3C_2T_x$.

NSs and CoPc-TA/Mn@$Ti_3C_2T_x$ are calculated to be 1.50, 2.12 and 1.52 eV, respectively. As compared with CoPc-TA/Mn, this finding hints the CoPc-TA/Mn@$Ti_3C_2T_x$ junction shows an increased band gap. Based on the ultraviolet photoelectron spectroscopy (UPS) spectra of all samples (**Figure 117c**), the calculated work functions (WF, Φ) of CoPc-TA@Mn, $Ti_3C_2T_x$ NSs and CoPc-TA/Mn@$Ti_3C_2T_x$ are 3.84, 4.11, and 4.23 eV, respectively, by subtracting the excitation energy of He I (21.22 eV). In addition, the low binding energy tail (E_{edge}) of CoPc-TA@Mn, $Ti_3C_2T_x$ NSs and CoPc-TA/Mn@$Ti_3C_2T_x$ is around 1.35, 0.98, and 1.21 eV, respectively. Consequently, the Fermi levels (E_F) of CoPc-TA@Mn, $Ti_3C_2T_x$ NSs and CoPc-TA/Mn@$Ti_3C_2T_x$ are −3.84, −4.11, and −4.23 eV, respectively. Moreover, the UPS was performed to verify the position of valence band (CB) according to the equation (Eqs. (9) and (10)) [202]:

$$E_F - E_{VB} = E_{edge} \qquad (9)$$

$$E_{CB} = E_g - E_{VB} \qquad (10)$$

. Thus, the E_{VB} and conduction band (E_{CB}) of CoPc-TA@Mn are −5.19 eV and −3.69 eV, respectively, while the E_{VB} and E_{CB} of CoPc-TA/Mn@$Ti_3C_2T_x$ are −5.44 eV and −3.92 eV, respectively.

Further, Mott-Schottky (M-S) plots can also be used to confirm the flat band potential of as-prepared materials. **Figure 117b** depicts the M-S plots for CoPc-TA@Mn, $Ti_3C_2T_x$ NSs and CoPc-TA/Mn@$Ti_3C_2T_x$ display positive slopes, meaning their *n*-type properties. In consequence, the flat band potentials of CoPc-TA@Mn, $Ti_3C_2T_x$ NSs and CoPc-TA/Mn@$Ti_3C_2T_x$ are −0.91, 0.50 and −0.71 V (vs. Ag/AgCl), respectively. Owing that the CB potentials of *n*-type CoPc-TA@Mn, $Ti_3C_2T_x$ NSs and CoPc-TA/Mn@$Ti_3C_2T_x$ are very close to the flat-band potential (about 0.10 V more negative), it can decline the CB positions of CoPc-TA@Mn and CoPc-TA/Mn@$Ti_3C_2T_x$ to −1.01 and −0.81 V (vs. Ag/AgCl), respectively. According to the equation (**Eqs. (11)**):

$$E(vs\ NHE) = E\left(vs\frac{Ag}{AgCl}\right) + 0.197\ eV \qquad (11)$$

, the standard band potential (vs. NHE) of CoPc-TA@Mn and CoPc-TA/Mn@$Ti_3C_2T_x$ are estimated to be −0.81 and −0.61 V, respectively, which coincides with the result of UPS curves (−3.69 and −3.92 eV vs vac). Thereby, the VB top of CoPc-TA/Mn can be determined as 0.69 V vs NHE (−5.19 eV vs vac).

According to theoretical calculations and characterization results of photocatalytic performances, the energy band schematic diagrams of the CoPc-TA/Mn@$Ti_3C_2T_x$ Schottky junction in the photocatalytic process are provided in **Figure 118**. Before the contact of CoPc-TA/Mn and $Ti_3C_2T_x$ NSs, according to the result of band gap (1.50 eV), the E_F of CoPc-TA/Mn is close to its CB, indicating the formation of an n-type semiconductor. Owing that the E_F of CoPc-TA/Mn (-3.84 eV) is higher than that of $Ti_3C_2T_x$ (-4.11 eV), a Schottky junction can be formed at the interface between them. As for the CoPc-TA/Mn@$Ti_3C_2T_x$ Schottky junction, the electrons spontaneously flow from CoPc-TA/Mn to $Ti_3C_2T_x$ NSs considering the higher E_F of CoPc-TA/Mn until a balance is realized. During this process, a positively charged layer on the CoPc-TA/Mn

surface can be created due to the missing electrons, thus forming an electron depletion zone and an upward bend in the band edge. It thus results in the negatively charged layer of electrons accumulated on the $Ti_3C_2T_x$ NSs surface. Consequently, the Schottky barrier and a built-in electric field are formed at the interface of the Schottky heterojunction. When irradiated by the NIR light irridiation, the photogenerated electrons from CoPc-TA/Mn leap into the CB and rapidly migrate to the $Ti_3C_2T_x$ NSs surface. The Schottky barrier nearly impeds the backflow of electrons, which efficiently separates the photogenerated electron–hole pairs and increases the free carrier concentration. It thus enables $Ti_3C_2T_x$ as the electron reservoir, remarkably facilitating the separation ability of photoinduced electrons and holes, prolonging charge carriers lifetime and enhancing CDT and PDT performances.

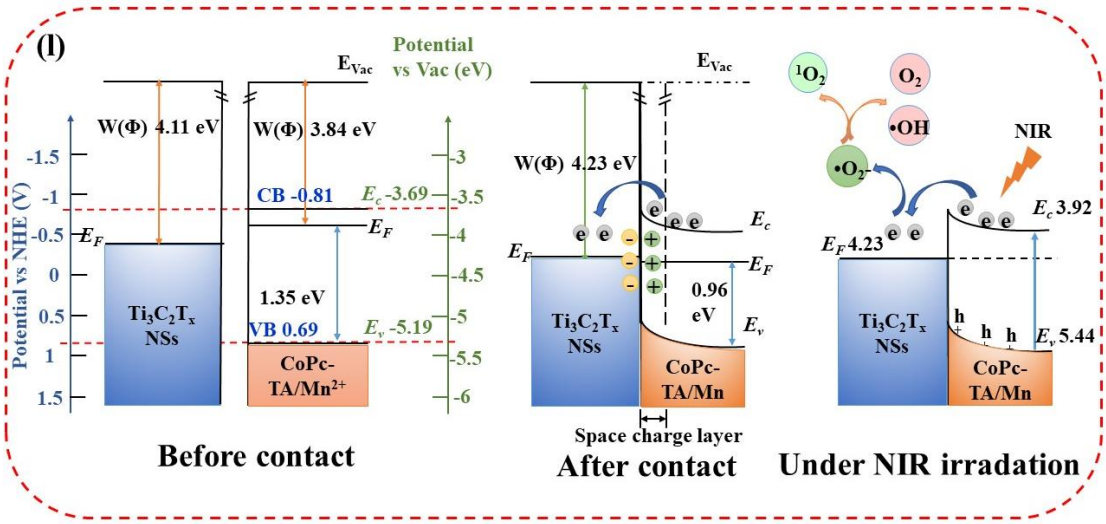

Figure 118. (l) Schematic diagram of the changes in the energy band structure and internal electric field near the interface of the two phases under different conditions (before contact, after contact, and under NIR irradation) for $Ti_3C_2T_x$ NSs and CoPc-TA/Mn, and the specific process of ROS production during photocatalysis.

Besides, photoelectrochemical tests were carried out to evaluate the separation and transfer of photogenerated carriers of materials (**Figure 119a**). All samples present reversible photocurrent responses on each irradiation. As compared, the photocurrent intensity of CoPc-TA/Mn@$Ti_3C_2T_x$ is higher than those of CoPc-TA/Mn and $Ti_3C_2T_x$ NSs. As a cocatalyst, $Ti_3C_2T_x$ can produce more effectively receiving photoexcited

electrons.

Moreover, PL spectra of all samples (**Figure 119b**) were also measured, which were used to assess the charge transfer and recombination behaviors of photocatalyst. The fluorescence intensities of CoPc-TA/Mn and CoPc-TA/Mn@$Ti_3C_2T_x$ significantly decline with the excitation wavelength at 350 nm in comparison with $Ti_3C_2T_x$ NSs. Given that a lower fluorescence intensity of catalyst suggests a lower recombination rate, the recombination rate of electron and hole of CoPc-TA/Mn@$Ti_3C_2T_x$ distinctly decreases. It further demonstrates that a Schottky junction is formed at CoPc-TA/Mn@$Ti_3C_2T_x$ interface, greatly promoting the separation of photogenerated carriers.

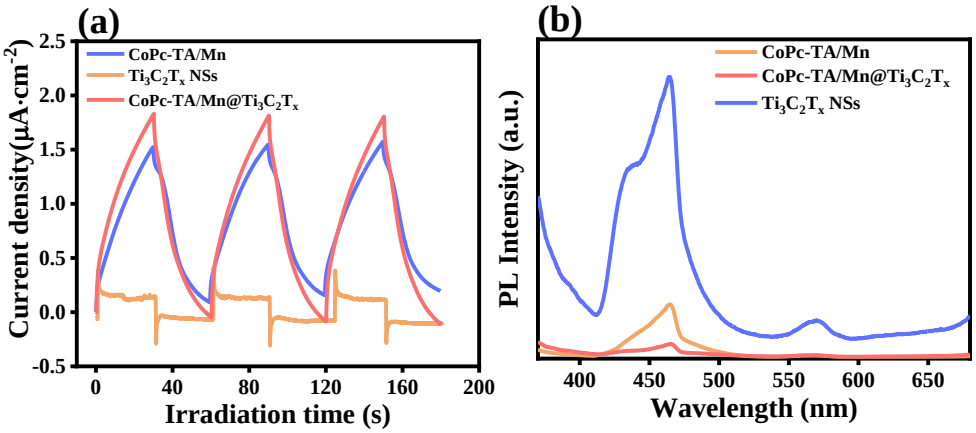

Figure 119. (a) Transient photocurrent responses and (b) PL spectraof CoPc-TA/Mn, $Ti_3C_2T_x$ NSs, and CoPc-TA/Mn@$Ti_3C_2T_x$.

Under the NIR irradiation, the electrons in the VB of CoPc-TA@Mn are excited to CB, generating photo-activated electrons and holes (**Eq. (12)**). Owing to the excellent electronic conductivity of $Ti_3C_2T_x$ NSs and the large interface between $Ti_3C_2T_x$ NSs and CoPc-TA@Mn, the photogenerated electrons in CB of CoPc-TA@Mn can migrate immediately to $Ti_3C_2T_x$ NSs, thus boosting the separation of photoinduced electron-hole pairs. The photoinduced electrons preferably transfer to $Ti_3C_2T_x$ NSs due to the Schottky junction of CoPc-TA/Mn@$Ti_3C_2T_x$, further declining the generation of $\bullet O_2^-$ (**Eq. (13)**), which is more negative than −0.13 V vs NHE.

Furthermore, the generated $O_2^{\bullet-}$, as the primary ROS, can be further converted into other more reactive ROS (such as hydroxyl radical (OH•) and superoxide radical $^1O_2$) through various approaches (**Eq. (14** and **15)**), providing potent injury and O_2 to cancer

cells. As aforementioned, $\bullet O_2^-$ and •OH generated via electron transfer fulfill a type I PDT. Consequently, the CoPc-TA/Mn@$Ti_3C_2T_x$ Schottky junction would promote highly efficient ROS generation via the type I mechanism under 808 nm laser, for which the reaction process is listed as follows:

$$\mathrm{CoPc-TA/Mn^{2+}@Ti_3C_2} + hv \rightarrow h^+ + e^- \quad (12)$$

$$O_2 + e^- \rightarrow \bullet O_2^- \quad (13)$$

$$\bullet O_2^- + H_2O_2 \rightarrow \bullet OH + OH^- + O_2 \quad (14)$$

$$2 \bullet O_2^- + H_2O \rightarrow {}^1O_2 \quad (15)$$

As discussed, plenty of $\bullet O_2^-$ species were yieled in the presence of CoPc-TA/Mn@$Ti_3C_2T_x$@PEG upon the NIR laser irradiation without H_2O_2. To clarify the category of generated radicals, ESR measurements were performed upon the light irradiation or in dark for 10 min with diverse catalysts such as CoPc-TA/Mn, $Ti_3C_2T_x$ NSs, CoPc-TA/Mn@$Ti_3C_2T_x$, and CoPc-TA/Mn@$Ti_3C_2T_x$@PEG (**Figure 120**). In dark, no evident ESR signal was gained for all catalysts, hinging no ROS species was found. On contrary, four typical characteristic peaks with intensity ratios of 1:1:1:1 of DMPO-$^{\bullet}O_2^-$ were obtained for the four samples under NIR irradiation (**Figure 120a**). Among diverse catalysts, the signal intensities of $\bullet O_2-$ irritated by CoPc-TA/Mn@$Ti_3C_2T_x$@PEG under the NIR irradiation were the highest, enabling that the introduction of PEG optimize photo-degradation activity [90]. **Figure 120b** depicted that the peak intensity of DMPO-$\bullet O_2^-$ signals increased along with the irradiation time from 5 to 10 min, verifying that $\bullet O_2^-$ specises generated by CoPc-TA/Mn@$Ti_3C_2T_x$@PEG via electron transfer under NIR irradiation.

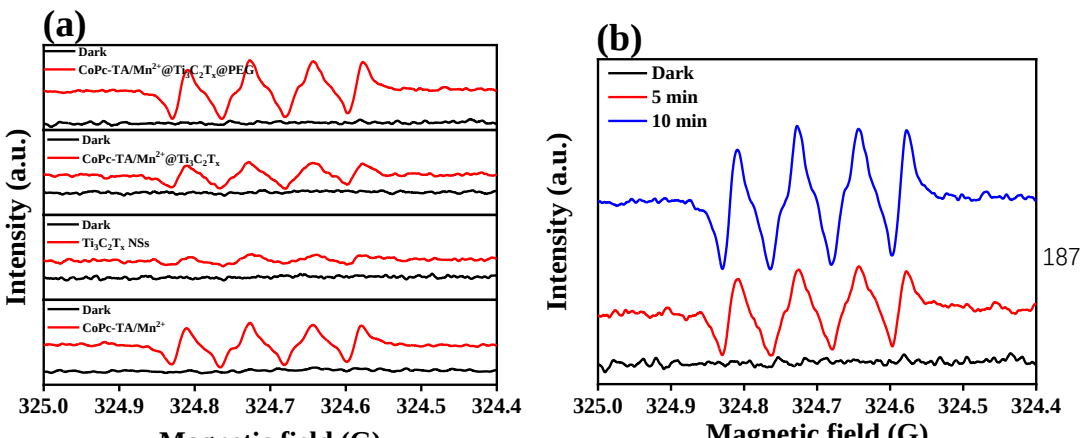

Figure 120. (a) ESR spectra of CoPc-TA/Mn, $Ti_3C_2T_x$ NSs, CoPc-TA/Mn@$Ti_3C_2T_x$ and CoPc-TA/Mn@$Ti_3C_2T_x$@PEG upon irradiation for 10 min in the presence of DMPO-•O_2^-. (b) ESR spectra of CoPc-TA/Mn@$Ti_3C_2T_x$@PEG in dark and upon irradiation for 5 and 10 min in the presence of DMPO-•O_2^-.

According to **Eq. (14)**, •O_2^- can be converted into •OH by reacting with H_2O_2, so we proved the generation of •OH by testing the content of O_2. As expected, the increased O_2 content and O_2 bubbles can be detected by Dissolved oxygen meter (WTW, Multi3420) (**Figure 121a**). It demonstrates that a small concentration of dissolved O_2 is observed in H_2O_2 solution (100 μM) under an 808 nm laser irradiation (1 W cm^{-2}) for 10 min, hinting the insignificant O_2 generation under this condition. Similarly, the concentration of dissolved O_2 of CoPc-TA/Mn@$Ti_3C_2T_x$@PEG (100 μg mL^{-1}) + NIR and CoPc-TA/Mn@$Ti_3C_2T_x$@PEG (100 μg mL^{-1}) + H_2O_2 groups are also very small, comparable with the system of H_2O_2 solution under an 808 nm laser irradiation (1 W cm^{-2}). On contrast, a high concentration of dissolved O_2 of CoPc-TA/Mn@$Ti_3C_2T_x$@PEG (100 μg mL^{-1}) + H_2O_2 + NIR group can be observed. It is mainly owed that O_2^-• is generated under 808 nm laser irradiation in the presence of CoPc-TA/Mn@$Ti_3C_2T_x$@PEG, which can result in the continuous conversion of H_2O_2 (100 μM) to •OH and O_2 via **Eq. (14)**. **Figure 121b** depicts a large number of O_2 bubbles can be seen from the photograph of the CoPc-TA/Mn@$Ti_3C_2T_x$@PEG (100 μg mL^{-1}) + H_2O_2 (100 μM) + NIR group. However, no obvious O_2 bubble is observed for the CoPc-TA/Mn@$Ti_3C_2T_x$@PEG (100 μg mL^{-1}) + H_2O_2 (**Figure 121c**) and CoPc-TA/Mn@$Ti_3C_2T_x$@PEG (100 μg mL^{-1}) + NIR (**Figure 121d)** groups. Notably, the O_2 generation ability of CoPc-TA/Mn@$Ti_3C_2T_x$@PEG in H_2O_2 solution (100 μM) under the 808 nm laser irradiation could relieve the hypoxia of the TME, boosting CDT and PDT effects.

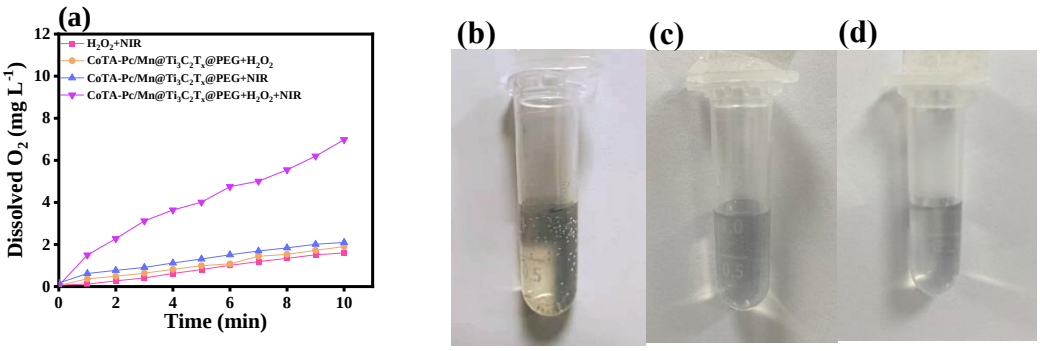

Figure 121. (a) O_2 generation trend for CoPc-TA/Mn@Ti_3C_2@PEG with different conduction. Oxygen bubbles for the systems of (b) CoPc-TA/Mn@$Ti_3C_2T_x$@PEG +H_2O_2+NIR, (c) CoPc-TA/Mn@$Ti_3C_2T_x$@PEG +H_2O_2 (c), and (d) CoPc-TA/Mn@$Ti_3C_2T_x$@PEG +NIR groups.

10.2.9 Generation of ROS and O_2

To deeply understand the effect of active species produced by CoPc-TA/Mn@$Ti_3C_2T_x$ and CoPc-TA/Mn@$Ti_3C_2T_x$@PEG, capture experiments for radicals •OH and $^1O_2$ using MB and DPBF, respectively, were performed (**Figure 122**, **123**). As aforementioned, single atomic Co-N and Mn-N active sites are present in CoPc-TA/Mn@$Ti_3C_2T_x$ (**Figure 122**), which can react with H_2O_2 to generate •OH in according with Eqs. (16) and (17):

$$Co^{2+} + H_2O_2 \rightarrow Co^{3+} + \bullet OH \quad (16)$$

$$Mn^{2+} + H_2O_2 \rightarrow Mn^{3+} + \bullet OH \quad (17)$$

. As shown in **Figure 122b**, the absorbance of MB substantially decreases with the irradiation time going on for the three samples. **Figure 122c** shows the degradation efficacy of MB toward all samples. The results show the degradation rates of MB toward CoPc-TA/Mn@$Ti_3C_2T_x$@PEG is the highest (97.55%) within 30 min, slightly higher than those of CoPc-TA/Mn@$Ti_3C_2T_x$ (91.03%) and CoPc-TA/Mn (88%) and

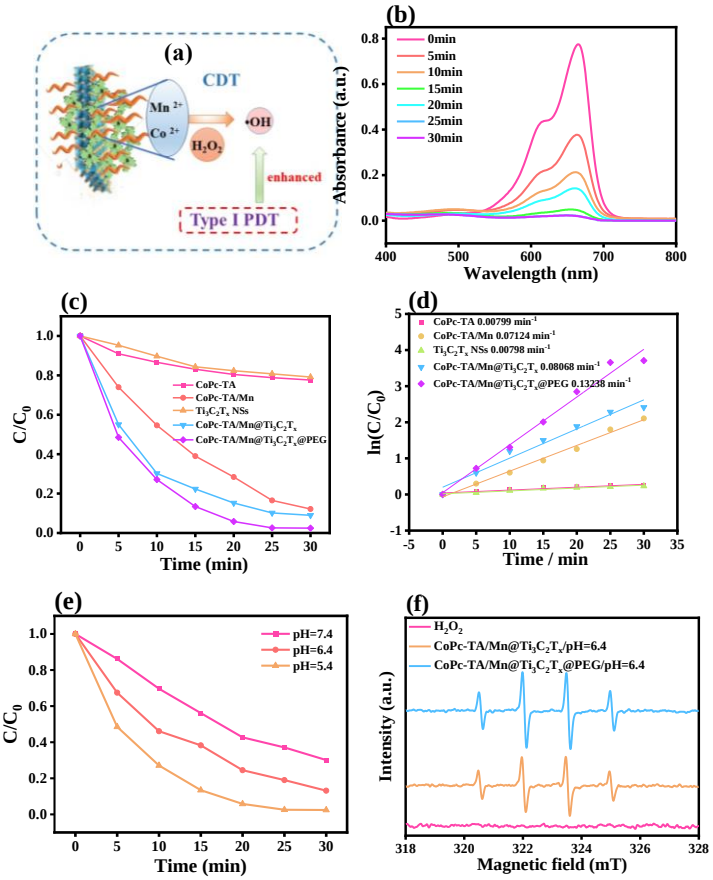

Figure 122 (a) Illustration of type I PDT enhanced CDT of CoPc-TA/Mn@$Ti_3C_2T_x$@PEG. (b) UV–vis absorption spectra of degradation by the CoPc-TA/Mn@$Ti_3C_2T_x$@PEG -mediated Fenton-like reaction within 30 min. (c) Time-dependent degradation of MB caused by different materials (CoPc-TA, CoPc-TA/Mn, $Ti_3C_2T_x$, CoPc-TA/Mn@$Ti_3C_2T_x$, and CoPc-TA@Mn@$Ti_3C_2T_x$@PEG) within 30 min. (d) The rate constant of MB decomposition in the presence of CoPc-TA, CoPc-TA/Mn, $Ti_3C_2T_x$ NSs, CoPc-TA/Mn@$Ti_3C_2T_x$, and CoPc-TA/Mn@$Ti_3C_2T_x$@PEG. Depletion of MB attributed to •OH generation by CoPc-TA/Mn@$Ti_3C_2T_x$ (e) Time-dependent degradation of MB caused by CoPc-TA/Mn@$Ti_3C_2T_x$@PEG, within 30 min, and (f) ESR spectra of CoPc-TA/Mn@$Ti_3C_2T_x$ and CoPc-TA/Mn@$Ti_3C_2T_x$@PEG upon the addition of DMPO• as spin-trapping agent for detecting •OH.

substantially larger than that of $Ti_3C_2T_x$ (21%). To further study the degradation rate of MB, the apparent rate constants (k_a) of MB (**Figure 122d**) photodegradation toward CoPc-TA, CoPc-TA@Mn, $Ti_3C_2T_x$ NSs, and CoPc-TA/Mn@ $Ti_3C_2T_x$ are calculated to 0.0080, 0.0712, 0.0080, 0.0807 and 0.1324 min^{-1} under same conditions. These

appearances mean CoPc-TA/Mn exhibits the high generation ability of •OH, affording the potential as an outstanding CDT agent. Integration of CoPc-TA/Mn and Ti3C2Tx can slightly accelerate generation of •OH, while the modification with PEG could not affect this process. As displayed in **Figure 122e**, the corresponding degradation curves of MB against CoPc-TA/Mn@$Ti_3C_2T_x$@PEG in the solutions with various pH values suggest the degradation rate for MB of CoPc-TA/Mn@$Ti_3C_2T_x$@PEG in the acidic solution (pH = 5.4) is as large as 97.55 %, outperforming to in the solutions (pH = 6.4 and 7.4). It implies that both CoPc-TA/Mn@$Ti_3C_2T_x$@PEG can efficiently stimulate the generation of •OH in the tumor cells (pH ≈ 4.5), whereas this behavior could be hampered in normal cells (pH ≈ 7.4). Furthermore, ESR measurements were carried out to identify the generated •OH, in which 5,5-dimethyl-1 -pyrroline-1-oxide (DMPO)was used as the trapping agent to detect the generation level of •OH. Further, **Figure 122f** depicts there is no peak for DMPO-•OH in water, while four typical characteristic peaks are observed in CoPc-TA/Mn@$Ti_3C_2T_x$ and CoPc-TA/Mn@$Ti_3C_2T_x$@PEG systems, showing the intensity ratio of 1:2:2:1 of DMPO-•OH. As compared, CoPc-TA/Mn@$Ti_3C_2T_x$@PEG displays the stronger •OH signal than that of CoPc-TA/Mn@$Ti_3C_2T_x$, indicating abundant •OH species generated from CoPc-TA/Mn@$Ti_3C_2T_x$@PEG.

Under 808 nm laser illumination, the PDT property of these materials could cause damage to cancer cells by generating $^1O_2$ (**Figure 123**). During the process of PDT, hypoxia is further aggravated due to the consumption of O_2, which results in PDT resistance However, CoPc-TA/Mn@$Ti_3C_2T_x$@PEG with spatiotemporally synchronous O_2 self-supply, which is convert O_2 to •OH and O_2 (**Eqs. (12)-(14),** type II PDT), can reduce impact of this defect. DPBF was utilized for the assessment of the production rate of $^1O_2$ of different catalysts under NIR irradiation as DPBF can undergo a Diels−Alder 1,4-cycloaddition reaction with $^1O_2$, declining its absorption at 410 nm. The self-degradation curve of DPBF (**Figure 123b**) were recorded and the degradation efficacy of DPBF toward all samples under various conditions were analyzed to investigate the PDT performance of one catalyst (**Figure 123c**). In the presence of the

$Ti_3C_2T_x$ NSs, the degradation efficacy of the absorption peak decreases insignificantly within 10 min (**Figure 123c**), hinting its inferior generation ability of $^1O_2$. On the contrary, the degradation efficacy of the DPBF absorbance against CoPc-TA/Mn and CoPc-TA substantially reduces under light irradiation, verifying the generation of $^1O_2$. As compared, the degradation efficacy of the DPBF absorbance against CoPc-TA/Mn greatly is much lower than that of CoPc-TA under the light irradiation. Apparently, single metal atomic sites of Co-N and Mn-N active sites containing CoPc-TA@Mn also play important role in the generation of of $^1O_2$ from $^3O_2$ under 808 nm irradiation. When irradiated by laser light, the excited triplet state ^{3}PSs (CoPc-TA@Mn)* is obtained by intersystem crossing. Afterward, the active catalysts would react with the ground state triplet oxygen ($^3O_2$), leading to the production of highly active $^1O_2$. The generated $^1O_2$ species accordingly results in the immediate decomposition of DPBF. Accordingly, this catalysis reaction belongs to the type II PDT due to energy transfer occurred. The similar appearance is also gained for CoPc-TA/Mn@$Ti_3C_2T_x$, but showing even higher peak intensity than that of CoPc-TA/Mn within 10 min. It can be owing to an Schottky junction formed at the CoPc-TA/Mn and $Ti_3C_2T_x$ interface, remarkably boosting the PDT performance. In terms of CoPc-TA/Mn@$Ti_3C_2T_x$@PEG, however, the reduction of the characteristic DPBF absorbance peak is slightly smaller than that of CoPc-TA/Mn@$Ti_3C_2T_x$, owing that the PEG layer can block some active sites to simulate the generation of $^1O_2$. To further study the degradation rate of DPBF, the reaction kinetics was fitted well into the first-order kinetic equation (**Eqs. (7)**). **Figure 123d** indicates the apparent rate constants (k_a) of DPBF photodegradation toward CoPc-TA, CoPc-TA@Mn, $Ti_3C_2T_x$ NSs, and CoPc-TA/Mn@$Ti_3C_2T_x$ are 0.0080, 0.0244, 0.0092, and 0.1109 min^{-1}, respectively, under same conditions. However, the k_a (0.0630 min^{-1}) of CoPc-TA/Mn@$Ti_3C_2T_x$@PEG is smaller than that of CoPc-TA/Mn@$Ti_3C_2T_x$, suggesting it can reduce the generation ability of $^1O_2$.

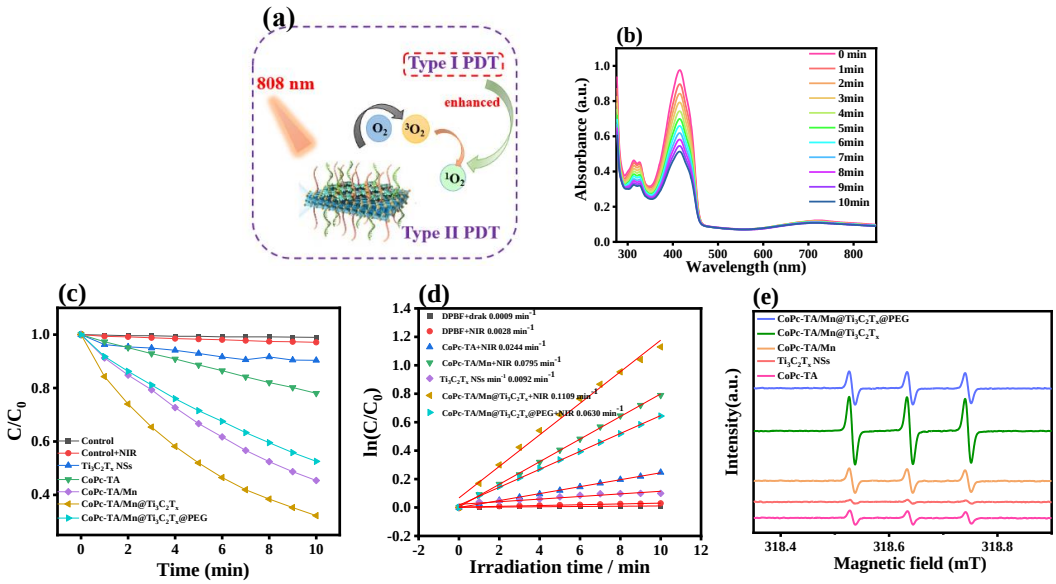

Figure 123 In vitro PDT performance evaluation for samples. (a) Illustration of type I PDT enhanced PDT of CoPc-TA/Mn@$Ti_3C_2T_x$@PEG. (b) UV-vis spectra of DPBF with CoPc-TA/Mn@$Ti_3C_2T_x$@PEG dispersions under 808 nm laser irradiation (1 W cm^{-2}) within 10 min. (c) Time-dependent absorbance of DPBF at 417 nm (C/C_0) irradiated with an 808 nm laser without and with the NIR (containing $Ti_3C_2T_x$ NSs, CoPc-TA, CoPc-TA/Mn, CoPc-TA/Mn@$Ti_3C_2T_x$, and CoPc-TA@Mn@$Ti_3C_2T_x$@PEG) for 10 mins, respectively. C_0 and C are the initial absorbance of DPBF and the absorbance under definite irradiation time, respectively. (d) The rate constant of DPBF decomposition in the presence of CoPc-TA, CoPc-TA/Mn, $Ti_3C_2T_x$ NSs, CoPc-TA/Mn@$Ti_3C_2T_x$, and CoPc-TA/Mn@$Ti_3C_2T_x$@PEG under NIR 808 nm laser irradiation (1 W cm^{-2}). (e) ESR spectra of different materials upon irradiation for 10 min in the presence of TEMP (trapping agent of $^1O_2$).

In addition, ESR measurements were also performed to identify the generation of $^1O_2$, for which 2,2,6,6-tetramethylpiperidine (TEMP) was used as the trapping agent to determine the $^1O_2$ generation. **Figure 123e** shows obvious peak signals of CoPc-TA-contained catalysts under light irradiation recorded in the presence of TEMP with the intensity ratio of 1:1:1 of TEMP-$^1O_2$. However, only little peak intensity of TEMP-$^1O_2$ can be formed for $Ti_3C_2T_x$ NSs, revealing its low PDT effect. **Figure 123e** depicts the ESR spectrum against CoPc-TA/Mn@$Ti_3C_2T_x$@PEG at different durations only shows insignificant signal of TEMP-•$^1O_2$ without the light irradiation.

Based on the above analysis, it can be concluded that CoPc-TA/Mn@$Ti_3C_2T_x$ not

only can enable the generation of $^1O_2$ (type II PDT) via energy transfer, but also can greatly activate hypoxia resistant type I PDT by electron transfer under NIR irradiation, enhancing the synergistic effect of PDT/PTT and PDT/CDT of CoPc-TA/Mn@$Ti_3C_2T_x$. The schematic illustration of the multimodal PDT/PTT/CDT effect of CoPc-TA/Mn@$Ti_3C_2T_x$ is provided in **Scheme 21**. After the CoPc-TA/Mn@$Ti_3C_2T_x$@PEG@AS1411 are endocytosed into tumor cells, the presence of CoPc-TA/Mn endows CoPc-TA/Mn@$Ti_3C_2T_x$@PEG@AS1411 with catalase-like activities for catalyzing H_2O_2 to produce •OH via the Fenton-like reaction even without NIR irradiation to induce cancer cell apoptosis. Simultaneously, CoPc-TA/Mn@$Ti_3C_2T_x$@PEG@AS1411 also demonstrate superiuor type II PDT/PTT effect for tumor imaging and therapy under NIR laser irradiation due to CoPc-TA/Mn. Importantly, the CoPc-TA/Mn@ $Ti_3C_2T_x$ Schottky junction also can trigger type I PDT under NIR laser irradiation, generating $•O_2^-$ species, which can be further converted into other ROS (•OH and $^1O_2$) and generate O_2 to boost the efficiency of CDT and PDT under NIR laser irradiation. In this regard, the integration of type I PDT enhanced synergy therapy (type II PDT/PTT/CDT) could afford CoPc-TA/Mn@$Ti_3C_2T_x$@PEG@AS1411 ability as potential nanotheranostic agent for anticancer.

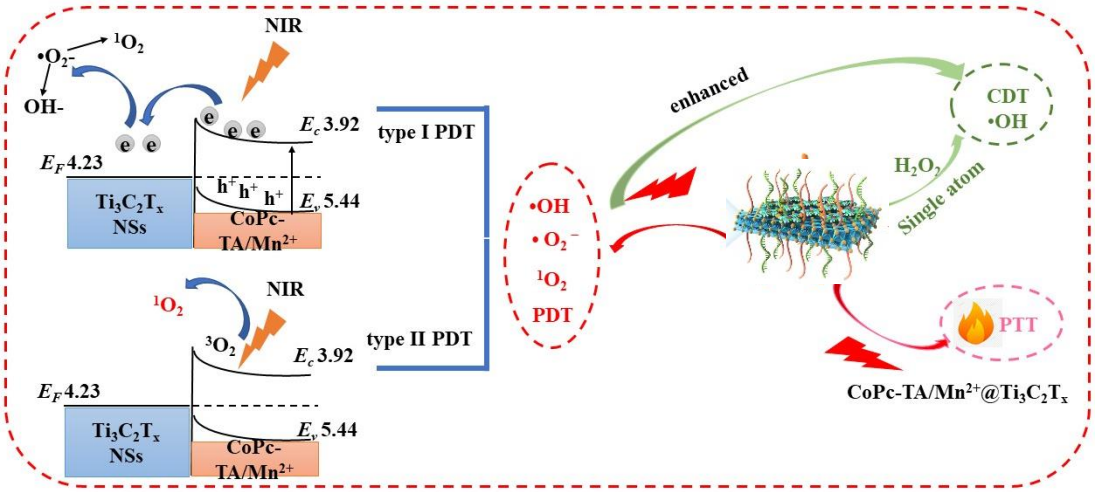

Scheme 21 Schematic illustration of NIR PTT, PDT and CDT effects of CoPc-TA/Mn@$Ti_3C_2T_x$@PEG.

According to the above results, CoPc-TA/Mn@$Ti_3C_2T_x$@PEG can be utilized as a surperior multimodal agents for the PTT/PDT/CDT therapy. Consequently, the generation of ROS behavior was investigated in B16 cells, which were cultured in the CoPc-TA/Mn@$Ti_3C_2T_x$@PEG suspension. The production of ROS was further detected at the cellular level using DCFH-DA, as fluorescent probe, DCFH-DA, can be oxidized by ROS and transferred to 2,7-dichlorofluorescein (DCF, green fluorescence). **Figure 124** displays that no intracellular green fluorescence signals in dark is found for both control groups and CoPc-TA/Mn@$Ti_3C_2T_x$@PEG. It suggests the ROS species cannot be generated without the NIR irradiation and addition of H_2O_2. Moreover, the group of CoPc-TA/Mn@$Ti_3C_2T_x$@PEG + H_2O_2 exhibits weak green fluorescence signal, hinging the insignificant production of •OH, which is attributed to the Fenton-like reaction mediated by Co^{2+} and Mn^{2+}. Likely, the group of CoPc-TA/Mn@$Ti_3C_2T_x$@PEG + NIR also shows weak green fluorescence signal, which is ascribed to $^1O_2$ generated via the PDT effect. However, strong green fluorescence signal distinctlyappears for the CoPc-TA/Mn@$Ti_3C_2T_x$@PEG + H_2O_2 + NIR group, demonstrating its superiority of PTT/PDT/CDT as a synergistic treatment.

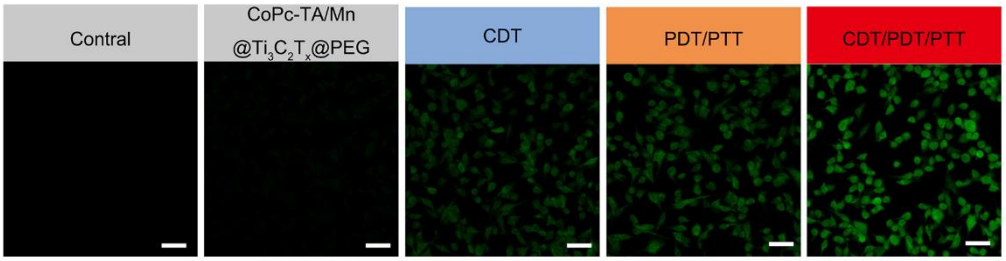

Figure 124 (h) DCF fluorescence images of DCFH-DA-stained B16 cells treated with CoPc-TA/Mn@$Ti_3C_2T_x$@PEG (100 μg mL^{-1}) without or with laser irradiation (scale bars: 50 μm).

10.2.10 In vitro cytotoxicity of the samples

The cytotoxicity of diverse catalysts, including CoPc-TA@Mn, $Ti_3C_2T_x$, CoPc-TA/Mn@$Ti_3C_2T_x$, and CoPc-TA/Mn@$Ti_3C_2T_x$@PEG, were assessed toward both L929 and B16 cells. **Figure 125a** indicates the cytotoxicity of four samples toward different concentrations of L929 cells are low. The survival rate of L929 cells is as high as 90.77% after treated with CoPc-TA/Mn@$Ti_3C_2T_x$@PEG (200 μg mL^{-1}), higher than that of

CoPc-TA/Mn@$Ti_3C_2T_x$ (80.79%). This finding verifies that the modification of CoPc-TA/Mn@$Ti_3C_2T_x$ with PEG layer can substantially boosts biocompatibility. Moreover, the survival rates of L929 cells are as high as 80.26% and 86.62% by incubating with CoPc-TA@Mn and $Ti_3C_2T_x$ NSs, separately, hinting their low cytotoxicity. The similar appearance can be gained for the investigation of the survival rate of B16 cells against the four samples (**Figure 125b**). Also, the CoPc-TA/Mn@$Ti_3C_2T_x$@PEG (200 μg mL^{-1}) group shows the higher survival rate (89.98 %) than that of CoPc-TA@Mn (80.69 %). These results suggests that CoPc-TA/Mn@$Ti_3C_2T_x$ exhibits low cytotoxicity toward L929 and B16 cells, while the modification of PEG not only can improve the dispersion ability of CoPc-TA/Mn@$Ti_3C_2T_x$ in aqueous solution, but also can slightly enhance biocompatibility.

The cytotoxicity of CoPc-TA/Mn@$Ti_3C_2T_x$@PEG by various strategies was compared in vitro to further differentiate each contribution. After treating by various strategies, the cell viability of B16 cells declines with increasing the concentration of CoPc-TA/Mn@$Ti_3C_2T_x$@PEG. The result suggests the cell viability of B16 cells for the PDT/PTT and CDT groups are 54.28 and 29.31%, respectively, at the dosage of CoPc-TA/Mn@$Ti_3C_2T_x$@PEG of 200 μg mL^{-1}, while the cell viability of the PTT/PDT/CDT group is as low as 10.32% due to the synergistic effect (**Figure 125c**). Apparently, the integrated PDT/CDT/PTT therapy strategy ensures the great specific cytotoxicity against cancer cells, making the developed CoPc-TA/Mn@$Ti_3C_2T_x$@PEG acting as a potential photosensitizer for cancer therapy.

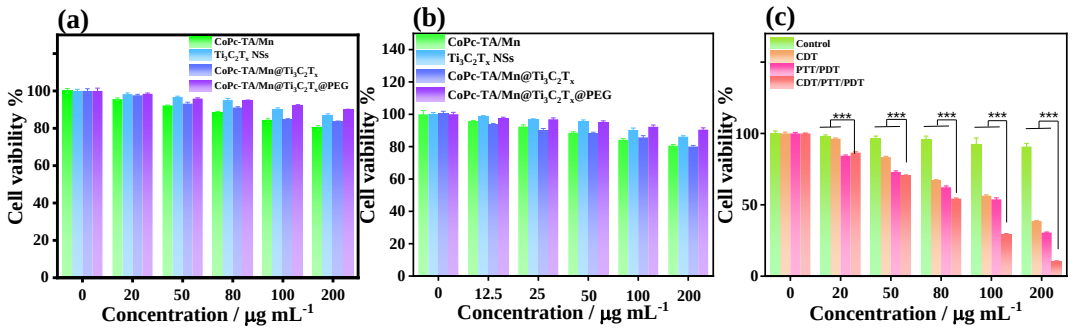

Figure 125. Cell viability of L929 cells (a), B16 cells (b), and B16 cells (c) incubated with CoPc-TA/Mn, $Ti_3C_2T_x$ NSs, CoPc-TA/Mn@$Ti_3C_2T_x$, and CoPc-TA/Mn@$Ti_3C_2T_x$@PEG (concentration:

0, 20, 50, 80, 100, and 200 μg mL^{-1}) for 24 h under different condition.

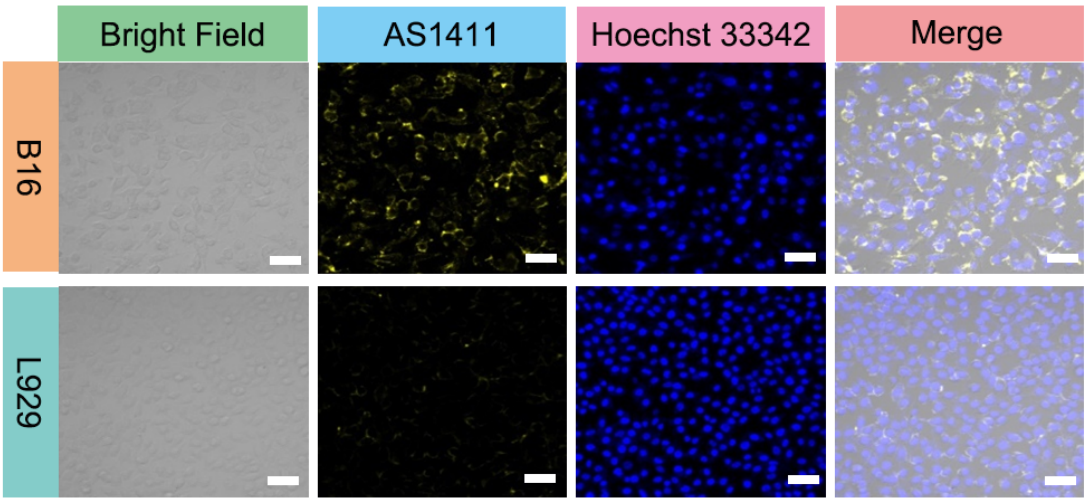

Figure 126. Targeting behavior of CoPc-TA/Mn@$Ti_3C_2T_x$@PEG in B16 and L929 cells (scale bars: 50 μm).

The targeting ability of the CoPc-TA/Mn@$Ti_3C_2T_x$@PEG@AS1411, both L929 and B16 cells were incubated with the CoPc-TA/Mn@$Ti_3C_2T_x$@PEG@AS1411 suspension, for which the cellular uptake efficiencies were monitored by measuring the intracellular fluorescence of 5' Cy3-labeled AS1411 using CLSM. **Figure 126** shows apparently yellow fluorescence signal can be observed with B16 cells, while only weak fluorescence signal is present in L929 cells. This finding indicates B16 cells internalizes CoPc-TA/Mn@$Ti_3C_2T_x$@PEG@AS1411 via active targeting.

To further comprehend the effects of PDT, CDT, and PTT, LIVE/DEAD staining kit using the calcein AM/PI were stained with B16 cells, in which the cell activity was determined by CLSM (**Figure 127**). Clearly, only green fluorescent signal is present in cells when incubated with CoPc-TA/Mn@$Ti_3C_2T_x$@PEG@AS1411, suggesting low killing effect toward cancer cells. Moreover, few red fluorescents signal appears, accompanying with green fluorescent signal when adding H_2O_2 into the material system. As aforementioned, plenty of •OH species can be generated by catalyzing with the catalyst, thus leading to the apoptosis of a few of cells. As compared, the red fluorescence signal of cells becomes stronger under NIR laser irradiation, only remaining low green fluorescence signal. It is ascribed to the combined therapy effects

of PDT and PTT. Further, by integrating H_2O_2 and NIR light irradiation, only red fluorescence signal can be obtained in cells due to the PTT/PDT/CDT synergistic therapy. It means that almost all B16 cells can be killed in the presence of CoPc-TA/Mn@$Ti_3C_2T_x$@PEG@AS1411 and H_2O_2 under NIR 808 nm laser irradiation. The efficient killing result can be owed to the outstandingly synergistic effect of PTT/PDT/CDT for ROS-induced tumor elimination.

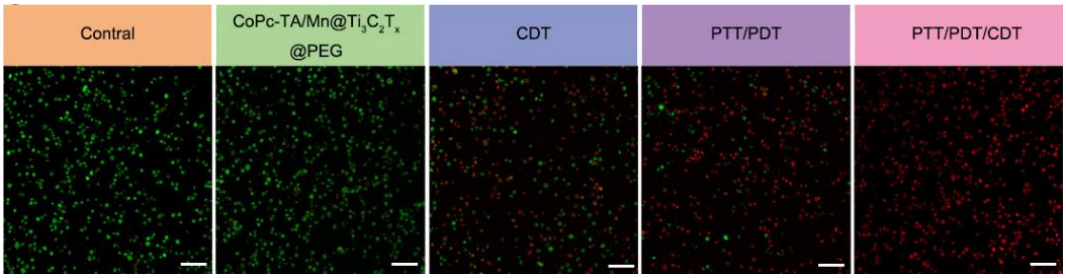

Figure 127 Fluorescence images of Calcein-AM/PI costained B16 cells under different conditions (scale bars: 100 μm).

Moreover, flow cytometry analysis technology was used to further understand the apoptotic and necrotic behaviors of B16 cells. **Figure 128** depicts the control group only treated with 808 nm laser irradiation shows unapparent cell apoptosis (18%), revealing the NIR laser light cannot induce the cell damage without any catalyst. After B16 cells were incubated with the CoPc-TA/Mn@$Ti_3C_2T_x$@PEG@AS1411 suspension for 12 h without laser irradiation, the late apoptosis rate and early apoptotic of B16 cells increase to 25.6% and 5.9 %, respectively. Moreover, the late apoptosis rate of B16 cells rises to 26.5 % when incubated with CoPc-TA/Mn@$Ti_3C_2T_x$@PEG@AS1411 + H_2O_2 for chemotherapy, but without laser irradiation. Further, under 808 nm irradiation, the late apoptosis rate of B16 cells is around 28.6 %, necrosis rate of B16 cells is 3.26 %, and the early apoptosis rate is 3.21 % for the PDT/PTT efficacy. Moreover, the synergistic PTT/PDT/CDT can remarkably enhance the late apoptosis (95.3%) and reduce the necrosis (0.93%) and early apoptosis (0.93%), further confirming that the synergistic PTT/PDT/CDT is a preferred approach for cancer treatment because apoptotic cell death has anti-inflammatory effects. These results are consistent with the live and dead cell staining experiments, clearly demonstrating the superior therapy

ability by combining PDT, CDT, and PTT.

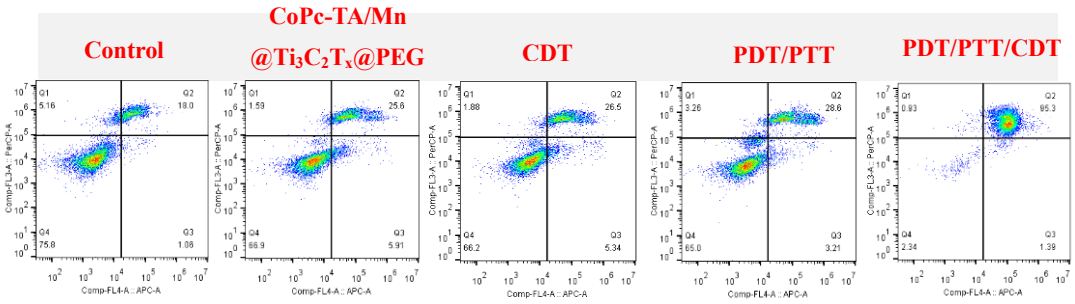

Figure 128 Flow cytometry apoptosis assay of B16 cells after different treatments followed by staining with Annexin-FITC and PI. The groups were (1) Control, (2) CoPc-TA/Mn@$Ti_3C_2T_x$@PEG, (3) CoPc-TA/Mn@$Ti_3C_2T_x$@PEG + H_2O_2, (4) CoPc-TA/Mn@$Ti_3C_2T_x$@PEG + NIR, (5) CoPc-TA/Mn@$Ti_3C_2T_x$@PEG + H_2O_2 + NIR.

10.2.11 In vivo PAI

Besides, the in vivo performance of CoPc-TA/Mn@$Ti_3C_2T_x$@PEG@AS1411 as PAI agent was further accessed in B16-tumor-bearing mice model. The images were taken after intravenous injection at different time intervals and the PA signal of tumor sites were collected (**Figure 129**). After post-injection for 2 h, the PA signal at tumor sites increases clearly, hinting the accumulation of PAI agent in the tumor site. After 3 h, the PA signal intensity reaches the peak and later begins to decay. These results verify that CoPc-TA/Mn@$Ti_3C_2T_x$@PEG@AS1411 exhibits the excellent ability to image tumor site, showing great potential for PAI-guided photo-related cancer therapy. Actually, the in vivo PA images also demonstrate the similar trend for oxyhemoglobin and hemoglobin signal intensity around the tumor vasculature, further proving the oxygen generation and alleviation of hypoxia around tumor site. These collective results verify the in vivo ability of CoPc-TA/Mn@$Ti_3C_2T_x$@PEG@AS1411 as PAI and PTT/PDT agents. After post-injection for 2 h, the tumor sites were irradiated with 808 nm laser for 10 min (0.8 W cm^{-2}), and the temperature for tumor sites were also monitored during the irradiation procedure (**Figure 129c** and **129d**). Compared with control group (treated with PBS and 808 nm laser), the CoPc-TA/Mn@$Ti_3C_2T_x$@PEG@AS1411-treated group shows obviously elevated

temperature. The maximum temperature at tumor site reaches as high as 48.2 °C, which can induce the tumor cell apoptosis, as along with maintaining the safety for normal tissue.

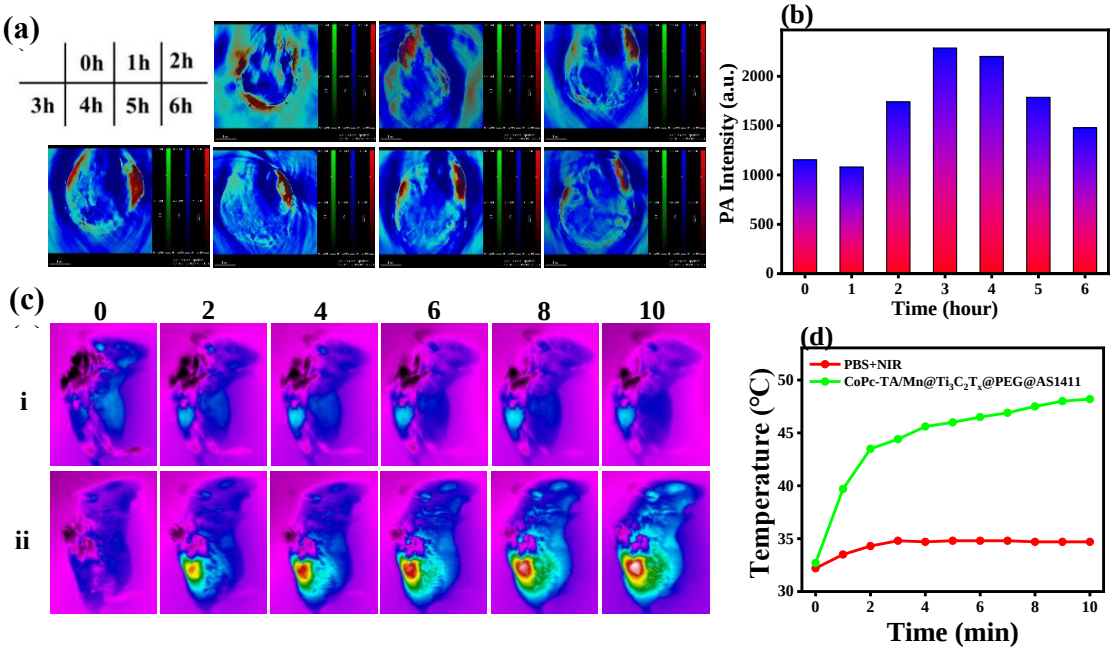

Figure 129 In vivo PAI performances of CoPc-TA/Mn@$Ti_3C_2T_x$@PEG@AS1411 (a) Time-dependent PA images of B16-tumor-bearing mice after post-injection of CoPc-TA/Mn@$Ti_3C_2T_x$@PEG@AS1411 at various time points. (b) The evolution of PA signal intensity as the function of time post-injection. (c) IR thermal images (i PBS + NIR and ii CoPc-TA/Mn@$Ti_3C_2T_x$@PEG@AS141 1+ NIR) and (d) tumor temperature change of B16-tumor-bearing mice injected with PBS (as control) and CoPc-TA/Mn@$Ti_3C_2T_x$@PEG@AS1411 followed by 808 nm laser irradiation (0.8 W cm^{-2}, 10 min).

10.2.12 In vivo antitumor treatment study

The in vivo synergistic PTT/PDT/CDT therapeutic efficacy under 808 nm laser irradiation was further assessed on B16-tumor-bearing mice model via tail vein injection (**Figure 130**). The treatment process for 21 consecutive days is shown in **Figure 130a**. When the tumor volume reached 70 mm^3, each mouse was intravenously injected with the corresponding nanomaterials in the first day, and laser irradiation was executed after 2 h. The mice were randomly divided into four groups (n = 5) treated at

different conditions, including PBS (0.01 M), PBS + NIR, CoPc-TA/Mn@$Ti_3C_2T_x$@PEG@AS1411, and CoPc-TA/Mn@$Ti_3C_2T_x$@PEG@AS1411 + NIR. The body weights for control groups slightly decline after treated for 10 days, while the weights for CoPc-TA/Mn@$Ti_3C_2T_x$@PEG@AS1411-treated group slightly increases, indicating the outstanding biocompatibility of CoPc-TA/Mn@$Ti_3C_2T_x$@PEG@AS1411 (**Figure 130b**). After different group treatment during 14 days (**Figure 130c**), the rapid growth of tumor volume in the NIR group indicated that laser irradiation alone had slightly therapeutic effect on tumors. Comparatively, the mice treated with CoPc-TA/Mn@$Ti_3C_2T_x$@PEG@AS1411 without laser irradiation achieved a moderate tumor suppression effect, having a lower tumor growth inhibition (TGI) rate of 47.1%, indicating that CDT were insufficient to inhibit tumor growth in hypoxia. Obviously, tumor suppression was obtained in the CoPc-TA/Mn@$Ti_3C_2T_x$@PEG@AS1411 + NIR group, showing the TGI rate of 95.77%, which was attributed to the type I/II PDT with the self-sufficient O_2, the production of •OH caused by type I PDT enhanced Co^{2+}/Mn^{2+}-mediated CDT, and the PTT effect of CoPc-TA/Mn@$Ti_3C_2T_x$@PEG@AS1411. The photographs of tumor tissues at day 14 are consistent with the tumor growth trend, hinting that the tumor size decreases with increasing the therapy time for the CoPc-TA/Mn@$Ti_3C_2T_x$@PEG@AS1411+NIR groups. In particular, the tumor in one mouse was completely ablation for the PTT/PDT/CDT-treated group (**Figure 130d**).

Further, main organs and tumors were harvested after treated and stained by H&E, for which no obvious damage and metastases can be found (**Figure 130e**). This finding suggests that tumor cells can be remarkably eliminated via the PTT/PDT/CDT synergistic treatment. Based on the above results and analysis, the superior therapeutic performance can be ascribed to the CoPc-TA/Mn@$Ti_3C_2T_x$@AS1411-mediated high efficient synergistic PTT/PDT/CDT therapeutic efficacy.

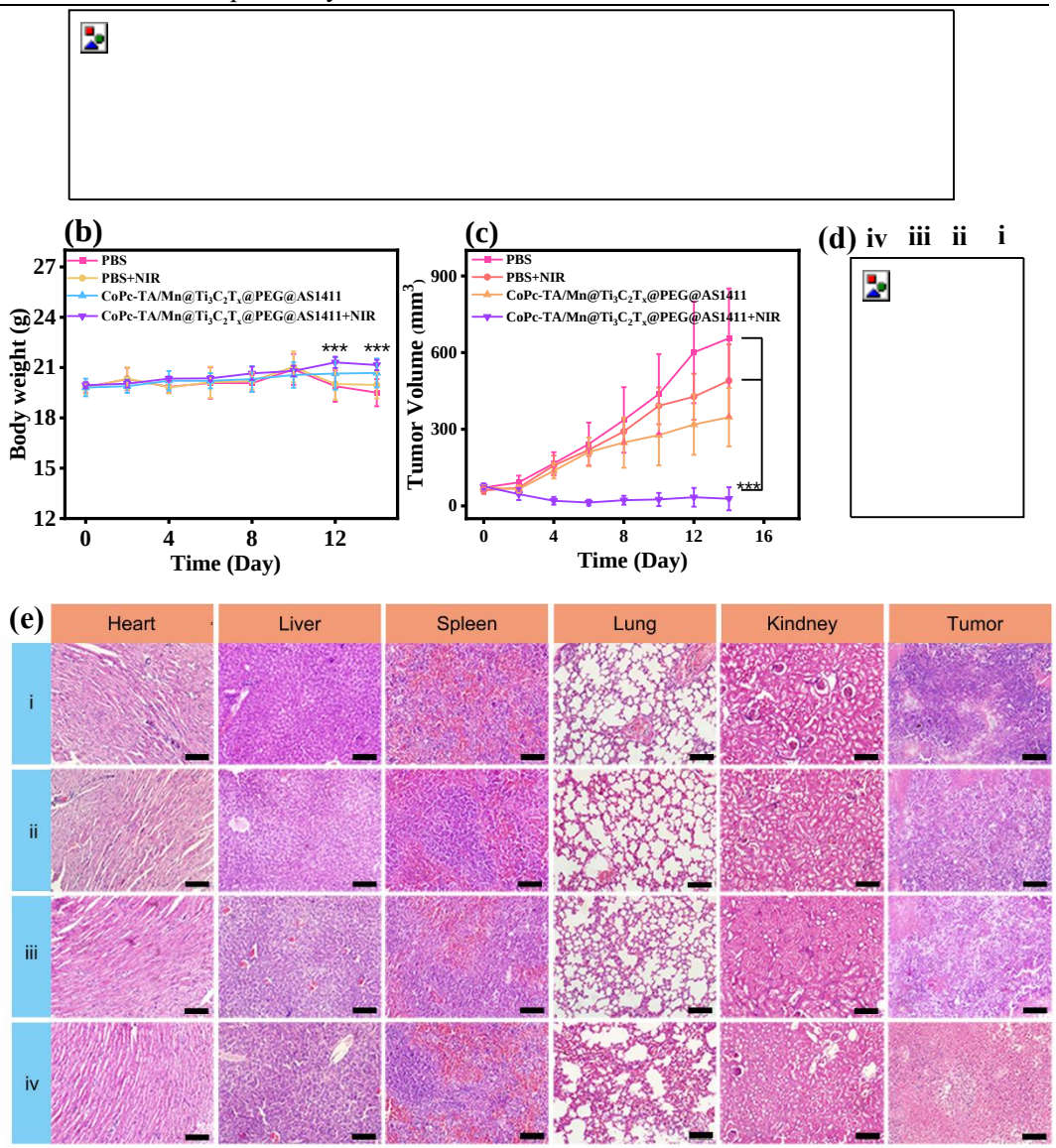

Figure 130 The in vivo synergistic PTT/PDT/CDT therapeutic efficacy of CoPc-TA/Mn@$Ti_3C_2T_x$@PEG@AS1411 against B16-tumor-bearing mice. (a) Treatment schedule of utilizing CoPc-TA/Mn@$Ti_3C_2T_x$@PEG@AS1411 for antitumor therapy. (b) Body weight and (c) tumor volume growth curves of mice after different treatments. (d) Photographs of tumors collected after the whole treatment were finished. (e) H&E histological staining of the main organs and tumor tissues for different groups. Scale bars: 100 μm. Data are means ± SD (n = 5). *P < 0.05, ** P < 0.01, *** P < 0.001.

10.3 Conclusions

In summary, a multimodal cancer therapy platform was provided based on a Schottky barrier junction generated at the Mn doped CoPc-TA and $Ti_3C_2T_x$ NSs, which

demonstrated the effifient NIR-triggered ROS generation ability and excellent performance for cancer cell-targeted PAI-guided PDT/CDT/PTT therapeutic efficacy. Given the efficient CDT effect of the Co^{3+}/Co^{2+} and Mn^{2+}/Mn^{3+} redox and active atomic Co-N and Mn-N sites of CoPc-TA/Mn, the enhanced photoinduced charge separation efficiency due to the Schottky barrier junction, and high photothermal conversion efficiency of $Ti_3C_2T_x$ NSs, the gained junction exhibited PTT-enhanced CDT/PDT effect, in which the integrated Type I and Type II PDT mechanism was realized, accpmpanying with the self-supplying O_2 ability. The CoPc-TA/Mn@$Ti_3C_2T_x$@PEG-mediated combined treatment resulted in synergistic cytotoxicity and apoptosis-inducing activity in B16 cells, which also obviously suppressed tumor growth. The in vivo experiments showed outstanding tumor accumulation of photo-agents, excellent biocompatibility, and tumor-targeting ability by using CoPc-TA/Mn@$Ti_3C_2T_x$@PEG@AS1411. As a result, complete tumor ablation was achieved by a single application of PDT/PTT/CDT procedure in solid tumor bearing mice. This work would extend the exploration of the Schottky barrier junction and its application as a multifunctional nanoplatform for synergistic antitumor therapy of solid tumor.

References:

(1) Nabiyeva, T.; Marschner, C.; Blom, B. *European Journal of Medicinal Chemistry* **2020**, *201*, 112483.

(2) ROSENBERG, B.; VAN CAMP, L.; KRIGAS, T. *Nature* **1965**, *205*, 698-699.

(3) Miller, R. P.; Tadagavadi, R. K.; Ramesh, G.; Reeves, W. B. In *Toxins*, 2010; Vol. 2.

(4) Wang, L.; Liu, X.; Ren, Y.; Zhang, J.; Chen, J.; Zhou, W.; Guo, W.; Wang, X.; Chen, H.; Li, M.; Yuan, X.; Zhang, X.; Yang, J.; Wu, C. *Cell Death & Disease* **2017**, *8*, e2746-e2746.

(5) Li, X.; Gorle, A. K.; Sundaraneedi, M. K.; Keene, F. R.; Collins, J. G. *Coordination Chemistry Reviews* **2018**, *375*, 134-147.

(6) Delasoie, J.; Pavic, A.; Voutier, N.; Vojnovic, S.; Crochet, A.; Nikodinovic-Runic, J.; Zobi, F. *European Journal of Medicinal Chemistry* **2020**, *204*, 112583.

(7) Novohradsky, V.; Markova, L.; Kostrhunova, H.; Trávníček, Z.; Brabec, V.; Kasparkova, J. *Scientific Reports* **2019**, *9*, 13327.

(8) Seyferth, D. *Organometallics* **2002**, *21*, 2800-2820.

(9) Winkhaus, G.; Singer, H. *Journal of Organometallic Chemistry* **1967**, *7*, 487-491.

(10) Crochet, P.; Cadierno, V. In *Inorganics*, 2021; Vol. 9.

(11) González-Fernández, R.; Crochet, P.; Cadierno, V. *Inorganica Chimica Acta* **2021**, *517*, 120180.

(12) Werner, H. *Organometallics* **2005**, *24*, 1036-1049.

(13) Dorcier, A.; Dyson, P. J.; Gossens, C.; Rothlisberger, U.; Scopelliti, R.; Tavernelli, I. *Organometallics* **2005**, *24*, 2114-2123.

(14) Allardyce, C. S.; Dyson, P. J.; Ellis, D. J.; Salter, P. A.; Scopelliti, R. *Journal of Organometallic Chemistry* **2003**, *668*, 35-42.

(15) Allardyce, C. S.; Dyson, P. J.; Ellis, D. J.; Heath, S. L. *Chemical Communications* **2001**, 1396-1397.

(16) Murray, B. S.; Babak, M. V.; Hartinger, C. G.; Dyson, P. J. *Coordination*

Chemistry Reviews **2016**, *306*, 86-114.

(17) Hartinger, C. G.; Zorbas-Seifried, S.; Jakupec, M. A.; Kynast, B.; Zorbas, H.; Keppler, B. K. *Journal of Inorganic Biochemistry* **2006**, *100*, 891-904.

(18) Rausch, M.; Dyson, P. J.; Nowak-Sliwinska, P. *Advanced Therapeutics* **2019**, *2*, 1900042.

(19) Wu, B.; Ong, M. S.; Groessl, M.; Adhireksan, Z.; Hartinger, C. G.; Dyson, P. J.; Davey, C. A. *Chemistry – A European Journal* **2011**, *17*, 3562-3566.

(20) Allardyce, C. S.; Dyson, P. J. *Dalton Transactions* **2016**, *45*, 3201-3209.

(21) Jakupec, M. A.; Galanski, M.; Arion, V. B.; Hartinger, C. G.; Keppler, B. K. *Dalton Transactions* **2008**, 183-194.

(22) Kelland, L. *Nature Reviews Cancer* **2007**, *7*, 573-584.

(23) Hartinger, C. G.; Dyson, P. J. *Chemical Society Reviews* **2009**, *38*, 391-401.

(24) Hanif, M.; Nazarov, A. A.; Hartinger, C. G.; Kandioller, W.; Jakupec, M. A.; Arion, V. B.; Dyson, P. J.; Keppler, B. K. *Dalton Transactions* **2010**, *39*, 7345-7352.

(25) DeWitt, D. L.; El-Harith, E. A.; Kraemer, S. A.; Andrews, M. J.; Yao, E. F.; Armstrong, R. L.; Smith, W. L. *Journal of Biological Chemistry* **1990**, *265*, 5192-5198.

(26) Schmid, W. F.; John, R. O.; Arion, V. B.; Jakupec, M. A.; Keppler, B. K. *Organometallics* **2007**, *26*, 6643-6652.

(27) Zhang, P.; Huang, H. *Dalton Transactions* **2018**, *47*, 14841-14854.

(28) Johnstone, T. C.; Suntharalingam, K.; Lippard, S. J. *Philosophical Transactions of the Royal Society A: Mathematical, Physical and Engineering Sciences* **2015**, *373*, 20140185.

(29) Romero-Canelón, I.; Salassa, L.; Sadler, P. J. *Journal of Medicinal Chemistry* **2013**, *56*, 1291-1300.

(30) Li, P.; Modica, J. A.; Howarth, A. J.; Vargas L., E.; Moghadam, P. Z.; Snurr, R. Q.; Mrksich, M.; Hupp, J. T.; Farha, O. K. *Chem* **2016**, *1*, 154-169.

(31) Zimpel, A.; Al Danaf, N.; Steinborn, B.; Kuhn, J.; Höhn, M.; Bauer, T.; Hirschle, P.; Schrimpf, W.; Engelke, H.; Wagner, E.; Barz, M.; Lamb, D. C.; Lächelt, U.; Wuttke, S. *ACS Nano* **2019**, *13*, 3884-3895.

(32) Goesmann, H.; Feldmann, C. *Angewandte Chemie International Edition* **2010**, *49*, 1362-1395.

(33) Bai, L.; Phua, S. Z. F.; Lim, W. Q.; Jana, A.; Luo, Z.; Tham, H. P.; Zhao, L.; Gao, Q.; Zhao, Y. *Chemical Communications* **2016**, *52*, 4128-4131.

(34) LaMer, V. K.; Dinegar, R. H. *Journal of the American Chemical Society* **1950**, *72*, 4847-4854.

(35) Ploetz, E.; Engelke, H.; Lächelt, U.; Wuttke, S. *Advanced Functional Materials* **2020**, *30*, 1909062.

(36) Barros, B. S.; de Lima Neto, O. J.; de Oliveira Frós, A. C.; Kulesza, J. *ChemistrySelect* **2018**, *3*, 7459-7471.

(37) Freund, R.; Zaremba, O.; Arnauts, G.; Ameloot, R.; Skorupskii, G.; Dincă, M.; Bavykina, A.; Gascon, J.; Ejsmont, A.; Goscianska, J.; Kalmutzki, M.; Lächelt, U.; Ploetz, E.; Diercks, C. S.; Wuttke, S. *Angewandte Chemie International Edition* **2021**, *60*, 23975-24001.

(38) Agostoni, V.; Horcajada, P.; Noiray, M.; Malanga, M.; Aykaç, A.; Jicsinszky, L.; Vargas-Berenguel, A.; Semiramoth, N.; Daoud-Mahammed, S.; Nicolas, V.; Martineau, C.; Taulelle, F.; Vigneron, J.; Etcheberry, A.; Serre, C.; Gref, R. *Scientific Reports* **2015**, *5*, 7925.

(39) Wang, Y.; Hu, Y.; He, Q.; Yan, J.; Xiong, H.; Wen, N.; Cai, S.; Peng, D.; Liu, Y.; Liu, Z. *Biosensors and Bioelectronics* **2020**, *169*, 112604.

(40) Dong, J.; Li, X.; Peh, S. B.; Yuan, Y. D.; Wang, Y.; Ji, D.; Peng, S.; Liu, G.; Ying, S.; Yuan, D.; Jiang, J.; Ramakrishna, S.; Zhao, D. *Chemistry of Materials* **2019**, *31*, 146-160.

(41) Zhang, Z.; Duan, F.; Tian, J.; He, J.; Yang, L.; Zhao, H.; Zhang, S.; Liu, C.; He, L.; Chen, M.; Chen, D.; Du, M. *ACS Sensors* **2017**, *2*, 982-989.

(42) Gu, C.; Guo, C.; Li, Z.; Wang, M.; Zhou, N.; He, L.; Zhang, Z.; Du, M. *Biosensors and Bioelectronics* **2019**, *134*, 8-15.

(43) Dong, S.; Peng, L.; Wei, W.; Huang, T. *ACS Applied Materials & Interfaces* **2018**, *10*, 14665-14672.

(44)Ko, M.; Mendecki, L.; Eagleton, A. M.; Durbin, C. G.; Stolz, R. M.; Meng, Z.; Mirica, K. A. *Journal of the American Chemical Society* **2020**, *142*, 11717-11733.

(45)Liu, S.; Bai, J.; Huo, Y.; Ning, B.; Peng, Y.; Li, S.; Han, D.; Kang, W.; Gao, Z. *Biosensors and Bioelectronics* **2020**, *149*, 111801.

(46)Wang, M.; Hu, M.; Liu, J.; Guo, C.; Peng, D.; Jia, Q.; He, L.; Zhang, Z.; Du, M. *Biosensors and Bioelectronics* **2019**, *132*, 8-16.

(47)Wang, Y.; Wang, L.; Huang, W.; Zhang, T.; Hu, X.; Perman, J. A.; Ma, S. *Journal of Materials Chemistry A* **2017**, *5*, 8385-8393.

(48)Wang, F.; Chen, X.; Chen, L.; Yang, J.; Wang, Q. *Materials Science and Engineering: C* **2019**, *96*, 41-50.

(49)Lu, M.; Deng, Y.; Li, Y.; Li, T.; Xu, J.; Chen, S.; Wang, J. *Analytica Chimica Acta* **2020**, *1110*, 35-43.

(50)Lei, J.; Qian, R.; Ling, P.; Cui, L.; Ju, H. *TrAC Trends in Analytical Chemistry* **2014**, *58*, 71-78.

(51)Zhu, Q.; Zhang, W.; Zhang, H.; Yuan, R.; He, H. *Journal of Materials Chemistry C* **2020**, *8*, 16984-16991.

(52)Guo, L.; Wang, Y.; Pang, Y.; Shen, X.; Yang, N.; Ma, Y.; Zhang, Y. *Journal of Electroanalytical Chemistry* **2021**, *881*, 114931.

(53)Liu, X.; Huang, D.; Lai, C.; Zeng, G.; Qin, L.; Wang, H.; Yi, H.; Li, B.; Liu, S.; Zhang, M.; Deng, R.; Fu, Y.; Li, L.; Xue, W.; Chen, S. *Chemical Society Reviews* **2019**, *48*, 5266-5302.

(54)Liang, D.; Zhang, X.; Wang, Y.; Huo, T.; Qian, M.; Xie, Y.; Li, W.; Yu, Y.; Shi, W.; Liu, Q.; Zhu, J.; Luo, C.; Cao, Z.; Huang, R. *Bioactive Materials* **2022**, *14*, 145-151.

(55)Zhang, T.; Chen, Y.; Huang, W.; Wang, Y.; Hu, X. *Sensors and Actuators B: Chemical* **2018**, *276*, 362-369.

(56)Liu, X.; Hu, M.; Wang, M.; Song, Y.; Zhou, N.; He, L.; Zhang, Z. *Biosensors and Bioelectronics* **2019**, *123*, 59-68.

(57)Ma, J.; Shu, T.; Sun, Y.; Zhou, X.; Ren, C.; Su, L.; Zhang, X. *Small* **2022**, *18*,

2103516.

(58) Das, G.; Benyettou, F.; Sharama, S. K.; Prakasam, T.; Gándara, F.; de la Peña-O Shea, V. A.; Saleh, N.; Pasricha, R.; Jagannathan, R.; Olson, M. A.; Trabolsi, A. *Chemical Science* **2018**, *9*, 8382-8387.

(59) Pandey, A.; Dhas, N.; Deshmukh, P.; Caro, C.; Patil, P.; Luisa García-Martín, M.; Padya, B.; Nikam, A.; Mehta, T.; Mutalik, S. *Coordination Chemistry Reviews* **2020**, *409*, 213212.

(60) Feng, J.; Ren, W.; Kong, F.; Dong, Y. *Inorganic Chemistry Frontiers* **2021**, *8*, 848-879.

(61) Jin, T.; Cheng, D.; Jiang, G.; Xing, W.; Liu, P.; Wang, B.; Zhu, W.; Sun, H.; Sun, Z.; Xu, Y.; Qian, X. *Bioactive Materials* **2022**, *14*, 42-51.

(62) Wang, Y.; Liu, X.; Wu, W.; Mao, D.; Wang, B.; Tang, G.; Liu, B. *Advanced Therapeutics* **2020**, *3*, 2000011.

(63) Shang, W.; Peng, L.; Guo, P.; Hui, H.; Yang, X.; Tian, J. *ACS Biomaterials Science & Engineering* **2020**, *6*, 1008-1016.

(64) Wang, L.; Qu, X.; Zhao, Y.; Weng, Y.; Waterhouse, G. I. N.; Yan, H.; Guan, S.; Zhou, S. *ACS Applied Materials & Interfaces* **2019**, *11*, 35228-35237.

(65) Li, B.; Wang, X.; Chen, L.; Zhou, Y.; Dang, W.; Chang, J.; Wu, C. *Theranostics* **2018**, *8*, 4086-4096.

(66) Zheng, X.; Wang, L.; Liu, M.; Lei, P.; Liu, F.; Xie, Z. *Chemistry of Materials* **2018**, *30*, 6867-6876.

(67) Liang, S.; Deng, X.; Chang, Y.; Sun, C.; Shao, S.; Xie, Z.; Xiao, X.; Ma, P. A.; Zhang, H.; Cheng, Z.; Lin, J. *Nano Letters* **2019**, *19*, 4134-4145.

(68) Cheng, Y.; Wen, C.; Sun, Y.; Yu, H.; Yin, X. *Advanced Functional Materials* **2021**, *31*, 2104378.

(69) Zhao, K.; Gong, P.; Huang, J.; Huang, Y.; Wang, D.; Peng, J.; Shen, D.; Zheng, X.; You, J.; Liu, Z. *Microporous and Mesoporous Materials* **2021**, *311*, 110713.

(70) Hu, C.; Zhang, Z.; Liu, S.; Liu, X.; Pang, M. *ACS Applied Materials & Interfaces* **2019**, *11*, 23072-23082.

(71) Wang, D.; Zhang, Z.; Lin, L.; Liu, F.; Wang, Y.; Guo, Z.; Li, Y.; Tian, H.; Chen, X. *Biomaterials* **2019**, *223*, 119459.

(72) Guan, Q.; Zhou, L.; Li, Y.; Li, W.; Wang, S.; Song, C.; Dong, Y. *ACS Nano* **2019**, *13*, 13304-13316.

(73) Hanif, M.; Arshad, J.; Astin, J. W.; Rana, Z.; Zafar, A.; Movassaghi, S.; Leung, E.; Patel, K.; Söhnel, T.; Reynisson, J.; Sarojini, V.; Rosengren, R. J.; Jamieson, S. M. F.; Hartinger, C. G. *Angewandte Chemie International Edition* **2020**, *59*, 14609-14614.

(74) Palmucci, J.; Marchetti, F.; Pettinari, R.; Pettinari, C.; Scopelliti, R.; Riedel, T.; Therrien, B.; Galindo, A.; Dyson, P. J. *Inorganic Chemistry* **2016**, *55*, 11770-11781.

(75) Spasyuk, D.; Smith, S.; Gusev, D. G. *Angewandte Chemie International Edition* **2012**, *51*, 2772-2775.

(76) Pettinari, R.; Marchetti, F.; Condello, F.; Pettinari, C.; Lupidi, G.; Scopelliti, R.; Mukhopadhyay, S.; Riedel, T.; Dyson, P. J. *Organometallics* **2014**, *33*, 3709-3715.

(77) Pettinari, R.; Marchetti, F.; Di Nicola, C.; Pettinari, C.; Cuccioloni, M.; Bonfili, L.; Eleuteri, A. M.; Therrien, B.; Batchelor, L. K.; Dyson, P. J. *Inorganic Chemistry Frontiers* **2019**, *6*, 2448-2457.

(78) Harringer, S.; Wernitznig, D.; Gajic, N.; Diridl, A.; Wenisch, D.; Hejl, M.; Jakupec, M. A.; Theiner, S.; Koellensperger, G.; Kandioller, W.; Keppler, B. K. *Dalton Transactions* **2020**, *49*, 15693-15711.

(79) Rosenthal, M. R. *Journal of Chemical Education* **1973**, *50*, 331.

(80) Ragazzon, G.; Bratsos, I.; Alessio, E.; Salassa, L.; Habtemariam, A.; McQuitty, R. J.; Clarkson, G. J.; Sadler, P. J. *Inorganica Chimica Acta* **2012**, *393*, 230-238.

(81) Pettinari, R.; Petrini, A.; Marchetti, F.; Di Nicola, C.; Scopelliti, R.; Riedel, T.; Pittet, L. D.; Galindo, A.; Dyson., P. J. *ChemistrySelect* **2018**, *3*, 6696-6700.

(82) Rilak Simović, A.; Masnikosa, R.; Bratsos, I.; Alessio, E. *Coordination Chemistry Reviews* **2019**, *398*, 113011.

(83) Merlino, A.; Marzo, T.; Messori, L. *Chemistry – A European Journal* **2017**, *23*, 6942-6947.

(84) Cirri, D.; Pillozzi, S.; Gabbiani, C.; Tricomi, J.; Bartoli, G.; Stefanini, M.;

Michelucci, E.; Arcangeli, A.; Messori, L.; Marzo, T. *Dalton Transactions* **2017**, *46*, 3311-3317.

(85) Messori, L.; Marzo, T.; Merlino, A. *Chemical Communications* **2014**, *50*, 8360-8362.

(86) Güner, A. *Toxin Reviews* **2021**, *40*, 25-34.

(87) Zhao, F.; Shen, Q.; Wang, H.; Han, X.; Yang, Z. *Food Control* **2017**, *79*, 227-233.

(88) Caglayan, M. O.; Şahin, S.; Üstündağ, Z. *Critical reviews in analytical chemistry* **2020**, 1-20.

(89) Zhang, K.; Li, H.; Wang, W.; Cao, J.; Gan, N.; Han, H. *ACS Sensors* **2020**, *5*, 3721-3738.

(90) He, B.; Yan, X. *Sensors and Actuators B: Chemical* **2019**, *290*, 477-483.

(91) Zhang, K.; Kirlikovali, K. O.; Le, Q. V.; Jin, Z.; Varma, R. S.; Jang, H. W.; Farha, O. K.; Shokouhimehr, M. *ACS Applied Nano Materials* **2020**, *3*, 3964-3990.

(92) Zhang, Z.; Nguyen, H. T. H.; Miller, S. A.; Cohen, S. M. *Angewandte Chemie International Edition* **2015**, *54*, 6152-6157.

(93) Zhu, J.; Li, P.; Guo, W.; Zhao, Y.; Zou, R. *Coordination Chemistry Reviews* **2018**, *359*, 80-101.

(94) Feng, L.; Yuan, S.; Li, J.; Wang, K.; Day, G. S.; Zhang, P.; Wang, Y.; Zhou, H. *ACS Central Science* **2018**, *4*, 1719-1726.

(95) Samanta, P.; Desai, A. V.; Sharma, S.; Chandra, P.; Ghosh, S. K. *Inorganic Chemistry* **2018**, *57*, 2360-2364.

(96) Allegrini, F.; Olivieri, A. C. *Analytical Chemistry* **2014**, *86*, 7858-7866.

(97) Wu, Z.; Xu, E.; Chughtai, M. F. J.; Jin, Z.; Irudayaraj, J. *Food Chemistry* **2017**, *230*, 673-680.

(98) Duan, F.; Hu, M.; Guo, C.; Song, Y.; Wang, M.; He, L.; Zhang, Z.; Pettinari, R.; Zhou, L. *Chemical Engineering Journal* **2020**, *398*, 125452.

(99) Yang, Y.; Yin, Y.; Wang, S.; Dong, Y. *Analytica Chimica Acta* **2021**, *1155*, 338345.

(100) Sha, J.; Zhao, N.; Liu, E.; Shi, C.; He, C.; Li, J. *Carbon* **2014**, *68*, 352-359.

(101) Luo, P.; Ji, Z.; Li, C.; Shi, G. *Nanoscale* **2013**, *5*, 7361-7367.

(102) Jin, J.; Li, P.; Chun, D. H.; Jin, B.; Zhang, K.; Park, J. H. *Advanced Functional Materials* **2021**, *n/a*, 2102511.

(103) Jia, C.; Bai, J.; Liu, Z.; Gao, S.; Han, Y.; Yan, H. *Analytica Chimica Acta* **2020**, *1128*, 99-106.

(104) Chen, H.; Wang, S.; Tang, Y.; Zeng, F.; Schobert, H.; Zhang, X. *Fuel* **2021**, *292*, 120373.

(105) Zhang, Y.; Zhang, Y.; Huang, Y.; Jia, Y.; Chen, L.; Pan, Y.; Wang, M. *Journal of Alloys and Compounds* **2021**, *867*, 159020.

(106) He, Y.; Luo, S.; Hu, X.; Cheng, Y.; Huang, Y.; Chen, S.; Fu, M.; Jia, Y.; Liu, X. *Chemical Engineering Journal* **2021**, *420*, 127643.

(107) Zhang, Z.; Huang, L.; Sheng, S.; Jiang, C.; Wang, Y. *Sensors and Actuators B: Chemical* **2021**, *343*, 130119.

(108) Yang, C.; Liu, Y.; Sun, X.; Zhang, Y.; Hou, L.; Zhang, Q.; Yuan, C. *Electrochimica Acta* **2018**, *271*, 165-172.

(109) Li, J.; Tang, S.; Lu, L.; Zeng, H. C. *Journal of the American Chemical Society* **2007**, *129*, 9401-9409.

(110) Li, N.; Zhang, Z.; Zhang, J.; Ma, Y.; Chen, X.; Fan, Y. *Dalton T.* **2021**, *50*, 6506-6511.

(111) Fu, Y.; Sun, D.; Chen, Y.; Huang, R.; Ding, Z.; Fu, X.; Li, Z. *Angewandte Chemie International Edition* **2012**, *51*, 3364-3367.

(112) Wang, M.; Yang, L.; Guo, C.; Liu, X.; He, L.; Song, Y.; Zhang, Q.; Qu, X.; Zhang, H.; Zhang, Z.; Fang, S. *ChemistrySelect* **2018**, *3*, 3664-3674.

(113) Cui, J.; Kan, L.; Li, Z.; Yang, L.; Wang, M.; He, L.; Lou, Y.; Xue, Y.; Zhang, Z. *Talanta* **2021**, *228*, 122060.

(114) Liu, C.; Sun, C.; Tian, J.; Wang, Z.; Ji, H.; Song, Y.; Zhang, S.; Zhang, Z.; He, L.; Du, M. *Biosensors and Bioelectronics* **2017**, *91*, 804-810.

(115) Ramezanzadeh, M.; Ramezanzadeh, B.; Bahlakeh, G.; Tati, A.; Mahdavian, M. *Chemical Engineering Journal* **2021**, *408*, 127361.

(116) Wang, Y.; Zhao, G.; Zhang, G.; Zhang, Y.; Wang, H.; Cao, W.; Li, T.; Wei, Q. *Sensors and Actuators B: Chemical* **2020**, *319*, 128313.

(117) Zhang, Z.; Ji, H.; Song, Y.; Zhang, S.; Wang, M.; Jia, C.; Tian, J.; He, L.; Zhang, X.; Liu, C. *Biosensors and Bioelectronics* **2017**, *94*, 358-364.

(118) Wang, S.; Li, Z.; Duan, F.; Hu, B.; He, L.; Wang, M.; Zhou, N.; Jia, Q.; Zhang, Z. *Analytica Chimica Acta* **2019**, *1047*, 150-162.

(119) Huang, P.; Lei, J.; Sun, Z.; Hu, X. *Chemosphere* **2021**, *268*, 129157.

(120) Fragoso, A.; Laboria, N.; Latta, D.; O'Sullivan, C. K. *Analytical Chemistry* **2008**, *80*, 2556-2563.

(121) Mu, Z.; Ma, L.; Wang, J.; Zhou, J.; Yuan, Y.; Bai, L. *Food Chemistry* **2021**, *340*, 128128.

(122) Han, Z.; Tang, Z.; Jiang, K.; Huang, Q.; Meng, J.; Nie, D.; Zhao, Z. *Biosensors and Bioelectronics* **2020**, *150*, 111894.

(123) Ma, L.; Bai, L.; Zhao, M.; Zhou, J.; Chen, Y.; Mu, Z. *Analytica Chimica Acta* **2019**, *1060*, 71-78.

(124) Khan, I. M.; Niazi, S.; Yu, Y.; Mohsin, A.; Mushtaq, B. S.; Iqbal, M. W.; Rehman, A.; Akhtar, W.; Wang, Z. *Analytical Chemistry* **2019**, *91*, 14085-14092.

(125) Azri, F. A.; Eissa, S.; Zourob, M.; Chinnappan, R.; Sukor, R.; Yusof, N. A.; Raston, N. H. A.; Alhoshani, A.; Jinap, S. *Microchimica Acta* **2020**, *187*, 266.

(126) Xu, W.; Qing, Y.; Chen, S.; Chen, J.; Qin, Z.; Qiu, J.; Li, C. *Microchimica Acta* **2017**, *184*, 3339-3347.

(127) Anik, Ü.; Timur, S.; Dursun, Z. *Microchimica Acta* **2019**, *186*, 196.

(128) Zhao, Z.; Ding, J.; Zhu, R.; Pang, H. *Journal of Materials Chemistry A* **2019**, *7*, 15519-15540.

(129) Guo, C.; Su, F.; Song, Y.; Hu, B.; Wang, M.; He, L.; Peng, D.; Zhang, Z. *ACS Appl. Mater. Inter.* **2017**, *9*, 41188-41199.

(130) Zhang, Z.; Ji, H.; Song, Y.; Zhang, S.; Wang, M.; Jia, C.; Tian, J.; He, L.;

Zhang, X.; Liu, C. *Biosensors and Bioelectronics* **2017**, *94*, 358-364.

(131) Bagheri, M.; Masoomi, M. Y.; Morsali, A. *Sensors and Actuators B-Chemical* **2017**, *243*, 353-360.

(132) Wang, M.; Hu, M.; Li, Z.; He, L.; Song, Y.; Jia, Q.; Zhang, Z.; Du, M. *Biosensors and Bioelectronics* **2019**, *142*, 111536.

(133) Li, Y.; Hu, M.; Huang, X.; Wang, M.; He, L.; Song, Y.; Jia, Q.; Zhou, N.; Zhang, Z.; Du, M. *Sensors and Actuators B-Chemical* **2020**, *306*, 127608.

(134) Al-Sagur, H.; Shanmuga Sundaram, K.; Kaya, E. N.; Durmuş, M.; Basova, T. V.; Hassan, A. *Biosensors & Bioelectronics* **2019**, *139*, 111323.

(135) Liang, J.; Xie, Y.; Wang, X.; Wang, Q.; Liu, T.; Huang, Y.; Cao, R. *Chemical Communications* **2018**, *54*, 342-345.

(136) de Fátima Giarola, J.; César Pereira, A. *Electroanalysis* **2016**, *28*, 1348-1355.

(137) Al-Sagur, H.; Komathi, S.; Khan, M. A.; Gurek, A. G.; Hassan, A. *Biosensors & Bioelectronics* **2017**, *92*, 638-645.

(138) Zeng, Z.; Fang, X.; Miao, W.; Liu, Y.; Maiyalagan, T.; Mao, S. *ACS Sensors* **2019**, *4*, 1934-1941.

(139) Xu, H.; Liao, C.; Liu, Y.; Ye, B.; Liu, B. *Analytical Chemistry* **2018**, *90*, 4438-4444.

(140) Wang, H.; Bu, Y.; Dai, W.; Li, K.; Wang, H.; Zuo, X. *Sensors and Actuators B-Chemical* **2015**, *216*, 298-306.

(141) Sheng, H.; Chen, D.; Li, N.; Xu, Q.; Li, H.; He, J.; Lu, J. *Chemistry of Materials* **2017**, *29*, 5612-5616.

(142) Hong, D.; Hwang, Y. K.; Serre, C.; Férey, G.; Chang, J. *Advanced Functional Materials* **2009**, *19*, 1537-1552.

(143) Guo, Q.; Ren, L.; Kumar, P.; Cybulskis, V. J.; Mkhoyan, K. A.; Davis, M. E.; Tsapatsis, M. *Angewandte Chemie* **2018**, *130*, 5020-5024.

(144) Peng, J.; Han, S.; Chen, Z.; Yang, J.; Pei, Y.; Bao, C.; Qiao, L.; Chen, W.; Liu, B. *Biochemical and Biophysical Research Communications* **2020**, *522*, 348-354.

(145) Karmakar, S.; Roy, D.; Janiak, C.; De, S. *Separation and Purification Technology* **2019**, *215*, 259-275.

(146) Hou, Y.; Liu, J.; Hong, M.; Li, X.; Ma, Y.; Yue, Q.; Li, C. *Biosensors & Bioelectronics* **2017**, *92*, 259-265.

(147) Li, X.; Zhao, Q.; Qiao, J.; Zhang, Q.; Zhou, X. *RSC Advances* **2019**, *9*, 10865-10869.

(148) Prajapati, P. K.; Kumar, A.; Jain, S. L. *ACS Sustainable Chemistry & Engineering* **2018**, *6*, 7799-7809.

(149) Asadi, F.; Azizi, S. N.; Chaichi, M. J. *Mater. Sci. Eng. C* **2019**, *105*, 110058.

(150) Zhang, W.; Zhang, R.; Huang, Y.; Yang, J. *Crystal Growth & Design* **2018**, *18*, 7533-7540.

(151) Jarrah, A.; Farhadi, S. *Acta Chimica Slovenica* **2019**, *66*, 1.

(152) Wang, Q.; Shao, L.; Ma, Z.; Xu, J.; Li, Y.; Wang, C. *Electrochimica Acta* **2018**, *281*, 582-593.

(153) Sivanesan, A.; John, S. A. *Electrochimica Acta* **2009**, *54*, 7458-7463.

(154) Chen, X.; Chen, X.; Cai, S.; Yu, E.; Chen, J.; Jia, H. *Applied Surface Science* **2019**, *475*, 312-324.

(155) Kuo, C.; Lan, W.; Chen, C. *Nanoscale* **2014**, *6*, 334-341.

(156) McArthur, S. L. *Surface and Interface Analysis* **2006**, *38*, 1380-1385.

(157) Chen, X.; Gao, H.; Yang, M.; Xing, L.; Dong, W.; Li, A.; Zheng, H.; Wang, G. *Energy Storage Materials* **2019**, *18*, 349-355.

(158) Wang, M.; Hu, M.; Li, Z.; He, L.; Song, Y.; Jia, Q.; Zhang, Z.; Du, M. *Biosensors and Bioelectronics* **2019**, *142*, 111536.

(159) Yan, X.; Song, Y.; Liu, J.; Zhou, N.; Zhang, C.; He, L.; Zhang, Z.; Liu, Z. *Biosensors & Bioelectronics* **2019**, *126*, 734-742.

(160) Neisi, Z.; Ansari-Asl, Z.; Jafarinejad-Farsangi, S.; Tarzi, M. E.; Sedaghat, T.; Nobakht, V. *Colloids and Surfaces B-Biointerfaces* **2019**, *178*, 365-376.

(161) Hu, M.; Li, Z.; Guo, C.; Wang, M.; He, L.; Zhang, Z. *Applied Surface*

Science **2019**, *489*, 13-24.

(162) He, L.; Duan, F.; Song, Y.; Guo, C.; Zhao, H.; Tian, J.; Zhang, Z.; Liu, C.; Zhang, X.; Wang, P.; Du, M.; Fang, S. *2D Materials* **2017**, *4*, 025098.

(163) He, L.; Li, Z.; Guo, C.; Hu, B.; Wang, M.; Zhang, Z.; Du, M. *Sensors and Actuators B-Chemical* **2019**, *298*, 126852.

(164) Tian, K.; Ma, Y.; Liu, Y.; Wang, M.; Guo, C.; He, L.; Song, Y.; Zhang, Z.; Du, M. *Sensors and Actuators B: Chemical* **2020**, *303*, 127199.

(165) Kasyanenko, N. A.; Tikhomirov, R. A.; Bakulev, V. M.; Demidov, V. N.; Chikhirzhina, E. V.; Moroshkina, E. B. *ACS Omega* **2019**, *4*, 16935-16942.

(166) Wuttke, S.; Zimpel, A.; Bein, T.; Braig, S.; Stoiber, K.; Vollmar, A.; Müller, D.; Haastert-Talini, K.; Schaeske, J.; Stiesch, M.; Zahn, G.; Mohmeyer, A.; Behrens, P.; Eickelberg, O.; Bölükbas, D. A.; Meiners, S. *Advanced Healthcare Materials* **2017**, *6*, 1600818.

(167) Hashkavayi, A. B.; Raoof, J. B.; Ojani, R.; Kavoosian, S. *Biosensors & Bioelectronics* **2017**, *92*, 630-637.

(168) Zhang, F. R.; Lu, J. Y.; Yao, Q. F.; Zhu, Q. Y.; Zhang, X. X.; Huang, W. T.; Xia, L. Q.; Ding, X. Z. *Analyst* **2019**, *144*, 1881-1891.

(169) Jia, S.; Li, P.; Koh, K.; Chen, H. *Microchimica Acta* **2016**, *183*, 683-688.

(170) Sharma, R.; Agrawal, V. V.; Sharma, P.; Varshney, R.; Sinha, R. K.; Malhotra, B. D. *Journal of Physics-Conference Series* **2012**, *358*, 012001.

(171) Cao, J.; Zhao, X.; Younis, M. R.; Li, Z.; Xia, X.; Wang, C. *Analytical Chemistry* **2017**, *89*, 10957-10964.

(172) Bi, S.; Ji, B.; Zhang, Z.; Zhang, S. *Chemical Communications* **2013**, *49*, 3452-3454.

(173) Mohammadi, S.; Salimi, A.; Hamd-Ghadareh, S.; Fathi, F.; Soleimani, F. *Analytical Biochemistry* **2018**, *557*, 18-26.

(174) Ding, X.; Han, B. *Angewandte Chemie International Edition* **2015**, *54*, 6536-6539.

(175) Chen, S.; Sun, T.; Zheng, M.; Xie, Z. *Advanced Functional Materials*

2020, *30*, 2004680.

(176) Jia, Q.; Li, Z.; Guo, C.; Huang, X.; Kang, M.; Song, Y.; He, L.; Zhou, N.; Wang, M.; Zhang, Z.; Fu, G.; Du, M. *Chemical Engineering Journal* **2020**, *389*, 124468.

(177) Neti, V. S. P. K.; Wu, X.; Hosseini, M.; Bernal, R. A.; Deng, S.; Echegoyen, L. *CrystEngComm* **2013**, *15*, 7157-7160.

(178) Chen, H.; Wang, S.; Tang, Y.; Zeng, F.; Schobert, H.; Zhang, X. *Fuel* **2021**, *292*, 120373.

(179) Zhang, L.; Xiao, Y.; Yang, Q.; Yang, L.; Wan, S.; Wang, S.; Zhang, L.; Deng, H.; Sun, Z. *Advanced Functional Materials* **2022**, *n/a*, 2201542.

(180) Zhao, S.; Li, J.; Song, S. *Journal of Energy Storage* **2022**, *51*, 104416.

(181) Chen, K.; Cao, M.; Lin, Y.; Fu, J.; Liao, H.; Zhou, Y.; Li, H.; Qiu, X.; Hu, J.; Zheng, X.; Shakouri, M.; Xiao, Q.; Hu, Y.; Li, J.; Liu, J.; Cortés, E.; Liu, M. *Advanced Functional Materials* **2022**, *32*, 2111322.

(182) Li, M.; Khoshdel, E.; Haddleton, D. M. *Polymer Chemistry* **2013**, *4*, 4405-4411.

(183) Mejia-Ariza, R.; Huskens, J. *Journal of Materials Chemistry B* **2016**, *4*, 1108-1115.

(184) Guo, J.; Dai, J.; Peng, X.; Wang, Q.; Wang, S.; Lou, X.; Xia, F.; Zhao, Z.; Tang, B. Z. *ACS Nano* **2021**, *15*, 20042-20055.

(185) Li, S.; Yang, W.; Liu, Y.; Song, X.; Liu, R.; Chen, G.; Lu, C.; Yang, H. *Nano Research* **2018**, *11*, 4859-4873.

(186) Zhong, Y.; Zhang, X.; Yang, L.; Liang, F.; Zhang, J.; Jiang, Y.; Chen, X.; Ren, F. *Materials Science and Engineering: C* **2021**, *131*, 112524.

(187) Zheng, B.; He, Q.; Li, X.; Yoon, J.; Huang, J. *Coordination Chemistry Reviews* **2021**, *426*, 213548.

(188) Mu, J.; Xiao, M.; Shi, Y.; Geng, X.; Li, H.; Yin, Y.; Chen, X. *Angewandte Chemie International Edition* **2022**, *61*, e202114722.

(189) Wang, J.; Li, J.; Wang, L.; Han, T.; Wang, D.; Tang, B. Z. *ACS Applied Polymer Materials* **2020**, *2*, 4306-4318.

(190) Li, S.; Jiang, P.; Jiang, F.; Liu, Y. *Advanced Functional Materials* **2021**, *31*, 2100243.

(191) Zhai, T.; Zhong, W.; Gao, Y.; Zhou, H.; Zhou, Z.; Liu, X.; Yang, S.; Yang, H. *ACS Applied Materials & Interfaces* **2021**, *13*, 39100-39111.

(192) Zhang, Y.; Sha, W.; Liu, Y.; Wang, W.; Yuan, Z. *Materials Chemistry Frontiers* **2020**, *4*, 3047-3056.

(193) Jin, H.; Zhong, W.; Yin, S.; Zhang, X.; Zhao, Y.; Wang, Y.; Yuan, L.; Zhang, X. *ACS Applied Materials & Interfaces* **2019**, *11*, 3800-3808.

(194) Zhu, L.; Liang, G.; Guo, C.; Xu, M.; Wang, M.; Wang, C.; Zhang, Z.; Du, M. *Food Chemistry* **2022**, *366*, 130575.

(195) Chen, L.; Ye, X.; Chen, S.; Ma, L.; Wang, Z.; Wang, Q.; Hua, N.; Xiao, X.; Cai, S.; Liu, X. *Ceramics International* **2020**, *46*, 25895-25904.

(196) Reji, R. P.; Marappan, G.; Sivalingam, Y.; Jayaraman Surya, V. *Materials Letters* **2022**, *306*, 130945.

(197) Duan, F.; Hu, M.; Guo, C.; Song, Y.; Wang, M.; He, L.; Zhang, Z.; Pettinari, R.; Zhou, L. *Chemical Engineering Journal* **2020**, *398*, 125452.

(198) Han, X.; Si, T.; Liu, Q.; Zhu, F.; Li, R.; Chen, X.; Liu, J.; Sun, H.; Zhao, J.; Ling, H.; Zhang, Q.; Wang, H. *Chemical Engineering Journal* **2021**, *426*, 130824.

(199) Bilgiçli, A. T.; Hepokur, C.; Bilgicli, H. G.; Tüzün, B.; Günsel, A.; Mısır, S.; Zengin, M.; Yarasir, M. N. *Dalton Transactions* **2021**, *50*, 15778-15792.

(200) Zhang, X.; Yu, L.; Zhuang, C.; Peng, T.; Li, R.; Li, X. *ACS Catalysis* **2014**, *4*, 162-170.

(201) Zhang, H.; Zhang, J.; Li, Y.; Jiang, H.; Jiang, H.; Li, C. *Journal of Materials Chemistry A* **2019**, *7*, 13506-13510.

(202) Wu, F.; Zhang, Q.; Sun, B.; Chu, X.; Zhang, M.; She, Z.; Li, Z.; Zhou, N.; Wang, J.; Li, A. *Journal of Controlled Release* **2021**, *338*, 46-55.

Acknowledgements

I would like to give my heartfelt thanks to all the people who have ever helped me during my PhD studies.

My sincere and hearty thanks and appreciations go to my supervisor, Prof. Riccardo Pettinari, who's carefully guided me to synthesize a series of organometallic complexes. It has been a great privilege to study under his guidance and supervision. Furthermore, I am very grateful to Prof. Zhihong Zhang, whose advice and encouragement enabled me to have more understanding of the research of porous framework materials. I am honored to have benefited from the personality and diligence of two professors that I will cherish all my life. My gratitude to them knows no bounds.

I am also extremely grateful to Prof. Liming Zhou and Dr Qiaojuan Jia, who have kindly provided me assistance while preparing this paper.

I also express my appreciation to all my friends and classmates who have lectured me for their insightful lectures which are of great benefit to me in my research.

Finally, many thanks go to my family for their unfailing love and unwavering support.

List of Publications

[1] R. Pettinari, F. Marchetti, A. Tombesi, **F. Duan**, L. Zhou, L. Messori, C. Giacomelli, L. Marchetti, M.L. Trincavelli, T. Marzo, D. La Mendola, G. Balducci, E. Alessio, Ruthenium(II) 1,4,7-trithiacyclononane complexes of curcumin and bisdemethoxycurcumin: Synthesis, characterization, and biological activity, J. Inorg. Biochem. 218 (2021) 111387.

[2] **F. Duan**, M. Hu, C. Guo, Y. Song, M. Wang, L. He, Z. Zhang, R. Pettinari, L. Zhou, Chromium-based metal-organic framework embedded with cobalt phthalocyanine for the sensitively impedimetric cytosensing of colorectal cancer (CT26) cells and cell imaging, Chem. Eng. J. 398 (2020) 125452.

[3] F. Duan, C. Guo, M. Hu, Y. Song, M. Wang, L. He, Z. Zhang, R. Pettinari, L. Zhou, Construction of the 0D/2D heterojunction of $Ti_3C_2T_x$ MXene nanosheets and iron phthalocyanine quantum dots for the impedimetric aptasensing of microRNA-155, Sensors and Actuators B: Chemical. 310 (2020) 127844.

[4] **F. Duan**, F. Rong, C. Guo, K. Chen, MH Wang, ZH Zhang, R. Pettinari, LM Zhou, M. Du. Electrochemical aptasensing strategy based on a multivariate polymertitanium-metal-organic framework for zearalenone analysis[J]. Food Chemistry, 2022, 385: 132654.